SHOCK COMPRESSION INDUCED PHASE CHANGES IN CERIUM-BASED METALLIC GLASS

A Thesis
Presented to
The Academic Faculty

By

Alex W. Bryant

In Partial Fulfillment
of the Requirements for the Degree
Doctor of Philosopy in the
School of Materials Science and Engineering

Georgia Institute of Technology

August 2018

SHOCK COMPRESSION INDUCED PHASE CHANGES IN CERIUM-BASED METALLIC GLASS

Approved by:

Dr. Naresh Thadhani
School of Materials Science and Engineering
Georgia Institute of Technology

Dr. Faisal Alamgir
School of Materials Science and Engineering
Georgia Institute of Technology

Dr. Josh Kacher
School of Materials Science and Engineering
Georgia Institute of Technology

Dr. Arun M. Gokhale
School of Materials Science and Engineering
Georgia Institute of Technology

Dr. Christopher Wehrenberg
NIF and Photon Science Directorate
Lawrence Livermore National Laboratory

Date Approved: April 30, 2018

For my brother, who inspired me to look deeper into everything and everyone, and for my friends and family who help me see further.

ACKNOWLEDGEMENTS

This work was funded by ARO Grant No. W9HNF-09-1-0403 and the NSF Graduate Research Fellowship awarded to Alex Bryant under Grant No. 0946809. Synchrotron characterization was performed at Brookhaven National Laboratory's National Synchrotron Light Source (NSLS) and NSLS-2, beamlines X-7B and X-3B (NSLS) and 28-ID-2 (NSLS-2), U.S. DOE Office of Science User Facilities operated under Contract No. DE-AC02-98CH10886 and DE-SC0012704, respectively. OMEGA laser experiments were performed at the Laboratory for Laser Energetics through a partnership with Dr. Chris Wehrenberg at Lawrence Livermore National Laboratory. Atom Probe Tomography and TEM experiments were performed at the Center for Nanophase Materials Sciences, a DOE Office of Science User Facility at Oak Ridge National Laboratory. Ce_3Al metallic glass melt-spun ribbons were produced at Ames Laboratory.

I want to particularly thank Dr. Wenqian Xu and Dr. Erik Farquhar for their help at Beamlines X7B and X3B, respectively, and Dr. Samson Lai for help and discussion at both while at NSLS. Similarly, I could not have gathered the data or made the analyses I did without the help of Dr. Eric Dooryhee and Dr. Sanjit Ghose at Beamline 28-ID-2 at NSLS-2. Dr. Karren More at ORNL was a tremendous help with TEM measurements and analyses and Dr. Jonathan Poplawsky was very supportive with APT experiments and interpretation. Both made my trips to ORNL impactful and fun. This work could not have been done without the generous support of experts across the country.

I am indebted to my advisor, Dr. Naresh Thadhani, for his guidance and feedback throughout the process of creating this project and pivoting it through all of the unexpected paths. I sincerely appreciate his support for my ideas as well as for emphasizing work/life balance - something truly rare in the field of academia. I would also like to thank Dr. Chris Wehrenberg for helping significantly with the development and implementation of my OMEGA experiments, his HYADES simulations, discussion about analyses, and his

support for further collaboration. Similarly, I would like to thank Dr. Faisal Alamgir for helping me expand my research into synchrotron characterization (a personal dream of mine since I first heard about the technique) and helping with my EXAFS analysis and interpretation of results. Finally, I would like to thank my committee members, Dr. Josh Kacher and Dr. Arun Gokhale for their helpful discussions about my work and support for my ideas.

I could not have made it through the Ph.D. without my family and all the close friends I made. In particular, Dr. David Scripka and Dr. Rene Diaz helped me navigate my research and personal life and are now like a second family - I could not have expected to have made such tight bonds with my officemates in grad school but I am very thankful I did. Dr. Stefany Holguin was with me from the days of grad school visits and was always supportive and up for a good long conversation. Dr. Samson Lai was there for my research highs and lows and chats about philosophy and nerd culture in between. Everyone in the Thadhani research group has been incredibly great to get to know and work with. Thank you to Sukanya Sharma for the support at the end and fun chats along the way, Travis Voorhees for always keeping a calm head, Dr. Jennifer Breidenich for the sage advice at the beginning, Dr. Manny Gonzales for the deep talks and serious support, Andrew Boddorff for the laughs and board games, Dr. Sean Kelly for getting the laser up and running, and Dr. Greg Kennedy for keeping the lab going.

Thank you to my parents for always pushing me to succeed at whatever I was interested in, keeping me focused on the important things, and helping me whenever I got off-track.

TABLE OF CONTENTS

LIST OF TABLES

LIST OF FIGURES

SUMMARY

The research performed in this work was aimed at investigating pressure-induced phase changes in a Ce-based metallic glass (MG) through the use of laser-driven shock experiments and atomic resolution structural characterization. MGs exhibit very high strength, have intrinsically low density, and plastically deform by shear banding. MGs are also metastable and can undergo phase changes upon heating and/or application of high pressure into higher density configurations. The atomic structure changes concomitant with these phase transitions occurring during high pressure shock compression are not well understood, which provides the motivation for the present work.

Thermal analysis of Ce_3Al MG melt-spun ribbons was first performed to characterize the crystallization response and structure. Ce_3Al MG was found to strongly resist growth of crystallites but easily nucleate. Thermal crystallization occurs via a two-stage primary path wherein a metastable phase forms and converts fully into the hexagonal-intermetallic α-Ce_3Al. The Avrami number and dimensionality constants indicate the crystallization occurs via plate-like growth, resulting in thermally crystallized grains on the order of 6 nm and a density $\sim$4% greater than the reference α-Ce_3Al.

Shock compression experiments performed using the Nd:YAG 3 J laser and velocity interferometry allowed for *in operando* measurements of particle velocity coupled with sample recovery for structural analysis. The results provide a clear indication of the Hugoniot Elastic Limit (at $\simeq$ 1.8 GPa) as evidenced by the presence of a two wave structure in the velocity profile. At shock pressures exceeding the elastic limit, plastic deformation of the Ce_3Al MG occurs via structural transformation to the crystalline state forming α-Ce_3Al with nanocrystalline grain sizes, higher densities, and plate-like growth. The trends suggest that shock compression causes break-up of grains, higher densities due to Ce 4f delocalization, and increased preferred orientation.

Shock compression experiments were also performed using the 50 J Omega laser fa-

cility at the Laboratory for Laser Energetics. A stack of samples was shock-compressed with pressures progressively decreasing across the stack thickness, resulting in two regimes of recovered samples. Highly deformed and partly damaged samples close to the shock front showed varying degrees of long-range order, medium-range order, and short-range order with distance away from the shock front. Visually undeformed samples showed decreased bond lengths for the nearest-neighbors, second nearest-neighbors, and fourth nearest-neighbors but increased bond lengths for the third nearest-neighbors, with associated densification of $\sim$2-6% in all layers. These changes in the undeformed samples are indicative of polyamorphism. The visually undeformed samples also reveal an increase in magnitude of structural change with increased distance away from the shock-front, up to a maximum beyond which increasing distance decreases the magnitude of the bond length shifts. This trend is indicative of competing effects for densification and dilation, associated with the extreme and complex states generated.

The mechanism and characteristics of the shock induced crystallized Ce_3Al MG are different from the hydrostatic pressure-induced crystallization of Ce_3Al MG (which occurs via a coordinated and instantaneous rearrangement of all atoms into the FCC-Ce_3Al phase) and thermal crystallization into α-Ce_3Al (which occurs via diffusional nucleation and growth). Shock-induced crystallization during shock compression occurs in a nucleation-like collective rearrangement with limited kinetic allowance for growth, resulting in larger crystallites than could nucleate through thermal processes. The dilatory effects and increased driving forces caused by shear bands and shock-induced heating result in larger grain sizes and longer lattice parameters. Increases in shock pressures appear to create larger driving forces for the formation of [020] preferred orientations (possibly indicative of lower energy plate-like geometries) and higher densities while simultaneously breaking crystallites into smaller sizes.

CHAPTER 1
INTRODUCTION AND OBJECTIVES

Metallic glasses (MGs) are of significant interest due to their unique amorphous structure. This structure lacks any of the directionality of ionic and covalent type glasses and results in preferable properties such as superior strengths, low densities, and excellent corrosion and wear resistance [1]. Without directional bonding, there are many more potential short-range order (SRO) atomic clusters and medium-range order (MRO) packings of these atomic clusters possible. Experimental studies and simulations have indicated MG SRO trends toward high coordination numbers (CNs), demonstrating a preference in MGs for lower energy atomic packing arrangements. Similarly, these high-CN SRO clusters appear to be themselves packed together in an efficient way - resulting in MRO [2, 3, 4]. Recent structural models, which take into account the composition and atomic radii differences to predict an efficient topological packing in the SRO and MRO, show strong matches with the experimental data [5, 6, 7, 8, 9, 10]. For all MGs, however, there are a range of CNs, SRO, and MRO structures heterogeneously distributed through the material. These structures can be tuned via thermal or mechanical processing toward higher free volumes through rejuvenation [11, 12, 13] or lower free volumes through relaxation [14, 15, 16, 17].

Areas of the local structure with greater free volume are theorized to act as strain localization sites, converting into shear transformation zones (STZs) [18]. As these STZs grow in number and size under applied stress, they connect and form shear bands - causing permanent deformation. Shear bands can also form along with [19, 20, 21, 22, 23] or without [24, 25] crystallization. When they form without crystallization, the free volume within each of the bands is significantly increased, and the thermodynamic barrier to crystallization is lowered. Crystallization observed concomitant with shear band formation is theorized to be due to localized heating around the STZs or shear band, which indicates that

crystallization may not occur simultaneously with shear band formation. With increased pressure, one would expect there to be a larger driving force for crystallization; however, hydrostatic compression studies indicate reduced atomic mobility is of greater effect, retarding crystallization [26, 27]. Conversely, increased temperatures or other dilatory effects such as shear can aid atomic mobility and accelerate crystallization [28].

Under hydrostatic compression, shear is non-existent, STZs cannot form, and deformation does not occur in a MG. Therefore, hydrostatic compression allows for the study of isolated pressure effects in a MG. Hydrostatic compression of Ce_3Al MG between 1.5 to 5 GPa causes Ce 4f electron delocalization, resulting in effectively smaller Ce atoms. It has been shown that initially, this results in a polyamorphous transition to a higher density amorphous phase [29, 30], and at 25 GPa, Ce_3Al MG instantly crystallizes into a single crystal, solid solution FCC phase [31].

Under higher strain rate shock-compression conditions, larger amounts of free volume are created during deformation of a MG [32]. This increase in free volume decreases the barrier to shear band formation. According to Demetriou and Johnson [33] studies of shear rate effects on crystallization kinetics of a deeply undercooled glass-forming liquid, higher strain rates result in decreased viscosity, which causes crystallization at lower temperatures.

Few experiments have been performed characterizing the effects on the MG structure under high-strain-rate or shock-compression loading [34]. Velocimetry measurements performed during shock-compression of bulk MGs have indicated the shock-induced formation of a higher density amorphous phase [35, 36]. X-ray diffraction (XRD) characterization of a recovered sample showed no observable change, indicating the density increase was reversible on unloading in the shocked bulk MG [36]. Laser shock-compression experiments performed by Chen et. al. [37] on Ce_3Al metallic glass showed evidence of a pressure-induced 7% densification. The pressure at which the densification began and the magnitude of densification were both comparable to the hydrostatically-induced polyamorphous transition for Ce_3Al MG.

Computational simulations indicate that under shock-compression beyond the Hugoniot elastic limit, STZs form behind the shock front, increasing in number and homogeneity as pressures increase [38, 39, 40]. Beyond a certain pressure, the sample is observed to have much higher atomic mobility, indicating melting. At the pressures below melting, the region behind the shock front is shown to have increased CN, likely representing the effects of high shear and pressure in allowing for reorganization into denser atomic packing. However, limitations of simulations in size and duration mean that it is unclear if crystallization can occur due to shock-compression, if the higher CN reverts upon unloading, or what role melting may play on the final structure. Further, limitations of atomic potentials prevent simulations from taking into account effects of any elements in the MG which can themselves undergo pressure-induced changes, like the 4f delocalization of Ce.

There exists a clear need for in depth structural characterization of shock-compressed metallic glass samples. This work fulfills that need and correlates the structural measurements with velocimetry characterization of time-resolved changes in compressibility, coupled with the in-depth structural characterization of the recovered samples following shock compression. Comparisons also need to be made between thermal and shock-compression effects on structural changes to help determine what role, if any, shock-induced heating may play in the overall shock-compression response.

The overall objective of this research is to better understand the shock-induced phase changes and structural evolutions in binary Ce_3Al MG melt-spun ribbon samples. Shock-compression experiments were performed using Nd:YAG and OMEGA lasers with velocimetry providing information about the loading conditions. Recovery of the samples was followed by advanced structural characterization via synchrotron X-ray scattering and extended X-ray-absorption fine-structure analyses. This research is the first of its kind to characterize the effects of shock-compression on the structure of the Ce_3Al MG.

The particular objectives of this work are:

1. To determine the occurrence of shock-induced phase changes in the Ce_3Al metallic

glass at pressures up to $\sim 90\,\mathrm{GPa}$

2. To characterize the atomic-scale structural changes corresponding to different pressure regimes

3. To investigate the role of temperature and pressure on the observed phase transitions based on thermal analysis, time-resolved velocimetry measurements, and *post-mortem* structural characterization.

In this dissertation, Chapter 2 provides a brief background on structure, phase stability, and deformation behavior of metallic glass and their response to high pressure shock-compression. Chapter 3 furnishes details about the material investigated and the experimental procedures. Chapters 4-6 report the results of experiments involving thermal analysis, shock compression experiments performed using Nd:YAG laser with velocimetry and recovery, and OMEGA laser shock compression experiments with X-ray characterization of the recovered shock compressed Ce_3Al samples. A summary and discussion in Chapter 7 compiles and analyzes the results of all experiments and loading conditions, culminating in the conclusions and recommendations for future work presented in Chapter 8.

CHAPTER 2
BACKGROUND

Metallic glasses (MGs) are solids that have an atomic structure similar to that of a viscous liquid. Due to their metastable state, MGs require unique processing and compositional control to be created [41]. Further, the metastability means there are many potential low energy structural arrangements within the glassy phase or upon crystallization, which can be reached through thermal or mechanical processes [42, 43]. For some compositions, phase transformations can be induced under hydrostatic compression due to electronic structure changes of component elements at high pressures [44, 45]. The amorphous structure often provides high strength, wear resistance, and brittleness due to deformation occurring via shear banding, [1]. Crystallization of the glass can also occur under conditions of stress application [18]. Increasing strain rate raises the propensity for shear localization, causing more shear bands to form and increasing the likelihood and resultant crystallization [34]. Under shock-compression, new high-pressure phases can form [35, 36], and reorganization can occur behind the shock front producing higher density amorphous phases [40, 39]. In this chapter, the metallic glass structure, and the synthesis, phase stability, and deformation behavior of metallic glass under quasistatic and dynamic loading conditions will be discussed.

2.1 Metallic Glass Structure

Since metallic glasses were first discovered, experimental observations have shown that they lack long-range order (LRO) but appear to have short- (SRO) and medium-range order (MRO). While this might be expected for covalent or ionic bonded glasses because their limited bonding angles result in distinct short-range units which connect into medium-range order networks, the metallic bonds in MGs do not restrict bonding angles and there-

fore allow for a much wider range of short-range ordering. As such, there has been significant interest in determining what causes the short and medium-range order in MGs.

Theoretical considerations of these structures have improved greatly as simulations have become more common, and an interested reader can find a great overview of this history and the current status in the 2011 review article by Cheng and Ma [46]. For each theory, the goal has been to match experimental observations. However, this is not currently possible for MGs with more than three elemental components as the number and overlap of constituent atomic bond lengths grows rapidly with additions of more elements, making it very difficult to confirm validity of structural models. As such, most detailed structural analysis research for MGs has focused on two or three element (binary or tertiary) MGs, where the number of bonds are limited to three or six, respectively. An overview of the experimental observations, interpretations, and current structural theories for these binary and tertiary MGs follows.

2.1.1 Experimental Methods of Metallic Glass Structure Characterization

X-ray and Neutron Diffraction

X-ray diffraction (XRD) and neutron diffraction analysis allow for the direct measurement of the average structure of a material. Due to tunable energies, the X-ray or neutron wavelengths are on a similar order of magnitude as the atoms, allowing for representative scattering from atoms within the material. Figure 2.1 illustrates an example of an XRD trace for a crystalline material as well as a MG with comparable composition. Whereas the crystalline peaks correspond to fulfillment of the Bragg condition, representing distinct repeating planes of atoms in the atomic lattice, the broad peaks of the amorphous sample are due to scattering of the atomic nearest neighbors (SRO) and next nearest neighbors (MRO). The increased spread in the local atomic coordination of a MG as compared to the atomic planes of crystalline unit cells results in a wider range of atomic bond lengths each partially fulfilling the Bragg condition and a concomitant increase in the broadness of the

XRD peaks. The lack of peaks at higher 2θ angles in the MG scattering trace is representative of significant statistical spread in atomic positions when considering regimes beyond the MRO, meaning there is no long-range order.

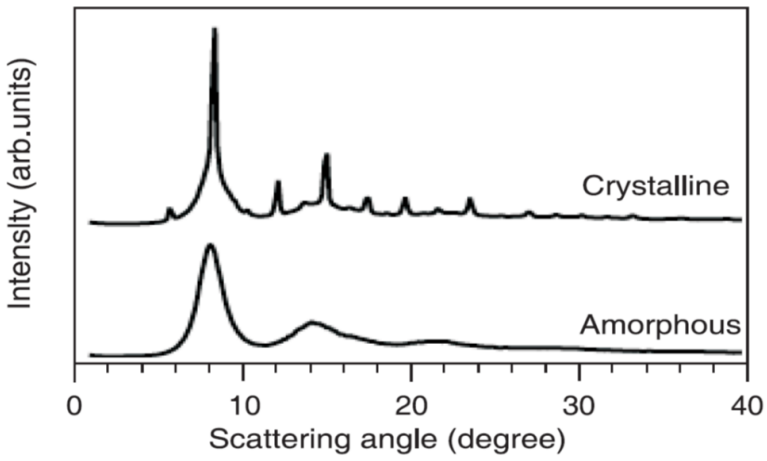

Figure 2.1: Example of X-ray diffraction (XRD) traces of a MG and its comparable crystalline state. Due to the amorphous structure of a MG, its scattering fulfills the Bragg diffraction condition for a wide range of atomic bond lengths and yields broad peaks. Furthermore, due to a lack of long-range order, the MG does not exhibit peaks at higher 2θ angles unlike the sharp peaks in the crystalline material. [47]

Structure Factor

The measured scattering intensity from X-ray or neutron diffraction experiments can also be converted to the total structure factor, $S(q)$, via Equation 2.1:

$$S(q) = \frac{I_C(q) - \langle f^2 \rangle + \langle f \rangle^2}{\langle f \rangle^2} \tag{2.1}$$

where I_C is the measured coherent scattering determined from the original data after processing (e.g. removing background, or removing multiple or incoherent scattering, etc.) and $\langle f \rangle$ is the average atomic scattering factor for all of the components ($\langle f \rangle = \sum_\alpha (c_\alpha f_\alpha)$).

Equation 2.1 shows that the general trends of the structure factor are very similar to $I_C(q)$ and will therefore be similar to those of X-ray diffraction. However, because the structure factor takes into account the scattering factor for the material, it can be used to

determine additional properties of the material. For example, it has been shown that for MGs the position of the first peak of the structure factor, q_1 follows a power-law scaling relationship with respect to the atomic volume, v_a, as shown in Equation 2.2 [48], and recently validated with high pressure studies [49, 50].

$$q_1 \cdot v_a^{0.433} = 9.3 \tag{2.2}$$

Notably, this calculated atomic volume only takes into account the short and medium-range order from the first peak of the structure factor; it does not capture information of any mesoscale or macroscopic structures, and, while it can be used to compare relative changes in density, it may not provide absolute values of density.

Pair Distribution Function

Through a Fourier transform, the structure factor can be converted to the atomic pair distribution function (PDF), $g(r)$, defined in Equation 2.3:

$$g(r) = \frac{1}{4\pi r^2 \rho N} \sum_{i=1}^{N} \sum_{j=1, j\neq i}^{N} \delta(r - |\vec{r}_{ij}|) \tag{2.3}$$

where ρ is the number density of atoms in the system of N atoms, r is the radial distance from an average center atom, and $|\vec{r}_{ij}|$ is the interatomic distance between two atoms (i and j). If measured using a technique that allows for elemental specificity (e.g., extended X-ray-absorption fine-structure analysis (EXAFS) or neutron scattering), the $\alpha - \beta$ partial PDF (where α and β are specific elements) may be determined as well, which is defined as Equation 2.4:

$$g_{\alpha\beta}(r) = \frac{N}{4\pi r^2 \rho N_\alpha N_\beta} \sum_{i=1}^{N_\alpha} \sum_{j=1}^{N_\beta} \delta(r - |\vec{r}_{ij}|) \tag{2.4}$$

where N_α and N_β are the number of atoms of type α and β, respectively, and the interatomic distance $|\vec{r}_{ij}|$ is between atom i of type α and atom j of type β.

The total PDF is an averaging measurement of all elemental bond lengths (e.g., A-A, B-B, and A-B for a A_xB_y material) in radial distances from an average center atom in a probed area. In a plot of the PDF, as a function of radial distance, each measured bond length contributes to a peak positioned along the x-axis, and the intensity corresponds to the number of bonds measured of that particular length. The peak increases in width as the possible range of values increases for this bond length. For a MG, the lack of atomic periodicity produces a wider range of bond lengths than would exist for a crystalline material, resulting in wider peaks for a MG. The limited MRO and lack of long-range periodicity in a MG results in a steady decrease in intensity of peaks beyond the first, and a complete loss of intensity as the radial distance extends beyond the first few nearest neighbors (corresponding to $\sim$1-2 nm for most compositions).

Figure 2.2 shows, as an example, a schematic of a PDF profile for an amorphous material and an illustration of the atomic coordination contribution. In this example, the sample only has one atom size, causing the average first nearest neighbor position to center around the diameter of one atom, σ, as shown in the illustration. The deviations from the one-atom-diameter position are representative of the disorder and overall spread of potential positions of atoms within the sample. For samples with more than one element (e.g., A_xB_y), there are more possible bond lengths (e.g. A-A, A-B, or B-B) and the peaks accordingly increase in width. If short or medium-range order increases in a MG with more than one element, the peaks may separate into multiple distinct peaks representing each of the bonds (e.g., a peak each for A-A, A-B, and B-B) [51].

As atomic order increases, PDF peaks separate into distinct peaks representing the periodic packing of atoms. In a crystalline material, there are distinct bond lengths corresponding to the periodic lattice planes and determined by the symmetry, composition, and atom sizes of the phase. The bond length for each of these planes, corresponding to the distance from a representative average center atom position to an atom in that plane, would be visible as individual peaks. Therefore, any broadness of the peaks is representative of

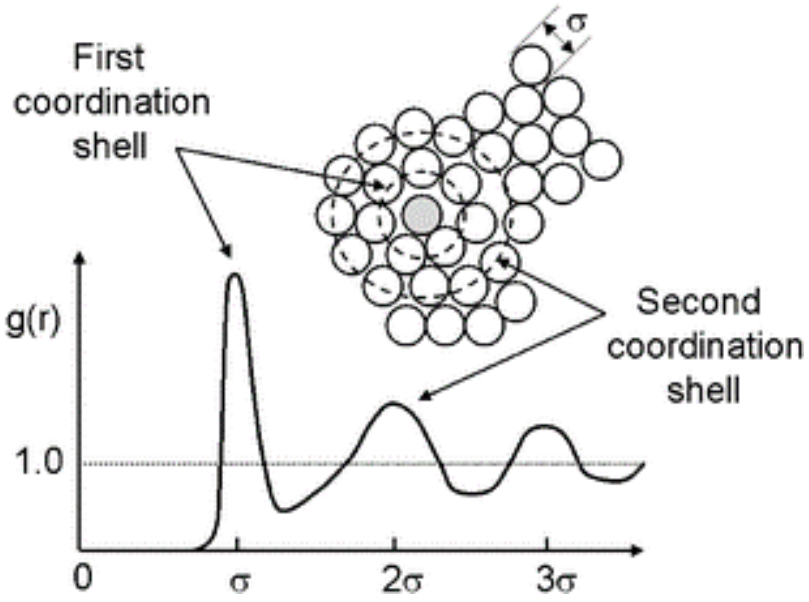

Figure 2.2: Schematic illustrating the contribution of the first and second atomic coordination shells of a single-element amorphous structure to the peaks of the pair distribution function (PDF), g(r). The atom diameter, σ, represents the average bond length for the first nearest neighbor, and disorder in the structure causes a distribution of potential bond lengths around σ. Beyond the first coordination shell, there are more potential arrangements and corresponding bond lengths leading to a broader second peak centered around the average of two atom diameters. If this were to show higher radial distances, the intensity of each peak would continue to decrease and eventually reach zero due to the lack of any long-range order in an amorphous material. [52]

disorder or overlapping bond lengths from different planes. Higher order periodicities, e.g., from considering multiples of planes ($[100] \rightarrow [200]$), are similarly visible, which is why crystalline materials have PDF peaks observable at higher radial distances as compared to MGs. However, the decreased statistical likelihood of finding an atom in one of the higher order periodic planes as compared to the lower order atomic planes results in decreased intensity for the higher radial distance peaks.

For example, Figure 2.3 shows the reduced PDF (the conversion between reduced PDF and PDF will be discussed in Chapter 3) for an initial $Fe_{72.5}Cu_1Nb_2Mo_2Si_{15.5}B_7$ MG sample, the same sample after annealing at $500\,^{\circ}\mathrm{C}$ for $30\,\mathrm{min}$ (causing partial crystallization), and the same sample after heating at $500\,^{\circ}\mathrm{C}$ for $120\,\mathrm{min}$ (causing full crystallization). As described previously, the PDF of the crystalline samples exhibit sharper peaks at longer

bond lengths as the annealing time increases, representing the increase in crystallinity with increased annealing time. The SRO and MRO corresponding to the first few nearest neighbors are very similar between the amorphous and crystalline conditions, indicating an efficiency of the SRO and MRO in the amorphous phase comparable to that of the crystalline phase.

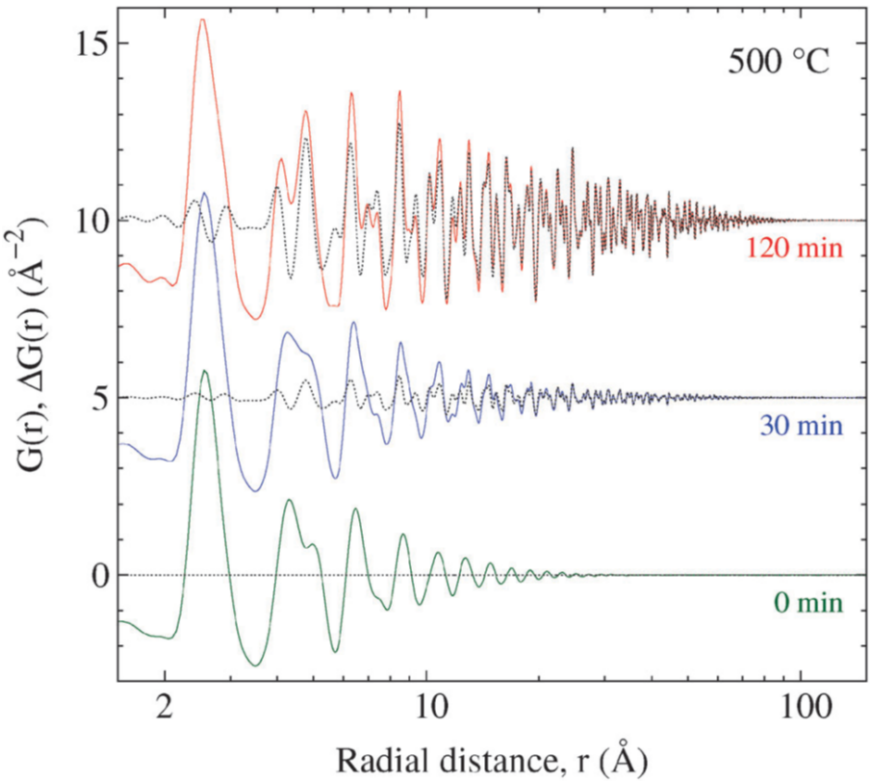

Figure 2.3: Example of reduced PDF (G(r)) traces for MG and crystalline samples of composition $Fe_{72.5}Cu_1Nb_2Mo_2Si_{15.5}B_7$. Increasing 500 °C isothermal annealing times correlate to increased crystallinity, observed as increasingly sharp peaks which persist to longer distances. Solid traces are the PDFs and dotted traces are the difference between the annealed PDF and the initial MG PDF. Amorphous samples, with disordered local structures and no long-range order, have wider peaks and more rapid attenuation of the peaks as compared to the crystalline samples. [53]

Transmission Electron Microscopy

Although high-resolution transmission electron microscopy (HRTEM) imaging enables direct observation of atomic-level structure and therefore might be expected to be an effective

way to characterize the structure of MG, it is limited to typically only 2D projections of multiple layers of atoms. In a periodic crystal, this can be effective due to atomic periodicity and the adjustable angles possible for the incident electrons and detector, but in a glass, there are no angles at which anything other than maze-like patterns are present. Further, sample preparation can easily introduce artifacts into the metastable MG, corrupting meaningful data [54, 55, 56, 57]. As such, HRTEM imaging is typically used for determining overall amorphous nature of the region or characterization of local voids or nanocrystals [58, 59, 60], but it is rarely used for quantitatively studying the structure of MGs.

In comparison, electron diffraction in a TEM may be used to characterize details about the structure of the MG. Similar limitations of sample preparation apply [54, 55, 56, 57], but the average measurements make it comparable to X-ray or neutron scattering when allowing for structure factor and PDF calculations. The resolution of electron diffraction is typically limited when compared to high energy, high intensity X-rays (as from a synchrotron) or neutrons (as from a spallation neutron source), so quantitative comparisons of minute changes are not feasible using this technique. However, in recent work the electron beam has been focused down to a spot small enough to measure SRO directly [61, 62, 63], potentially opening the door to characterization of the local order distribution in MGs through a raster-like scan of focused electron diffraction measurements.

2.1.2 Theoretical Models for Metallic Glass Structure

Although experimental studies of MGs showing the SRO and MRO described in Section 2.1.1 date back to the 1950s, the structure of metallic glasses is still not fully understood. Initial models based on random packing of hard spheres [64, 65, 66], microcrystalline ($\sim$150 atom "grains") [67, 68, 69], or quasicrystalline packing [70] have been unable to fully explain data obtained from experiments.

Miracle's recent model [5, 6, 7, 8, 9, 10, 71] of efficient packing of atoms has been shown to replicate structural measurements quite well. The model is based on the efficient

packing of atoms into SRO clusters and further economical packing of the SRO clusters into dense medium-range order. This topological consideration provides an explanation for the simulated and experimentally observed short and medium-range order of MGs wherein, for each composition, particular high coordination number (CN) atomic clusters appear in significantly higher frequencies than other CNs [4]. Further, the quantitative calculations of properties align well with those measured at the atomic and global scale. The model's current limitations are twofold: it does not take into account changes in effective atomic radii due to electron interactions in some compositions, and it cannot model the structure of MGs with more than three elements.

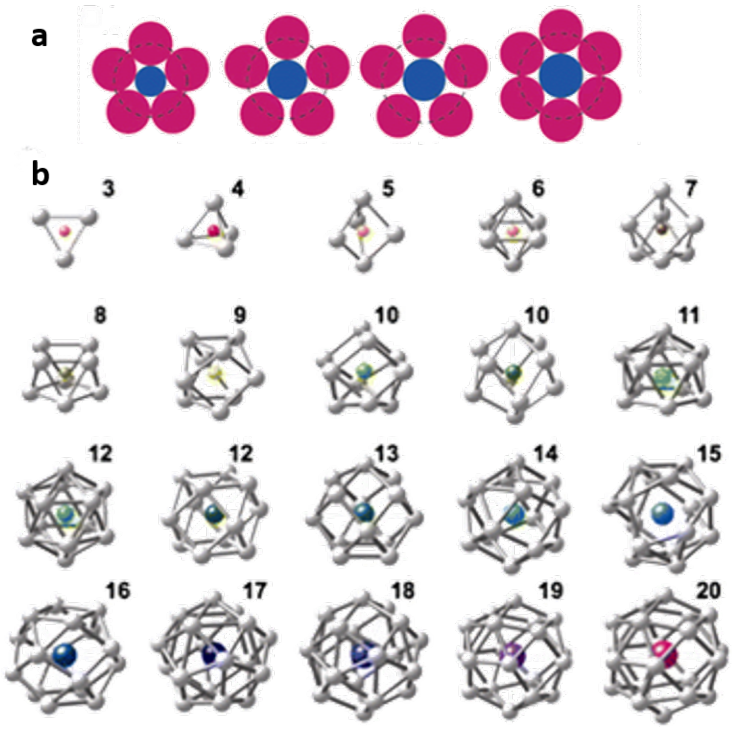

Figure 2.4: Schematic illustrations of SRO in Miracle's efficient cluster packing model in (a) 2D and (b) 3D for binary MGs with different atomic radii ratios. As the center atom increases in diameter relative to the surrounding atoms, a higher order of coordination can be achieved. [9]

Figure 2.4 shows the atomic cluster coordinations possible for a binary MG, with varying atomic radii ratios, using Miracle's model [9]. Voronoi polyhedra can be used to identify these coordinations in 3D simulations. When the ratio of atomic sizes changes, dif-

ferent atomic coordinations become preferable. As the atoms for a MG are themselves never perfectly homogeneously distributed, local changes in composition can change the locally preferred coordination. As such, a range of different atomic coordinations are heterogeneously distributed throughout a MG [4, 42]. The less efficiently packed atomic coordinations correspond to regions of increased free volume. These are sites which may be preferentially rearranged into a more efficient, dense coordination with an applied driving force. Further discussion about the heterogeneous distribution of different SRO and externally driven adjustments will be covered in Section 2.2.2.

2.2 Metallic Glass Phase Stability

Metallic glasses are not stable phases. With the range of bond lengths possible at every length scale in MGs, there is significant structural entropy as compared to a crystalline metal. Therefore, all glasses, given enough energy to overcome the reorganization barrier and time to rearrange, will lower their energy state by crystallizing. However, there are also many local minima of energy states along the way, wherein thermodynamic driving forces and kinetics allow for the structure to remain amorphous. As such, metallic glasses are considered metastable phases. This section will give an overview of (1) the theories one may use to produce metallic glass samples and avoid thermodynamic and kinetic conditions which would otherwise result in crystallization, (2) recent work indicating opportunities for structural rearrangements within the amorphous regime, (3) typical conditions for and observable effects of crystallization from the MG phase, and (4) unique composition-dependent pressure-induced hysteretic changes observed within some MGs.

2.2.1 Synthesis of Metallic Glass

In order to kinetically "lock in" the metastable phase, metallic glasses are typically produced via rapid quenching from the molten state [72]. The potential size of the formed metallic glass is determined by the rate of cooling needed to avoid crystallization, also

known as the glass-forming ability (GFA). Recent work has indicated that the reduced glass-transition temperature (T_{rg}) and fragility (m) may be effectively combined to describe the stability of the glass and potentially predict the GFA [73, 74, 75]. Both variables are intrinsically linked to the viscosity of the undercooled liquid, allowing for determination of T_{rg} and m via thermal characterization.

The reduced glass-transition temperature ($T_{rg} = T_g/T_m$), where T_g is the glass transition temperature and T_m is the melting temperature, was first developed by Turnbull [76]. This GFA variable is typically used in thermodynamic theories focusing on avoiding crystallization by suppressing homogeneous nucleation of crystals. When the size of the region between T_m (temperature at which there is no thermodynamic driving force for crystallization) and T_g (temperature below which there is insufficient mobility for crystallization) is minimized, there is a smaller temperature regime at which the melt can crystallize. Therefore, a MG composition with a larger T_{rg} (typically $\geq 2/3$) is generally a better glass-forming alloy and less likely to nucleate crystallites.

The fragility, m, is defined by Equation 2.5:

$$m = \left. \frac{\delta log(\tau)}{\delta(T_g/T)} \right|_{T=T_g} \tag{2.5}$$

where τ is the average relaxation time, T_g is the glass transition temperature, and T is the temperature. Fragility is often evaluated at a particular heating rate (typically 20 K/min) and the glass transition temperature associated with that heating rate.

The value of m corresponds to how stable the glass is at T_g, where a lower m value (≤ 30) corresponds to a glass which is fairly stable and unlikely to go through phase changes easily; these are called "strong" glasses. Conversely, a higher m value (~ 100) corresponds to a "fragile" or "weak" glass for which small fluctuations in driving forces can easily change the phase [77, 78]. In effect, the fragility is the kinetic component for GFA and corresponds to how easily nuclei in an undercooled liquid can grow into measur-

able crystals. Recent work has also correlated fragility values to Poisson's ratio [79] and the bulk modulus [80] of the glass.

Experiments by Na et al. [73], characterizing the GFA at different compositions in a Ni-Cr-Nb-P-B metallic glass-forming system, have shown that when both T_{rg} and m are optimized with respect to the composition, the GFA is an order of magnitude greater than any other composition. Figure 2.5 shows this trend, comparing (a) the overall GFA represented as the maximum glassy rod diameter squared, (b) the reduced glass transition temperature, and (c) the fragility, all as a function of the concentration of B atoms. Comparing the effects of each variable, the improving fragility component dominates the rapid rise in GFA in the regime of low at% of B, and the stable fragility trend at higher at% of B buffers the effects of the rapid drop of the reduced glass transition temperature.

The relationship between the fragility and reduced glass transition temperature becomes clearer when comparing the thermodynamic nucleation and kinetic growth rates as a function of temperature. Figure 2.6 provides plots of the (a) nucleation and (b) growth rates for crystallites in undercooled glass-forming liquids as a function of temperature (normalized by the melting temperature of the material). In Fig 2.6(a), the homogeneous nucleation rates, calculated by Turnbull using classical nucleation theory, are plotted as a function of the reduced temperature (T/T_m) [76]. The dashed horizontal line shows the limit of detectable nucleation rates. In Fig 2.6(b), growth rates for various glass-forming materials are plotted against the T/T_m scale [74]. Each curve in Fig 2.6 is labeled with the T_{rg}. Based on both curves, a higher T_{rg} correlates with narrower temperature ranges for significant rates of both nucleation and growth, lower maximum rates of nucleation and growth, and an overall higher GFA.

If the reduced glass transition temperature were fully representative of both the thermodynamic and kinetic components of GFA, one would expect the peak nucleation rate and peak growth rates to occur at the same temperature for a given material (where the given material is defined only by its reduced glass transition temperature). However, while the

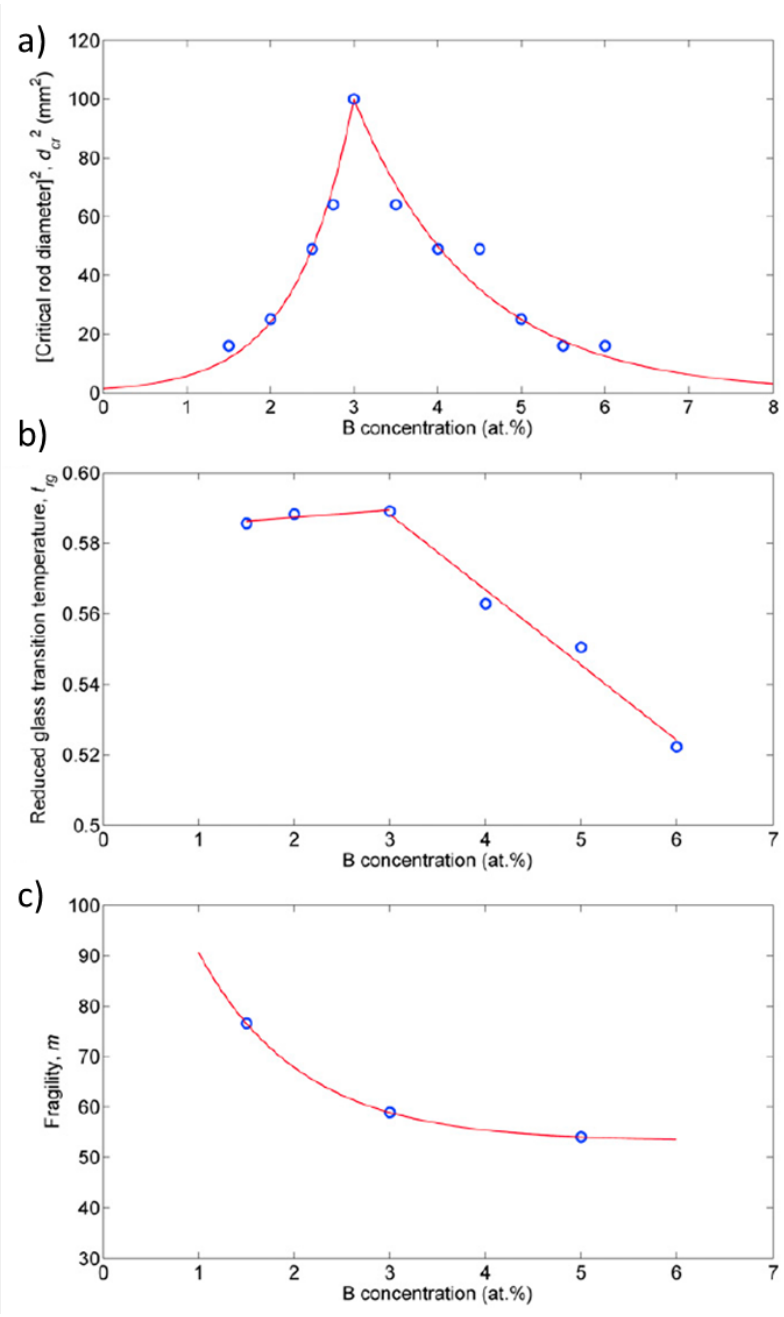

Figure 2.5: Plots showing (a) GFA represented in terms of critical glassy rod diameter squared, (b) reduced glass transition temperature T_{rg}, and (c) fragility m as a function of atomic concentration of the element B in the $Ni_{69}Cr_{8.5}Nb_3P_{19.5-z}B_z$ metallic glass. Circles are experimental data, and solid lines are numerical fits. The overall trend for GFA appears from combining the increasing stability trend for fragility with the increasing and then decreasing trend for stability of the reduced glass transition temperature, each as a function of the at% of B. [73]

two are similar, the reduced temperature at which the growth rate is maximized is consistently higher than the reduced temperature at which the nucleation rate is maximized. For example: the peak nucleation rate from Fig 2.6(a) for a T_{rg} of 0.67 occurs at a reduced temperature of about 0.78, but the peak growth rate from Fig 2.6(b) for the green square data (material: "ROY"), which has a T_{rg} of 0.66, is at a reduced temperature of about 0.88. This difference is attributed by Greer [75] to the crystal-liquid interfacial energy not influencing growth as it does nucleation. The reduced temperatures for each maximum rate can be matched, however, if a new parameter is devised to replace the reduced glass transition temperature for defining the material. Orava et al.[74] defined this new parameter as $T_{gu} = T_{rg} - m/505$ by taking into account the fragility. When T_{gu} is used instead of T_{rg} to define a material, the growth rate and nucleation rate maximums are in agreement. Therefore, the new parameter, T_{gu}, can and should be used to determine or compare the stability and GFA of different metallic glass compositions [75].

There is extensive research on expanding the maximum possible GFA of metallic glasses through compositional tuning, and an interested reader may find more information in the book *Bulk Metallic Glasses* by Suryanarayana and Inoue [1]. Typically, GFA is increased by enhancing the barrier to crystallization, stabilizing the amorphous state, and destabilizing the crystalline phase which would form if allowed to crystallize. Johnson [41] and Inoue et al. [81, 1] have shown the following composition criteria cause these changes:

1. Increase the number of constituent elements to three or more, each with large ($>$ 12%) atomic radius mismatch. This leads to higher packing densities in the glass, thereby stabilizing the glass, and causes the concomitant crystalline phase of the same composition to be very complex and energetically unfavorable.

2. Choose a composition with a negative heat of mixing. This increases the resistance of the glass to phase separate into other compositions potentially more energetically favorable for crystallization, thereby destabilizing the crystalline phases as compared

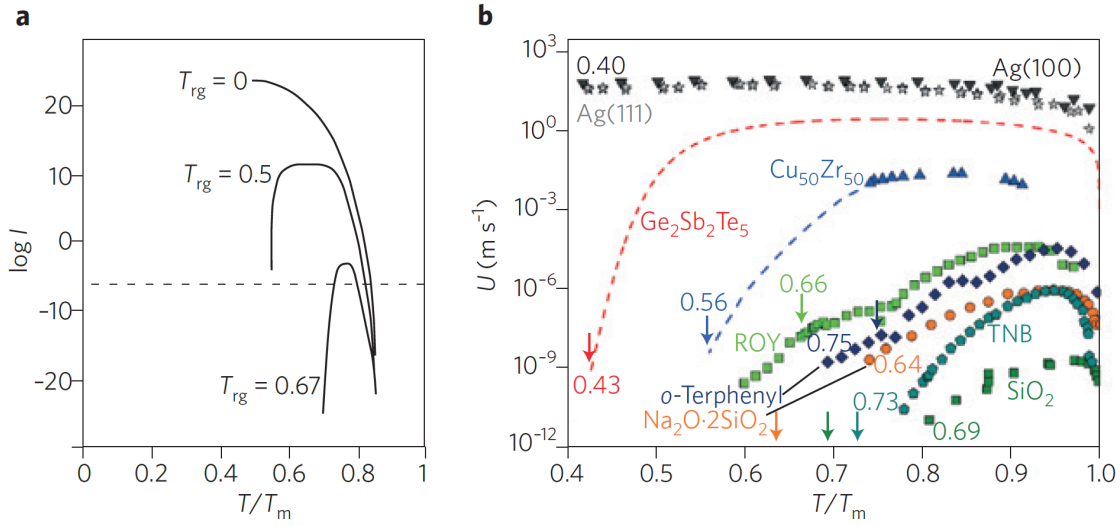

Figure 2.6: Plots showing (a) homogeneous nucleation rates and (b) growth rates on a reduced temperature scale (T/T_m) for systems where the liquid and crystalline phases have the same composition. Homogeneous nucleation rates in (a) are calculated by Turnbull [76] using classical nucleation theory, with the T_{rg} value labeled for each curve and the dashed horizontal line representing the limit of detectable nucleation rate. Growth rates in (b) are experimentally measured (except for Ag data which are from MD simulations) and collected by Orava et. al. [74]. Each curve is labeled with the material and reduced glass transition temperature, T_{rg}, and arrows indicate the T_g value on the x-axis. TNB is 1,3,5-tris(naphthyl)benzene and ROY is 5-methyl-2-((2-nitrophenyl)amino)-3-thiophenecarbonitrile. Peak growth rates occur at higher temperatures than peak nucleation rates for the same reduced glass transition temperature. [75]

to the glassy phase. It also increases viscosity for the liquid phase and raises the relative glass transition temperature, and therefore, enhancing glass stability.

3. Choose a composition near a deep eutectic. This decreases the melting temperature and therefore increases the stability (T/T_m) of the liquid at lower temperatures and the relative glass transition temperature (T_g/T_m), improving the stability of the resulting glass.

In the present work, "weak" glass-forming binary MGs are of focus as they allow for more clear determination of the atomic structure and therefore allow for improved correlations of structural rearrangements and observed property changes as a function of applied pressure. Due to their low GFA, "weak" glass-forming MG samples are necessarily thin

($\leq \sim 50\,\mu\mathrm{m}$) so as to retain the required high heat transfer rate ($\geq \sim 10^5 \frac{K}{s}$) that allows for avoiding crystallization throughout the thickness [41]. Sample geometries are typically in the form of melt-spun ribbons or splat quenched disks [82, 1]. The stability, in the form of T_{rg} and m, of the binary melt-spun MG ribbon used in this work will be calculated using thermal analyses and discussed in Chapter 4. Chapter 7 will discuss consideration of the effects of this stability on measured phase changes.

2.2.2 Rejuvenation and Relaxation of Metallic Glass

Owing to the heterogeneous distribution of SRO in MGs, there are many possible arrangements which fall within the regime of metastability. Recent work by Ma [42] summarized some of the current understandings of these SRO distributions in MGs. He described the MG structure as a combination of (1) geometrically unfavored motifs (GUMs) (also known as "liquid-like" local atomic structures) which have higher free volume, and (2) more dense, composition-specific, preferred coordinations which link together and form the backbone of the atomic structure. Unfortunately, direct experimental measurement of the SRO is currently only possible with advanced TEM techniques [61, 62, 63], and this method has, so far, been unable to describe the overall structural distribution. Average measurements of the structure through X-ray or neutron scattering or X-ray absorption, paired with simulations, can be used to estimate the internal structure and SRO distribution [4, 83, 46]. Utilizing the latter method and *ab-initio* simulations, correlations of the distribution on other properties have been determined.

Simulations of the SRO arrangements and mechanical properties have indicated that GUMs act as sites of stress localization in MGs [84, 85]. As such, an increased ratio of GUMs to preferred coordinations in a MG results in more stress delocalization, decreasing stiffness and increasing fracture toughness (extending into ductile-like necking behavior) [42, 86, 18, 87]. Conversely, an increased ratio of regions of preferred coordination increases the stability and stiffness of a MG [88]. The heterogeneous distribution of GUMs

and preferred orientation regions correlate well with observations of heterogeneous localized mechanical properties, including shear transformation zones (STZs) [42]. Section 2.3 will further discuss mechanical properties, STZs, and the known relations to MG atomic structure. Overall, a larger amount of preferred coordination increases the density [42] and the barrier to crystallization [89] and slows relaxation dynamics [90, 91]. Stated another way, decreasing the number of GUMs in a structure increases the stability of the system, concomitantly increasing the reduced glass transition temperature, T_{rg}, and decreasing the fragility, m (towards a "stronger" glass) [46].

Therefore, it is important to know how the overall distribution of SRO might be affected through external processing so that one might tune the properties of the MG. There are two main approaches for tuning the distribution: change the quench rate when producing the MG or process the MG after fabrication. Faster quenching of the liquid during MG preparation retains more of the liquid-like structure, increasing the ratio of GUMs to preferred coordination; conversely, slower quenching increases the density and overall amount of preferred coordination of the MG [42]. When processing the MG to achieve a higher ratio of preferred coordination to GUMs, the resulting effect is referred to as relaxation. This can be caused by annealing at a temperature below the glass transition temperature [42] or applying hydrostatic pressure [92, 93, 94]. Density increases from relaxation have typically been found to be below 0.5% [95, 96], although some MG compositions are able to achieve as high as 0.5 [97, 98, 99, 100] to 1% increases [101]. Polyamorphism (significant rearrangements which create a different symmetry and molar volume at the same composition), however, has only been reported for unique compositions at high pressures [42] (see Section 2.2.4 for more).

When processing to increase the ratio of GUMs, the effect is called rejuvenation. It has been reported that rejuvenation can be caused by ion irradiation [42] or shear, such as in mechanical loading (pre-straining) [18, 102], elastostatic deformation [103, 104, 105, 106, 107], or high pressure torsion-induced severe plastic deformation [13]. Of note, shear

can also cause crystallization by providing small atomic displacements which accumulate and can allow for ordering rearrangements. This rearranging mostly occurs over repeated gentle stress-strain cycles (e.g., fatigue) as it allows for more displacement accumulation and avoids fracture [18, 108]. Shear and other methods for crystallization will be discussed further in Section 2.2.3, and deformation of MG will be explored further in Section 2.3.

As shock-compression causes significant shear, high pressures, and elevated temperatures, there can be competing effects of relaxation and rejuvenation. Further examinations of structural changes in MG with shock-compression will be covered in Section 2.4 and Chapters 5, 6, and 7.

2.2.3 Crystallization of Metallic Glass

As a metastable material, metallic glasses are thermodynamically predisposed to crystallize. The crystallization process is a combination of initial nucleation and then growth of crystallites, wherein larger crystallites are energetically favorable due to reduced interfacial energies [109]. The material surface, presence of any foreign constituents, and defects all lower the local interfacial energy, decreasing barriers to crystallization. Heterogeneous nucleation off of surfaces, constituents, or defects is therefore the energetically preferred mode of nucleation, if they are present. However, if the driving force is large enough and/or there are few sites available, the nucleation will be distributed homogeneously through the sample. Due to the heterogeneous distribution of SRO in MG, as discussed in Sections 2.1.2 and 2.2.2, this "homogeneous" nucleation will preferentially begin in the SRO where there is greater configurational entropy due to packing inefficiencies, i.e., the GUMs [42, 110, 111]. Therefore, for homogeneous nucleation, decreasing the number of GUMs in a MG should logically decrease the rate of nucleation. Figure 2.6(a) [75] in Section 2.2.1 shows this effect indirectly, showing an increased reduced glass transition temperature, which a system with fewer GUMs has, correlates with a decreased nucleation rate. Interestingly, Figure 2.6(b) shows fewer GUMs also result in slower growth rates, perhaps because fewer

GUMs correlates with an increased viscosity, decreasing the rate of diffusion needed for growth.

Although the SRO and MRO structure and distribution clearly play a role in crystallization behavior, to the author's knowledge, few studies directly correlate the two [110, 111], potentially due to the difficulties in clearly measuring the atomic structure and distribution as discussed in Section 2.1.1. As such, this section will focus on the indirect effects of different compositions, temperatures, heating rates, pressures, shear stresses, and strain rates on the likelihood and microstructure of crystallization in metallic glasses.

Effects of Composition on Crystallization

There are three different crystallization behaviors depending on the composition of the MG and the thermodynamically stable phases near that composition. Polymorphous crystallization occurs when systems have thermodynamically-preferred crystalline phases with the same composition as the starting amorphous phase. Eutectic crystallization occurs for systems which have two or more crystalline phases equally thermodynamically-preferred such that each is nucleated simultaneously from the amorphous phase. Primary crystallization occurs in systems which thermodynamically prefer a single crystalline phase of a different composition, causing crystallization to occur in multiple stages: first metastable or stable crystallites nucleate within the amorphous matrix (changing the composition of the glassy phase), then the remaining amorphous matrix crystallizes via polymorphous, eutectic, or primary crystallization methods [43].

Following the synthesis rules from Section 2.2.1, metallic glasses which are stabilized by utilizing compositions with more than two elements generally have a composition which is unfavorable for crystallization into a single phase. As such, MGs with three or more component elements will typically crystallize into multiple lower energy crystalline phases via primary and eutectic pathways. In contrast, simpler MGs which have compositions the same as an intermetallic line compound or pure crystalline phase may polymorphously

crystallize. Because these compositions are more likely in binary MGs, polymorphism is more often observed in binary MGs than MGs with three or more elements.

Due to the need for phase separation to progress, primary and eutectic crystallization are dependent on long-range diffusion, increasing the initial barrier to crystallize and slowing subsequent growth of crystallites. In contrast, polymorphous crystallization requires limited diffusion and therefore has a smaller nucleation barrier and faster growth rate. External environments can exacerbate these differences. Hydrostatic pressure limits atomic movement and therefore slows crystal nucleation and growth in primary and eutectic crystallization more than in polymorphous crystallization [43].

Driving Forces for Crystallization

As with relaxation and rejuvenation discussed in Section 2.2.2, there are various external loading conditions which can provide the driving forces to overcome the activation energy and mechanisms for atomic reorganization and crystallization. Heat increases atomic movement through diffusion, and shear provides for rearrangement via non-diffusional atomic shifts. Thermal driving forces, including effects of heat paired with pressure, will be discussed first followed by an examination of the effects of shear.

Given enough time above the threshold temperature for nucleation and depending on the stability of the MG, crystallites of the more stable crystalline phase(s) for that composition will form and grow in varying quantities and sizes. An example of the structural progression of thermal crystallization can be observed in the in-situ PDF study of an Fe-based MG, shown in Figure 2.3 in Section 2.1.1. Of note, different annealing temperatures have been shown to affect phases which are thermodynamically favored. In studies by Louzguine et al. [112] and Iwasaki et al. [113], metastable and supersaturated crystalline phases were formed when annealed at a lower temperature instead of stable or metastable phases observed during annealing at higher temperatures.

The apparent activation energy required for thermal crystallization of the MG can be

determined through thermal analysis using differential scanning calorimetry (DSC) and/or *in-situ* structural characterization (e.g., via XRD) of crystallization rates with controlled heating. In DSC, phase changes are observable by relative absorption or release of energy while heating under a constant rate. At different heating rates, the onset temperature, observable as the change in slope initiating a thermal event, will shift according to the activation energy of the event. Additionally, for thermal crystallization, the onset temperature shift will be affected by the crystallite dimensionality (e.g., rod, planar, or spherical growth) and crystallization mechanisms (e.g., bulk or surface crystallization). These changes are representative of the specific material thermal properties and can therefore be used to directly calculate the activation energy, crystallite dimensionality, and crystallization mechanism. The theoretical background for these thermodynamic and kinetic analyses is outside of the scope of this work, however an interested reader can find more information in Celikbilek et al. [114]. Equations and methods for calculation of thermal properties will be discussed in the technical approach chapter (Ch. 3), and measurements, values, and meanings for the thermal properties of the Ce_3Al MG will be presented in Chapter 4.

Adjusting the heating rate, duration, and temperature at which the sample is held affects whether nucleation or growth dominates the crystallization. As seen in the plots of nucleation and growth rates as a function of temperature in Figure 2.6 from Section 2.2.1, increased temperatures generally increase both nucleation and growth rates with nucleation rates maximizing at lower temperatures and dropping off faster than growth rates. The relation between the two can be understood as an effect of activation energy for nucleation and diffusion once nucleated. There is a distribution of the degree of disorder for GUMs within MG; the few with more inefficiencies will activate with lower temperatures, but more will activate as temperatures increase. Once nucleated, growth is diffusion-limited and therefore increases with heat. As such, one can expect increasing temperatures to activate more GUMs, decreasing the onset time for nucleation. Then, nucleation and growth rates will increase with temperature, with both dropping off as GUMs preferentially melt instead of

crystallize as temperatures near T_m [115, 43]. Faster heating rates are typically applied for short durations, resulting in a small fraction of time at high temperatures, limiting the effects of diffusion but allowing for activation of GUMs and resulting in more significant amounts of nucleation than growth. In the extreme condition of very high heating rates (e.g. $\geq 10^{10} K s^{-1}$), as can be induced by pulsed laser heating, a recent study by LaGrange et al. [116] showed the activation energy for crystallization is substantially decreased (1.7 instead of 2.3 eV) and crystallization rates are greatly accelerated (kinetic parameter k grew from $\sim 1 s^{-1}$ to $\sim 7.78 \times 10^5 s^{-1}$). At this rapid heating rate, crystallization onset occurred 408 ns after the 12 ns initial laser irradiation (instead of $\sim$7 s with conventional heating), and complete crystallization was achieved after $\sim$2500 ns (instead of $\sim$35 s with conventional heating).

Under hydrostatic compression, crystallization may be either hindered or aided depending on the MG composition and the available crystalline phases at the given composition, temperature, and pressure. All crystallization for which significant diffusion is required (i.e., eutectic and primary crystallization) is kinetically retarded due to decreased atomic diffusivity at elevated pressures [26, 43]. However, if the crystalline phase is of a higher density than the amorphous phase, pressure may decrease the energetic barrier for crystallization. Conversely, crystalline phases which are of lower density than the amorphous phase will be energetically unfavored. Due to the increased pressure and retarded kinetics, new metastable crystalline phases have been observed to become energetically and kinetically favorable at elevated pressures [117]. For $Zr_{66.7}Pd_{33.3}$ MG, ambient pressure thermal crystallization forms a larger molar volume (lower density) quasicrystalline Zr_2Pd phase. Under hydrostatic compression up to $4\,\mathrm{GPa}$, the thermodynamic potential energy barrier rises due to increased difficulty from growing volume while under pressure, elevating the temperature at which crystallization occurs by 22 K/GPa [118].

The $Pd_{80}Si_{20}$ metallic glass polymorphically crystallizes into a supersaturated FCC crystalline phase at lower temperatures and follows a primary crystallization path at higher

temperatures forming an FCC phase first and then a complex crystalline phase. Under hydrostatic compression, the lower temperature phase never forms, indicating it may have a higher molar volume and thus is thermodynamically unfavored at elevated pressures. In contrast, the primary crystallization can occur under pressure either at a higher onset temperature or after a longer delay with a decreased crystallization rate in either condition. This indicates that primary crystallization may be diffusion-controlled, which causes the effects of retarded kinetics under increased pressure to dominate [113].

Under ambient pressures, $Nd_{60}Al_{10}Fe_{20}Co_{10}$ metallic glass forms a hexagonal Nd phase at 633 K and crystallizes the remaining amorphous matrix into first a metastable and finally a stable crystalline phase at elevated temperatures. At increased pressure, the hexagonal Nd phase forms at much lower temperatures (593 K at 5 GPa and 473 K at 8 GPa) and converts into a new phase at higher temperatures. The lowered crystallization temperature indicates that the precipitation of the hexagonal Nd phase is not diffusion-limited, and that the Nd phase is of a higher density than the amorphous phase, thereby becoming thermodynamically enhanced under pressure. The results also appear to show that a new crystalline phase is thermodynamically available at high pressures for this composition [117].

$Fe_{72}P_{11}C_6Al_5B_4Ga_2$ metallic glass eutectically crystallizes into three phases simultaneously at atmospheric pressure and 798 K: a $Ni-3P$-like phase, $Fe_3(NiN)_2$ phase, and a $Fe_{23}(CB)_6$ phase. At elevated pressures, the crystallization temperature follows the trend seen in Figure 2.12(b): first increasing, then decreasing, increasing again, and then remaining independent of pressure. The ratio of the three phases formed changes following this trend. Significantly less of the third phase forms at the pressure of the crystallization temperature minima. At greater pressures, much more of the third phase and less of the second phase forms. The differences in these phase formations are indicative of changes to the thermodynamic favorability of each phase under pressure and at elevated temperatures [27].

The electronic structure of many elements also changes with compression, resulting

different effective atomic sizes. Therefore MG with compositions which include these elements may be expected to have new crystallization behavior under pressure. Indeed, some MG compositions have been to observed to crystallize entirely through application of hydrostatic compression without additional heating. These effects will be discussed further in Section 2.2.4.

Shear stresses can promote diffusion-like atomic re-arrangements in MGs. This is observed as nonhomogeneous (non-affine) components of displacements accruing approximately linearly with time [42, 108]. Therefore, shear-dominant tensorial stresses can significantly lower thermal energy barriers for phase changes [119] or accelerate crystallization [120]. The activated volume in these shear transformations is relatively large, involving tens or even hundreds of atoms [18]. As such, as more of the shear-induced ordered regions form, they are able to link up and relax into more stable (fewer GUMs) amorphous phases or even crystalline regions without any temperature-induced mobility [42, 108]. However, as these changes are due to the non-affine components of displacements, the ordered regions form only with an increased number of tensorial cycles and are not correlated with the magnitude of the tension. As such, the accumulation is mostly associated with multiple gentle stress-strain cycles and not large shear as that could cause deformation or failure [108]. Discussion of shear-induced transformations when deformation does occur is provided in Section 2.3.2.

Microstructure of Crystallized Metallic Glass

The general microstructural progression for primary crystallization from $Zr_{65}Ni_{25}Ti_{10}$ and $Zr_{41.2}Ti_{13.8}Cu_{12.5}Ni_{10.0}Be_{22.5}$ MGs has recently been studied by Liu et al. [110, 111, 121] using high-resolution TEM with nanobeam diffraction capabilities, advanced image analysis with an autocorrelation function and fast Fourier transformation, and molecular dynamics simulations. This work found that the atomistic growth mechanism for MG crystallization involves three distinguishable steps in succession, starting with the compositionally

inhomogeneous GUMs as nuclei: formation of quasi-ordered structures with 1-D periodicity, growth to 2-D periodicity via arrangements in the close-packed directions on a length scale of 2-4 nm, and formation of 3-D nanocrystals with clear interfaces. Progression occurs in order, but it does not occur uniformly across the entire sample. No long-range diffusion was observed; compositional fluctuations allowed for similar local compositions as the resulting crystalline phases. The resulting 3-D crystallites have diameters of 10-20 nm with 1-D and 2-D ordered regions on the grain boundaries. Figure 2.7 provides an illustrative HRTEM image and its attendant FFT-derived diffraction images for the thermally induced crystallites which show the range of 1 to 3-D ordering.

The growth behavior observed by Liu et al. [111] is matched by MD simulations of crystallization of a pure Ni sample, indicating the mechanisms may be applicable for all MG crystallization types and not just the characterized primary crystallization of the Zr-based MG. Experimental consideration of a range of MG compositions suggests the typical minimum crystallite sizes formed upon thermal crystallization are often below 25 nm, with smaller grains in polymorphous and eutectic crystallizing samples as compared to those undergoing primary crystallization [122]. Table 2.1, Table 2.2, and Table 2.3 show experimental data of the crystallite phases formed, minimum observed grain sizes, and temperatures utilized during annealing for polymorphous, eutectic, and primary crystallizing MGs, respectively.

Table 2.1: Experimental data of the minimum grain sizes, $d*$, and the annealing temperature, T_a, relative to the melting temperature, T_m, for polymorphous crystallization of MGs and other amorphous solids.

System	Crystalline Phase(s)	$d*$ (nm)	T_a/T_m	Reference
Si	α-Si	7.0-8.0	0.50	[122]
Se	γ-Se	6.7-7.8	0.76	[123]
$Co_{33}Zr_{67}$	$CoZr_2$	8.0	0.50	[124]
$Ni_{33}Zr_{67}$	$NiZr_2$	8.0-10.0	0.49	[125]
$(Fe,Co)_{33}Zr_{67}$	$(Fe, Co)Zr_2$	4.0-5.0	(773 K)	[126]

Table 2.2: Experimental data of the minimum grain sizes, $d*$, and the annealing temperature, T_a, relative to the melting temperature, T_m, for eutectic crystallization of MGs and other amorphous solids.

System	Crystalline Phase(s)	$d*$ (nm)	T_a/T_m	Reference
$Ni_{80}P_{20}$	Ni_3P + Ni(P)	6.0-7.0	0.50	[127]
$Fe_{80}B_{20}$	Fe_3B + Fe(B)	8.0	0.46	[128]
$Fe_{40}Ni_{40}P_{14}B_6$	$(FeNi)_3$(PB) + FeNi(PB)	9.0	0.55	[129]

Table 2.3: Experimental data of the minimum grain sizes, $d*$, and the annealing temperature, T_a, relative to the melting temperature, T_m, for primary crystallization of MGs and other amorphous solids.

System	Crystalline Phase(s)	$d*$ (nm)	T_a/T_m	Reference
$Fe_{78}B_{13}Si_9$	Fe(Si) + Fe_3B	21-25	0.51	[130]
$Fe_{60}Co_{30}Zr_{10}$	Fe(Co) + $(FeCo)_2Zr$	15	0.51	[131]
$(Fe_{99}Mo_1)_{78}$-$B_{13}Si_9$	Fe(Si,Mo) + $(FeMo)_3Si$ + Fe_2B	17-20	0.52	[132]
$(Fe_{99}Cu_1)_{78}$-$B_{13}Si_9$	Fe(Si) + Fe_2B	27	0.50	[122]
$Pd_{78.1}Cu_{5.5}Si_{16.4}$	Pd(Si) + $(PdCu)_3Si$	19	0.62	[133]
$Fe_{76.5}Cu_1$-$B_9Si_{13.5}$	Fe(Si) + $Fe_{23}B_6$	18	0.53	[122]
$Fe_{73.5}Cu_1Ta_3$-$B_9Si_{13.5}$	Fe(Si) + Fe_3B	70	(790 K)	[134]
$Fe_{86}Cu_1B_6Zr_7$	Fe(Si) + Fe_2B	16	(793 K)	[135]

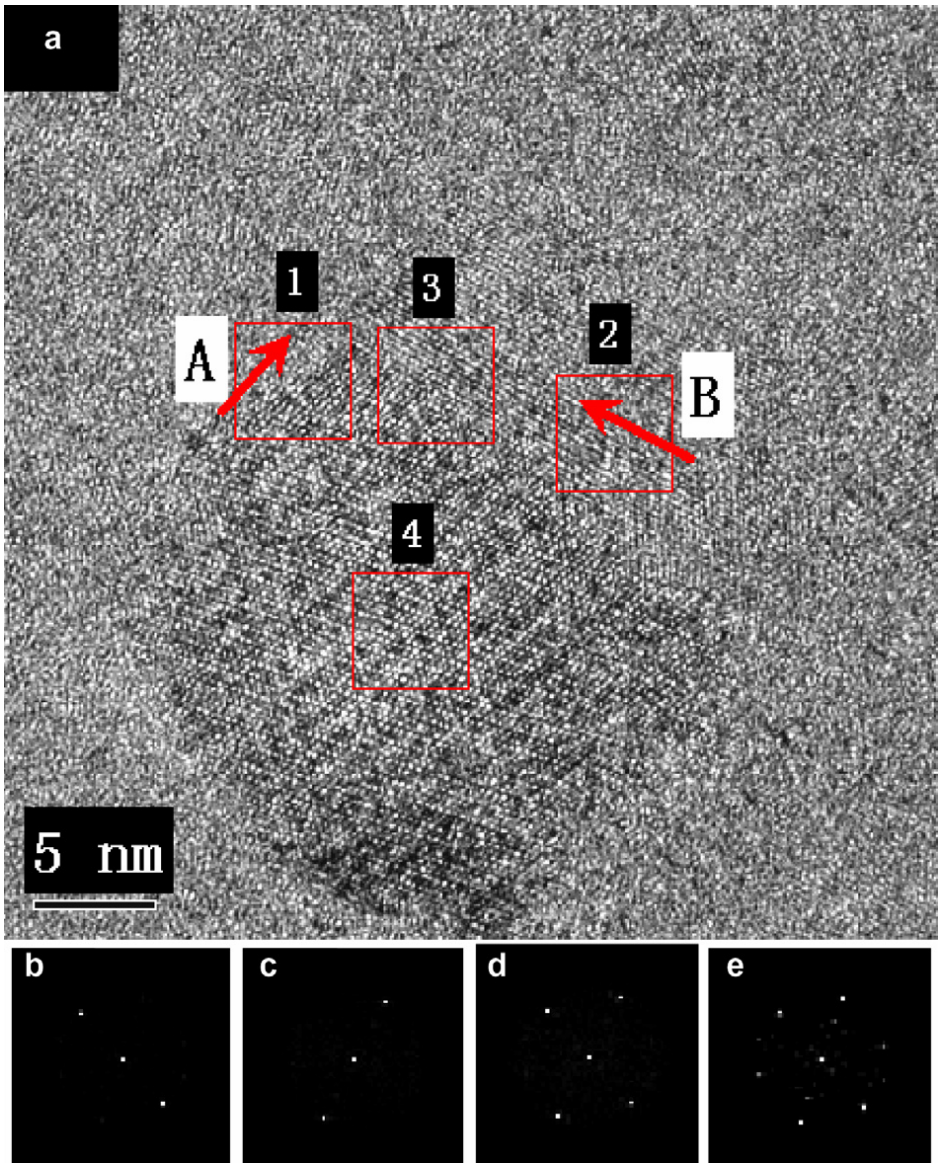

Figure 2.7: (a) High-resolution TEM image of the $Zr_{65}Ni_{25}Ti_{10}$ MG after annealing to partial crystallization. (b-e) FFT-derived 2-D diffraction patterns from boxed regions 1 through 4, respectively. Atomic clusters with 1-D periodicity are visible in (b) and (c), and the preferred growth directions for each are indicated with arrows in (a) boxes 1 and 2, respectively. 2-D ordering as seen in (d) is visible in box 3 of (a). Full 3-D ordering, as confirmed by FTT diffraction in (e), is visible in the largest area of the crystallite partially selected in box 4. [111]

The size of the crystallites may be adjusted through relaxation or rejuvenation of the MG prior to crystallization, which affects the amount of GUMs within the system, or by changing the pressure, shear, annealing temperature, or heating rate during thermal crys-

tallization. Increased amounts of GUMs result in a higher number of nucleation sites, generating smaller overall grain sizes for a given heating/shear condition [122]. Increased pressures, lower temperatures, or higher heating rates retard kinetic growth [135, 134], resulting in smaller nanocrystallites for a given duration. Shear and higher annealing temperatures allow for greater kinetic growth, resulting in larger nanocrystallites for a given duration. Minimum grain sizes are determined through maximization of the nucleation rate and minimization of the growth rate, which occurs at a temperature some fraction of T_m depending on the GUMs and GFA of the MG [75, 122]. Crystallization through mechanical deformation has been observed to enable the production of stable crystallites of a different composition and a smaller size than those created from thermal crystallization [136, 137]. The mechanism for mechanical deformation-induced crystallization will be discussed further in Section 2.3.2.

The stability of nanocrystallized MG is well-documented [122] but seemingly surprising. In conventional polycrystalline materials, high densities of interfaces provide driving forces for consolidation and grain growth. In the form of the Gibbs-Thomson equation, the driving force is inversely proportional to the grain size, indicating that nanocrystalline materials should be strongly driven to grow in grain size even at room temperature [122]. However, while significant grain growth has been observed at room temperature in some pure element materials which have melting temperatures below $600\,^{\circ}\mathrm{C}$ (e.g. doubling of grain size in 24 hrs) [138], significant grain growth is observed to only occur at much higher temperatures in other elements (e.g. $\sim 0.28 \cdot T_m$ for Cu and Pd) [139] and multi-component nanocrystallized MG (e.g., over 700 K for growth of a nanocrystalline Fe-Si-B above 30 nm [140]).

In addition, experiments have indicated some nanocrystalline materials (e.g. Ni-P [141], $HfNi_5$ [142], $NbAl_3$ [143]) manifest step-wise grain growth behavior. Upon heating a sample, it remains unchanged until a critical starting temperature (dependent on the heating rate) for grain growth is reached. Once grain growth begins, growth occurs gradually

up until a particular size and then stops. Increasing critical starting temperatures result in slightly larger final grain sizes, although all are found to be stable at temperatures above 700 K even with grain sizes of 10 - 40 nm. Interestingly, the minimum critical temperature for grain growth is found to increase with decreasing grain sizes (within the range of 50 nm to 7 nm) for a Ni-P nanocrystalline material [144].

Decreases in grain size are correlated with distortions of the lattice parameters. With grain sizes in the range of 8 - 30 nm, nanocrystalline Se trigonal "*a*" and "*c*" lattice parameters fluctuate between +/- $\sim$0.2% distortion relative to the reference polycrystalline state [123]. Nanocrystalline Ni lattice parameters increase with decreased grain sizes [145, 146, 147], and nanocrystalline gold and silver lattice parameters decrease with decreased grain sizes [148]. The explanation for these issues appears to be a complex effect of interfacial energy enhancing solubility of point defects [122], free volume in the grain boundaries straining the grains [149], and the limited number of lattice planes in these small grains relative to the amount of grain boundary distorting x-ray scattering [150]. A full and generalizable explanation does not appear to have been determined by the community at this time.

The microstructural effects of thermal crystallization for Ce_3Al MG performed in the present work will be discussed in Chapter 4 and compared with the effects of shock-compression in Chapter 7.

2.2.4 Composition-Dependent Pressure-Induced Phase Changes in Metallic Glass

Many pure, crystalline elements (e.g., Ce, Ca, Fe, Zr, Na, Mg, Al, Ga, In, Tl, Si, Ge, C, Eu, Yb, Tm, Am, Th, Pu, Cs, La, Ba, Y, Sc, Pr, etc.) and crystalline compounds (e.g., SiO_2, H_2O, SiC, YbO, $NaNO_3$, $CuGaS_2$, $AgGaS_2$, etc.) have been experimentally observed or theoretically predicted to undergo hydrostatic pressure-induced phase changes. Many phase changes are into otherwise unaccessible crystalline phases, although transitions into amorphous phases have also been observed [151, 152, 153, 154, 155]. Most of these phase

transitions are due to valence electron structure transitions (e.g., s→d, p→d, f→d, etc) in one or more element (in the case of compounds) which affect the effective size of the atoms [156, 157, 158, 159, 160, 161, 162, 163, 164], and others are not yet fully understood [165, 166, 167, 168]. The phase changes are visible as deviations in the equation of state for the material (i.e., relative changes in volume or density with pressure as measured with in-situ XRD) or as deviations in measurements of electronic properties (e.g., resistivity, X-ray emission/absorption spectra, Mössbauer spectra, Raman spectra, etc.) with pressure.

Recently, there have been some observations of hydrostatic pressure-induced phase changes in metallic glases. Work by Sun et al. in 2000 [169] has shown a reversible partial crystallization of a $Zr_{41.2}Ti_{13.8}Cu_{12.5}Ni_{10}Be_{22.5}$ MG, although the complexity of the MG and limited amount of crystallization precluded further explanation of the change. In 2007, Zeng et. al [170] reported the first indication of pressure-induced polyamorphism as a measurement of anomalous compression behavior in a $La_{32}Ce_{32}Al_{16}Ni_5Cu_{15}$ MG and theorized it may be due to Ce electronic structure changes within the utilized pressure regime. Sheng et. al [44] then followed up with the first clear evidence of pressure-induced reversible polyamorphism in a $Ce_{55}Al_{45}$ MG, evidenced by a deviation in the P-V compressibility. *Ab initio* and molecular dynamics modeling allowed for the creation of partial PDFs for Ce-Ce, Ce-Al, and Al-Al bonds, plotted in Figure 2.8. These simulated partial PDFs were created for the lower pressure (pre-polyamorphous EOS deviation) data (Fig 2.8(a)) as well as the high pressure (post-polyamorphous EOS deviation) data (Fig 2.8(b)). Clear changes in the Ce-Ce bonds at the higher pressures were observed with the development of some much shorter Ce-Ce bond lengths. These changes were attributed to 4f delocalization in the Ce at high pressures. The delocalization effectively reduces the atomic size to its next nearest valence shell, allowing for much shorter bond lengths.

Later work performed by Zeng et al. in 2010 [30, 29] further investigated this 4f delocalization in Ce through synchrotron XRD characterization of Ce_3Al MG under hydrostatic compression. Figure 2.9 shows plots of (a) the structure factor and (b) associated first sharp

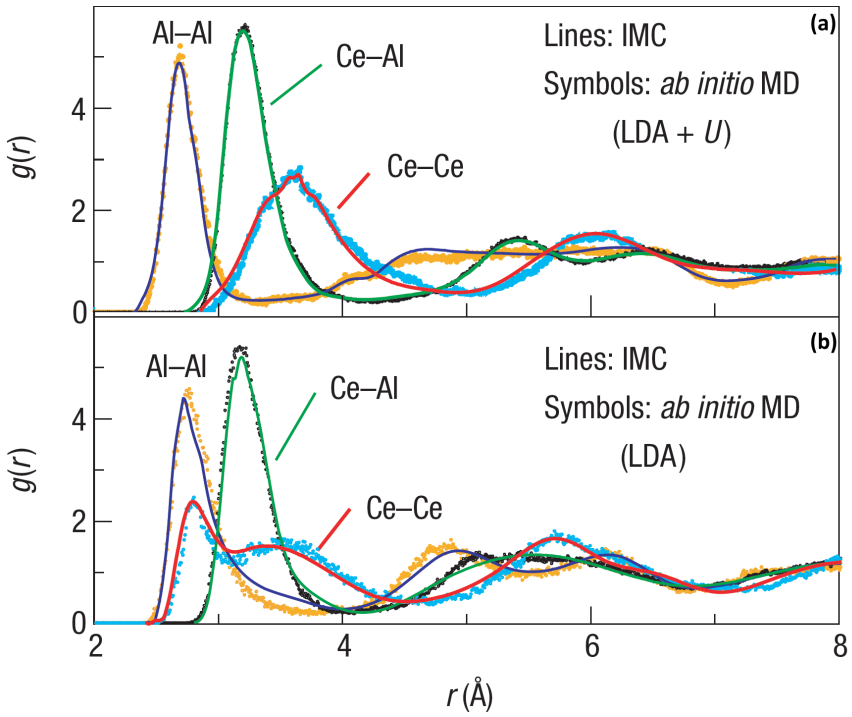

Figure 2.8: Hydrostatic pressure-induced polyamorphism in $Ce_{55}Al_{45}$ MG. Partial PDFs for the Ce-Ce, Al-Al, and Ce-Al bonds are indicated in both plots. The partial PDFs for the low pressure, localized Ce 4f electron state are shown in (a), and the high pressure delocalized Ce 4f electron state are shown in (b). Data was created from both molecular dynamics (MD) (symbols) and inverse Monte Carlo (IMC) (lines) simulations. Changes in the Ce-Ce and Ce-Al PDFs represent the new bond lengths possible with the smaller, delocalized 4f Ce state. Changes can be observed in the nearest neighbor orbital as well as the second and third shells of atomic coordination. [44]

diffraction peak (FSDP) positions with pressure for these studies. Shifts in the FSDP are indicative of density changes, and a general trend with pressure can be expected as an EOS for the material. As shown in Figure 2.9, however, there is a clear deviation in the trend corresponding to an increase in density which starts at 1.5 GPa and continues until 5 GPa. Increased pressures beyond 5 GPa follow a new EOS relation. This EOS deviation is indicative of phase change to a more dense material, and the overall structure factor indicates that this new material remains amorphous. X-ray absorption spectroscopy was utilized in combination with hydrostatic compression to characterize the electronic structure changes; this experimentally confirmed the 4f delocalization at pressures above 1.5 GPa.

Polyamorphism is also observed in other Ce-based MG [171, 172] and has since been

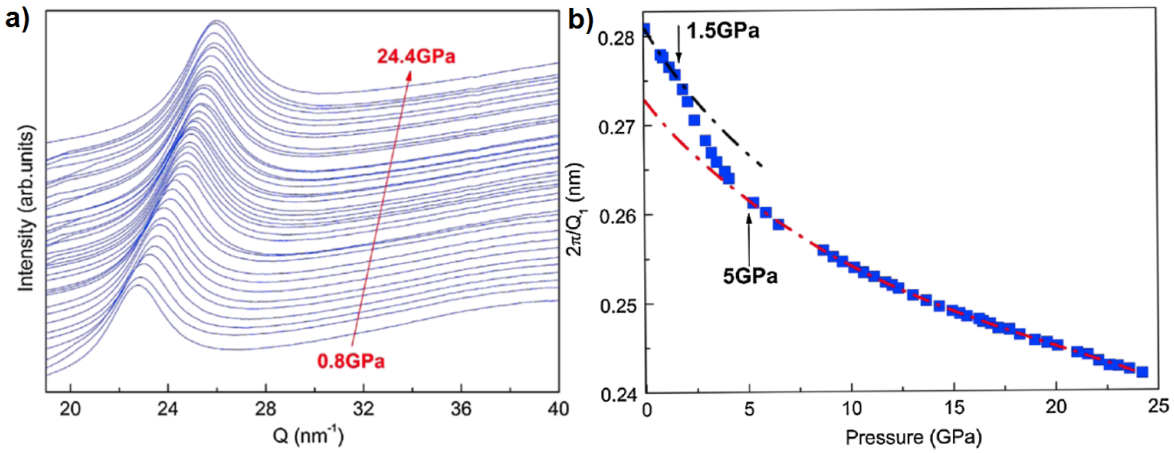

Figure 2.9: *In-situ* hydrostatic high-pressure polyamorphism in Ce_3Al MG as observed via a) the deviation in densification trend of the first sharp diffraction peak (FSDP) of the structure factor and b) the pressure-density EOS plot derived from the inverse of FSDP position changes with pressure. Densification is seen in the structure factor as a shift to larger Q (or 2θ) for the FSDP. The trend of densification with hydrostatic pressure illustrates two distinct states: low density amorphous (dashed black line) and high density amorphous (dashed red line) along with a transition region from 1.5 to 5 GPa. [30]

demonstrated by Li et al. [173] and Liu et al. [174] to exist in all lanthanide-based MGs, as one might expect from the similarities in pressure-induced electronic structure changes shared by all lanthanide elements. Of note, Li et al. [173] found the same effects were not observed when the lanthanide was not the solvent element, potentially indicating either a limitation in detection of smaller magnitude changes or a mechanistic requirement that the solvent element undergo pressure-induced phase changes for polyamorphism to occur. Currently, limitations on knowing and fully characterizing the atomic structure of MGs, as discussed in Section 2.1, have kept researchers from experimentally determining which atomic movements result in the observed average polyamorphism. Simulations are further limited due to molecular dynamic potentials being unable to account for electron structure changes, although recent work has indicated the resource may become available soon [175].

The effect of 4f delocalization in Ce_3Al MG further extends into crystallization at higher pressures. Work by Zeng et al. in 2009 and 2011 [176, 45] shows the irreversible evolution of a solid solution Ce_3Al FCC phase at pressures above 25 GPa. Figure 2.10

shows XRD plots of the Ce_3Al MG at various pressures with the FCC phase apparent at 25 GPa. The FCC phase was observed as an instantaneous and complete crystallization of the entire sample into a single crystal. Thermodynamically, the stable phase for Ce_3Al at ambient pressures and temperatures is a hexagonal close packed structure (α-Ce_3Al). As both Ce and Al are FCC phases independently, it was theorized that the reduced atomic size of Ce at elevated pressures may have allowed for sufficient similarities in atomic sizes between Ce and Al as to allow for the fulfillment of Hume Rothery rules for a solid solution [176]. The instantaneous and complete nature of crystallization was attributed to long-range topological order of the system, wherein the amorphous atomic structure was topologically similar enough to the FCC structure that minimal rearrangements were needed in all atoms for the phase change [45].

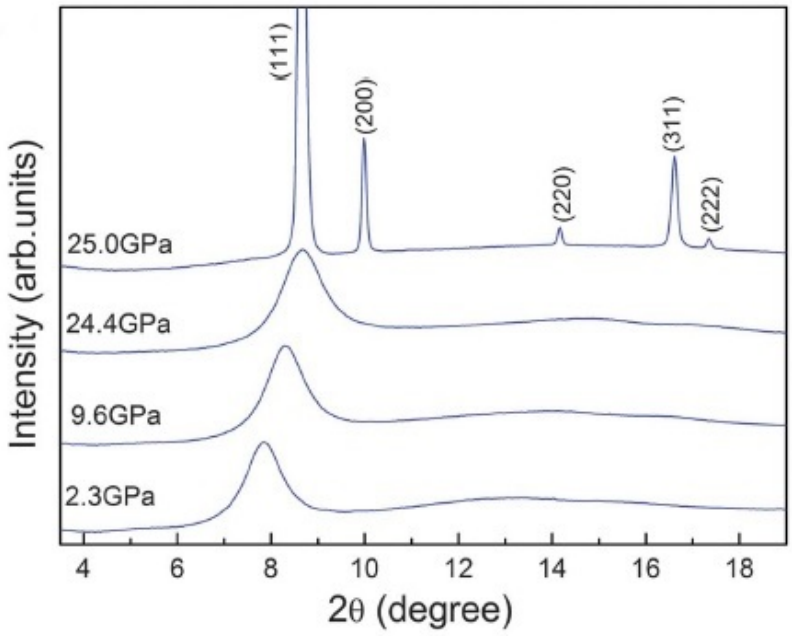

Figure 2.10: XRD traces of the Ce_3Al MG and the crystalline phase formed at 25.0 GPa hydrostatic pressure. Crystallization was instantaneous and complete, forming a single crystalline FCC phase which does not exist on the Ce-Al phase diagram. [45]

The FCC phase was also observed to evolve with uniaxial compression, although it was not formed into a single crystal. It crystallized much slower and required a higher pressure for full crystallization (46.8 GPa) [45]. As such, shear stress does not appear to enhance

the formation of the FCC phase from Ce_3Al MG and, indeed, it may hinder the formation.

Further characterization of Ce_3Al MG under hydrostatic pressure and elevated temperatures indicate that, although there is 4f delocalization at 1.5 GPa, there is no FCC phase formation when thermally crystallized. Instead, the phase formed with thermal crystallization at pressures above 1.5 GPa is the α-Ce_3Al HCP thermodynamically preferred phase at ambient pressures [29]. Figure 2.11 shows the crystallization temperature as a function of pressure. The crystallization temperature is observed to decrease with increasing pressure up to 1.5 GPa. The crystallization minimum at 1.5 GPa correlates with the pressure at which 4f delocalization is known to begin. Further increases in pressure result in an increase in the crystallization temperature. At pressures up to 1.5 GPa, it is hypothesized that there is a pressure-assisted reduction in the thermodynamic barrier for nucleation (necessarily producing a greater effect than any reduced atomic mobility under compression) as discussed in Section 2.2.3. At pressures above 1.5 GPa, it is theorized that the positive trend is partially caused by matching the $La_{75}Al_{25}$ behavior wherein it is observed that increasing pressure elevates the crystallization temperature. Additionally, the 4f delocalization above 1.5 GPa causes a further densification of the MG, potentially amplifying any pressure-mediated atomic mobility retardation [29].

Recently, Lou et al. discovered that Ca-Al MG also have polyamorphous phase transitions under room temperature hydrostatic compression [177]. The authors attribute these polyamorphous changes to pressure-induced phase transformations in pure polycrystalline Ca wherein "s" orbital electrons are transfered into the "d" orbitals. Results indicate higher Ca fractions of the compositions correlated with higher onsets for deviations in compressibility, towards the same value as observed in pure Ca. The authors theorize Al creates "chemical pressure" on Ca, promoting the transfer of "s" and "p" orbitals to "d" orbitals at lower externally applied pressures [177]. These results indicate two important trends: 1) it may be possible to predict the pressure at which phase changes can be observed in a two (or greater) component MG based on the pressure-induced changes of its solvent element

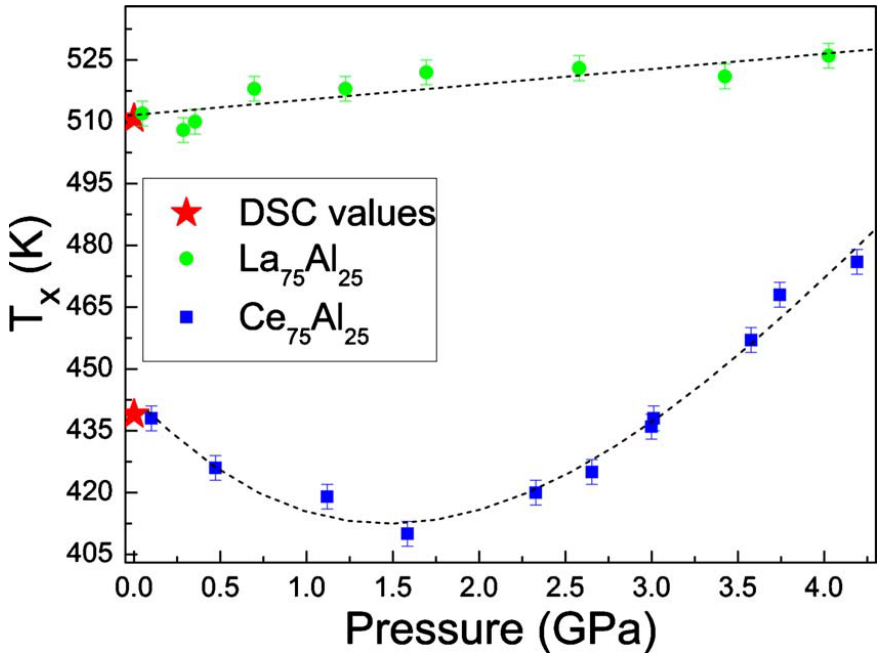

Figure 2.11: Crystallization onset temperature T_x for the $Ce_{75}Al_{25}$ (aka Ce_3Al) MG and comparable $La_{75}Al_{25}$ MG as a function of pressure. Ambient pressure values are marked with stars and are derived from DSC measurements. Ce_3Al MG is observed to have a decreasing and then increasing trend of crystallization temperature with pressure with its minimum crystallization temperature at the pressure for which 4f delocalization begins. [29]

and knowing how the surrounding elements mediate this onset, and 2) pressure-induced phase changes in MG can occur due to electron structure changes in non-lanthanide based MGs. As such, it may be that the explanation for the pressure-induced crystallization observed in the previously mentioned Zr-based MG is tied to the phase changes of Zr under compression [169].

Further, because these pressure-induced phase changes can be observed as changes in crystallization temperature with pressure, as shown for Ce_3Al in Figure 2.11, it may be possible to use this information to explain previously unexplained trends of MG at elevated pressures. For example, the Fe-based MG (discussed in Section 2.2.3) is observed to have a changing trend of crystallization temperature with compression. This may have been affected by changes in Fe under pressure [27]. Figure 2.12 shows (a) the compressibility of this MG and (b) the associated changes in crystallization onset temperature with pressure.

Although there is no discussion by the authors of the compressibility dip visible at $\sim$3 GPa, it may be related to the relative decrease in crystallization temperature also observed at $\sim$3 GPa. Further studies would need to be done to confirm this effect in this system and others; however, it appears to be a promising field of research.

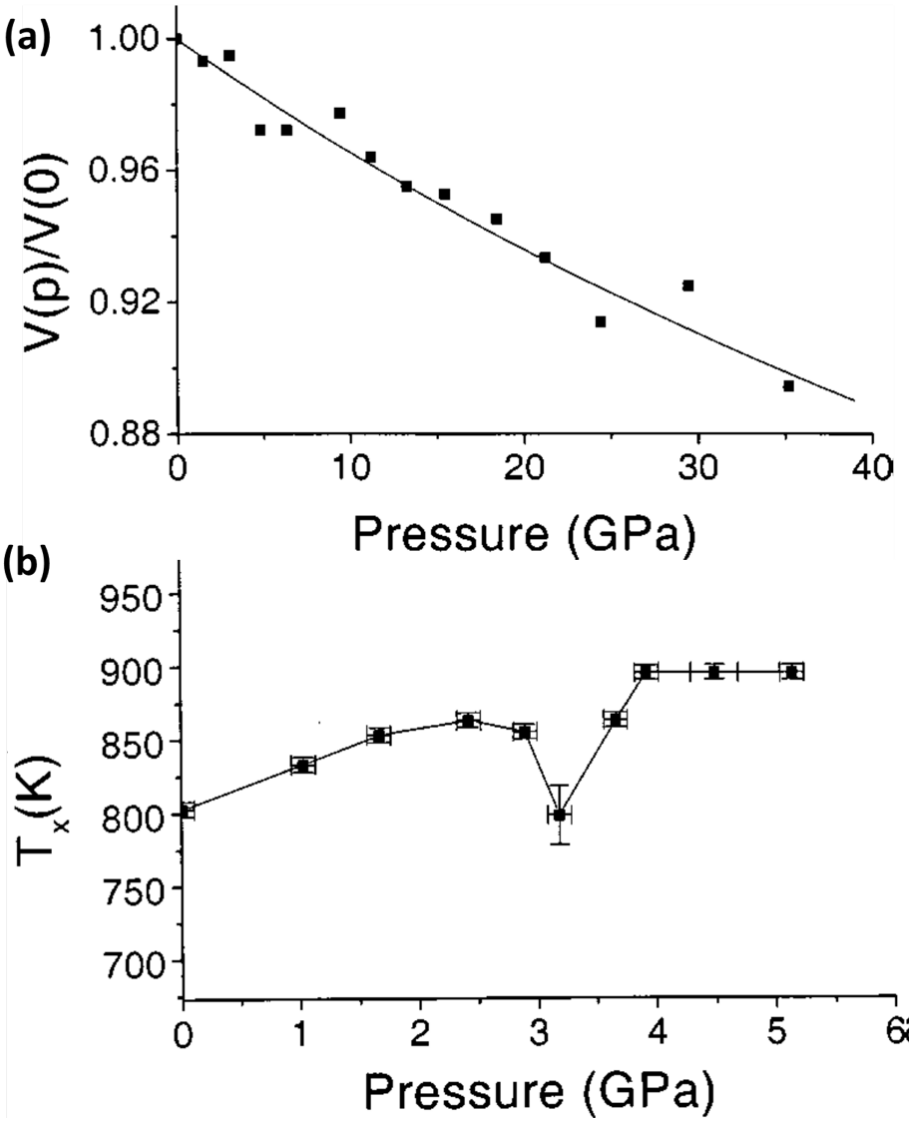

Figure 2.12: (a) Pressure-Volume compressibility of $Fe_{72}P_{11}C_6Al_5B_4Ga_2$ MG at room temperature with a solid curve fit to the data. Precipitous drop in specific volume at $\sim 3\,\mathrm{GPa}$ does not affect trendline. (b) Plot of crystallization temperature of the $Fe_{72}P_{11}C_6Al_5B_4Ga_2$ MG as a function of pressure. Clear deviation occurs at a pressure of $\sim 3\,\mathrm{GPa}$. [27]

2.3 Plastic Deformation of Metallic Glasses

Plastic deformation of solids occurs via shearing of part of a material relative to the rest, producing shape change. Crystalline materials have dislocations which can be generated, and serve as carriers of deformation via the process of glide. Motion of dislocations provide bulk ductility in the material as regions which are already strained can resist further deformation and delocalize the plastic flow. In contrast, the amorphous structure of MGs does not allow for the generation of dislocations or pathways by which they move, build up, and resist further deformation. Instead, MGs deform heterogeneously via shear banding wherein large shear strains are localized within a relatively thin band [18]. The following sections will discuss the mechanisms for shear band formation in MG and the effect of shear bands on MG atomic structure and phases.

2.3.1 Shear Band Formation in Metallic Glass

Shear bands form as local regions are plastically deformed and shear-soften. Shear-softening causes the local atomic regions to be softer than the surrounding undeformed regions and thus more likely to flow. When the soft regions grow in number and size enough to connect, they form shear bands. In MGs, these local regions in which initial deformation begins are called shear transformation zones (STZs), first conceptualized by Argon in 1979 [178]. In a STZ, localized stress allows for overcoming an energy barrier for the group of atoms to cooperatively rearrange into a less efficiently packed organization. The surrounding glassy matrix elastically accommodates this adjusted local shape, resulting in a macroscopic strain in the sample [179, 178]. Figure 2.13 shows a schematic illustration of the atomic rearrangement of a STZ for a model binary glass with the left image representing the initial structure and the right showing the atomic ordering after the shear transformation.

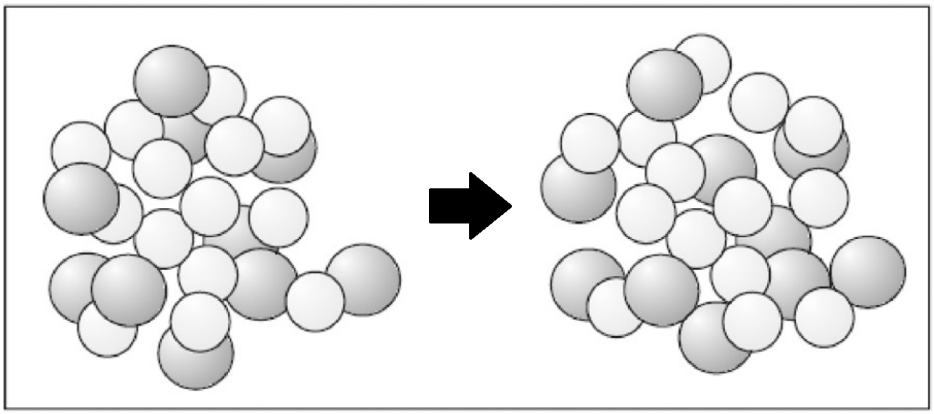

Figure 2.13: Schematic illustration of a local group of atoms before (left) and after (right) shear transformation. Free volume within the atomic packing increases after the transformation. Figure adapted from [180].

Shear Transformation Zones

Throughout the MG, there is a distribution of sizes and energetic barriers of STZ which must be overcome during the shear transformation. On average, STZs have a diameter (size) of $\sim$1 nm, representing a few tens to few hundred atoms, and an activation energy of several tenths of eV [18]. Figure 2.14 shows contour maps of four different representative sample regions, simulated with molecular dynamics, showing the heterogeneous distribution of atoms that are locally "soft" (e.g., GUMs) correlated with the atoms which contribute the most to deformation strain (STZs). The colors indicate how inefficient the local order is (increasing disorder matching a higher heat in the color scale as shown with the arrow and color scale bar). White circles indicate the top 10% locations of accumulated deformation (due to shear), representing the STZs. There is not a perfect one-to-one relation between GUMs and STZs; however, this is not surprising as it is unlikely that only SRO affects the likelihood of shear transformation. It is expected that the neighboring local order, and how interconnected it is with the local SRO (aka the MRO), should also affect where STZs occur [85, 42]. Although GUMs are not a perfect predictor of STZ position, they appear to correlate well with the space of initial stress localization [85, 42, 180, 181]. Indeed, it has been observed that as the number of GUMs is reduced through annealing,

the size and number of STZs similarly decreases [14]. Further, because GUMs relate to the thermodynamic properties of the glass transition temperature (see Section 2.2.2) as well as STZs and yielding, STZs and yielding can also be related to the glass transition. For example, a higher reduced glass transition temperature correlates with a larger number of GUMs, and a larger number of GUMs correlates with a larger amount of STZs and lower yield stress. Therefore, GUMs can allow for a qualitative comparison of the reduced glass transition temperature with mechanical properties [182, 183, 184, 185].

Although the average activation energy of a STZ is a few tenths of eV, the observed distribution of activation energies indicates that some STZs have much lower activation energies [186]. These "easy" STZs operate even within the elastic regime, contributing to the observation that the elastic moduli of MGs are lower than those of their crystalline counterparts [187]. STZs likely contribute to the observed shear-induced rejuvenation behavior discussed in Section 2.2.2 [188, 189, 190], but they do not lead to irreversible macroscopic plastic deformation. The average activation energy for STZs is also the typical barrier for activating enough STZs for global deformation [191]. This relatively high average activation energy associated with the cooperation and simultaneous rearrangement of a significant number of atoms, along with the immobile nature of STZs, likely explains why the macroscopically-measured yield strength of a MG is typically an order of magnitude greater than its crystalline counterpart [18].

Theory for Shear Band Formation from Shear Transformation Zones

The way in which STZs interact to form shear bands has been significantly debated, with three main theories developing. In the first theory, structural fluctuations inherent in the metallic glass itself result in homogeneous nucleation of STZs along the plane with maximum shear stress. The STZs form a softened deformation band, concentrating subsequent shear strains and creating the shear band(s) which lead to deformation. This model is frequently observed in computer simulations with periodic boundary conditions [192] but

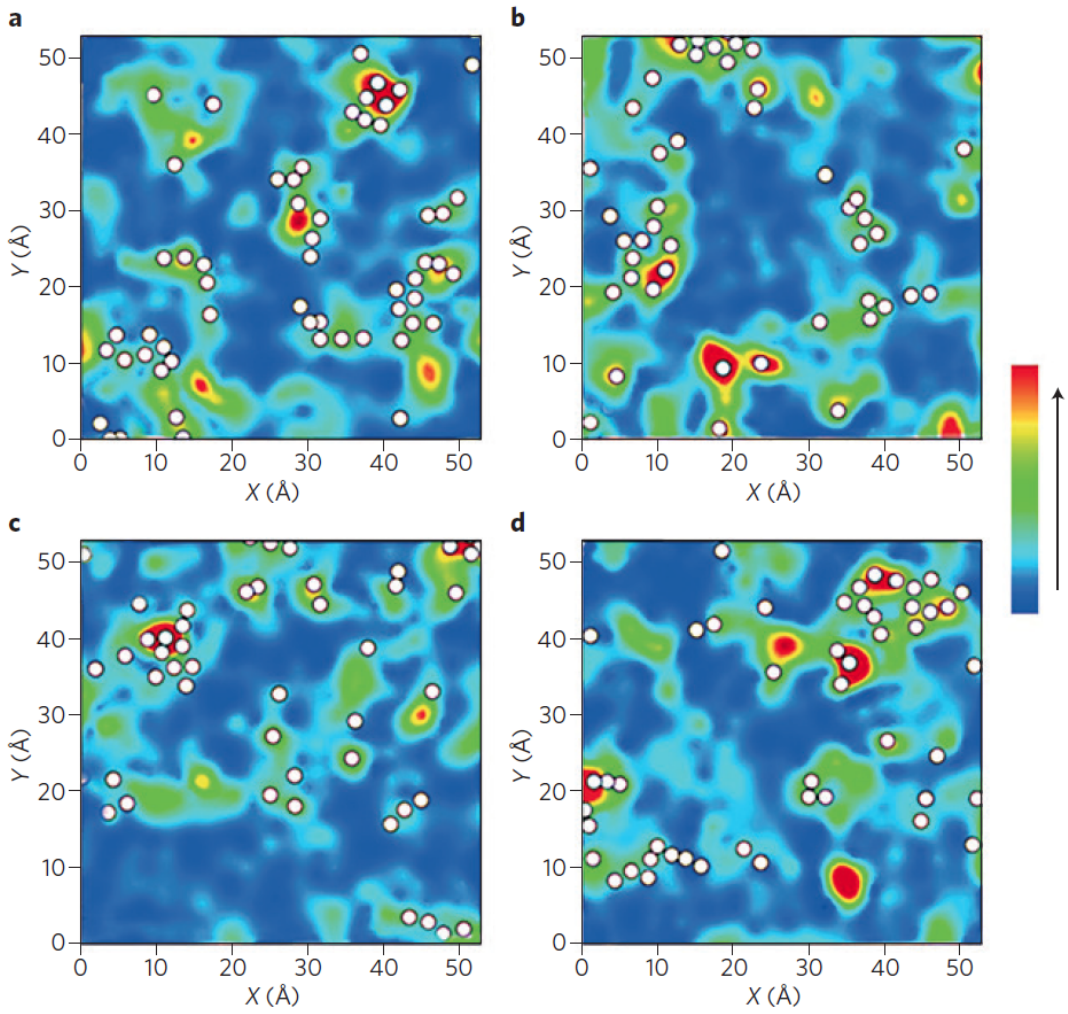

Figure 2.14: Contour map of local SRO and strain distribution in four (a-b) representative 25 nm^2 areas of MG strained to 5% in an MD simulation. Increasing "heat" of the color (following the arrow direction in the color scale on the right) represents increased "disorder" of the local order (where red regions are indicative of GUMs). White circles represent regions with the top 10% of localized strain (aka the STZs). There is an imperfect correlation between GUM and STZ locations. [42, 85]

does not appear in typical experiments [193]. The homogeneous nucleation theory requires the greatest stress for shear band creation of the different theories, representing the ideal strength of the glass.

In the second theory, imperfections such as micro or nano-voids or surface notches act as stress concentrators under external loading conditions and create preferential nucleation sites for STZs. When enough STZs are activated locally (estimated to be $\sim$100 nm in

length), the band self propagates and develops into a full shear band [194]. In general, it propagates by first forming a rejuvenated zone, then a glue-like viscous zone, and finally a melted zone that is at a temperature greater than the the glass transition. Simulations match this model [194], but experiments only show the initial heating observed around a defect and do not correlate with the model beyond the initial nucleation [195, 196].

The third theory considers the shear band formation in two consecutive stages. In the first, STZs activate along a band, creating a regime of disordered atoms with atoms mobilized and the material softened. This rejuvenation progression may be similar to the second theory wherein stress concentrators may allow for faster band formation; but, in this theory, the temperature remains cool. The justification for the low temperature is that the rejuvenation front propagates as a shear wave (around the speed of the transverse sound velocity, $\sim 10^3$ m/s), so the limited duration of this stage (sample of $\sim$ 10s of μm would take $\sim$ 10 ns) precludes any significant shear offset or local heating [197]. The second stage is synchronized with sliding and shear along the rejuvenated plane. Due to the shear-induced large plastic strains during this stage, significant local heating can occur. Figure 2.15 schematically illustrates this two-stage scenario for shear band formation. Both simulations [198] and experiments [199, 200, 201, 202] corroborate this third theory.

Effects of External Loading Conditions on Shear Band Formation

As stresses increase, more GUMs and preferred orientation regions are provided enough energy to activate and overcome the barrier for STZ formation. This results in more interconnected STZs forming a greater number of shear bands. Similarly, increased temperatures provide energy for the activation of STZs, increasing the likelihood of forming shear bands. As the temperature reaches the glass transition, all strain localization is lost as the sample acts as a viscous liquid and undergoes homogeneous flow. In contrast, higher strain rates limit the distribution of shear, causing increasing shear localization and greater amounts of free volume to be generated. As such, the barrier to shear band formation de-

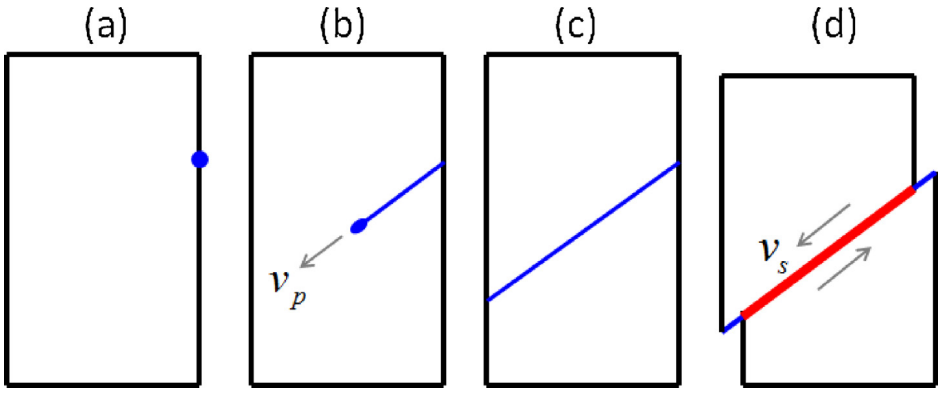

Figure 2.15: Schematics showing how shear bands form in a metallic glass under compression. (a) A stress concentrator (e.g., micro or nano-void or surface notch) creates a localized high stress point. (b) Structural disordering (rejuvenation) propagates at a velocity (v_p) on the order of the shear-wave speed ($\sim 10^3$ m/s). (c) The shear band reaches the other side of the sample leaving behind a rejuvenated plane. The strains and shear offsets are small, and the band is cold. (d) Cooperative rearrangement in the form of shearing/sliding from both ends, resulting in a growth of the shear offset. Depending on the sample size and loading conditions, the shearing may be stable or unstable, the band may remain cold or become hot, and the shear velocity (v_s, the relative velocity difference between the two sides of the shear band) can either follow cycles of acceleration and deceleration (e.g., stick-slip) or increase monotonically. Note v_s is typically $<< v_p$. [18]

creases at high strain rates and shear-banding occurs more frequently [32]. An example of a deformation mechanism map showing the effects of stress, heat, and strain rate is shown in Figure 2.16. For metallic glasses loaded at normal strain rates at room temperature, localization is always expected. When MG are loaded at high strain rates, however, it is expected that many shear bands will form instead of just one.

Of note, the temperature and strain-rate sensitivities are much greater in the ideal model of homogeneous nucleation of shear bands as compared to heterogeneous nucleation. This results in higher shear strength and sensitivity in simulations and models than experiments [193, 204]. When samples are sub-micron in dimensionality, the size limits defects and heterogeneities, allowing for measured responses similar to those of homogeneous nucleation simulations [204].

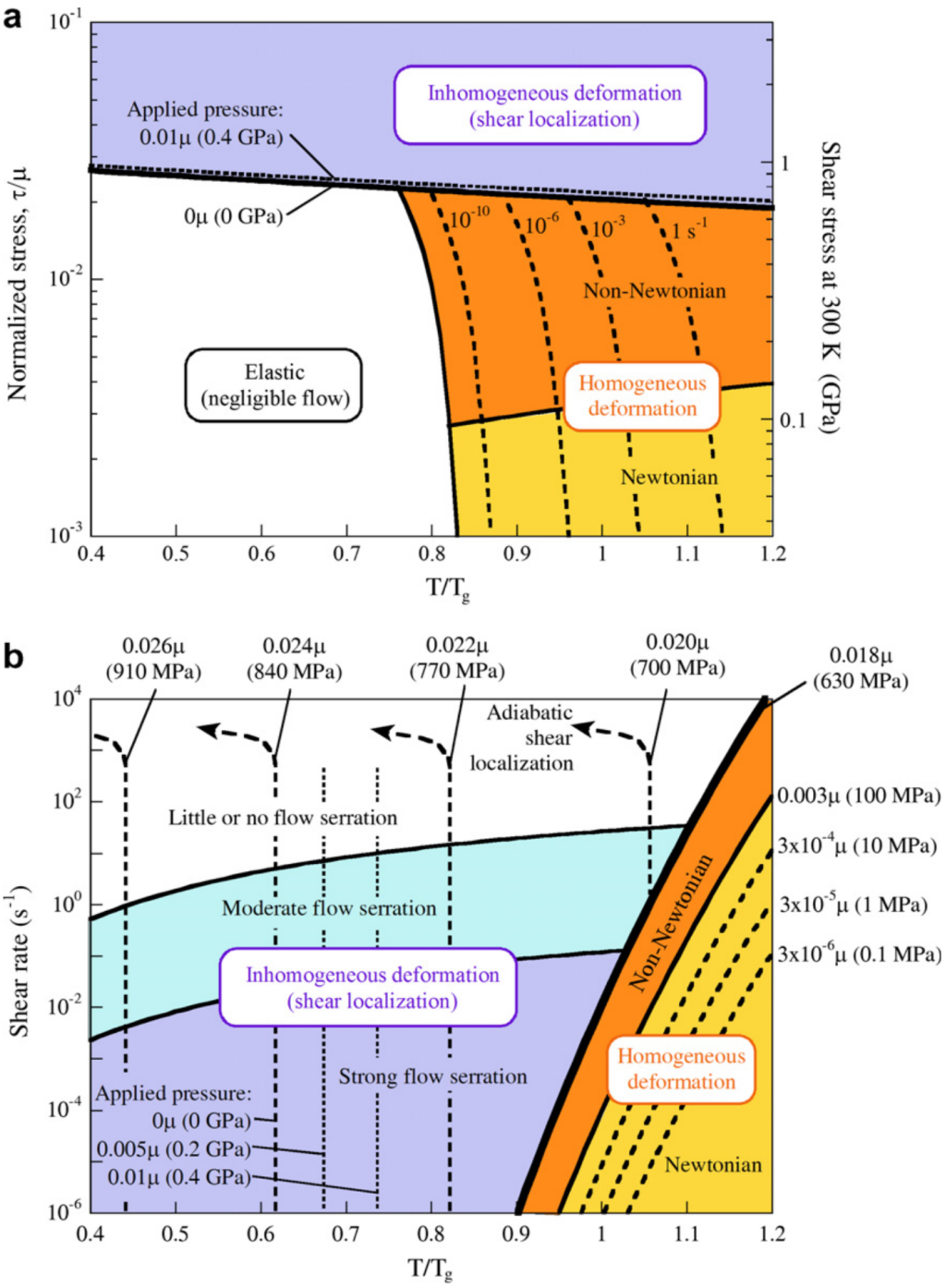

Figure 2.16: Deformation-mechanism map for metallic glasses with (a) stress vs temperature and (b) strain rate vs temperature axes. The plots show the shear localization and flow serration dependence on stress, temperature, and strain rate. Different tested stress values are drawn as lines on the strain rate versus temperature plot. Stress values were measured for a particular glass and given in absolute values but also normalized based on the shear modulus μ to be generalizable for all metallic glasses. [203]

Internal Structure and Temperature in a Shear Band

Figure 2.17 shows the effects of shear band formation on the atomic structure of a MG, based on a representative simulation by Cao et al. [198]. Fig. 2.17(a) presents the dilation induced during the formation of a shear band as determined by the Voronoi volume of atoms. Clear dilation is observable ($\sim$1.5 Å^3) within the band during initial growth and after traversing the width of the material. Fig. 2.17(b) traces the fraction of icosahedra-ordered atomic packing within the MG, showing a significant decrease ($\sim$12%) inside the shear band. As STZs are activated and a rejuvenated plane of connected STZ progresses, the SRO within the shear band changes to accommodate the strain. The change lowers the thermodynamic barrier for crystallization (as discussed in Section 2.2.3 and as will be considered further in Section 2.3.2).

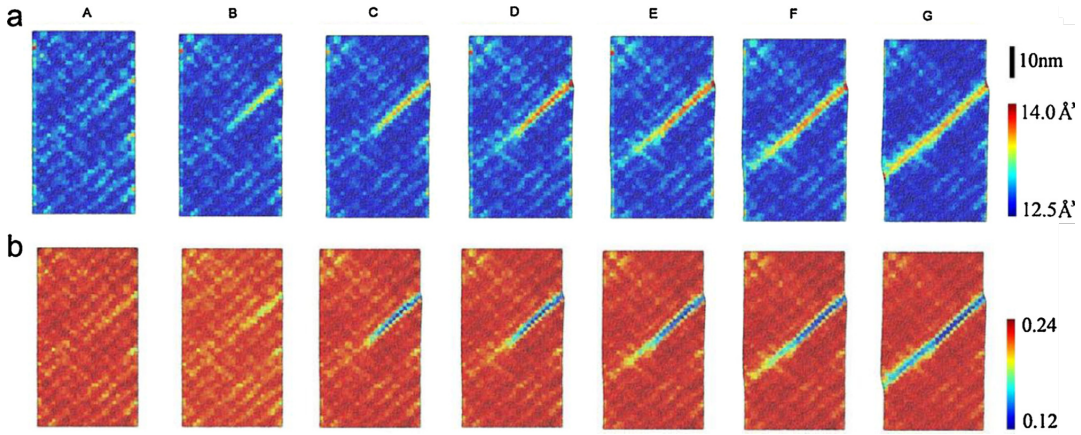

Figure 2.17: Simulated shear band in a MG following the two-stage model at seven time steps (A-G) from initiation of the rejuvenation plane to complete shear band traversal of the width of the material. (a) Dilation during the shear band formation with the Voronoi volume of the atoms illustrated with the color map. Volumes within the shear band are increased $\sim$1.5 Å^3 compared with the surrounding atoms. (b) Fraction of icosahedra atomic packing distributed through the material with the color map representing the fraction. Icosahedral order drops $\sim$12% within the shear band as compared to the surrounding regions. [198]

Synchrotron XRD experiments by Yavari et al. [205], where the first peak position of the structure factor was used to indicate the density, found that the free volume is doubled in a severely deformed MG foil. Dmowski et al. [13] used neutron diffraction to charac-

terize a severely deformed MG (after high-pressure torsion) and observed overall density reduction, as well as both increases and decreases in the atomic bond lengths, representative of the disordering shown in Figure 2.17. Direct HRTEM measurements by Li et al. [206, 58] indicated $\sim$1 nm voids within shear bands, although later studies with careful sample preparation by Chen et al. [207] and Liu et al. [208] did not show evidence of any voids, indicating the voids seen by Li may have been due to sample preparation.

Dmowski and Egami [209] studied the structure of an Fe-based MG after mechanical creep deformation via 2-D XRD and determined that the shear band results in local bond anisotropy. This was also observed in simulations by Karmakar et al. [210], leading to the Bauschinger effect: a deformed glass has asymmetric strength when loaded along and against the original deformation direction.

Initial studies of shear bands indicate significant heating, with some believing the heat was a cause of shear band formation. Recent studies have indicated heating is not a prerequisite for shear banding and only occurs after shear band formation and as a consequence of dissipated plastic work [18]. Direct measurement of the heat produced from shear bands is difficult, with the best resolution thermal camera measurements detecting at a time frame longer than the time for shear band formation (10^{-3}s resolution vs 10^{-5}s time for shear band to propagate) and over a physical size larger than a shear band ($\sim 10\,\mu\mathrm{m}$ resolution vs $\sim 10\,\mathrm{nm}$ shear band diameter) [195, 211]. By measuring the average increase in temperature after complete shear band formation and assuming it diffuses to the visible resolution, it has been determined that the temperatures within shear bands can increase by $\sim$650-1200 K [18]. Similar studies show higher strain rates result in greater temperature rises [212].

Indirect measurements of temperature appear to allow for higher spatial resolution ($\sim$100 nm vs $\sim 10\,\mu\mathrm{m}$ for thermal cameras) detection of duration and magnitude of temperature increases. By coating a Zr-based MG with tin and checking for melting of the tin around shear bands, Lewandowski and Greer [213] found two different shear-band thermal regimes with the calculated heat content (from the shear band) of 0.4 kJ/m^2 and 2.2

kJ/m^2. This results in durations at which the temperature was above the melting limit for tin (232 °C) of 7 and 167 ns, shear durations of 3.9-7.0 and 20.9-37.3 ns, temperature increases at the center of the shear band of 560-740 and 1490-1990 K, and regimes of sample heated of 500-700 and 1000-1400 nm [213]. As the shear-band thickness is 10-20 nm [214], the heating effects clearly extend greatly outside of the shear band, although the higher temperature spatial regimes do not affect the size of the shear bands [18]. Of note, this is different from the behavior of polycrystalline metals which have shear banding in which thermal softening competes with work hardening and low thermal conductivity causes the shear band thickness to be comparable to the thermal diffusion length. Without work hardening, significantly more localization of shear can occur in MG [18].

As shown in Figure 2.16, the localization can cause a "stick-slip" or serrated flow of shear in MG during deformation. At lower strain rates, shear band formation is limited by the viscosity of the MG and therefore is $\sim 10^6$ times slower, temperature increases are $\sim 10^3$ lower, and a single shear band does not always cause failure. As such, when a shear band forms, there is time for multiple other simultaneous shear bands to form off the dominant one, causing the observed "stick-slip" or serrated flow behavior [18]. In contrast, as strain rates rise, shear occurs much faster within the MG, temperatures grow within the shear bands, and greater localization of shear causes the number of shear bands simultaneously formed to increase. As such, there is no subsequent creation of shear bands as one grows, removing the serrated flow behavior. These changes appear to correlate with the onset of ductility at higher strain rates [213, 215] and increased likelihoods of shear-band-induced crystallization, as will be discussed in the next Section.

2.3.2 Deformation-Induced Crystallization of Metallic Glass

It has been known since the mid-1980's that room-temperature mechanical deformation (e.g., ball-milling, bending, nanoindentation, uniaxial compression, high-pressure torsion, cold-rolling, etc.) can induce crystallization in MG [216, 217, 218, 19, 219, 220, 220, 60].

The first study correlating crystallization with shear bands was performed by Chen et al. [19] via TEM analysis of a bent MG ribbon. The study found crystallites 7-10 nm in diameter within the shear band. There is some consensus that nanocrystals within cold shear bands (e.g., low strain rate) are typically formed due to the rejuvenation stage of shear band formation (from which the increased free volume decreases the thermodynamic barrier for crystallization) and shear-induced atomic movement instead of heating effects [221, 222, 223, 224]. However, in hot shear bands, there is typically limited crystallization within the shear band as the heat causes re-amorphization through melting and rapid cooling ($\sim 10^9$ K s^{-11}) [18]. The diffused heat from the shear band has been observed to cause crystallization in the surrounding area [22, 23].

Limited durations of the rejuvenation stage and subsequent temperature increase preclude any significant diffusion-based crystallization (e.g., primary or eutectic crystallization) and therefore often results in different crystallization phases than those formed through purely thermal means [225, 60, 217]. In addition, deformation-induced nanocrystals frequently have elongated shapes and contain dislocations [226].

As discussed in Section 2.2.3, pressure provides an increased driving force for crystallization of metallic glasses, and elevated temperature or other dilatory effects such as shear can aid atomic mobility. Yavari et. al. [28] showed that crystallization can be significantly accelerated under compression while the sample is at an elevated temperature. Similar acceleration of crystallization is also likely during compression-induced shear band formation.

It is unclear when crystal formation occurs, i.e., during or after compressive loading and shear band formation, in MGs [18]. Many studies indicate shear bands aid the driving forces for nucleation and the rate of crystallization, with the timing dependent on the MG composition, magnitude of the driving forces, and degree of acceleration. Metallic glasses with lower fragility (e.g., higher GFA) resist crystallization and therefore are less likely to crystallize during shear band formation [227]. However, under the right conditions (e.g.,

higher strain rates and pressures), crystallization may occur simultaneously with shear band formation. When it does, it is associated with improvements in the strengthening of MG as the nucleated crystallites impede shear bands and allow for greater strain before failure [18]. With the high strain rates and pressures of shock-compression, it might be expected that shock-compression that results in deformation will likely form crystallization-inducing shear bands. Further discussion of shock-compression effects on MG will be discussed in the next Section.

2.4 Shock-Compression Response of Metallic Glass

Shock-compression results in a very rapid to discontinuous rise in pressure and energy. Effectively, this results in pressures into the GPa regime or greater, significant shear stresses, elevated temperatures, and plastic deformation at strain rates of 10^4 s^{-1} or greater [228]. At pressures below the Hugoniot elastic limit (HEL), an elastic stress wave propagates at the speed of sound, with but limited total strain and no plastic deformation.

Shock-compression pressures above the HEL, the plastic deformation in MGs occurs at high strain rates likely via significant strain localization to the point of forming multiple shear bands simultaneously throughout the sample. The shear bands can induce significant heating (in addition to that caused by shock-compression). The formation of increased free volume in the shear bands and highly localized temperatures can result in significantly rejuvenated MG, crystallization, or even melting (and subsequent rejuvenation or crystallization) depending on the material and applied shock pressure. Additionally, pressure-induced electron-structure changes can affect the effective atomic sizes of component elements and potentially facilitate formation of higher density amorphous or crystalline phases.

Pressure-induced changes in the electron-structure of component elements and associated decreases in effective atomic sizes can also occur at pressures below the HEL. These changes coupled with significant shear may allow for rearrangement into new, higher density amorphous phases. Furthermore, the dynamic nature of shock-compression can allow

for changes which typically relax under traditional loading to be "trapped-in."

Studies of shock-compression of MGs are limited [34] and experimental complexities of shock-compression have restricted time-resolved structural analyses of the high-pressure states of materials. Velocimetry and stress-gauge measurements performed during shock-compression allow for determination of the shock-compressibility of MG. Simulations of the shock-compression of MGs allow for more detailed study of the atomic structure changes tied to the loading conditions; however, limitations of structural and temporal scales and atomic potentials restrict definitive conclusions.

2.4.1 Experimental Studies of Shock Compression of MGs

The equation of state (EOS) of a Zr-based MG of composition $Zr_{55}Al_{10}Ni_5Cu_{30}$ was studied by Mashimo et al. [36, 229], using a powder gun and the inclined-mirror photographic technique at pressures up to 50 GPa. A comparison set of experiments was also performed on thermally crystallized samples (composed of three different phases) of the same composition. Figure 2.18 illustrates the plot of (a) shock velocity (U_S) and particle velocity (U_P) and (b) the pressure-density for the MG and pre-crystallized samples. For the MG, there is initially a positive U_S - U_P slope with a kink at a U_P of 380 m/s. Above the kink, the U_S - U_P slope is almost zero. The change in slope is attributed to a structural phase transition. No phase transition or kink is observed for the crystalline sample.

The Pressure-Density compressibility curves in Figure 2.18(b) indicates the HEL at $\simeq 7$ GPa and the glass transition point at approximately 14 GPa to a higher density phase. X-ray diffraction (XRD) characterization of the recovered MG samples after shock-compression showed no evidence of crystallization. The authors theorized that the cause for the observed kink in the Hugoniot-compressibility curves was due to three potentialities: (1) crystallization that didn't progress enough during the nano to microsecond duration of shock-compression to be identifiable *post-mortem* with XRD analysis, (2) a polyamorphous transition resulting in a higher density amorphous phase, or (3) a transformation

(crystallization or polyamorphous) which reverted to the parent amorphous phase upon release [36, 229]. It is also possible that the Cu K-α tabletop XRD measurements of the recovered sample may not have enough resolution to detect a polyamorphous change.

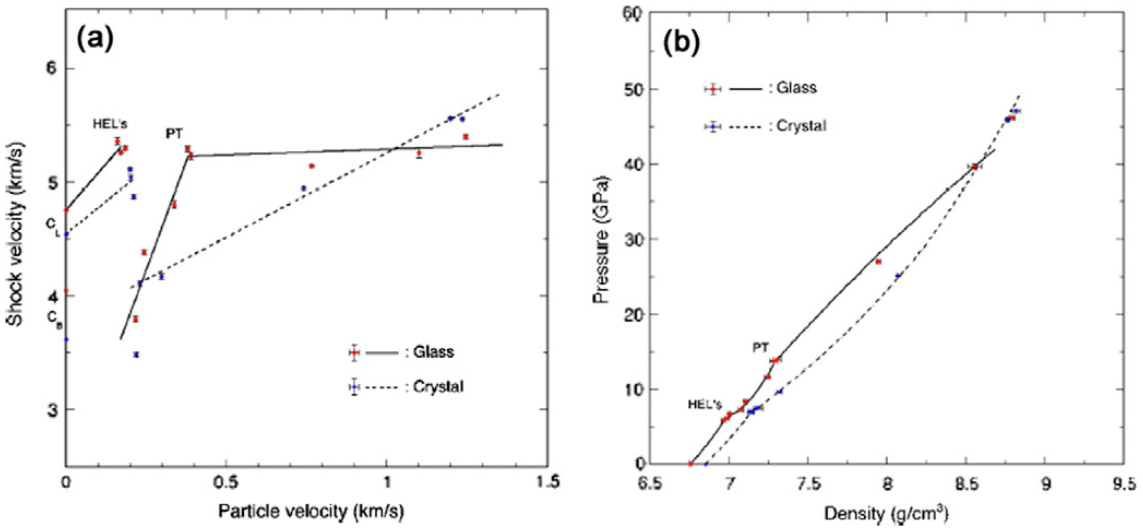

Figure 2.18: Hugoniot data for the $Zr_{55}Al_{10}Ni_5Cu_{30}$ MG and its fully-crystalline alloy at pressures up to 50 GPa. (a) Measured $U_S - U_P$ data up to and above the Hugoniot Elastic Limit (HEL) for $Zr_{55}Al_{10}Ni_5Cu_{30}$ MG and crystal. A change in slope attributed to a phase transition (PT on plot) was observed in the MG at a particle velocity of 380 m/s but was not observed in the crystalline sample. (b) Pressure-density data for the MG and crystalline phases based on measured shock velocity data. A deviation in the slope for the MG at approximately 13.6 GPa is attributed to a phase change. [36]

The EOS of a Zr-based MG of composition $Zr_{57}Nb_5Cu_{15.4}Ni_{12.6}Al_{10}$ was also studied by Martin et al. [35, 34]. Single and two stage gas gun experiments were performed at pressures ranging from 5 to 123 GPa. As shown in the $U_S - U_P$ plot in Figure 2.19(a) and the Hugoniot Pressure-Density compressibility curve (Pressure vs Density) in Figure 2.19(b), two changes in slope are observed. In the $U_S - U_P$ plot, the kinks are observed at a U_P of 720 m/s and 1710 m/s. The low pressure region of the P-ρ plot fit with the Birch-Murnaghan EOS [230, 231], yielding a bulk modulus which matched its experimentally determined value. Fitting the Birch-Muraghan EOS to the data in the high pressure range yielded a bulk modulus value 144% greater than that of the unshocked sample, indicating significant *in-operando* strengthening of the MG, due to a possible phase transition. The

bulk modulus does not match that of any known crystalline phase(s), which led the authors to conjecture the transformation is to a higher modulus polyamorphous state.

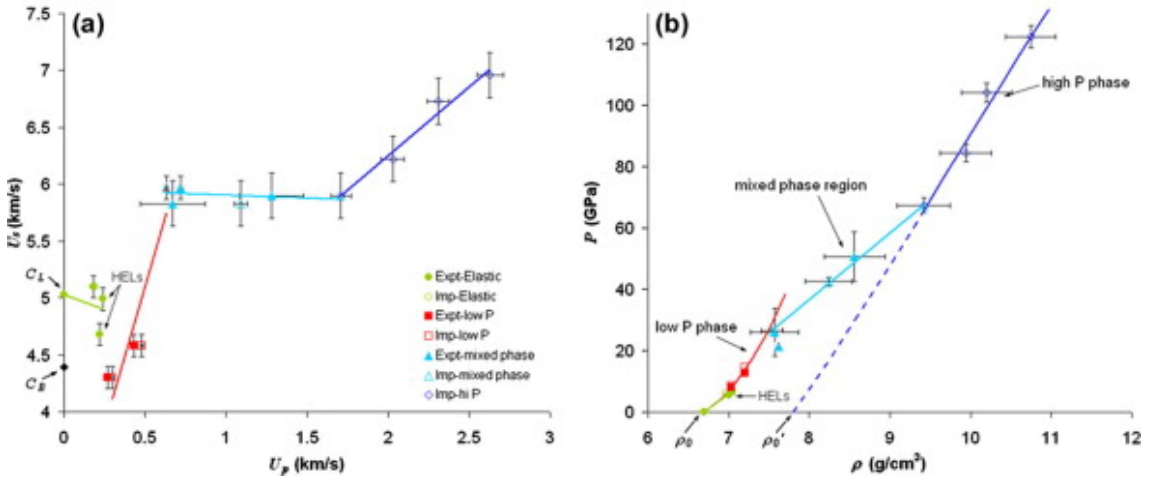

Figure 2.19: (a) Measured $U_S - U_P$ data of the $Zr_{57}Nb_5Cu_{15.4}Ni_{12.6}Al_{10}$ MG with fit lines to the data indicating two phase changes. (b) Hugoniot P-ρ compressibility curves for the MG with Birch-Murnaghan EOS fits to the low and high pressure regions. [35]

Laser driven shock-compression experiments on samples of Ce_3Al MG ribbons have been performed by Chen et al. [37] at pressures of 1.3, 2.3, and 3 GPa. A comparison set of measurements was performed on thermally crystallized samples of the same composition. Time-resolved particle velocity profiles were obtained with velocity interferometry and a temporal fiducial. Figure 2.20(a) shows the particle velocity profiles of the MG, and Figure 2.20(b) shows the associated stress-volume plot converted from the particle velocity profiles using the temporal fiducial data for sound speed with respect to time. The particle velocity trace shows a decrease in the rise for the 2.3 GPa peak pressure loading condition indicative of a phase change. This deviation is not observed in the 1.3 or 3 GPa conditions. The deviation in the rise for the 2.3 GPa velocity profile is visible as a deviation from the stress-volume trend in Figure 2.20(b). The reduction in volume is calculated to be approximately 7% and begins at $\sim$1.5 GPa. This densification occurs at a similar pressure ($\sim$1.5 to 2.3 vs 1.5 to 5 GPa) as the hydrostatic-compression-induced phase change in Ce_3Al and is of similar magnitude [30]. As such, the authors attributed the result to a sim-

ilar shock-compression induced polyamorphous phase transition to a denser metallic glass phase. The phase transition observed at 2.3 GPa is not revealed by the velocity profiles in experiments at higher pressures, indicating the transition can be over-driven. No structural measurements were performed on the recovered shock-compressed samples.

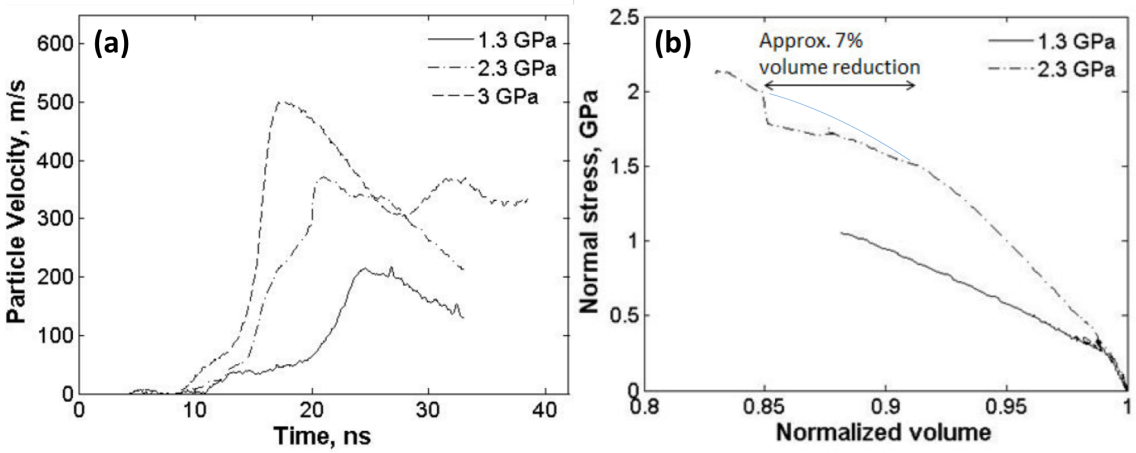

Figure 2.20: (a) Measured particle velocity profiles for the Ce_3Al MG at increasing laser drive energies. Each trace is labeled according to the calculated stresses at the peak state. An intermediate loading wave is observed for the sample driven to 2.3 GPa which is not observed in the 1.3 or 3 GPa measurement. (b) Converted stress-volume traces for the 1.3 and 2.3 GPa loading conditions. The intermediate loading wave in 2.3 GPa corresponds to a $\sim$7% volume reduction, visible as a deviation in the stress-volume trend which starts at $\sim$1.5 GPa and reverts at the onset of the second wave. The solid line is added to show where the deviation occurs. Figure adapted from [37].

2.4.2 Computation Studies of Shock Compression of MGs

Molecular dynamics (MD) simulations can allow for characterization of the atomic structure changes within MG during shock-compression. Most computed simulations have been performed with the Cu-Zr MG system due to the availability of an atomic potential which has been validated with experimental data [38, 39, 40]. The simulations appear to indicate that shock-compression effects are similar to what one might expect for deformation occurring at higher strain rates and high pressure conditions. Jian et al. [38] simulated the shock-compression response of $Cu_{46}Zr_{54}$ MG at pressures up to 80 GPa, utilizing the Holian and Ravelo Hugoniostat [232]. The simulation approach maintained the ensemble

pressure, temperature, and atom number at the Hugoniot condition while satisfying the Rankine-Hugoniot jump conditions for steady shocks. Additionally, the authors performed two calculations using the non-equilibrium MD (NEMD) approach wherein direct impact is modeled. For comparison, the authors also performed simulations of hydrostatic isothermal compression at 300 K and isobaric heating at 60 GPa. Structural analyses were performed via Voronoi tessellation, allowing for determination of the SRO and MRO connectivity. Simulated 2D XRD measurements were used to measure phase changes; no crystallization was observed for any shock-compression conditions. The authors theorized crystallization was possible but would occur too slowly to be observed in the timescale of MD simulations.

Figure 2.21 shows the simulated shock-induced changes revealed in plots of (a) particle velocity U_p, (b) temperature, and (c) diffusivity D as a function of increasing shock stress σ_{xx}. In (a) and (b), the red dots correspond to the Hugoniostat simulations, black squares correspond to NEMD simulation results from Arman et al. [40], and blue triangles correspond to NEMD simulations. In (c), the red circles correspond to the shock-compression data and the black squares represent the comparable pressure hydrostatic-compression changes in diffusivity at 300 K. At 60 GPa, the particle velocity is $\sim$1500 m/s, temperatures reach $\sim$1300 K, and the diffusivity of the shock-compressed data begins to exponentially grow. There is a kink in the $T - \sigma_{xx}$ trend at 60 GPa (Fig 2.21(b)), which, combined with the rise in diffusivity, corresponds to the onset of shock-induced melting [38].

Structural changes correlate with shock-induced melting. Figure 2.22 illustrates the SRO of the MG via the number of efficiently-packed icosahedra (n_{ico} - red circles) and the MRO through the number of icosahedron networks (n_{nw} - blue squares) and associated maximum size of the icosahedron networks (s_{max} - black triangles). These values are plotted as a function of (a) hydrostatic pressure at 300 K, (b) temperature at a hydrostatic pressure of 60 GPa, and (c) shock-compression stress (σ_{xx}). The number of icosahedron SRO grows with pressure and shock-compression stress, with the most rapid and largest

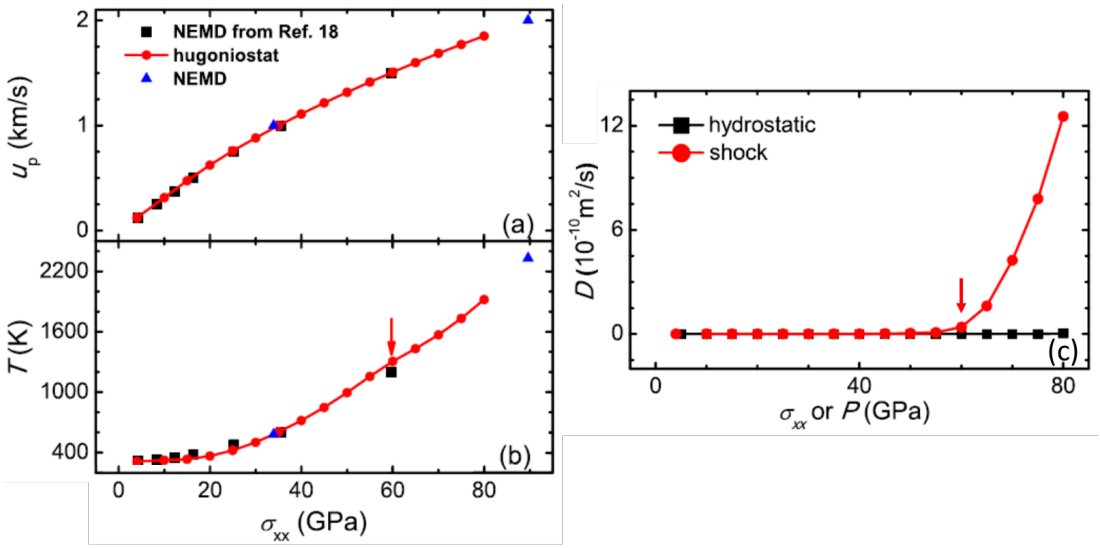

Figure 2.21: Simulated shock-compression effects revealed in plots of (a) particle velocity U_p, (b) temperature, and (c) diffusivity D with increasing shock stress σ_{xx}. In (a) & (b), red dots correspond to the hugoniostat simulations, black squares correspond to NEMD simulations results from Arman et al. [40], and blue triangles correspond to NEMD simulations. In (c), the red circles correspond to the shock-compression data and the black squares represent the comparable pressure hydrostatic compression changes in diffusivity. Arrows point to the values at 60 GPa, illustrating a kink in the $T - \sigma_{xx}$ trend and the onset of exponential diffusivity growth. Figure adapted from [38].

magnitude growth observed with shock-compression. Heating does not appear to affect the SRO or MRO significantly. The size of the icosahedron networks follows a similar trend with an associated decrease in the number of networks. The icosahedron networks appear to connect as the number of icosahedra increase with elevated pressures or shock-compression stresses. Complex changes in non-icosahedral SRO are also observed, with an overall increase in high CN and decrease in low CN as pressures increase, with the trend reversing at the onset of shock-melting.

At ∼50 GPa shock-compression stress, an onset of decay in SRO and MRO begins and is visible as a decrease in n_{ico} and n_{nw} and associated rise in s_{max}. This indicates structural changes occur prior to the observed "shock-melting" at 60 GPa in Figure 2.21. Decreases in order with hydrostatic compression at 60 GPa indicates disorder can be induced via pressure without diffusivity increases (as seen in Figure 2.21). The authors claim large lo-

calized deformation of constituent atoms via shearing causes the icosahedra order collapse with hydrostatic-compression at 60 GPa. Similar effects likely cause the structural changes at 50 GPa, prior to melting, for shock-compression. The authors note that the increased short and medium-range ordering with shock-compression stresses revert upon unloading until 60 GPa. The decrease in order above 60 GPa is irreversible due to melting.

A similar MD shock-compression study of $Cu_{46}Zr_{54}$ MG by Arman et al. [40] was performed with the NEMD method and Voronoi tesselation for determining structural changes. Similar to lower strain-rate loading conditions, STZs and shear bands were determined to be the mechanism for these observed plastic deformation. Additionally, GUMs were the preferred site for STZ activation, and increasing shock stresses were found to activate more STZs and elevate temperatures. STZs were not observed to be of any higher temperature than the surrounding atoms, indicating there is significant homogeneity of activated STZs and high thermal conduction under shock-compression. Upon release, some STZs were observed to persist. The authors note that MD simulation time scales preclude clear understanding of thermal effects on the structure and deformation behavior. Formation of STZs correlated with creation of higher CN SRO behind the shock front, agreeing with the results of Jian et al. [38].

A piston-driven-shock-compression MD simulation study by Wen et al. [39] with Cu_xZr_{100-x} MG indicated that there may be three regimes of the shock-compression response. Figure 2.23 illustrates the $U_s - U_p$ relation derived by these simulations. In region I, a single elastic wave develops and results in negligible shear stress relaxation behind the shock wave front. In region II, a plastic wave develops, which is of lower velocity than the elastic precursor, and the two waves separate during propagation. This plastic wave velocity increases with input pressure at a faster pace than the elastic wave. In region III, the plastic wave over-drives the response and is the only visible wave. The authors observe that at the pressures corresponding to the boundary between region II and III, the temperature increase with pressure begins to accelerate. This change in the temperature

trend with pressure may be indicative of saturated STZ activation and increased deformation in region III [40]. In Region II, plastic waves may be more indicative of densification of the SRO with limited plasticity [40, 38]. In addition, comparisons of the different MG compositions indicate that higher Cu-content MG, known to have more icosahedral order, greater stability, and a higher GFA [233, 83], have the following characteristics: higher U_s, greater maximum peak shear stresses, and lower temperature increases with increasing shock-compression pressures; that is, increased MG stability correlates with greater shock-compression strengths.

Results of simulation studies indicate that shock-compression results in STZ formation and densification through SRO rearrangement into higher CN clusters. The STZs are retained on release, but the densification from SRO rearrangement reverts on release. There appear to be multiple regimes of change with increasing shock-compression stresses: (1) STZ activation and rapid increases in icosahedral order; (2) STZ saturation and less rapid increases in icosahedral order; (3) shock melting and reduction in SRO and MRO order. MD simulations are limited in temporal scope and therefore cannot predict what would be observed in recovery of shock-compressed MG. However, the results indicate that one might expect to observe the following trends in recovered MG as a function of shock-compression pressure: (1) elastic waves causing densification which reverts on release (no visible change); (2) plastic wave-induced STZ formation which is retained on release, resulting in lower CN SRO and decreased densities; (3) STZ saturation maximizing decrease in CN but also increased heat production and associated relaxation or crystallization prior to recovery analysis; (4) high-pressure shock melting of STZs and possibly surrounding regions, resulting in either re-amorphization (and rejuvenation) or crystallization depending on the GFA and quench rate. In Chapters 5, 6, and 7, the results of shock-compression of Ce_3Al MG, including structural analysis of the recovered samples and theories for the observed changes in Ce_3Al MG and the Zr-based MGs will be discussed.

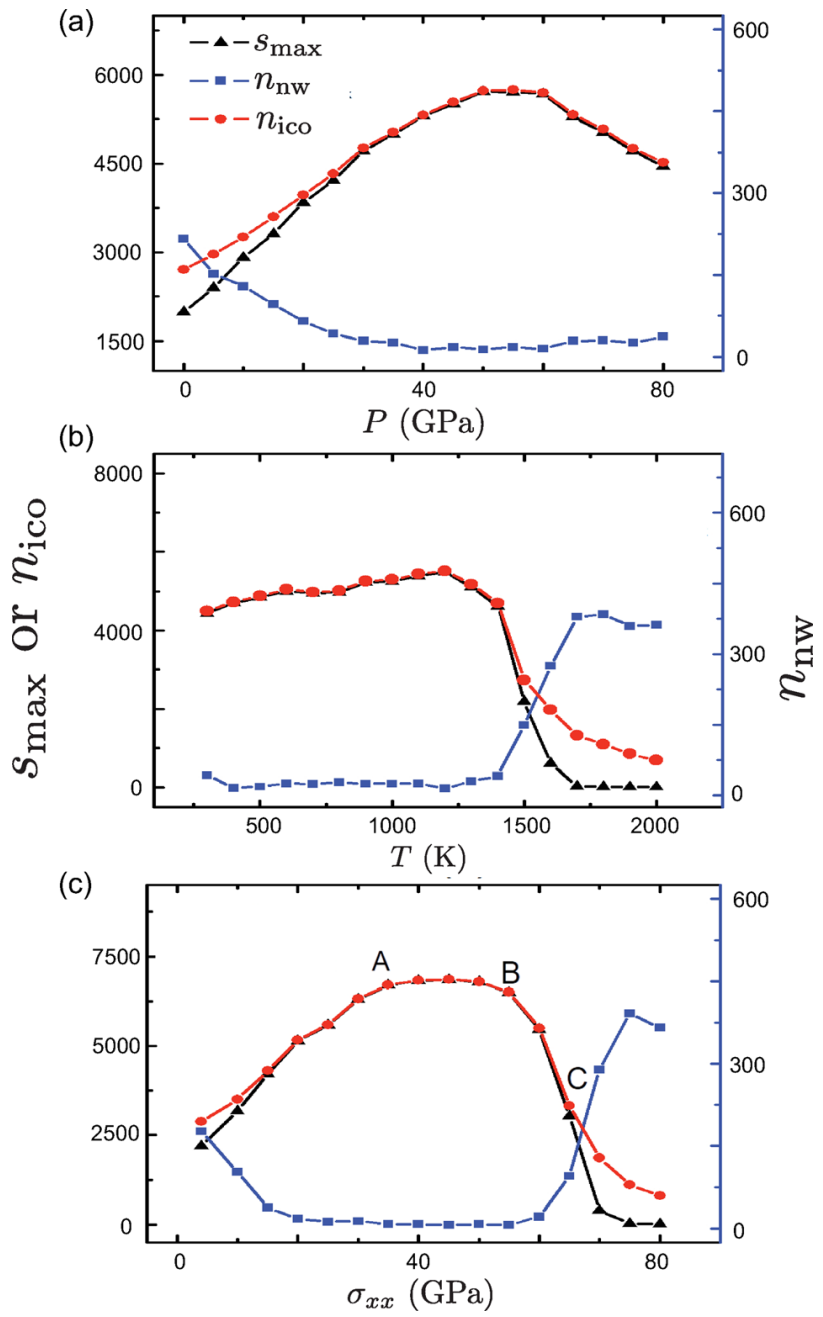

Figure 2.22: Simulated SRO and MRO changes with (a) hydrostatic-compression, (b) isobaric heating, and (c) shock-compression. SRO visualized as a function of the number of icosahedra efficiently-packed clusters (n_{ico} - red circles), and MRO is shown as a function of the number of icosahedron networks (n_{nw} - blue squares) and associated maximum size of the icosahedron networks (s_{max} - black triangles). Pressure and shock-compression increase SRO and MRO with shock-compression providing the increase at a faster rate and in greater magnitude than pressure. Temperature has no significant effect on SRO and MRO. Disorder begins at 60 GPa in hydrostatic-compression, 1300 K in isobaric heating, and 50 GPa in shock-compression. Decreased structural order begins at a lower shock-compression stress than the 60 GPa at which diffusivity growth starts. [38]

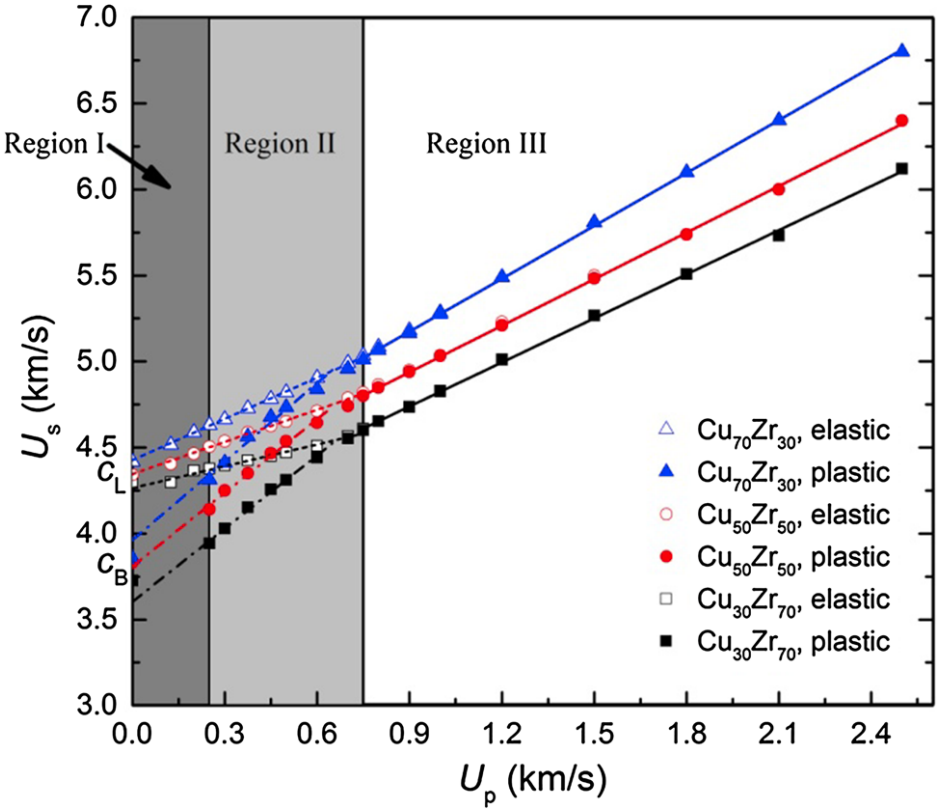

Figure 2.23: Simulated shock-compression $U_s - U_p$ Hugoniot curves for $Cu_{30}Zr_{70}$, $Cu_{50}Zr_{50}$, and $Cu_{70}Zr_{30}$ MG. Three regimes are visible: in region I, there is only an elastic wave; in region II, a plastic wave develops which is of a slower velocity than the elastic wave; in region III, the plastic wave overtakes the elastic wave and is the only visible wave. [39]

CHAPTER 3
TECHNICAL APPROACH

The objectives of the research performed in this work were to (a) determine the occurrence of shock-induced changes in the Ce_3Al MG, (b) characterize the atomic structural changes corresponding to different pressure regimes, and (c) investigate the role of pressure and temperature on the observed transitions based on thermal analysis, time-resolved velocimetry measurements, and *post-mortem* structural characterization.

To achieve these objectives, this work progressed in three stages. First, the initial structural and thermal properties of the Ce_3Al MG were characterized to confirm the amorphous character and determine the MG stability and activation energy for thermal crystallization. Thermal crystallization was studied in order to compare and contrast with any observed shock-compression-induced structural changes. Second, two different laser-based shock-compression techniques were utilized to explore the effects of a wide range of loading conditions (pressure, temperature, and strain rate) on Ce_3Al MG. The Nd:YAG laser-based shock-compression experiments were coupled with time-resolved velocimetry measurement. The velocity profile for Ce_3Al MG, optical microscopy observations of deformation, and comparisons of the peak velocity as a function of laser energy were used to evaluate phase changes occurring in Ce_3Al MG during shock-compression. Hydrodynamic simulation of the OMEGA laser pressure distribution was used for evaluation of the loading conditions applied to shock-compressed Ce_3Al MG samples. Third, detailed structural characterization was performed on the initial Ce_3Al MG, thermally crystallized Ce_3Al, and recovered shock-compressed Ce_3Al MG. Synchrotron X-ray diffraction (XRD) and Rietveld analysis was used to determine the phase, grain size, density, and anisotropy of crystallized samples. This data was converted to the structure factor and pair distribution function (PDF), both of which were used to evaluate the density, atomic bond lengths, and

overall short and medium-range order (SRO and MRO) of the amorphous samples. Synchrotron extended X-ray absorption fine structure (EXAFS) measurements were performed to study Ce-specific bond characteristics. Atom probe tomography (APT) was used to determine nanometer-resolution elemental segregation. Transmission electron microscopy (TEM) was utilized to study the thermally crystallized Ce_3Al and validate the Rietveld analysis grain size calculations. The detailed approach for all of these techniques are described in this chapter.

3.1 Material System

The material investigated in this study is a binary Ce_3Al MG. Melt-spun ribbons of 40 μm thickness and 1 mm width were obtained from Ames Lab. The ribbons were fabricated starting with the Ce_3Al ingot held at 800 °C, followed by melt ejection at a rate of 20 m/s through a 0.81 mm hole at 120 Torr overpressure. Rapid cooling was achieved via conduction from contact with a water-cooled copper wheel. An inert atmosphere of 1/3 atm He gas was used to limit oxidation of the molten metal. Figure 3.1 shows an image of the representative ribbon.

Figure 3.2 illustrates the phase diagram of Al-Ce, indicating the line compound corresponding to the stable crystalline α-Ce_3Al hexagonal intermetallic phase. The density of α-Ce_3Al intermetallic is 6.34 g/cm^3. The MG ribbons were measured via the Archimedes technique to have a density of 6.14 g/cm^3, indicating an $\sim$3% lower density than the crystalline α-Ce_3Al phase.

A recreation of the α-Ce_3Al phase in the software Balls & Sticks [235] allowed for determination of the representative bonds and bond lengths in the hexagonal crystal, as might be observed in a PDF measurement. Table 3.1 illustrates the first 10 Å of bond lengths and the contributions of the elemental bond combinations. Bond lengths are rounded to three significant figures, so several slightly different elemental bond lengths are represented with the same value. With three times as many Ce atoms as Al within Ce_3Al, the majority of

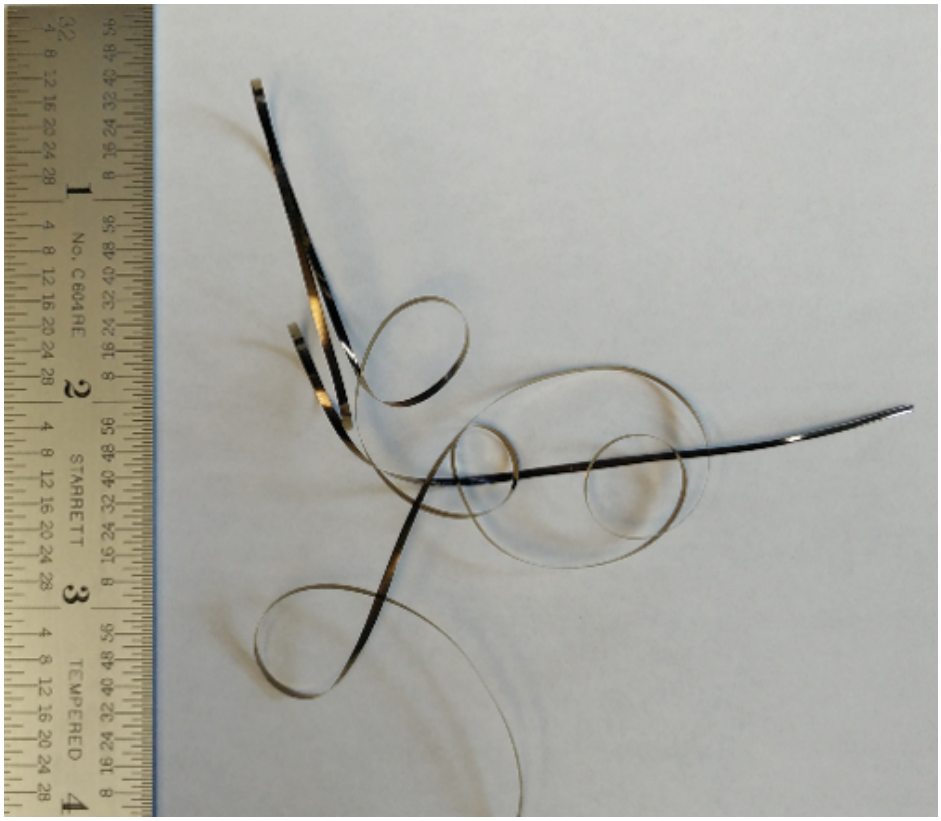

Figure 3.1: Representative image of the Ce_3Al MG melt-spun ribbon as received. The side which came in contact with the Cu wheel has a roughness matching the surface of the wheel and the side in contact with the 1/3 atm He gas is smooth. Ribbon width is 1 mm and thickness is $40\,\mu\mathrm{m}$.

bonds include Ce atoms. Therefore, any changes in bond lengths, as determined from total or partial PDF measurements, can be attributed predominantly to Ce-based changes.

3.1.1 Initial Material Characteristics

A summary of the initial properties of the Ce_3Al MG ribbon sample confirming the amorphous structure is presented below. The methodologies used to determine these characteristics will be discussed in the following sections.

Figure 3.3 shows the 20 K/min DSC profile of the Ce_3Al MG, showing the endotherm corresponding to the glass transition temperature (T_g = 403.4 K) prior to an undercooled region and subsequent exotherms for the two-stage (primary) crystallization (T_{x1} = 436.0 K and T_{x2} = 450.1 K). These thermal events are not observed upon reheating the samples,

Table 3.1: Elemental bonds and corresponding bond lengths for the stable α-Ce_3Al hexagonal crystalline phase. Values from Balls & Sticks software [235] recreation of the powder diffraction file reference by Vucht et al. [236].

Bond Length (Å)	Contributing Elemental Bonds
3.40	Ce-Ce, Ce-Al
3.52	Ce-Ce, Ce-Al, Ce-Ce
4.90	Ce-Ce, Al-Al, Ce-Ce
5.45	Al-Al, Ce-Ce
6.03	Ce-Al, Ce-Ce
6.10	Ce-Al, Ce-Ce, Ce-Al
6.49	Ce-Ce, Ce-Al, Ce-Ce
7.04	Al-Al, Ce-Ce
7.82	Ce-Ce, Ce-Al
8.18	Ce-Al, Ce-Ce, Ce-Al
8.43	Ce-Ce, Ce-Al
8.58	Ce-Ce, Al-Al, Ce-Ce
8.91	Al-Al, Ce-Ce
9.13	Ce-Ce, Al-Al, Ce-Ce
9.27	Ce-Ce, Ce-Al
9.32	Ce-Ce, Ce-Al, Ce-Al, Ce-Ce
9.79	Ce-Al, Ce-Ce

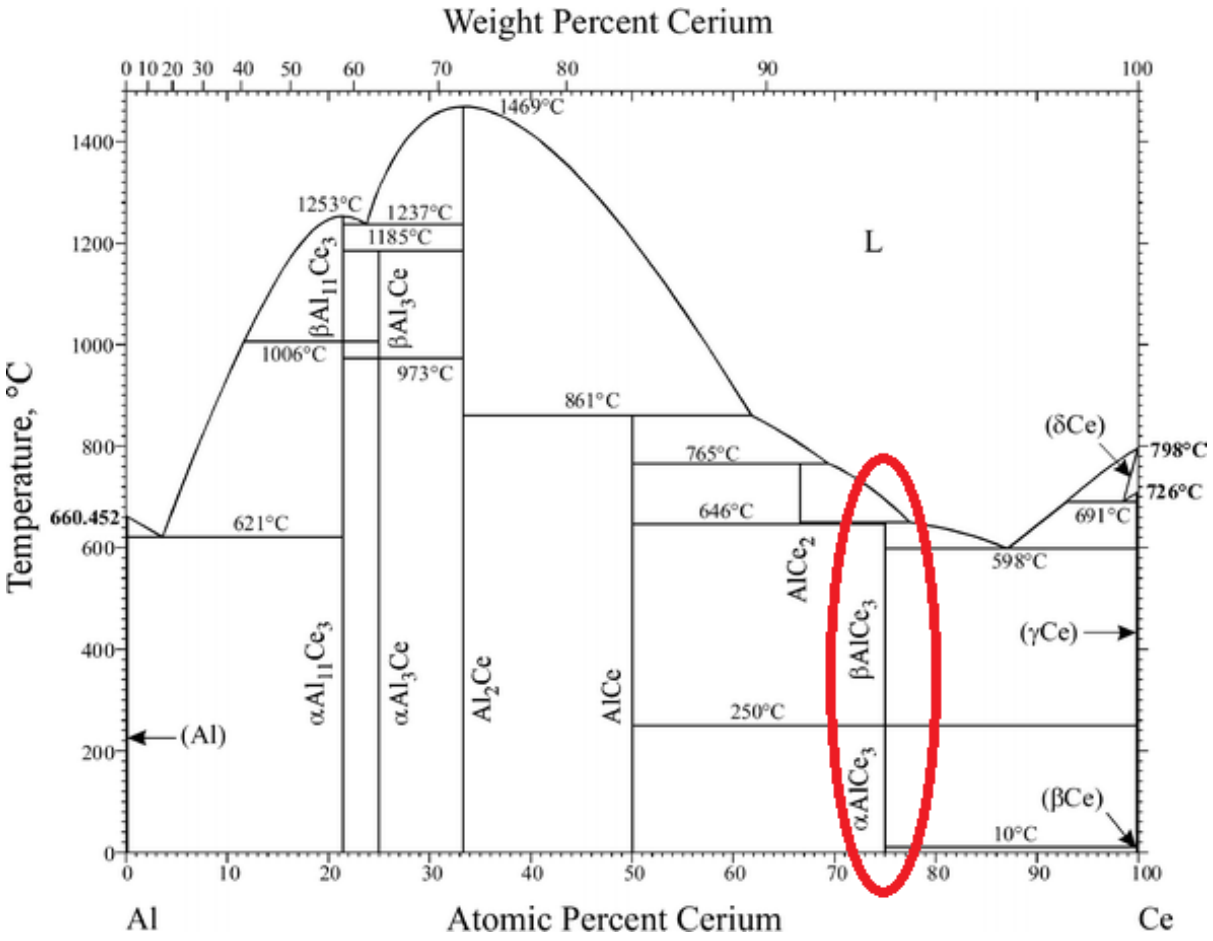

Figure 3.2: Phase Diagram for the Ce-Al system calculated and optimized via the FactSage thermodynamic software using properties from the SGTE database by Jin *et. al.* At the Ce_3Al composition, the stable phase is the HCP intermetallic, α-Ce_3Al, and the melting temperature is 655 °C. [234]

indicating that the MG is fully crystallized and is no longer amorphous. The crystallization peak exothermic temperatures were determined to be T_{peak1} = 438.9 K and T_{peak2} = 490.8 K, and the melting temperature (T_m) was determined to be 931.4 K. The calculated reduced glass transition temperature ($T_{rg} = T_g/T_m$) is therefore ~0.43. This is far from the high GFA value of 0.66, indicating that the Ce_3Al MG is not a very strong glass former and may be relatively easily crystallized except under rapid solidification conditions.

Figure 3.4 plots the XRD trace for the initial Ce_3Al MG ribbon. The characteristic amorphous broad scattering is evident in this trace, confirming the initial amorphous structure of the Ce_3Al MG samples used in this study.

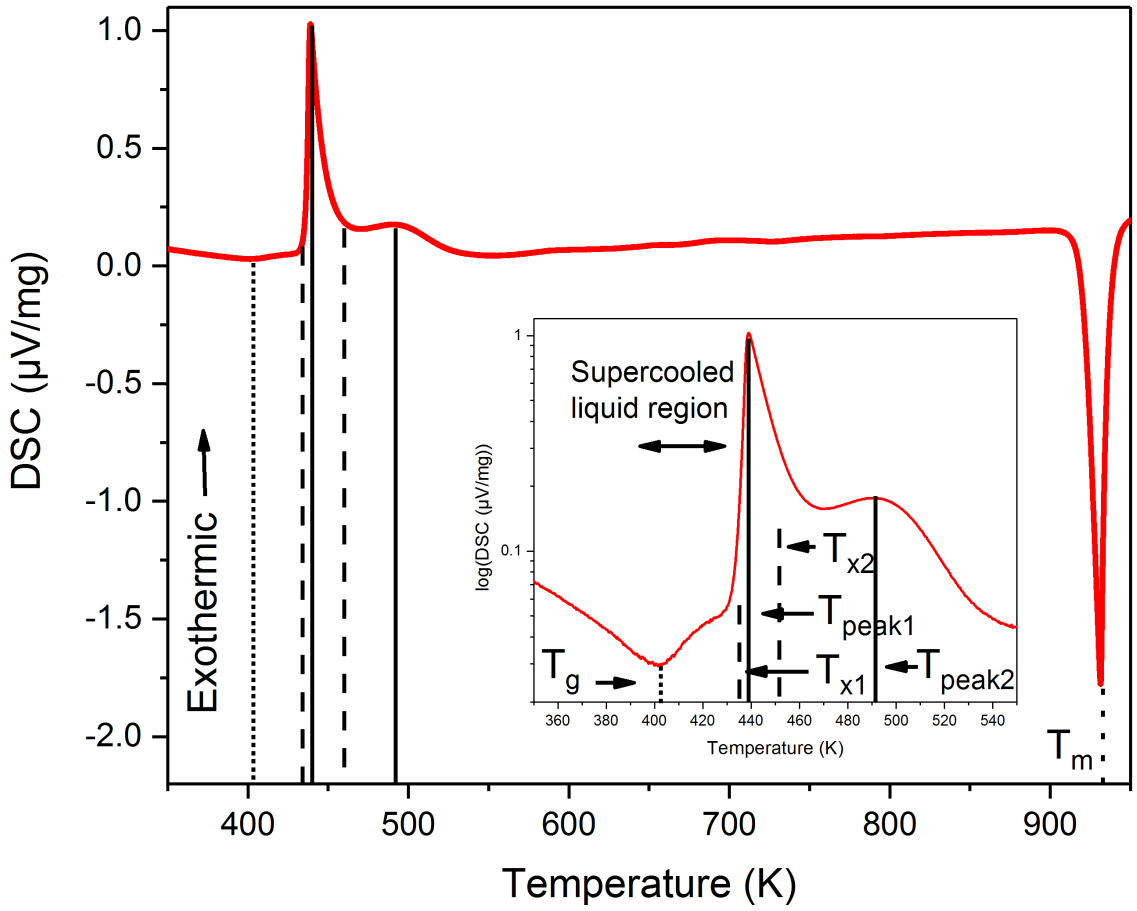

Figure 3.3: Plot of DSC data for the Ce_3Al MG heated at 20 K/min illustrating the onset of the glass transition (short dot line) and crystallization (dashed line) temperatures, T_g, T_x1, and T_x2 respectively, the temperature of peak crystallization (solid line) T_{peak1} and T_{peak2}, and the melting temperature T_m (dot line). Inset is a logarithmic plot of the DSC data showing a magnified view of T_g, T_x1, the supercooled liquid region between the two, T_x2, T_{peak1}, and T_{peak2}.

Figure 3.5 illustrates the total PDF data for the initial Ce_3Al MG ribbon. The trace has few broad peaks which attenuate in intensity to 0 within 30 Angstroms, representative of an amorphous material which lacks any long range order.

A magnified view of the first ten angstroms of the total PDF for the initial Ce_3Al MG is shown in Figure 3.6. The bonds (Ce-Ce, Ce-Al, and Al-Al) defined for the counterpart crystalline α-Ce_3Al hexagonal phase, as listed in Table 3.1, are overlaid on top of the PDF plot. Dashed lines correspond to the bonds lengths, composed of Ce-Ce and Ce-Al bonds, and dash-dot lines represent the bond lengths which are composed of Ce-Ce and

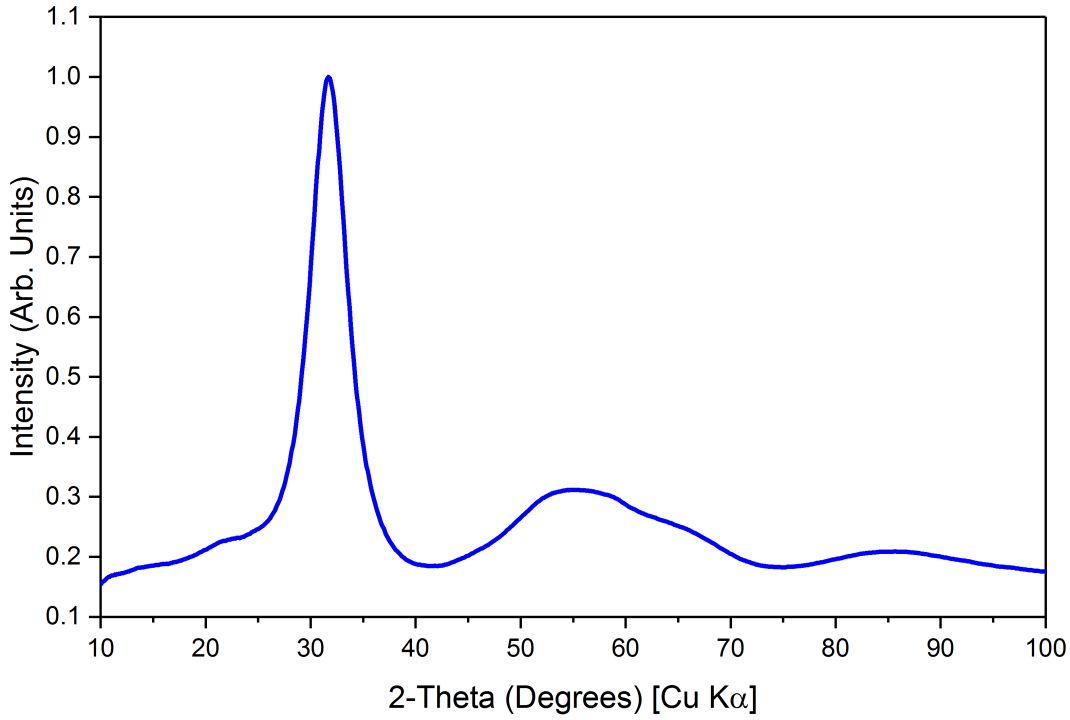

Figure 3.4: XRD trace of the initial Ce_3Al MG ribbon sample. The few broad peaks are representative of an amorphous structure.

Al-Al bonds. The first and second peaks of the PDF ($\sim$3-7.5 Å) for the initial MG phase align fairly well with the hexagonal phase bond lengths indicating similar SRO and MRO between the amorphous and crystalline phases.

Figure 3.7 portrays the EXAFS-derived partial PDF for Ce-specific (e.g., Ce-Ce and Ce-Al) bonds for the initial Ce_3Al MG ribbon. The center position of the main peak is 2.27 Å. Since there was no calibration, the peak position is not absolute and therefore not comparable with the total PDF value or bond lengths presented in Table 3.1. However, the position is comparable with those of other samples, as will be shown in Chapters 4 and 6. As only the main peak is close (with a shift assumed for calibration) to a clear bond length from Table 3.1, the other smaller peaks appear to be an effect of multiple scattering paths taken by the X-rays. These do not provide meaningful information about the structure.

The elemental distribution was measured with APT. As shown in the proxigram of Figure 3.8, there was no chemical ordering or segregation observed. The proxigram is

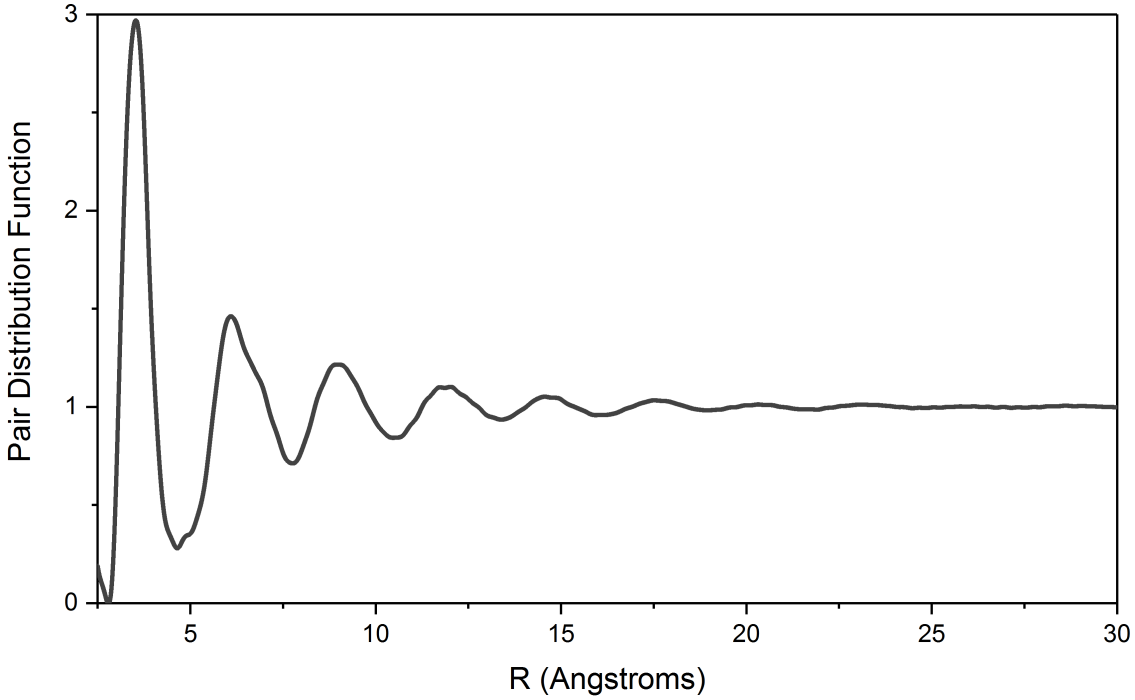

Figure 3.5: PDF trace of the initial Ce_3Al MG ribbon sample. Peak positions represent combinations of all of the Ce-Ce, Ce-Al, and Al-Al bond lengths. The broad peaks and rapid loss of visible order are representative of a MG.

indicative of a homogeneous Ce:Al distribution in the expected 3:1 ratio throughout the amorphous structure. Resolution limits of the technique preclude direct measurements of the atomic coordination. As shown in the frequency distribution plot for Ce and Al in Figure 3.9, the overall measured structure does maintain a 3:1 Ce:Al ratio on average. However, there is a wide, binomial distribution to these concentrations, indicating local heterogeneities throughout the probed samples. The heterogeneous regions with decreased local coordination densities can become sites of reordering during phase changes.

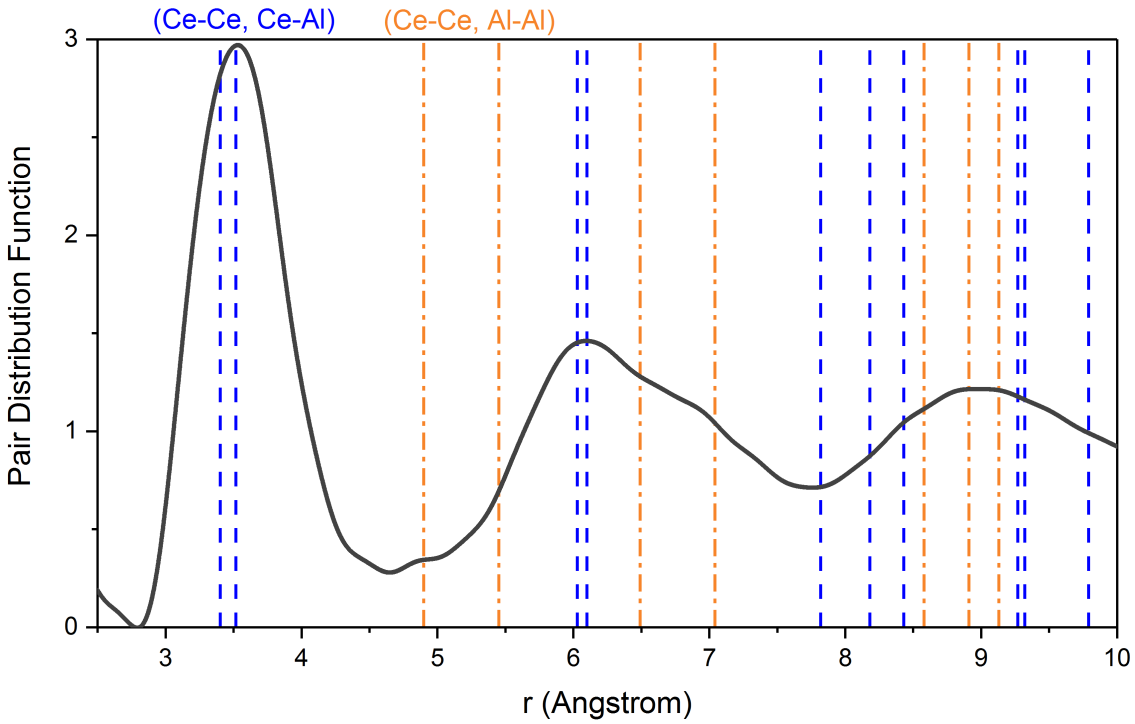

Figure 3.6: PDF trace of the initial Ce_3Al MG ribbon sample, magnified about the first $10\,$Å. Lines corresponding to the lengths for the elemental bonds (Ce-Ce, Ce-Al, and Al-Al) of the hexagonal α-Ce_3Al crystalline phase are overlaid. Dashed lines correspond to Ce-Ce and Ce-Al bonds, and dash dot lines correspond to Ce-Ce and Al-Al bonds. Up to $\sim 7.5\,$Å, there appears to be strong similarities between the amorphous peak positions (aka occupied bond lengths) and the hexagonal phase bond lengths.

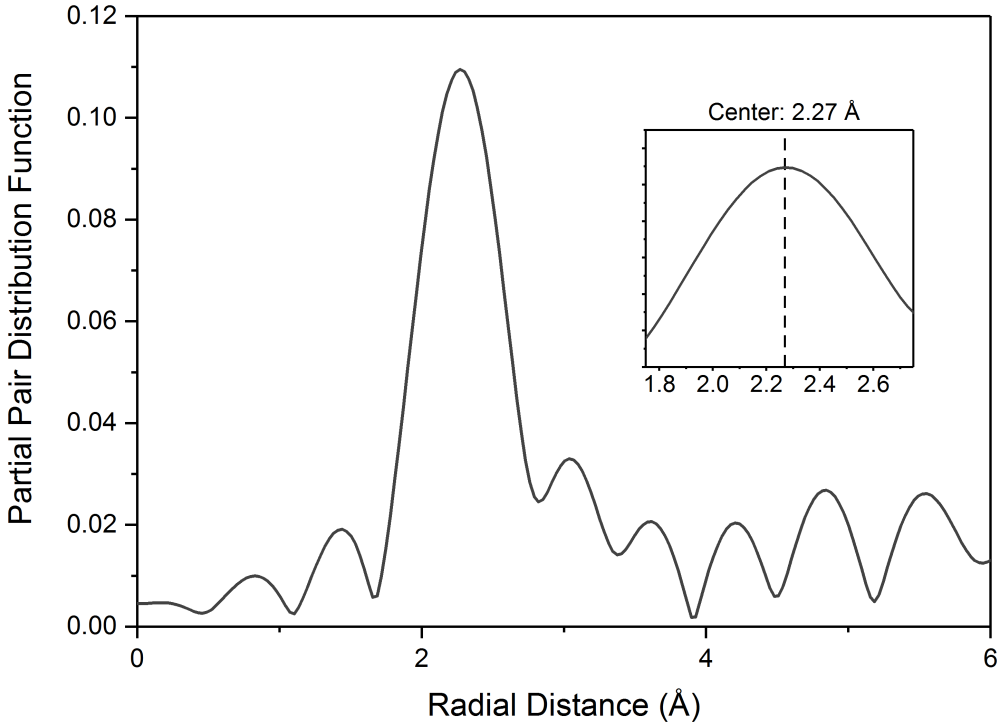

Figure 3.7: Partial PDF trace of the Ce-based bonds for the initial Ce_3Al MG ribbon sample. Peak positions represent combinations of all of the Ce-Ce and Ce-Al bond lengths. The main peak position is centered at 2.27 Å. The other small peaks appear to be due to the multiple scattering paths possible for the X-rays and do not provide meaningful structural information.

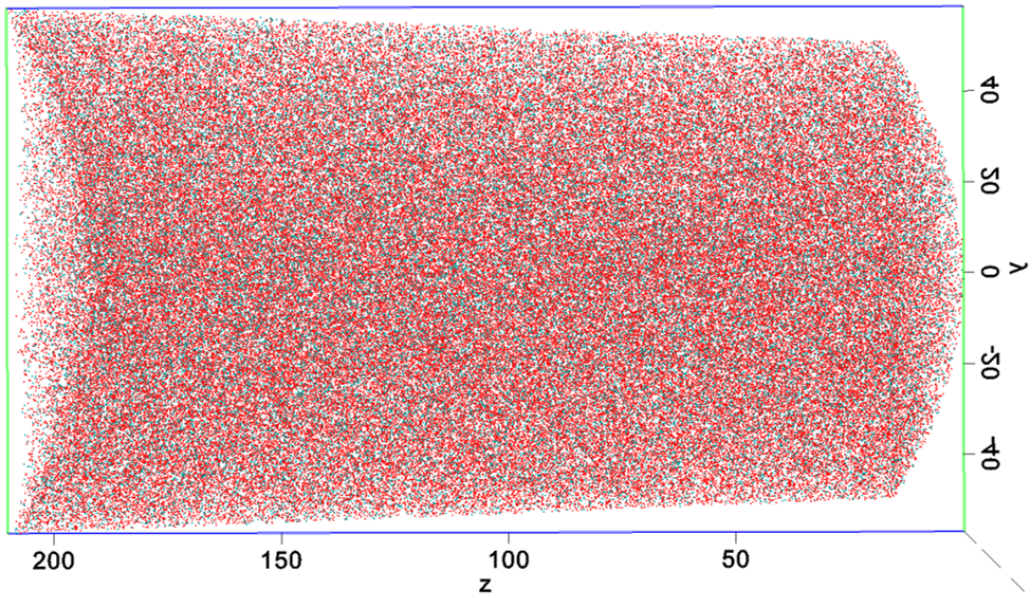

Figure 3.8: Reconstructed 3D proxigram of Ce (red) and Al (blue) atoms in a needle of Ce_3Al MG as measured via APT. The scale of the units along respective axes are in nanometers. Proxigram is representative of homogeneous Ce:Al distribution with no ordering or segregation evident. Resolution limits of APT disallow atomic coordination analysis.

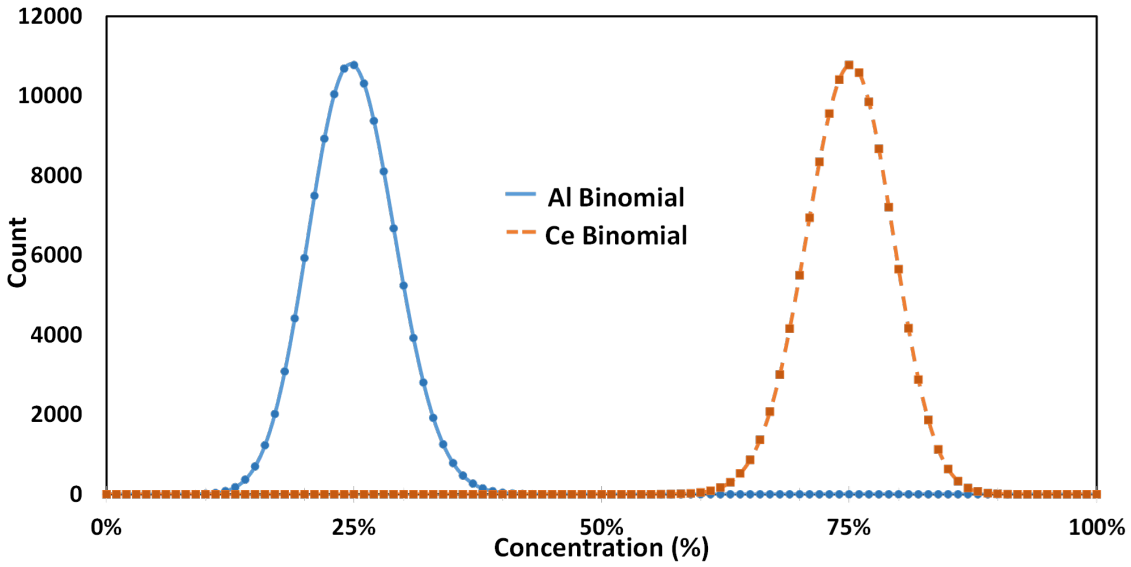

Figure 3.9: Frequency distribution plot of Ce (dashed orange) and Al (solid blue) binomials. Statistical bins were each 100 atoms. 117399 bins were counted. Ce is centered around 75% and Al around 25% as expected. Spread in concentration is indicative of local heterogeneities in composition and structure throughout the measured samples.

3.2 Thermal Analysis of MGs

Thermal analyses of Ce_3Al MG were performed using a Netzsch 404 F1 differential scanning calorimeter (DSC). Scans were performed under 45 ml/min ultra-high purity argon gas flow in an Al_2O_3 lined Pt-Rh crucible with a Pt-Rh lid in a rhodium furnace. Baseline corrections were performed in advance with empty crucibles. Sample weights of 10 to 20 mg were used for all experiments and achieved by measuring groups of $\sim$20 pieces of $1\,\mathrm{mm}$ x $1\,\mathrm{mm}$ x $40\,\mu\mathrm{m}$ Ce_3Al MG ribbon.

Measurements were performed at constant heating rates to confirm the amorphous structure and determine the glass transition and crystallization (onset and peak) temperatures. Melted and cooled samples were reheated to test energy release associated with grain growth, and samples were thermally crystallized at temperatures below the melt for subsequent structural characterization.

Thermogravimetric analysis (TGA) scans were performed using a TA Instruments SDT Q600 TGA. Scans were performed under 100 mL/min of N_2 gas at a heating rate of 20 K/min using an Al_2O_3 crucible. Sample weights of $\sim$10 mg were used and achieved by measuring groups of $\sim$20 pieces of $1\,\mathrm{mm}$ x $1\,\mathrm{mm}$ x $40\,\mu\mathrm{m}$ Ce_3Al MG ribbon. Experiments were performed to determine the oxidation behavior and compare this with the exothermic events observed in DSC experiments.

Multiple different heating rates were used with the DSC to characterize the change in glass transition and crystallization temperatures. The values of glass transition and crystallization temperatures as a function of heating rate were used to calculate activation energies for glass transition and crystallization as well as characteristic properties of crystallization behavior. Details of the methodology for these calculations follow.

The crystallization mechanism, assuming no pre-nucleation, for a MG can be classified into four types: bulk three-dimensional growth of crystals (e.g., spherical), bulk two-dimensional growth of crystals (e.g., disk-like), bulk one-dimensional growth of crystals

(e.g., rod-like), or surface crystallization. The mechanism can be determined (with some variability) through thermal analyses, wherein the Avrami constant n is related to the dimensionality (defined by the constant D) as $n = D + 1$ where D has values of 3 for 3D, 2 for 2D, and 1 for 1D crystallization. Surface crystallization results in $n = D = 1$ [114].

The volume fraction crystallized, x, at any temperature T can be calculated from $x = S_T/S$ where S is the total area of the exothermic peak between the temperature T_x, the onset temperature for crystallization, and T_f, the temperature at which crystallization is completed, and S_T is the partial area of the exothermic peak up to the temperature T [237].

The Avrami constant n can be calculated for a particular temperature from the fraction crystallized at different heating rates β using the Ozawa relation [238], shown in Equation 3.1 below:

$$ln(-ln(1-x)) = -nln(\beta) + const \tag{3.1}$$

By plotting $ln(-ln(1-x))$ vs $ln(\beta)$, with data points for the values of x at each β value for a chosen temperature, a least squares linear fit can be determined where the slope is $-n$. Knowing the Avrami constant allows for calculating the dimensionality of crystallization D from knowing that $n = D + 1$ except when $n = 1$ (which indicates surface crystallization).

Knowing the heating rate β and the temperature of peak crystallization T_{peak}, the activation energy for crystallization E_A^{cryst} and frequency factor k_0 of the Arrhenius equation can be calculated from the Augis and Bennett relation [239] shown in Equation 3.2 below:

$$ln(\beta/T_{peak}) = -E_A^{cryst}/(RT_{peak}) + ln(k_0) \tag{3.2}$$

where R is the gas constant. The frequency factor k_0 is defined as the number of attempts made by the nuclei per second to overcome the energy barrier. This is related to the number of nucleation sites present in the material for crystal growth (e.g., the number of GUMs) and therefore the ease of crystallization (more GUMs result in higher k_0 values and easier

crystallization) [114].

With a known Avrami constant n and dimensionality for crystallization D, the activation energy for crystallization E_A^{cryst} can also be calculated from a form of the Kissinger equation modified to take into account nucleation, growth, and dimensionality, as illustrated by Matusita et al. [240, 241] using Equation 3.3:

$$ln(\beta/T_{peak}^2) = -(D/n)(E_A^{cryst}/(RT_{peak})) + const \tag{3.3}$$

In a plot of $ln(\beta/(T_{peak})^2)$ vs $1000/T_{peak}$, a least squares linear fit to data points from different heating rates provides the activation energy from the slope (slope = $-(D/n)(E_A^{cryst}/R)$).

The general Kissinger analysis, shown in Equation 3.4 below, can be used to calculate the activation energies for the glass transition and the onset of crystallization.

$$ln(\beta/T_{event}) = -E_A/(RT_{event}) + const. \tag{3.4}$$

Comparisons between the activation energy for the onset and peak of crystallization allow for determining if crystallization is dominated by nucleation or growth. A higher value of the activation energy for the onset indicates more difficulty in nucleation whereas a higher activation energy at the peak represents a greater difficulty for growth [242].

The fragility of the MG can be determined from viscosity data calculated using the Vogel-Fulcher relation [78, 243] shown in Equation 3.5 below:

$$ln(\beta) = ln(B) - (AT_0)/(T_g - T_0) \tag{3.5}$$

where B is a parameter representing the time scale in the glass-forming system (large values indicate a long waiting time would be required to bring the system close to an ideal state), A is the strength parameter in the Vogel-Fulcher equation (which controls how closely the liquid system obeys the Arrhenius law), and T_0 is the asymptotic value of T_g approximated as the onset of the glass transition within the limit of an infinitely slow cooling and heating

rate.

Knowing the values from Equation 3.5, the fragility m can be calculated from the relation shown in Equation 3.6 below [78]:

$$m = (AT_0T_g)/((T_g - T_0)^2 ln(10)) \tag{3.6}$$

In addition, the fragility can be directly calculated from the DSC-calculated effective activation energy of the glass transition and the measured glass transition temperature [244, 245] as shown in Equation 3.7 below:

$$m = \frac{E_a^g}{ln(10) \cdot RT_g} \tag{3.7}$$

3.3 Shock-Compression Experiments

There are a range of shock-compression techniques available for creating well-controlled uniaxial-strain conditions with many different benefits and drawbacks. A detailed discussion of the history and current options can be found in the books by Meyers [228] and Forbes [246]. The present work utilizes laser-driven shock loading due to the size of the samples being shocked (1 mm x 1 mm x 40 μm thick). This technique induces shock-compression through laser ablation of the surface of a material, creating a localized plasma. The rapid expansion of the plasma in all directions creates a pseudo-1D planar shock wave in the surrounding material. The shock wave can either propagate directly into the sample or be used to launch foils into samples.

For both direct laser and laser-accelerated-foil-based shock-compression, the scale of sample and timing are dramatically different from traditional gas gun and explosively-driven experiments. Whereas traditional experiments can use samples of larger dimension (factors of several millimeters), laser experiments utilize smaller scale samples (tens of microns thick). Even more importantly, laser-driven shock-compression experiments gen-

erate nanosecond duration shock pulses, compared to microsecond duration pulses typical of other platforms [247]. As such, the strain rates are even greater for laser-driven shock-compression allowing for exploration of extreme high rate loading conditions.

Over the last several decades, laser-based techniques have advanced significantly. Launched foils are now able to achieve speeds ranging from hundreds of m/s to several km/s [248]. Direct shock-compression approaches have also been optimized, allowing for pulse widths from tens of ps to hundreds of ns and achieving four to ten times greater pressures upon confining the plasma [249, 250]. In both open and confined direct shock-compression, illustrated in Figure 3.10, pressures are applied over a period approximately twice the duration of the laser-pulse [249]. Kelly [251] provides a thorough review of the complex physics and practical aspects of these shock wave generation techniques.

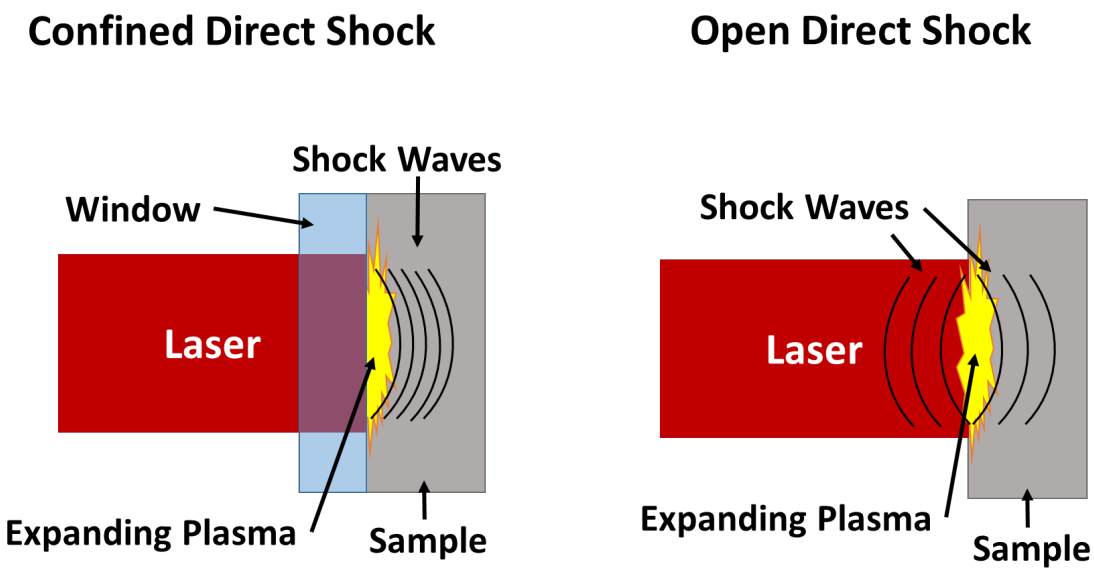

Figure 3.10: Schematic illustrating the laser-driven direct shock-compression configuration in the confined (left) and open (right) formats. Greater pressures are achieved in the confined setup due to a greater amount of reflection of shock waves into the sample from the higher impedance window as compared to the free surface in the open arrangement.

For the present work, two different laser-induced direct shock-compression techniques were utilized in order to probe a wide range of loading conditions: Nd:YAG 3 J laser (confined) and Omega 50 J laser (open). In both, the direct shock-compression configura-

tion was used as it allowed for easier recovery of samples, providing the opportunity for subsequent characterization. Table 3.2 presents the different shock-compression loading conditions provided by the Nd:YAG and Omega lasers in this work. Strain rates are estimated from known volumetric changes at pressure for a representative material EOS and rise times to peak pressure for each laser. The Nd:YAG laser results in a triangular pressure profile (typical of explosives and plasma generation) while the Omega laser produces a more square profile with rapid rise and release.

Table 3.2: Relevant laser details and induced loading conditions for the Nd:YAG and Omega lasers utilized in this work. Spot size is the diameter of a circular irradiation spot. Pressures and strain rates are for the incident position and will change with depth for significantly thick samples.

Laser	Energy	Spot Size	Pulse Rise	Pulse Width	Pressure Range	Strain Rate
Nd:YAG	0.15 - 2 J	1.9 mm	$\sim$5 ns	9 ns	1 - 10 GPa	$\sim 10^6$ - 10^7 s^{-1}
Omega	50 J	$750\,\mu m$	109 ps	992 ps	1 - 90 GPa	$\sim 10^8$ - 10^9 s^{-1}

The Nd:YAG $3\,J$ laser at Georgia Tech was used for shock-compression experiments at pressures up to $\sim$10 GPa. Simultaneous velocimetry measurements using the velocity interferometer system for any reflector (VISAR) and photon doppler velocimetry (PDV) techniques allowed for comparisons of the shock response with the recovered structural changes. For pressures of $\sim$5 - 90 GPa, the Laboratory for Laser Energetics (LLE) Omega laser was used. No *in operando* measurements were possible with the recovery setup, so Hyades hydrodynamic simulations were performed to estimate the pressures achieved. The details for these experiments and simulations will be described in the following sections.

3.3.1 GT Nd:YAG Laser Shock Experiments

To achieve shock-compression pressures up to $\sim$10 GPa and simultaneously gather velocimetry data, the Georgia Tech Nd:YAG Continuum Powerlite Precision II laser was utilized. Figure 3.11(a) illustrates the configuration. The laser operates at 1064 nm with up to 3 J of energy per pulse. The initial beam is $\sim$10 mm in diameter with a pseudo-Gaussian

spatial distribution. As the laser passes through the "π-Shaper 12_12_1064_HP" beam shaper, different tunable lenses within the device convert the beam to a super-Gaussian "tophat" spatial distribution. This effectively levels the spread of energies in space, producing a more uniform spatial distribution of pressure in the samples and allowing for a 1D approximation for the loading condition. The beam then passes through a "Edmund Optics 89442" focusing lens to bring the beam diameter to the desired 1.9 mm spot size. An interested reader can find more details about the development, properties, and optics of this laser in the thesis by Kelly [251].

As the drive laser interacts with the sample package shown in Figure 3.11(b), ablation of $25\,\mu\mathrm{m}$ thick Ni driver foil creates a plasma. The rapid expansion of this plasma generates a shock wave which is reflected by the borosilicate glass window and transmitted through the Ni driver foil into the $40\,\mu\mathrm{m}$ thick Ce_3Al MG sample. The Ni foil insulates the Ce_3Al MG sample from heating produced by the plasma [252]. The sample package is held together with a borosilicate glass window on the driver foil side and poly(methyl methacrylate) (PMMA) window on the sample side to allow for recovery with limited secondary effects. Glycerin is used between layers to ensure there are no air gaps.

For interferometry measurements, either a 1550 nm 0-2 watt PDV or 532 nm 0-2 watt VISAR laser was focused on the rear surface of the sample package. Each of these lasers transmits through the PMMA window and allows for direct measurement of the interface between the PMMA and Ce_3Al MG sample. Velocimetry measurements at this interface allowed for determination of the interface particle velocity over time. Measured particle velocities at the interface are assumed to be representative of the Ce_3Al MG behavior and not the PMMA window as there are few phase changes in PMMA in the effective pressure regime of this work.

Recovered samples were characterized using low magnification optical microscopy imaging and synchrotron-based XRD analysis. Optical microscopy provided macro-scale observations of laser shock-compression-induced surface and bulk changes. X-ray diffrac-

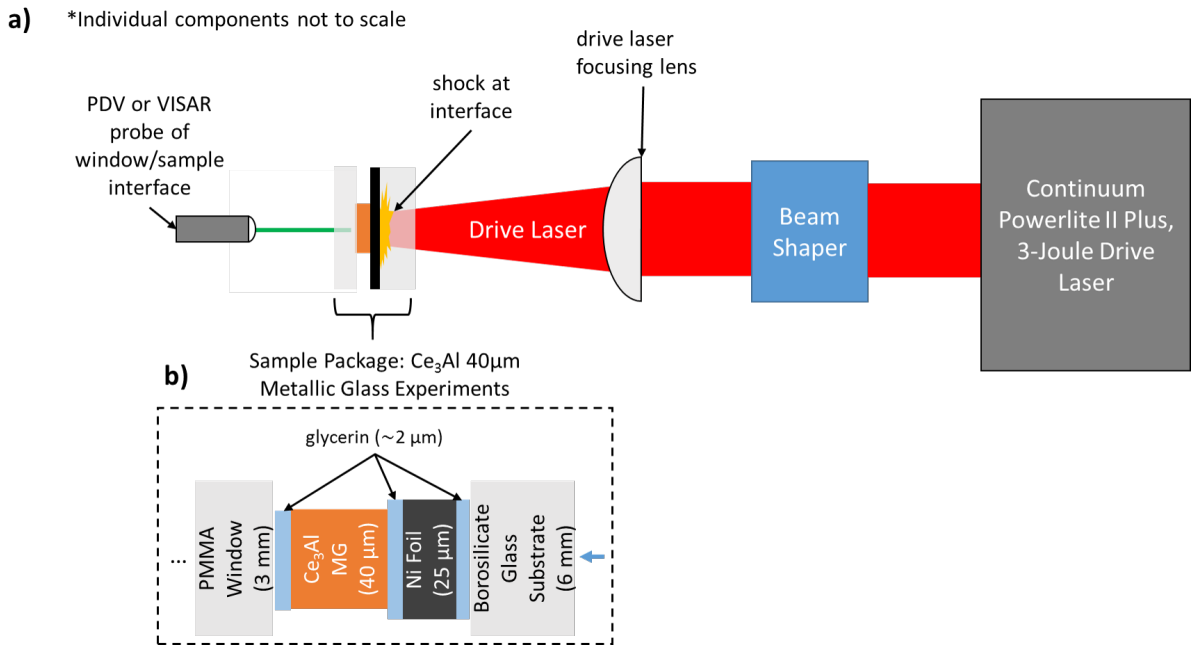

Figure 3.11: (a) Schematic of setup used for shock-compression experiments using the GT Nd:YAG laser. The 10 mm diameter pseudo-Gaussian spatially distributed beam passes through the beam shaper to become super-Gaussian or "tophat" shaped and is then focused down to the desired 1.9 mm diameter spot size via a focusing lens. Direct shock-compression is induced as the drive laser ablates the driver foil and glycerin interface, producing a rapidly expanding confined plasma. The sample package is shown in the magnified inset (b). The driver foil of $25\,\mu m$ thick Ni transmits the shock wave and shields the $40\,\mu m$ thick Ce_3Al MG sample from heat produced from the plasma. Recovery of the Ce_3Al MG sample with limited secondary shock effects is possible due to constraining the driver foil and sample between a borosilicate glass window on the drive laser side and PMMA window on the opposing side. A velocimetry probe (PDV or VISAR) directed at the Ce_3Al MG and PMMA window interface allows for direct measurement of the particle velocity change with time at this interface.

tion provided atomic and micro-scale information for shock-compression-induced structural changes. Results for these analyses are provided in Chapter 5.

Velocimetry Measurements and Analysis

Simultaneous velocimetry measurements were performed during shock-compression using either Photon-Doppler Velocimetry (PDV) or Velocity Interferometer System for Any Reflector (VISAR). Analysis of PDV data was performed using wavelet and Fast Fourier Transform methods [253]. The two PDV analysis techniques were compared for deter-

mination of error analyses and average peak particle velocities. Statistical analysis was performed using custom software, which an interested reader can find more information about in the thesis by Scripka [254]. Analysis of VISAR data was performed using PlotData software [255] taking into account a window correction for the changed speed of light in the PMMA window. VISAR corrections were also made to account for time delays from a combination of two SF6 etalons, one 19.012 mm and the other 38.082 mm thick.

Figure 3.12 illustrates a representative Nd:YAG laser temporal profile from the setup shown in Figure 3.11. The rise time is typically ∼5 ns, resulting in a strain rate of $\sim 10^6$ - 10^7 s^{-1}. The pulse width, measured at the FWHM, is ∼9 ns and the overall profile has a triangular shape with a longer decay in the release, representative of explosive or rapid plasma expansion-type shock-compression.

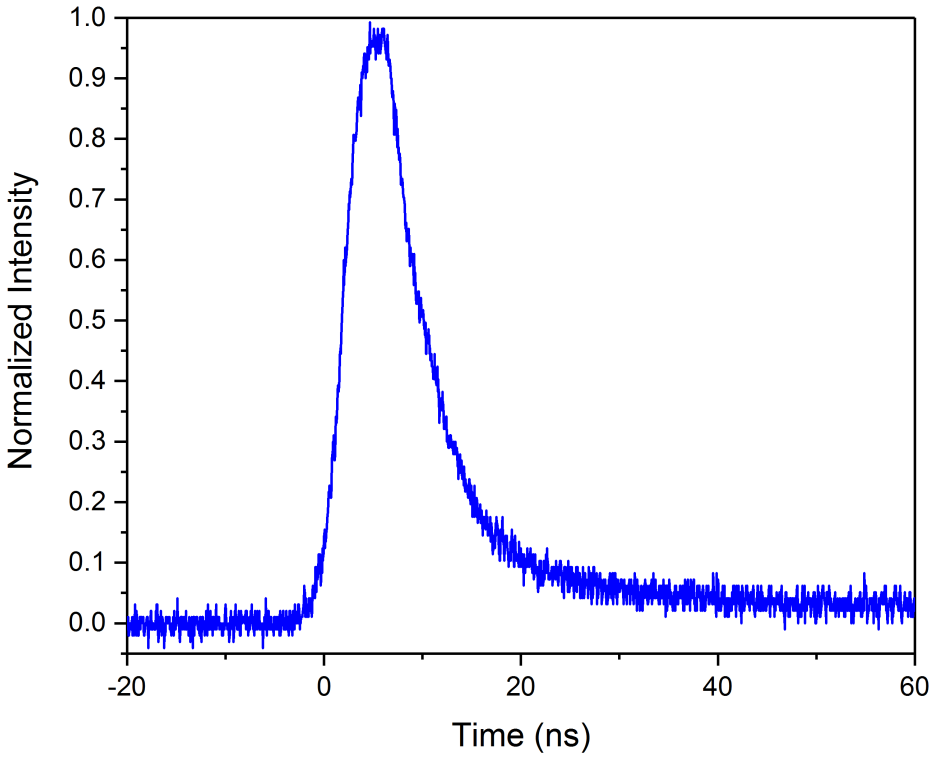

Figure 3.12: Representative profile for the temporal pulse shape of the Nd:YAG drive laser of the triangular laser shock temporal profile for the Nd:YAG laser.

Due to the unavailability of an EOS for the Ce_3Al MG, experiments were performed with comparative setups of both the Ni driver alone, and with a $50\,\mu m$ thick Ni reference

sample. The measurements allowed for qualitative comparisons of trends for particle velocity as a function of laser energy and further validation of observed trends in the Ce_3Al MG shock-compression response. The details and results from these reference and the Ce_3Al MG shock-compression experiments are presented in Chapter 5.

3.3.2 LLE Omega Laser Experiments

Recovery experiments performed at the Laboratory for Laser Energetics (LLE) research facility allowed for characterization of the shock-compression effects at higher pressures and higher strain rates. Figure 3.13 illustrates the laser pulse shape used with the 50 J Omega laser. The rise time is 109 ps, resulting in a strain rate of $\sim 10^8$ - 10^9 s^{-1}. The pulse width is 992 ps, followed by a rapid decline. The total area under the curve provides the 50 J laser energy.

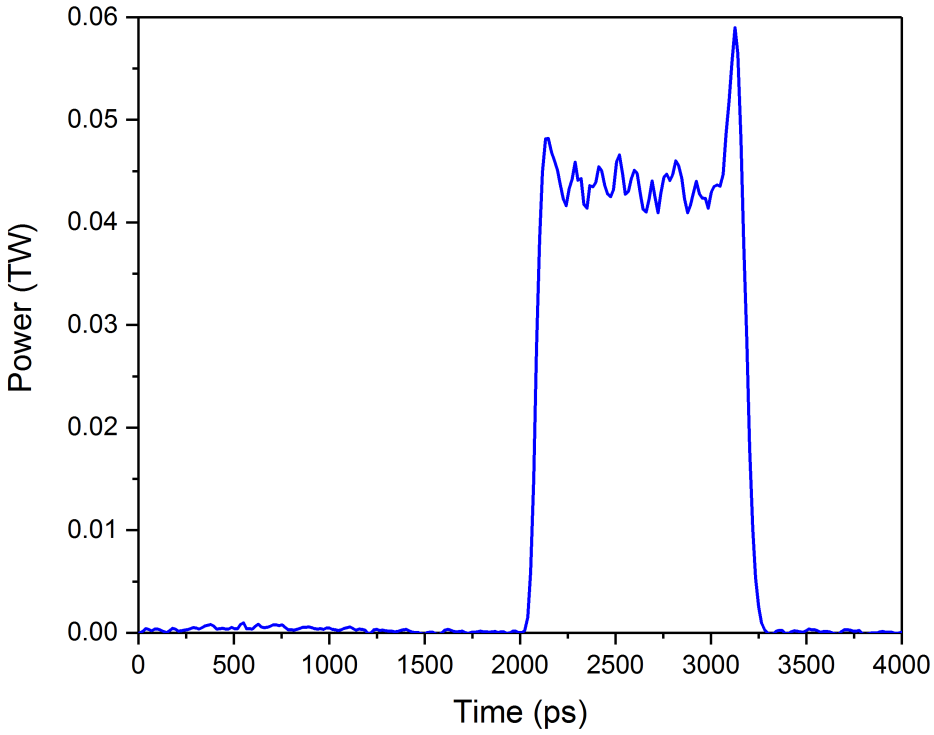

Figure 3.13: Trace for input square laser pulse shape of Omega laser during 50 J laser shock-compression experiment. Area under curve is 50 J, rise time is 109 ps, and pulse width is 992 ps.

The Omega laser was used with a phase plate to achieve a super-Gaussian (aka "flat top") spatial distribution with a diameter of $750\,\mu\mathrm{m}$. Many shock-compression states within Ce_3Al MG were probed by layering multiple samples and simulating the variation of pressure and strain rate as a function of the depth. Over 40 1mm x 1.5 mm x $40\,\mu\mathrm{m}$ Ce_3Al MG samples were cut from the ribbon and stacked together with $6\,\mu\mathrm{m}$ epoxy at each interface. Figure 3.14 shows a schematic of the open (non-confined) direct-laser-shock-compression configuration used for the recovery experiment. The overall setup, including the sample stack encased in the recovery tube and the connector to the Omega mount, is shown in Fig. 3.14(a). Silica aerogel and vent holes ensured soft recovery of the shock-compressed samples with limited secondary effects. The circled sample stack region of Fig. 3.14(a) is expanded in Fig. 3.14(b) for further detail. Stainless steel washers were used to hold the stack in the recovery mount and the 2.5 mm opening in the front washer allowed the $750\,\mu\mathrm{m}$ diameter laser beam to pass. The $300\,\mu\mathrm{m}$ thick polystyrene polymer reservoir was used as a sacrificial laser ablator for unconstrained plasma generation. The plasma-generated shock wave from the polymer directly impacted the 3 mm stack of $40\,\mu\mathrm{m}$ Ce_3Al MG samples.

Recovered samples were separated and characterized using synchrotron XRD and EXAFS analyses. Diffraction data was converted to the structure factor and PDF for further analysis of atomic structure changes.

Hydrodynamic Simulations for Pressure Caculation

There was no direct *in operando* characterization of the shock-compression loading condition induced with the Omega laser. Instead, hydrodynamic simulations were used to gather a qualitative understanding of the shock-compression states through the Ce_3Al MG sample stack.

Hyades is a radiation hydrodynamics simulation code which solves the conservation equations of mass, momentum, and energy in one dimension for varying geometries [256]. It models the laser-material interactions, hydrodynamics, thermal energy transport, ioniza-

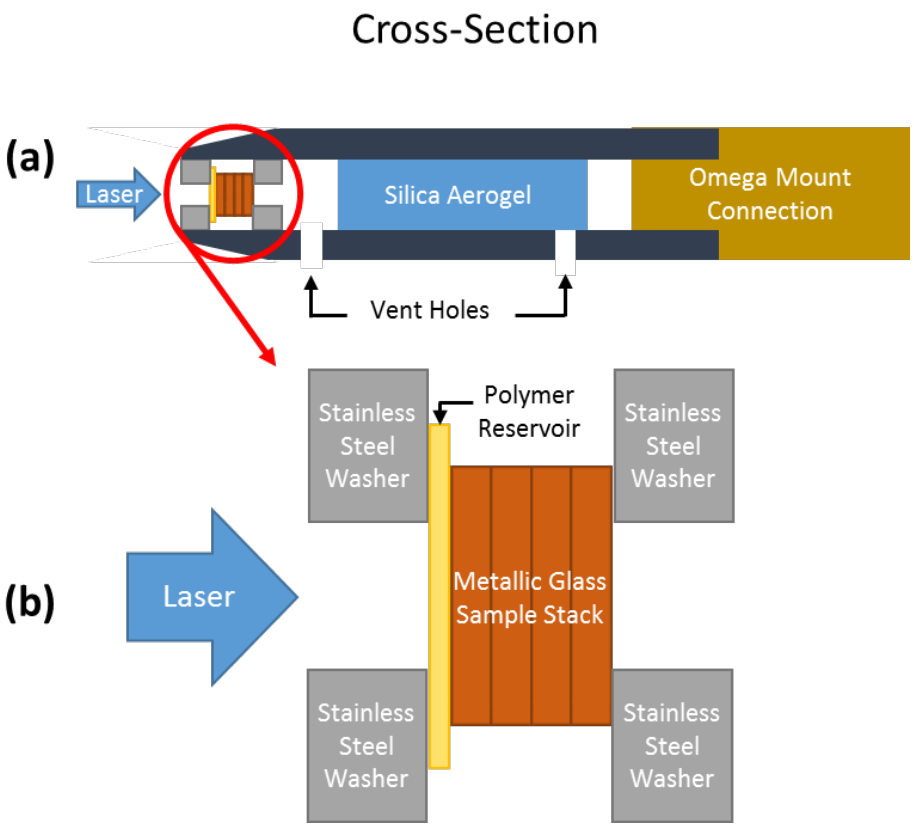

Figure 3.14: Cross-sectional schematic of setup used for recovery experiments with the LLE Omega 50 J laser. (a) Illustrates the components of the recovery tube used, including sample stack, vent holes, silica aerogel, and Omega mount connection. The circled region is magnified in (b) and shows the multi-layer Ce_3Al MG sample package, with an ablative polystyrene layer used as the plasma generation source and stainless steel washers used to hold the sample stack in the recovery tube. Over 40 1mm x 1.5 mm x $40\,\mu m$ Ce_3Al MG samples are stacked together with $6\,\mu m$ epoxy between them to achieve a total 3 mm thickness. After the unconstrained plasma-induced shock wave passes through the stack, the shocked samples are propelled into the silica aerogel behind for a soft recovery without secondary effects. Vent holes prevent gas pressure build-up behind the sample stack.

tion, radiation transport, and material strengths and EOS. Input into the Hyades simulation are the thicknesses and EOS of materials in order of shock wave progression and drive laser energy, shape, and timing. Outputs of Hyades simulations include the temperature, pressure, and particle velocity at different time increments.

A one-dimensional Hyades simulation of the 50 J Omega laser shock-compression experiment was performed [257] using the known laser energy and temporal profile, and Al as a representative sample material. The results allowed for an approximation of the peak

pressure value induced at the top and subsequent layers of the sample stack.

3.4 Phase and Atomic Structure Characterization and Analysis

The initial Ce_3Al MG, as well as those thermally crystallized and recovered after shock-compression, were characterized using multiple techniques to observe macro and atomic structure changes. Synchrotron X-ray diffraction experiments were used for direct XRD and Rietveld analysis of crystalline phases. The XRD data was converted to the total structure factor and reduced PDF using the atomic scattering factor for the composition. The reduced PDF was converted to total PDF. Synchrotron extended X-ray absorption fine structure (EXAFS) measurements were performed to determine the Ce-specific partial PDF. Structure factor and partial and total PDF data were used to characterize SRO and MRO atomic structure changes. Transmission electron microscopy measurements of the thermally crystallized sample allowed for characterization of the grain size and validation of Rietveld analysis values. Atom probe tomography was used to measure elemental distribution with nm resolution to determine if there were any heterogeneous distributions. The following sections will discuss the methodology for each of these techniques.

3.4.1 X-Ray Diffraction (XRD) Analysis

The unprocessed initial, thermally crystallized, and Omega laser shock-compressed Ce_3Al MG samples were characterized via two-dimensional XRD at the X-7B beamline at the National Synchrotron Light Source (NSLS) with x-ray energy of 38.8 keV corresponding to an X-ray wavelength of $0.320\,\text{Å}$. Omega laser shock-compressed Ce_3Al MG samples were held together in a stack after recovery and separated into sections representing general regimes of depth. When measuring a sample stack, only the top layer was characterized. To achieve this and avoid XRD of the lower layers, X-rays were scattered off the sample at a glancing angle. Figure 3.15 shows a schematic of this setup as well as pictures of the actual synchrotron setup and sample mount. Diffracted X-ray intensity in transmission

across the top surface of the samples was recorded by a two-dimensional Si detector placed perpendicular to the incident beam. The detector was positioned 120.56 mm away from the specimen to allow for high-angle measurements and limit scattering off other materials. To avoid diffraction off lower layers, measurements for each sample were gathered iteratively through micrometer increases in stage height from a position where only air was detected until significant fractions of sample were detected.

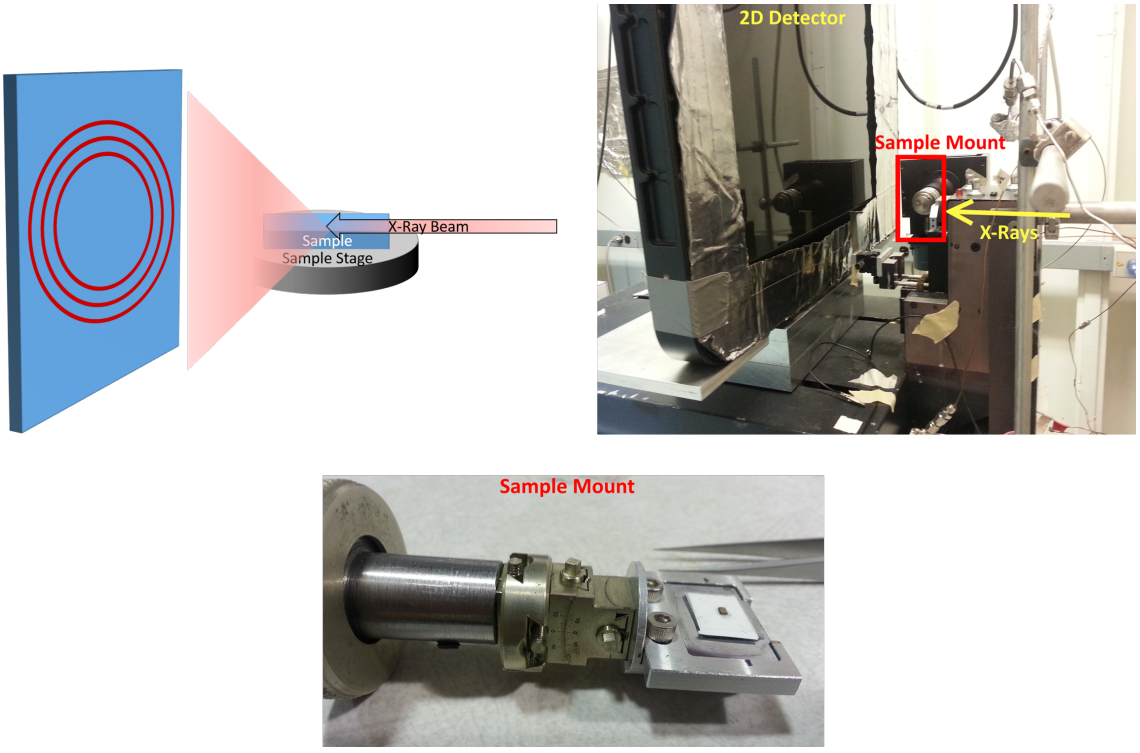

Figure 3.15: Schematic (left) and photo (right) of setup used for NSLS X-ray diffraction experiments. An image of the sample stage (bottom) illustrates the size of the samples relative to tweezers and the stage. X-rays scattered off the sample are measured with a 2D silicon detector. A glancing angle ensures only the sample is probed.

The unprocessed initial and Nd:YAG laser shock-compressed Ce_3Al MG samples were characterized via XRD at the 28-ID-2, XPD beamline at the National Synchrotron Light Source 2 (NSLS-2), with x-ray energy of 40.21 keV corresponding to a wavelength of 0.308 37 Å. In order to measure a high throughput of samples, a sample holder was developed that facilitated preparation of multiple samples at once. Measurements were then performed using an automated script and remote controlled stage. Because only individual

samples were measured at once (not stacks), X-ray diffraction was performed with transmission through the thickness of each sample. The X-ray beam was an ellipse with 1 mm major axis width, allowing for relatively close sample placement while avoiding any interfering sample scattering. Figure 3.16 shows images of the setup and sample holder used for these NSLS-2 experiments. Two-dimensional X-ray diffraction intensities were gathered with the two-dimensional Si detector. The detector was positioned 200.63 mm away from the sample specimen to allow for relatively high-angle detection and limit scattering off other materials. A beam block was placed in the center to avoid erroneous data from the high intensity source X-rays.

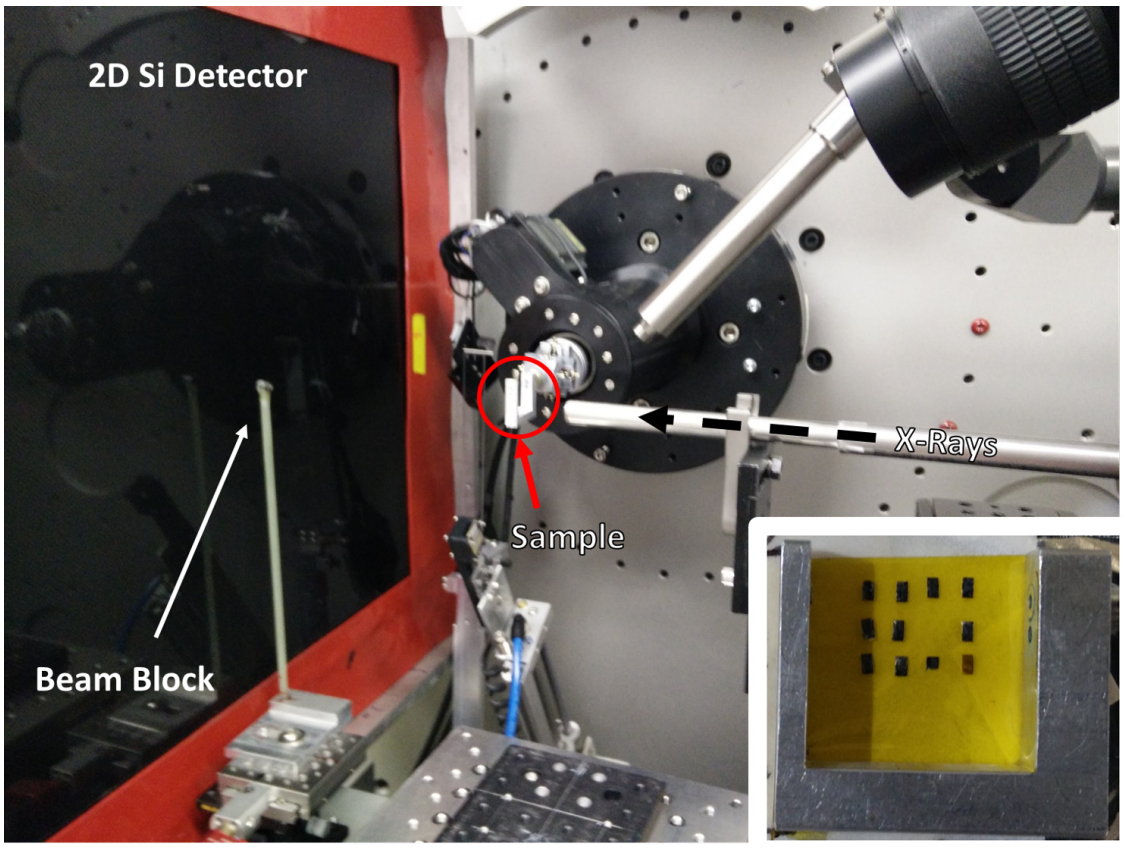

Figure 3.16: Photo of the setup used for NSLS-2 X-ray diffraction experiments. The source X-rays, samples, beam blocker, and two-dimensional Si detector are all visible. Inset shows the circled sample holder and representative samples. X-rays penetrate the sample through the thickness to allow for significant sample volume characterization. Scattered X-rays are measured with the 2D detector. Multiple samples were prepared at once on low-scatter kapton tape and moved between using an automated stage.

For both NSLS and NSLS-2 measured two-dimensional XRD data, a digital mask was either provided or created that removed effects of scattering off the detector or sample holder and erroneous detector pixels. The two-dimensional XRD data was then integrated using the Fit2D software package [258, 259, 260] to one-dimensional XRD data. The resulting one-dimensional XRD data x-axis values were then converted from the 2θ representative of the synchrotron wavelengths to Cu K-α 2θ values using Equation 3.8, which converts 2θ values to the wavelength-independent wavenumber q.

$$q = \frac{4\pi sin(\theta)}{\lambda} \tag{3.8}$$

where q is the wavenumber and λ is the wavelength. Values of 2θ can be converted for different wavelengths using this equation.

The converted Cu K-α XRD data was analyzed using the HighScore Plus XRD data analysis software [261]. Reference powder diffraction files for Ce-Al compounds were gathered from the XRD database at Oak Ridge National Laboratory. A model for the Ce_3Al FCC phase formed at large hydrostatic pressures [45] was created in the Balls & Sticks software [235] from the authors' provided structural details and exported as a CIF for use with HighScore Plus software. Peak and phase fitting was performed using these reference powder diffraction files and the measured XRD data.

Rietveld Analysis

Crystalline sample XRD data from NSLS and NSLS-2 experiments were further analyzed using the Rietveld analysis method in the HighScore Plus software. A detailed review and step-by-step guide for the methodology used in this analysis can be found at the MIT Center for Materials Science and Engineering X-ray Diffraction Education Resources website: http://prism.mit.edu/xray/education/downloads.html. Refined phase structures facilitated determination of lattice parameters, anisotropy, and densities. Williamson-Hall plots generated from the peaks provided information about grain size and strain. Values for preferred

orientation, determined using the March-Dollase parameter [262], indicate either preferences or avoidance of particular directions as positive or negative deviations from the value of 1. Percent deviations are used as representations of degree of preferred orientation.

3.4.2 Structure Factor

The measured two-dimensional scattering intensities from NSLS and NSLS-2 experiments were also integrated into one-dimensional diffraction data with respect to the wavelength-independent wavenumber. These data sets were converted to the total structure factor $S(q)$ via Equation 2.1 (Chapter 2) and the PDFgetX3 software [263]. The PDFgetX3 software utilizes a database of known element properties with given compositions to define the atomic scattering factor for the composition. Parameters for conversion were iteratively changed to optimize for data signal and avoid noise, low q erroneous data, or Fourier transformation termination ripples [264]. For NSLS data, the maximum q cutoff was chosen to be $17.5\,\text{Å}^{-1}$ and minimum q $1.2\,\text{Å}^{-1}$. For NSLS-2 data, the maximum q cutoff was chosen to be $10\,\text{Å}^{-1}$ and the minimum q $1.25\,\text{Å}^{-1}$. Background scaling was optimized for each sample in comparison to representative empty scans measured with each setup. Fluctuating X-ray intensities with time at the synchrotron necessitated different scale factors.

For amorphous samples, the position of the first maxima in the structure factor were converted to atomic volume using the relation shown in Equation 2.2 (Chapter 2). These atomic volumes were converted to densities by a dimensional analysis based on the methodology reported by Bakonyi [265] and shown in Equation 3.9 below.

$$v_a\,[\text{Å}^3/atom] = \frac{M_{Ce_3Al}\,[g/mol]}{(\rho\,[g/cm^3] \cdot N_A\,[atom/mol])} \cdot (10^{24}\,\text{Å}^3/cm^3) \tag{3.9}$$

where v_a is the atomic volume, ρ is the density, M_{Ce_3Al} is the composition-averaged molar mass, and N_A ($= 6.022 \cdot 10^{23}$ atom/mol) is Avogadro's number.

3.4.3 Pair Distribution Function (PDF)

As described in Chapter 2, the structure factor can be directly converted to the reduced atomic pair distribution function (PDF) via Fourier transform. Additionally, the measured XRD data can be converted to the reduced PDF in a similar manner as the structure factor was converted. Equation 3.10 illustrates this relation.

$$G(r) = \frac{2}{\pi} \int_0^\infty q \cdot I(q) \sin(qr) \mathrm{d}q, \tag{3.10}$$

where $G(r)$ is the reduced PDF, r is the radial distance, and $I(q)$ is the measured data as a function of wavenumber q.

XRD data from NSLS and NSLS-2 experiments were converted to reduced PDFs using the PDFgetX3 software [263] during the same step as the conversion to structure factor. The short distances between sample and two-dimensional Si detectors used for XRD measurements allowed for high 2θ angle detection and associated high q resolution in the PDF.

The reduced PDF $G(r)$ may also be expressed as a function of the total PDF as shown in Equation 3.11 below.

$$G(r) = 4\pi r \rho_0 [g(r) - 1] = \frac{2}{\pi} \int_0^\infty q \cdot I(q) \sin(qr) \mathrm{d}q, \tag{3.11}$$

where r is the radial distance, ρ_0 is the average atomic number density, and $g(r)$ is the pair distribution function.

The reduced PDF was converted to the PDF by utilizing the limit wherein as $r \to 0$, $g(r) \to 0$ due to no elemental bonds existing that are smaller than a single atom diameter. Therefore as $r \to 0$, $G(r) \to -4\pi r \rho_0$. For each measured sample, $G(r)$ was evaluated at r smaller than the first peak of the reduced PDF. These values were used to calculate ρ_0 for each sample. Knowing the average atomic number density, the PDF was calculated from

the rearranged Equation 3.11 shown as Equation 3.12 below.

$$g(r) = 1 + \frac{G(r)}{4\pi r \rho_0} \tag{3.12}$$

Of note, amplitudes of the structure factor and PDF are converted using an arbitrary scale factor within the PDFgetX3 software. Therefore, no meaning can be gathered by comparing amplitudes between experiments, and the coordination number cannot be accurately calculated from converting the PDF to the radial distribution function. Details for using PDFgetX3 and the calculated scale factors and average atomic number densities are provided in Appendix C.

3.4.4 Extended X-ray Absorption Fine Structure (EXAFS)

Extended X-ray Absorption Fine Structure (EXAFS) experiments were performed at the X3B beamline of NSLS for the initial Ce_3Al MG, thermally crystallized ribbon, and two different Omega laser shock-compressed samples representative of low and high pressures. X-ray beam energies were varied from 5622 to 6164 eV around the Ce L3 absorption edge of 5723 eV. Samples were measured in fluorescence configuration while held in kapton tape. An automated stage and camera facilitated remote movement between samples. A vanadium reference sample was used for internal energy calibration. Figure 3.17 illustrates the setup schematically and with photographs of the room and sample configuration. Fluorescence alignment detects X-ray fluorescence produced as electron "holes" are filled after X-ray absorption causes ejection of electrons. This indirect measurement of the amount of absorbed X-rays allows for characterization of the surface of samples and permitted measurement of the recovered Omega laser sample stacks without concern that deeper layers affected the results. The copper holder for the samples does not meaningfully interact with the X-rays with the utilized beam size and at the given energy. Scattering of fluorescent X-rays from the sample on the path to the detector is representative of the atomic structure of the sample. Tuning the energies around an elemental absorption edge results in preferential

fluorescence from only one element in the composition and causes structural measurements to be meaningfully representative of only bonds with those elements.

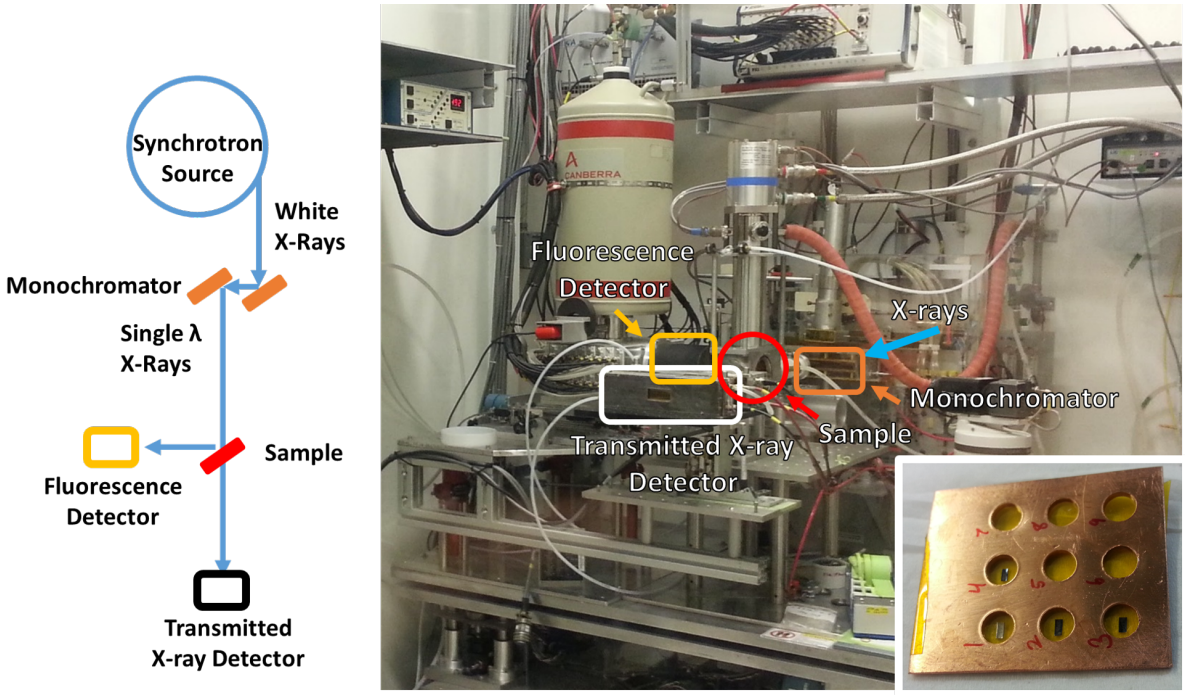

Figure 3.17: Schematic (left) and photo (right) of the setup used for NSLS extended X-ray absorption fine structure (EXAFS) experiments. The source X-rays, monochromator, samples, transmitted X-ray detector, and fluorescence detector are all visible. Inset shows a detailed view of the circled sample holder and representative samples. X-ray energies are filtered by the monochromator and varied through a range around a chosen absorption edge. Measured fluorescence, in fluorescence detection mode, represents the amount of electrons ejected due to absorption of X-rays. Interactions of fluorescent X-rays with the atomic structure results in structurally representative changes in detected X-ray intensities. Multiple samples were prepared at once on low-scatter kapton tape and an automated stage was used to move between samples.

Data was processed using the Athena software of the Demeter software package [266]. Measured values exclusively represent the partial pair distribution function for the Ce-Ce and Ce-Al bonds. EXAFS data is comparable to itself when processed the same way, but a shift is needed to compare it to the absolute radial distance values of PDF measurements from total scattering. Because the same data processing variables are used for all samples, all observed changes are meaningful. Relative peak position shifts represent differences in bond lengths. Increases in peak heights are indicative of increased bonds of that length and

type.

3.4.5 Atom Probe Tomography (APT)

Atom probe tomography (APT) experiments were performed at the Center for Nanophase Materials Sciences (CNMS) at Oak Ridge National Laboratory (ORNL) using a Cameca Instruments Local Electrode Atom Probe (LEAP) 4000X HR. Initial Ce_3Al MG and high-pressure Omega laser shock-compressed Ce_3Al samples were characterized. APT samples were prepared via focused ion beam (FIB) lift-outs and FIB-milling into a needle. Figure 3.18 shows a representative APT needle sample.

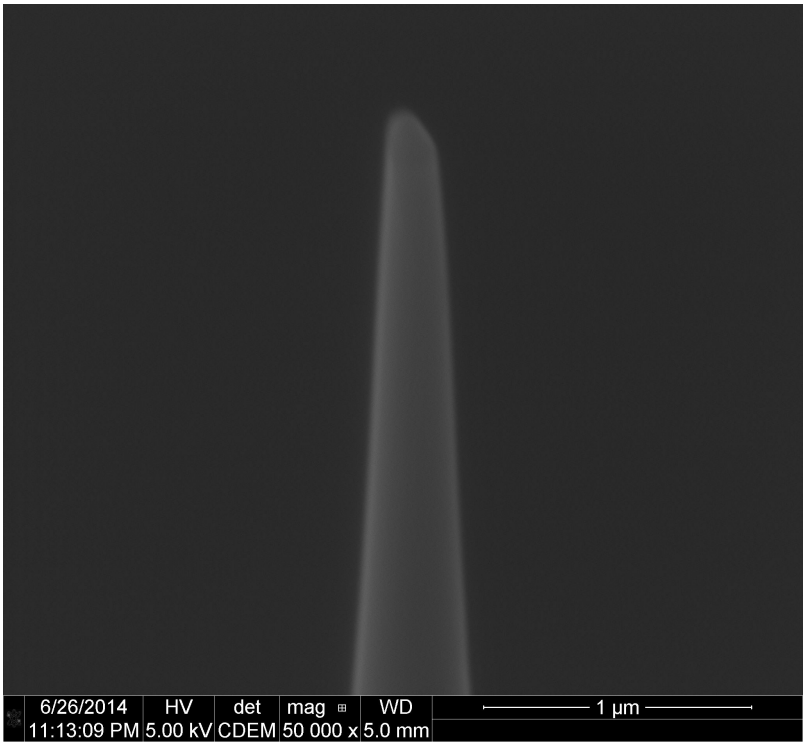

Figure 3.18: Scanning electron microscope (SEM) image of a needle of Ce_3Al MG prepared from a ribbon sample by FIB lift-out and milling into the shape of a needle.

In APT, atoms are individually removed from a needle tip, and the time-of-flight is measured to determine the element type. The area of detection on a circular detector is used to recreate the initial atomic position. Statistical analysis of the data was performed with the help of Dr. Jonathan Poplawsky at CNMS. Three-dimensional proxigrams were created,

and calculations of the atomic frequency distributions in the needles were performed to determine the homogeneity of the elemental composition distribution. Data from implantation of Ga ions into the outer surfaces of the sample from FIB-milling was discarded.

3.4.6 Transmission Electron Microscopy

Transmission electron microscopy (TEM) was performed for the thermally crystallized Ce_3Al sample using the facilities at the CNMS. Due to the amorphous structure and Al content, FIB sample preparation was found to implant Ga ions and disrupt accurate measurements. Sample preparation was performed using mechanical polishing, dimpling, and low temperature ion milling to avoid Ga implantation. Cross-sectional samples were prepared to evaluate changes throughout the bulk of the sample. Figure 3.19 illustrates the steps used for this TEM sample preparation methodology. Samples were initially cut, sandwiched between Si pieces, and then epoxied together. The sandwich was then rotated and placed in a C ring with epoxy. Each epoxy step included curing at 423 K for 1-2 hours. Samples were then manually polished down to $\sim 75\,\mu\mathrm{m}$ thicknesses and dimpled to reach sub-micrometer thickness in the center. Ion milling was performed at cryogenic temperatures to reduce the center to sub-nanometer thicknesses for electron transparency. Heating during curing may have caused some grain growth in the sample.

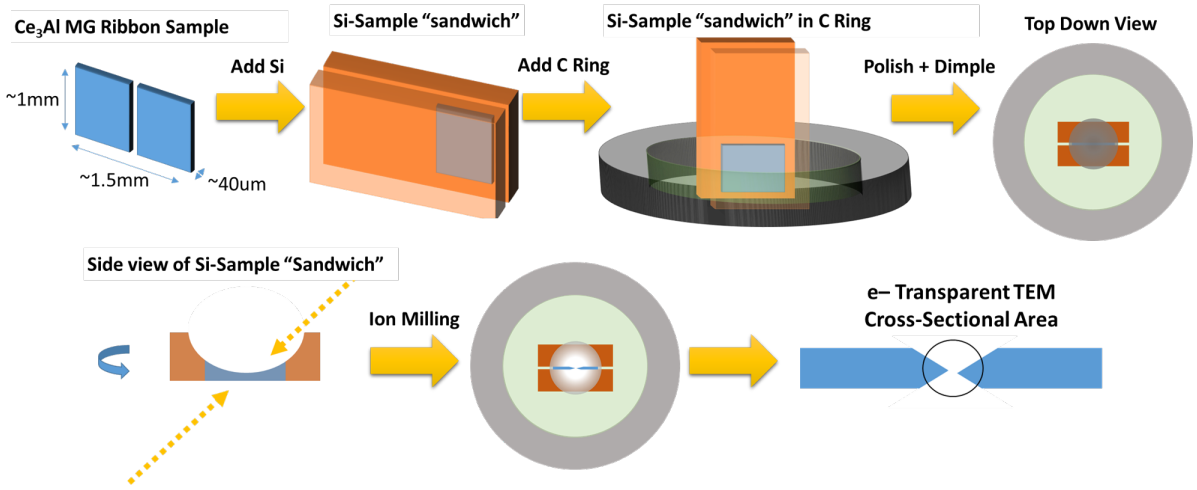

Figure 3.19: Transmission electron microscopy (TEM) cross-section sample preparation steps. The thermally crystallized Ce_3Al sample was separated into smaller pieces, sandwiched between Si, and epoxied together. This sandwich was then placed in a C ring for TEM imaging and epoxied in place. The sample package was polished down to $\sim 75\,\mu m$ thicknesses and dimpled to reach sub-micrometer thicknesses in the center. Cryogenic ion milling was performed to achieve sub-nanometer thicknesses in the center of the sample for electron transparency.

CHAPTER 4

THERMAL CHARACTERIZATION OF CE_3AL METALLIC GLASS

4.1 Overview

This chapter presents and discusses the results of the thermal characterization of Ce_3Al MG and structural characteristics of the thermally crystallized Ce_3Al MG ribbon. It is found that the activation energy for the onset of crystallization is lower than that of peak crystallization, the Arrhenius rate constant is 4.3×10^{19}, and the reduced glass transition temperature T_{rg} is 0.43 while the fragility m is $\sim$11.8. These values indicate nucleation of crystallites is thermodynamically preferred and growth is kinetically limited. Therefore, it is expected that crystallization will occur easily but result in very small crystallites. The crystallization pathway is two-stage, but only α-Ce_3Al is observable after completion, indicating that the first stage of crystallization is only metastable. Lattice parameters and bond lengths for the crystalline phase are all shorter than the reference, as is common with nanocrystalline metals formed from MGs. Crystallization appears to occur via 2D plate-like growth according to the Avrami model and dimensionality constant calculations, although these calculations may not be conclusive. This trend is also observable in TEM bright field images and may be the cause of [020] preferred orientation in SAED analysis. However, XRD preferred orientation analysis indicates that there is a small amount of preference for [002] directionality in the bulk sample, indicating there is mixed growth behavior or texturing. The high frequency factor constant k_0 and low activation energy for the glass transition are indicative of a large number of GUMs in the structure and a low barrier for structural relaxation into a denser glass.

4.2 Motivation and Approach

This chapter provides information about the thermal characteristics and crystallization behavior for the Ce_3Al MG. Details of the thermal characteristics are valuable for determining the stability of the MG and the mechanisms for crystallization under purely thermal conditions. Characterization of the structure provides information about the thermodynamically preferred phases which form with only thermal driving forces and a baseline for the associated microstructure of the crystalline phase(s). These properties provide a useful comparison for the structures observed under various thermal and shock-compression loading conditions as differences may be indicative of non-thermodynamically-preferred mechanisms leading to the structural changes induced via shock-compression.

Differential scanning calorimetry and thermogravimetric analysis experiments were performed using the Netzsch DSC 404 F1 at multiple heating rates and TA Instruments SDT Q600 TGA at 20 K/min, as described in Section 3.2. DSC scans at heating rates of 20 K/min at temperatures up to 960 K (above the 931.4 K melting temperature) were used to determine the glass transition, crystallization (onset and peak), and melting temperatures, and confirm the amorphous structure. Thermal treatment at 20 K/min up to 763 K (above the final crystallization peak temperature of 490.8 K) was used to crystallize samples for subsequent characterization of thermally-induced crystalline structure and grain size. Repeat scans at 20 K/min up to 763 K were performed on previously crystallized samples to determine if there was any remaining glass content or visible grain growth of crystallites after ambient cooling. TGA scans were performed to determine when oxidation occurs.

Scans performed at 1, 5, 10, 15, and 20 K/min up to 763 K were used for thermal analyses that allowed for calculations of the activation energy for the glass transition and crystallization, fragility, and the frequency factor k_0, Avrami n, and dimensionality D constants for crystallization. Section 3.2 details the equations used for thermal property calculations. The glass transition and crystallization onset temperatures are determined from

the intersection of a fit to the slope of the data before onset and the data during the phase change. Peak crystallization temperatures are determined from traditional peak fits. All temperatures were determined using the Netzsch Proteus Thermal Analysis software (more details are available in Appendix A.1).

The structural characteristics of crystallized samples was performed using HRTEM after sample preparation as described in Section 3.4.6. The hot stage was held at 423 K and samples remained on the stage for $\sim$ 3 hours, potentially causing extra grain growth. Samples which were not heated after the initial crystallization were characterized using XRD as described in Section 3.4.1. The traces were compared with the reference α-Ce_3Al hexagonal phase as well as the FCC phase observed to form under elevated hydrostatic pressures [176, 31] for phase identification. Rietveld and Williamson-Hall analyses were performed to determine the lattice parameters, anisotropy, grain size, and strain of the crystalline phase. Grain size values from Rietveld analysis of XRD data were compared and validated against TEM grain size values.

XRD traces were converted to the PDF (as described in Section 3.4.3) for comparison with the reference α-Ce_3Al bond lengths shown in Table 3.1 and plotted in Figure 3.6. EXAFS measurements were performed on the same thermally crystallized sample to determine if any Ce-specific SRO changes from the initial Ce_3Al MG were observable.

4.3 Results of Thermal Analysis

Figure 4.1 shows the TGA scan data plotted as percent of weight (relative to the initial weight) at temperatures from 20 to 1400 °C. There is no visible oxidation or weight gain until well above 300 °C, indicating the second exothermic event (starting at 454.8 K or 181.65 °C at 20 K/min) observed in the DSC (Fig 3.3) is likely not oxidation. Nitrogen should be more reactive than the Ar gas used in the DSC studies, so it is unexpected that there would be an oxidative event that is missed due to using a different gas. The higher temperature weight gain (at $\sim$500°C) may be due to a nitride formation which does not

occur in Ar. Samples prepared for characterization of the thermal crystallization behavior were heated at 20 K/min up to a final temperature of 763 K (489.85 °C), which is below the onset of weight gain. Therefore, no significant oxidation of these samples should have occurred.

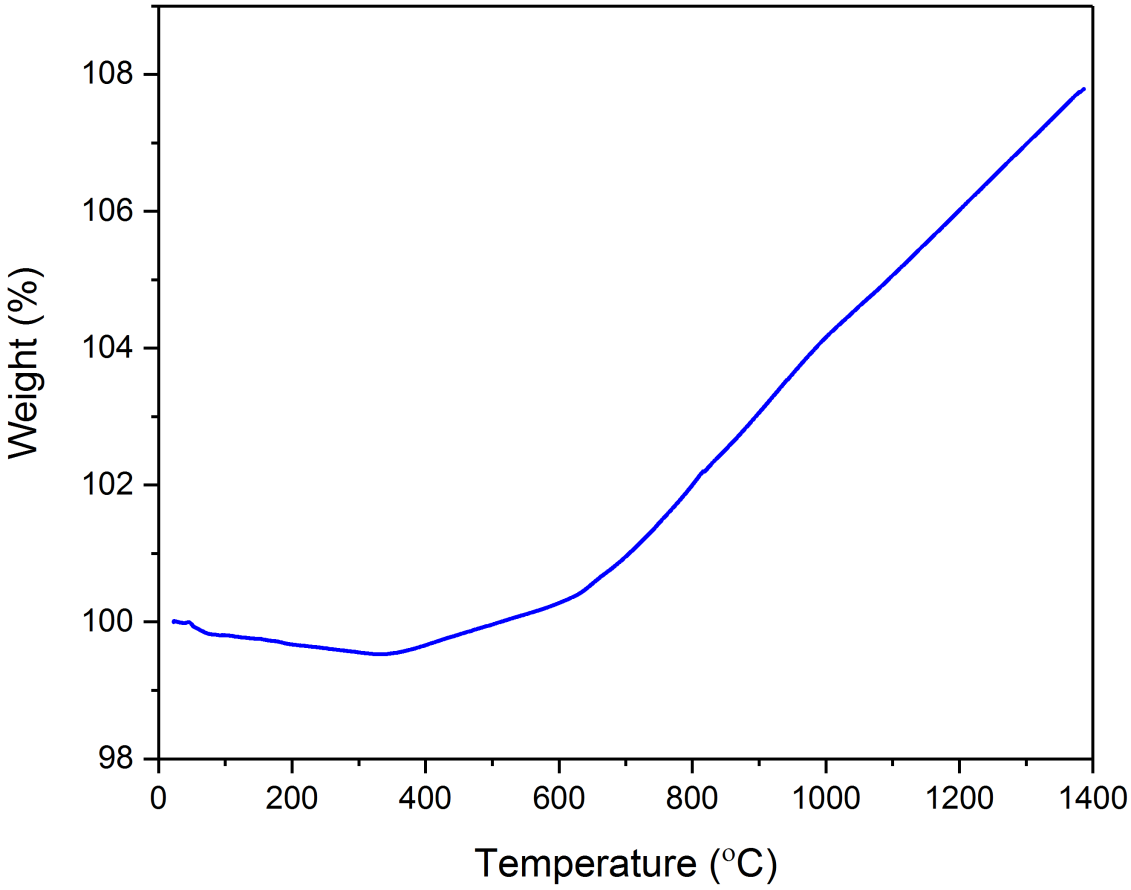

Figure 4.1: Thermogravimetric analysis of changing weight for Ce_3Al MG samples when heated at 20 K/min in 100 mL/min of nitrogen gas in an alumina pan. Clear weight gain is visible starting at ∼500°C. Nitrogen should be more reactive than the Ar gas used for DSC studies.

Figure 4.2 portrays the DSC traces for heating rates of 1, 5, 10, 15, and 20 K/min. The observed thermal event onset temperatures are each indicated by vertical lines: glass transitions are short dots and crystallization onsets are dashes. Crystallization peak temperatures are not labeled for clarity. As the heating rate increases, the temperature for the thermal events also increased, as expected. The measured values for each thermal event are tabulated in Table 4.1.

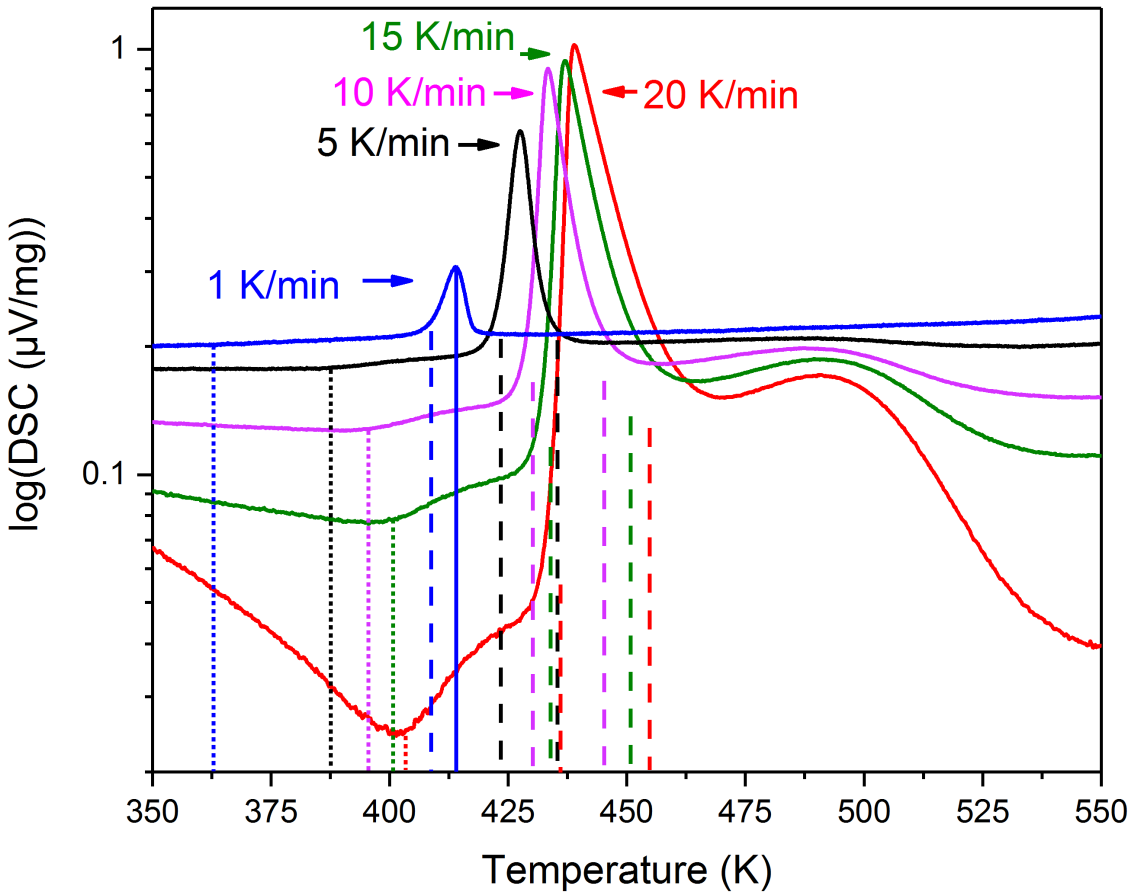

Figure 4.2: Logarithmic plot of differential scanning calorimetry data for the Ce_3Al MG heated at 1, 5, 10, 15, and 20 K/min. Y-values are offset for visibility. The glass transition onset temperature, Tg, is evident in the shoulder prior to the more exothermic crystallization onset, Tx. Increasing the heating rate increases the temperature at which events occur, representative of the activation energy of the thermal event. The temperatures for the onset of thermal events are indicated by lines: short dots for glass transition and dashes for crystallization onset. Crystallization peak temperatures are not labeled for clarity.

Table 4.1: Measured temperatures for the glass transition, onset of crystallization, and peak of crystallization at the heating rates of 1, 5, 10, 15, and 20 K/min.

Heating Rate	T_g	T_{x1}	T_{peak1}	T_{x2}	T_{peak2}
1 K/min	362.9 K	408.8 K	414.0 K	n/a	n/a
5 K/min	387.6	423.4 K	427.6 K	435.4 K	486.9 K
10 K/min	395.5 K	430.2 K	433.4 K	445.2 K	487.2 K
15 K/min	400.7 K	433.9 K	437.0 K	450.8 K	489.4 K
20 K/min	403.4 K	436.0 K	438.9 K	454.8 K	490.8 K

Figure 4.3 shows the initial heating trace for samples heated at 20 K/min to 763 K as well as the repeated DSC trace when reheated at 20 K/min to 763 K after cooling. No thermal events are visible upon reheating, indicating there is no grain growth observed at this heating rate up to 763 K.

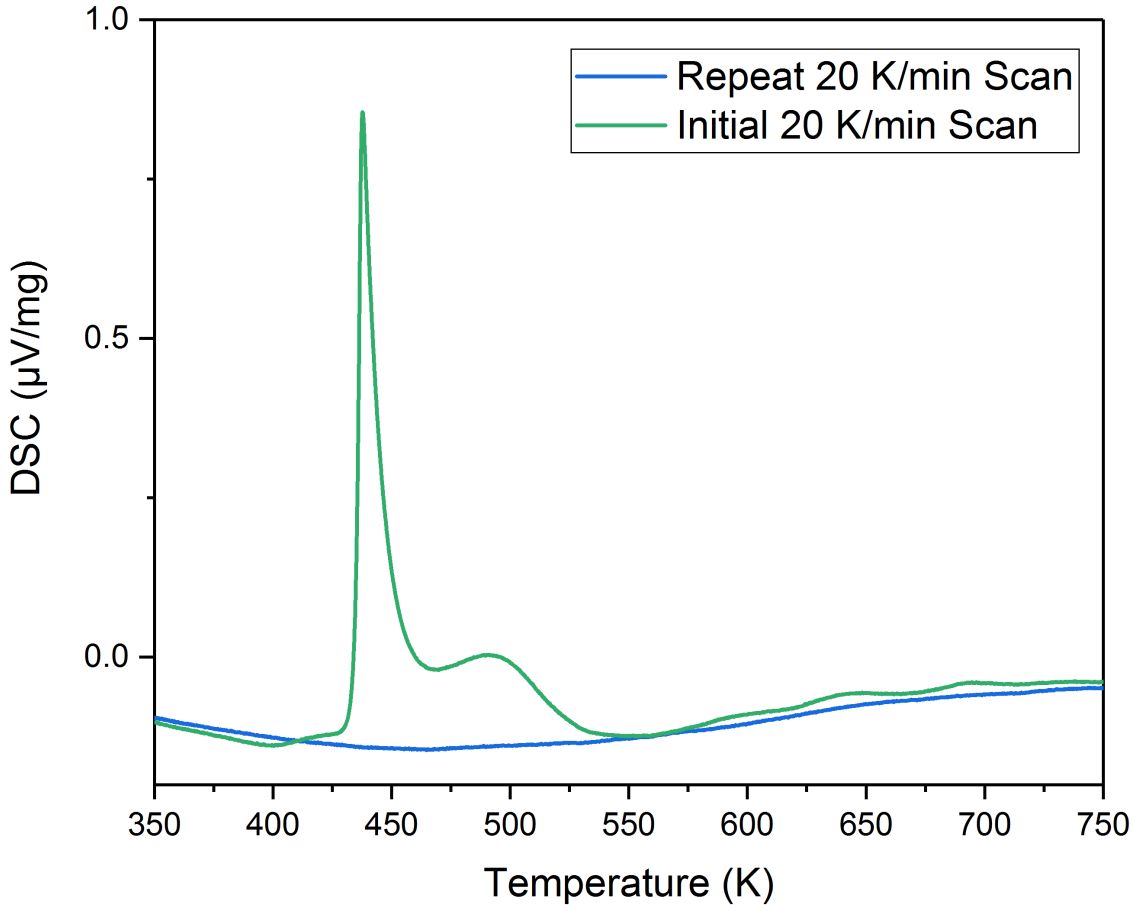

Figure 4.3: Plot of differential scanning calorimetry data for the Ce_3Al MG heated at 20 K/min up to 763 K, cooled to room temperature, and heated to 763 K again. No thermal events are visible during the second heating, indicating there is no observable grain growth exothermic event.

4.3.1 Activation Energy and Crystallization Behavior

The fraction crystallized at a given temperature for different heating rates is calculated from the fraction of the area under the crystallization peak. The total area under the first crystallization peak was calculated using the initial and subsequent onsets of crystallization

as boundaries. Figure 4.4 plots the percents crystallized as a function of temperature for the 5 K/min, 10 K/min, 15 K/min, and 20 K/min heating rates.

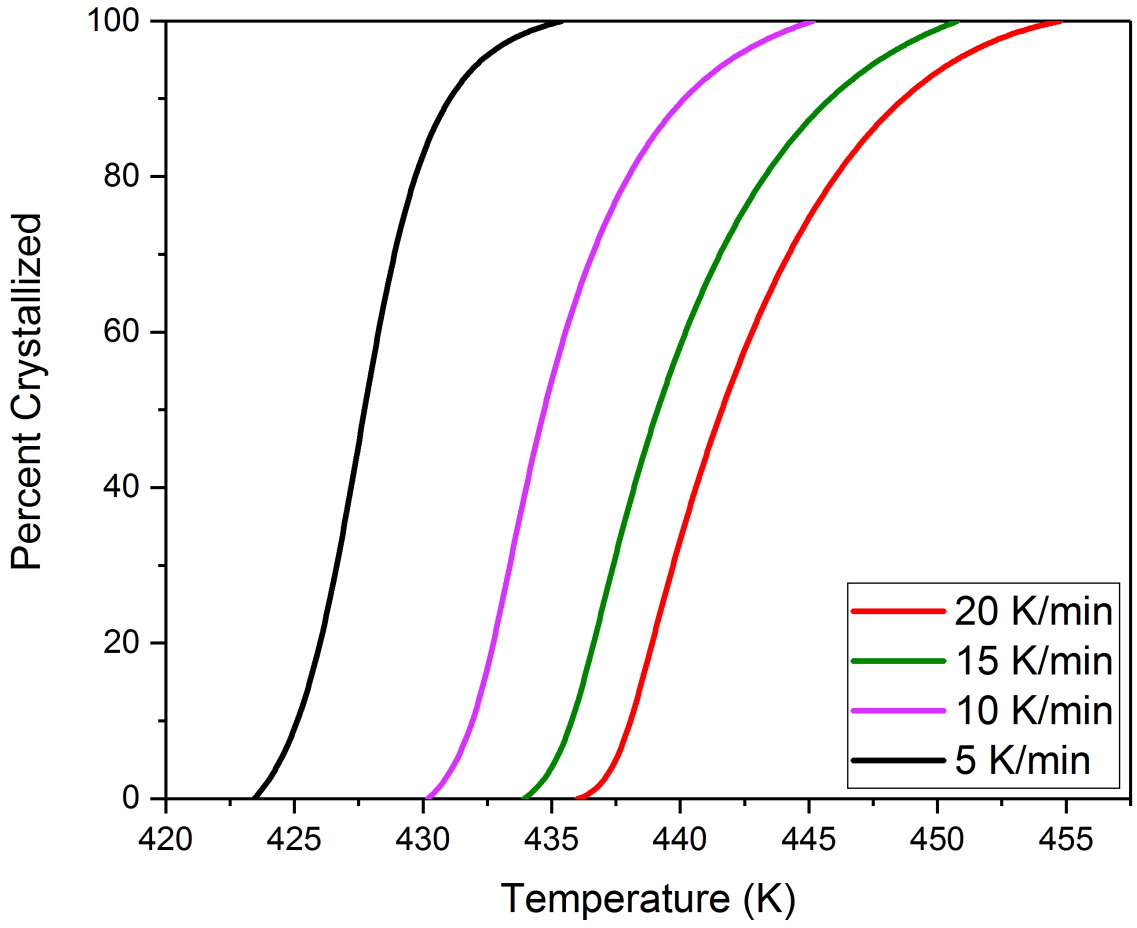

Figure 4.4: Plot of the fraction crystallized at various temperatures for the heating rates of 5, 10, 15, and 20 K/min. All traces follow the typical S-curve.

For the Ozawa relation (Equation 3.1), only the first crystallization event was considered. Multiple temperatures were chosen from the data in Figure 4.4 for comparison of percent crystallized at different heating rates. Figure 4.5 plots the fraction crystallized at these temperatures for the different heating rates in the format of $ln(-ln(1-x))$ vs $ln(\beta)$ as per the Ozawa relation [238]. The best linear fits to the data (for 439 and 440 K) give values for the slope of approximately 3 or 2.5. As the Avrami constant can only be an integer, it appears the Avrami constant n is approximately 3, meaning the dimensionality is D 2 and thermal crystallization occurs via disk-like growth. However, this Avrami analysis

of growth behavior may not be conclusive.

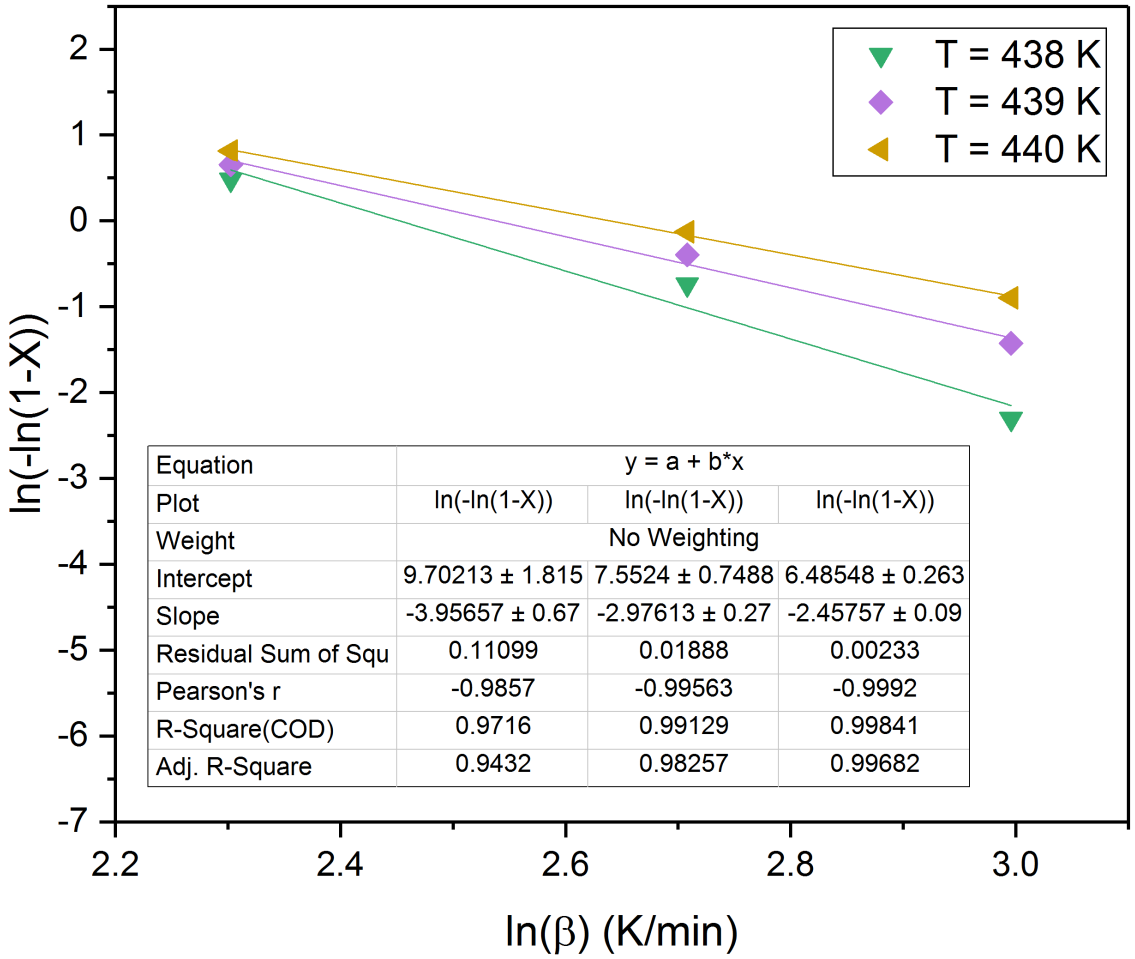

Equation	y = a + b*x		
Plot	ln(-ln(1-X))	ln(-ln(1-X))	ln(-ln(1-X))
Weight	No Weighting		
Intercept	9.70213 ± 1.815	7.5524 ± 0.7488	6.48548 ± 0.263
Slope	-3.95657 ± 0.67	-2.97613 ± 0.27	-2.45757 ± 0.09
Residual Sum of Squ	0.11099	0.01888	0.00233
Pearson's r	-0.9857	-0.99563	-0.9992
R-Square(COD)	0.9716	0.99129	0.99841
Adj. R-Square	0.9432	0.98257	0.99682

Figure 4.5: Plots of the fraction crystallized at 438, 439, and 440 K for the heating rates of 10, 15, and 20 K/min. Linear fits to the data are shown as well. The slope of linear fits to the data is a direct measure of the Avrami constant. There appears to be some fluctuation in the value around 3.

Knowing the Avrami number and dimensionality, Equation 3.3 can be used to calculate the activation energy for crystallization. Plotting $ln(\beta/T_{peak}^2)$ vs $1000/T_{peak}$ for different heating rates and the associated peak crystallization temperatures for the first crystallization event, the slope is $-(D/n)(E_A^{cryst}/R)$. Figure 4.6 shows this Matusita modified Kissinger relation [240, 241] for Ce_3Al MG. A linear fit to the data gives a slope of -20.8. With the known values of D = 2, n = 3, and R of 8.31446 $kJ/(K \cdot mol)$, the activation energy for crystallization is $E_A^{cryst} = 259kJ/mol$.

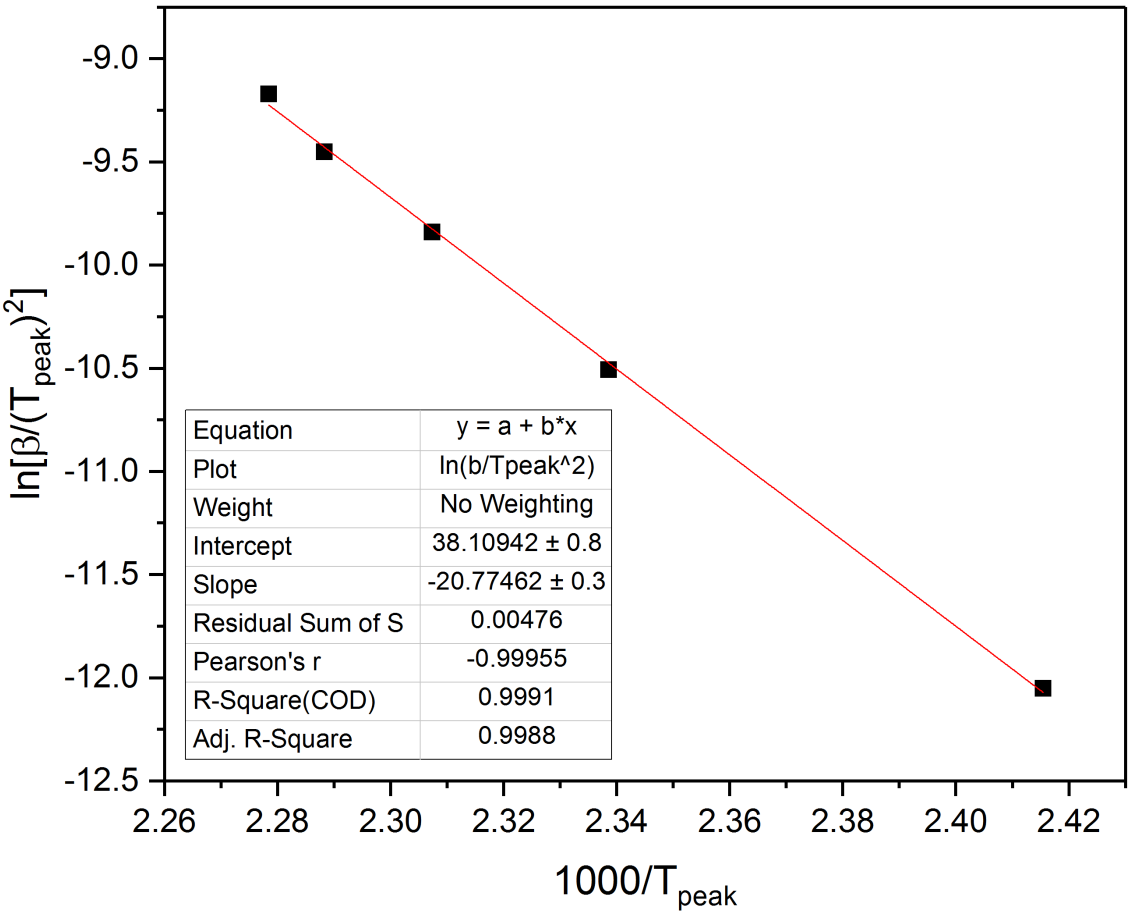

Figure 4.6: Matusita modified Kissinger plot for Ce_3Al MG. The natural log of the heating rate normalized by the measured peak temperature for crystallization squared is plotted against the peak temperature for crystallization. The slope of the linear fit to this data allows for the determination of the activation energy for crystallization ($E_A^{cryst} = 259kJ/mol$).

The activation energy for crystallization can also be calculated from the Augis and Bennett relation in Equation 3.2. Plotting $ln(\beta/T_{peak})$ vs $1000/T_{peak}$, the slope of the linear fit is $-(E_A^{cryst}/R)$ and the intercept is $ln(k_0)$. The frequency factor, k_0, provides an indication of the number of nucleation sites present in the material for crystal growth. Figure 4.7 shows the result of the Augis and Bennett relation applied to the Ce_3Al MG data. The slope of the linear fit to the data is -21.2, and the intercept is 45.2. Therefore, the activation energy for crystallization E_A^{cryst} is 176 kJ/mol, and the value for k_0 is 4.3×10^{19}. The frequency factor value k_0 is higher than many other glasses [237, 267], indicating a higher number of nucleation sites or GUMs than many other glasses. The high frequency

factor and low activation energy for crystallization together represent a relatively low glass stability and an expected high nucleation rate with concomitant small, nucleated grains.

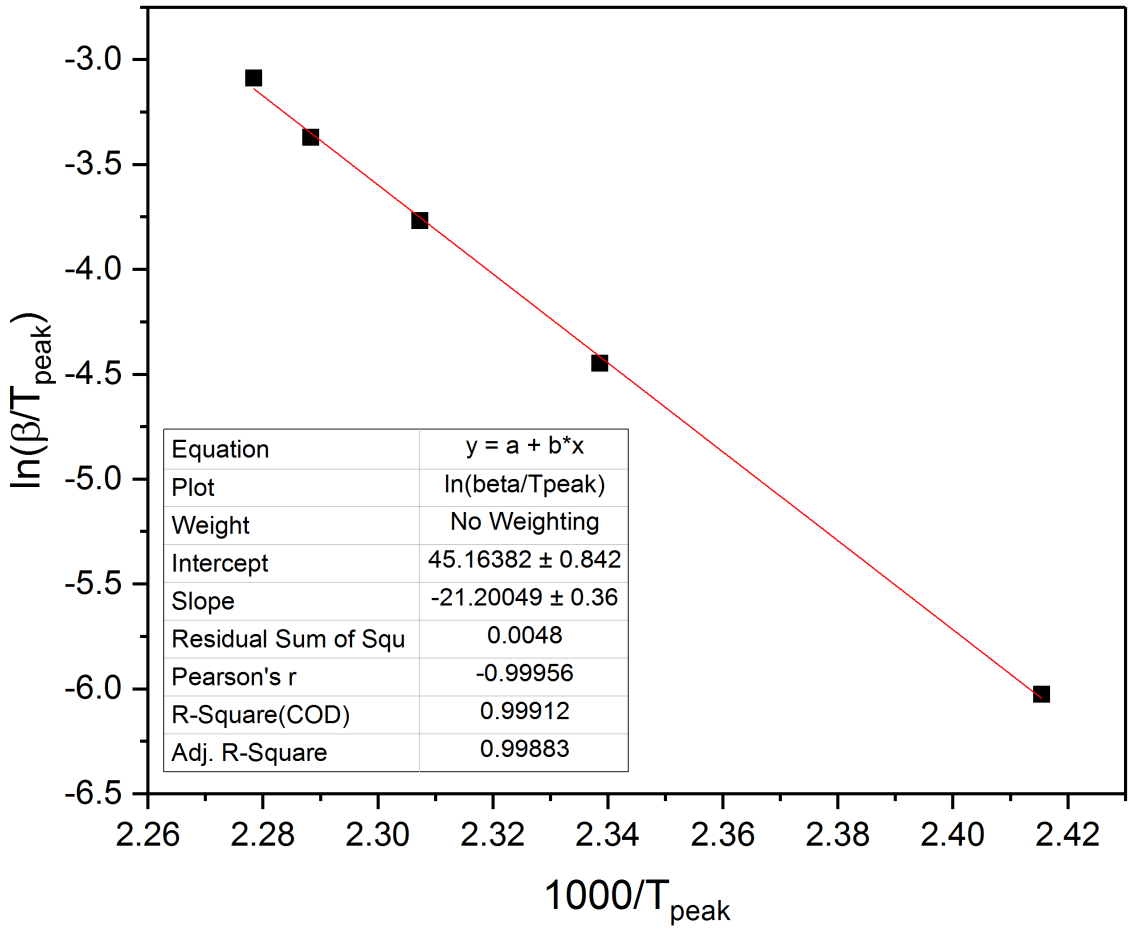

Figure 4.7: Augis and Bennett plot for Ce_3Al MG. The natural log of the heating rate normalized by the measured peak temperature for crystallization is plotted against the peak temperature for crystallization. The slope of the linear fit to this data allows for the determination of the activation energy for crystallization ($E_A^{cryst} = 176kJ/mol$) and the frequency factor for crystallization ($k_0 = 4.3 \cdot 10^{19}$).

Using the general form of the Kissinger equation (Eqn 3.4), the activation energy for each of the thermal events can be compared. Figure 4.8 plots the data for the glass transition temperature, onset of first crystallization, first crystallization peak, onset of second crystallization, and second crystallization peak temperatures in the Kissinger relation format as a function of heating rate using data from Table 4.1. The activation energy can be calculated from the slope via the formula $E_a = -slope \times R$, where R is the gas constant

8.31446 $kJ/(Kmol)$. The activation energies for each of these events calculated using the Kissinger method as well as the derived values from other methods are presented in Table 4.2.

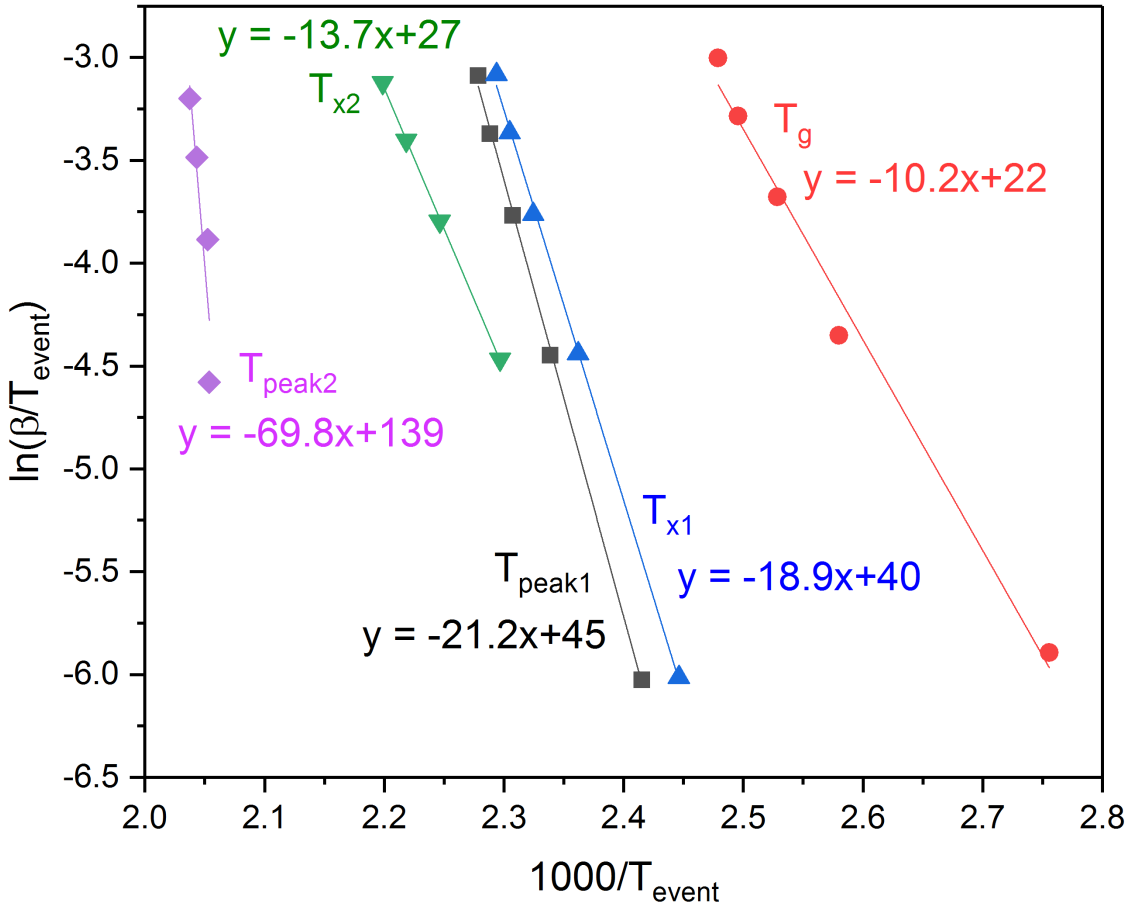

Figure 4.8: Kissinger plots for the glass transition, T_g, crystallization onset, T_{x1} and T_{x2}, and peak crystallization, T_{peak1} and T_{peak2}, of the Ce_3Al MG. Equations for linear fits to the data were used to calculate the activation energy for each thermal event.

It can be seen that the activation energies for the initial crystallization increase as more factors are taken into account in the model, e.g. with the Matusita modified Kissinger model, as is seen in other systems [114]. However, only the general form of the Kissinger model allows for comparisons of activation energies for the different thermal events. Therefore the discussion of activation energies will focus on those from the general Kissinger model. The large activation energy for the second crystallization event is not independently unusual, but it is unusually greater than that for the other thermal events [114]. A

Table 4.2: Calculated thermal properties from DSC data for Ce_3Al MG using the Ozawa [238], Matusita modified Kissinger [240, 241], Augis & Bennett [239], and General Kissinger equations.

Property	Ozawa	Matusita Kissinger	Augis & Bennett	Gen. Kissinger
E_a^g	n/a	n/a	n/a	84.8 kJ/mol
E_a^{x1}	n/a	n/a	n/a	157 kJ/mol
E_a^{peak1}	n/a	259 kJ/mol	176 kJ/mol	176 kJ/mol
E_a^{x2}	n/a	n/a	n/a	114 kJ/mol
E_a^{peak2}	n/a	n/a	n/a	580 kJ/mol
k_0	n/a	n/a	4.3×10^{19}	n/a
n	3	n/a	n/a	n/a
D	2	n/a	n/a	n/a

higher activation energy for the peak of crystallization than onset of crystallization is indicative of greater difficulty in grain growth as compared to nucleation, indicating that the resulting grain sizes should be particularly small. Both the onset and peak crystallization activation energies are relatively low, indicative of a poor glass former which easily crystallizes. Similarly, the high rate constant k_0 is indicative of a large number of nucleation sites, indicating easy nucleation. An Avrami constant of 3 and dimensionality of 2 indicates that the growth may occur in a two-dimensional disk-like fashion, potentially inducing distorted lattice parameters for very small grains. From these thermal analysis results, the thermally crystallized sample might be expected to have a structure which has nanometer-scale grains with distorted lattice parameters. The activation energy for the glass transition is indicative of the energy barrier for relaxation [268], and a low value is indicative of a low barrier for structural relaxation and the associated reduction of GUMs and increased densities.

4.3.2 Fragility of the Metallic Glass

The fragility of the glass m, an indicator of the resistance to the kinetics of crystallite growth in a glass, can be calculated from the thermal properties and two main equations: the Vogel-Fulcher relation (Equation 3.5) and subsequent calculation from fit parameters and Equation 3.6, or directly from the activation energy, glass transition temperature, and

Equation 3.7.

The Vogel-Fulcher equation parameters can be determined from a plot of $ln(\beta)$ vs T_g, where the data is fit by an equation of the form $ln(B) - \frac{AT0}{Tg-T0}$. Figure 4.9 shows the measured data and two fit lines. There is significant variability possible and no perfect fit to the data. Comparing the two fits, the lowest variability in values occur when the A is constrained to have lower values, but that does not necessarily make it the correct value. The resulting values that match the best fit are $A = 1.2$ or 2, $ln(B) = 8.1$ or 9.6, and $T0 = 327$ or 310, which are relatively close to those seen in literature for other glasses, where La-based glasses have large error in data fits [243].

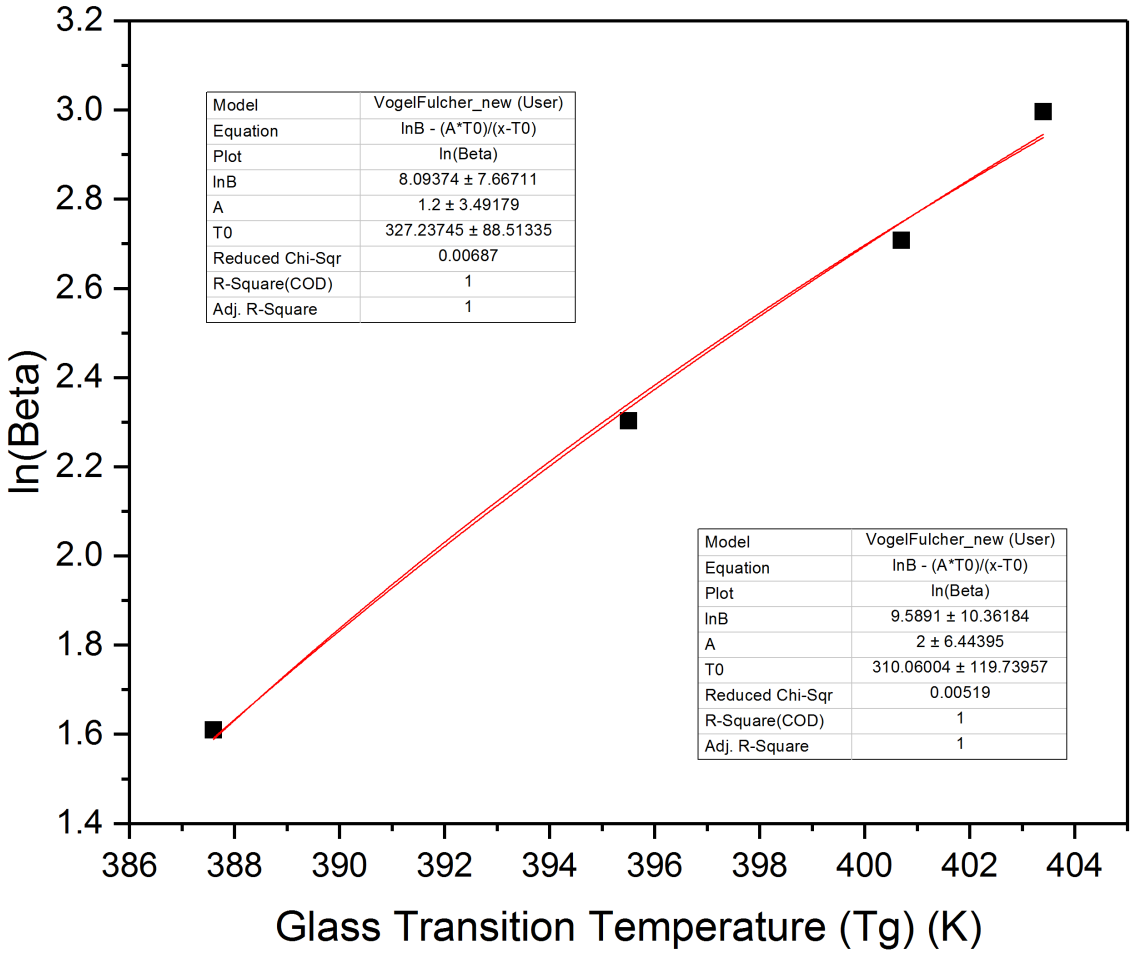

Figure 4.9: Vogel-Fulcher fit to measured T_g values at different heating rates. Multiple lines are fit using the Vogel-Fulcher relation with seemingly similar error. No perfect fit seems to be possible.

Using the fitted Vogel-Fulcher values and Equation 3.6, the fragility is calculated to be either 11.8 or 12.5. These fragility values are particularly low, indicating a strong kinetic resistance to crystallite growth. The large error in the fits brings these values into some question. Hence, Equation 3.7 is also used to calculate the fragility for comparison. This equation, evaluated with the activation energy from Table 4.2 and 20 K/min glass transition temperature from Table 4.1, results in a fragility value of 11.0, which is in surprising agreement with the value calculated from the Vogel-Fulcher method, indicating that the values are likely accurate.

4.4 Structural Characteristics of Thermally Treated MG

Ce_3Al MG samples heated at 20 K/min up to 763 K (above the final crystallization peak temperature of 490.8 K) were characterized using TEM, Synchrotron XRD (and converted PDF), and Synchrotron EXAFS. TEM samples were heated again at 423 K for $\sim$ 3 hours prior to analysis. The results of each of these characterization techniques are presented in the following sections.

4.4.1 TEM Analysis

Figure 4.10 illustrates the low magnification microstructure observed via STEM and EDS in the thermally crystallized sample. The boxed region is where the EDS maps were taken for Ce and Al. There are many domain-like regions visible which at first glance appear to be grains but actually correlate to regions of material surrounded by areas of few atoms, as seen in the EDS images. This is likely caused by phase separation which occurred during the two-stage crystallization. The regions which are observed to have fewer atoms would have been preferentially thinned during ion milling. Therefore, these regions must have had a structure more easily thinned, indicating the phase in these regions was of lower stability than the rest of the sample. These results indicate small amounts of the first metastable crystalline phase are retained in these domain-like edge regions which were subsequently

preferentially thinned during TEM sample preparation. More studies are needed to characterize the structure, amount, and distribution of this metastable phase.

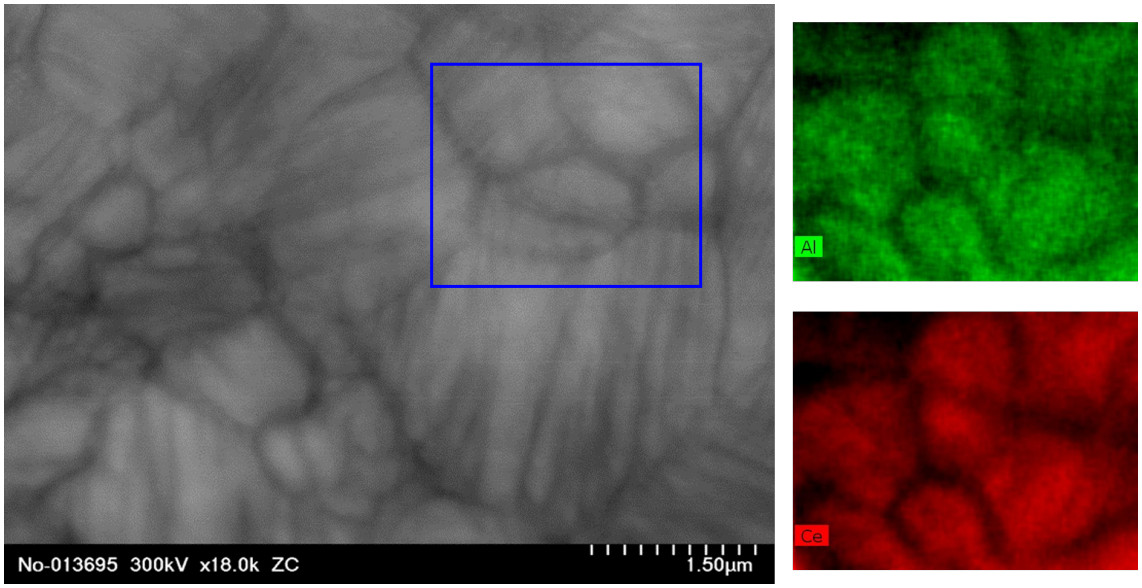

Figure 4.10: Low magnification STEM image (left) of thermally crystallized Ce_3Al ribbon, with EDS mappings for Ce and Al (right) taken from the boxed area of the STEM image. Dark areas of the STEM image correspond to areas with few Ce or Al atoms in the EDS mappings, indicating they are dark due to having fewer total atoms in the area. Dark areas may have been preferentially ion-milled due to phase-separation during the two-phase primary crystallization.

At higher magnifications, the domain-like structures are also visible in bright field TEM images as areas that are lighter or darker, according to the thickness. Figure 4.11 illustrates an example of a bright field image showing many nanoscale crystallites ($<$ 10 nm) visible as dark spots. The associated dark field image is also shown, with the bright spots indicating the nano-crystallites.

Figure 4.12 shows a high magnification view of the structure, wherein the crystallites are clearly visible to be on the order of 10 nm or smaller, with the average grain size being 6.3 nm and standard deviation of 2.4 nm. By measuring the distance between atomic planes visible in this image, the values for d-spacing are found to be 3.5, 2.9, 3.2, and 2.9 Å which match well with the α-Ce_3Al d-spacings of 3.53 and 3.05 Å. The 3.2 and 2.9 Å values perhaps indicate decreased atomic lattice parameters. The overall crystallite geometries

appear to resemble those of the 2D format as shown in Figure 2.7 from Section 2.2.3. This matches the dimensionality calculated from thermal analysis which indicated there may be predominantly 2D crystallite growth.

Figure 4.13 shows the corresponding select area electron diffraction (SAED) image for the region in Figure 4.11. The diffraction pattern indicate that the thermally crystallized sample has preferred orientations. The main rings were identified and the radii measured. Taking into account the camera constant of 58.6, the d-spacings were calculated and are provided in Table 4.3. Unfortunately, the phase could not be identified from this SAED. The values fit well to a cubic system with a lattice parameter of 6.3 Å, but lattice parameters for HCP structures are difficult to independently calculate for many of the possible planes from individual d-spacing values. For the [hkl] values of HCP which allow for direct calculation of a lattice parameter from one d-spacing value (e.g., [110], [200], [002], etc.), the d-spacings can correspond to either an *"a"* lattice parameter of 6.47 or 7.33 Å and a corresponding *"c"* lattice parameter of 5.2 or 5.7 Å. The α-Ce_3Al lattice parameters are 7.04 and 5.45 Å for *"a"* and *"c"* respectively. As such, the diffraction rings may correspond to the α-Ce_3Al phase with either larger or smaller lattice parameters than the reference. If a hexagonal phase is the correct fit, the brightest rings correspond to the [110] and [020] directions. However, if the α-Ce_3Al phase is correct, the brightest ring should be for the [201] direction [236], indicating that there is preferred orientation in the [110] and [020] directions in this sample. This appears to match the thermal analysis prediction and TEM bright field observation of 2D crystallite growth as it could indicate formation of more planar-like structures (for a hexagonal phase). It could also be representative of texturing within the material.

4.4.2 XRD Analysis

Figure 4.14 shows the XRD trace of the thermally crystallized Ce_3Al samples upon heating at 20 K/min up to 763 K (above the final crystallization peak temperature of 490.8 K). The

Table 4.3: Calculated d-spacings from the SAED pattern shown in Figure 4.13. The camera constant of 58.6 is divided by radius values in mm to directly calculate the d-spacing value in Å.

Radius (mm)	d-spacing (Å)
16	3.6625
18.5	3.1676
20.5	2.8585
22.5	2.604
28.5	2.0561
31.8	1.8428
33.8	1.7337

amorphous structure was fully transformed into crystalline phase(s). Phase analysis results show that there is only one phase, α-Ce_3Al. This indicates that the two-stage primary crystallization creates first a metastable phase and then converts all of that phase into α-Ce_3Al. Rietveld analysis was performed to optimize the structural parameters. The fit α-Ce_3Al reference pattern peak positions are overlaid with vertical red lines. Differences in peak center at low angles are accounted for with peak shape parameters in Rietveld analysis.

Table 4.4 provides the Rietveld-analysis-derived structural parameters for the α-Ce_3Al phase. The preferred orientation is determined using the March model from Dollase [262]. The percent of preferred orientation is determined from the fit parameter in HighScore Plus [261], where a positive value represents preference and a negative avoidance. The grain size of 6.2 nm matches very well with the value calculated from the TEM data. The preferred orientation away from [020] oddly contradicts the TEM SAED data, potentially indicating a decreased preference for plate-like growth or [002] texture in the bulk. The lattice parameters are lower than those of the reference, indicating the sample has d-spacing values smaller than the reference, matching the TEM data. Smaller lattice parameters and very small grain sizes is not unexpected for crystallization of MG, as discussed in Section 2.2.3. The density is calculated from the ideal unit cell. The decreased lattice parameters result in a smaller unit cell and higher density.

Table 4.4: Rietveld analysis derived parameters for the α-Ce_3Al phase fit to the measured XRD data for the thermally crystallized Ce_3Al ribbon.

Phase	Density (g/cm^3)	Grain Size (nm)	Pref. Orientation $[hkl]$ | %	Lattice Param. c | a (Å)
α-Ce_3Al	6.59 ± 0.01	6.2 ± 0.3	[020] | -10 ± 5%	5.380 ± 0.005 | 6.958 ± 0.004

4.4.3 PDF Analysis

Figure 4.15 plots the PDF trace for the thermally crystallized Ce_3Al ribbon as compared to the initial Ce_3Al MG PDF shown in Fig 3.5 and superimposed in Fig 4.15. The thermally crystallized data is the solid line and the initial MG data is a dashed trace. Crystallization leads to clear MRO and LRO evolution in the PDF with many peaks appearing and separating up to 30 Å. The peaks are all narrower, indicative of the smaller bond-length ranges for crystalline lattice planes. Residual broadness to the peaks as compared to an ideal crystalline material may be indicative of the lattice distortion observed in XRD analysis.

Figure 4.16 plots a magnified view of the first 10 Å of the PDF from Figure 4.15 with the reference bond-lengths for α-Ce_3Al from Table 3.1 overlaid on top. There is clear separation of peaks as compared to the initial Ce_3Al MG, representing elevated order. An increased peak amplitude around 4.9 Å paired with a narrowing of the first peak indicates a rearrangement of atoms from the SRO into a second nearest neighbor MRO position. Occupied bond lengths for the measured crystalline phase are shorter than those of the reference α-Ce_3Al, potentially indicating the source of shorter lattice parameters observed in XRD and TEM.

4.4.4 EXAFS Analysis

Figure 4.17 shows the EXAFS-derived Ce-based partial PDF for the thermally crystallized Ce_3Al ribbon (solid line) as compared to the initial Ce_3Al MG (dashed line). The first three peaks of the initial MG are shifted to lower values after thermal crystallization, and the amplitude of the first is decreased while those of the second and third increase. The overall

structural changes are indicative of ordering into distinct bond-lengths with crystallization, although the trend appears to result in an overall decrease in packing at short-range. The observed trend in the partial PDF appears to match the decreased bond-lengths and rearranged amplitudes observed in the first two peaks of the total PDF. The partial PDF shifts indicate Ce-based bond changes are major components of the thermal crystallization behavior.

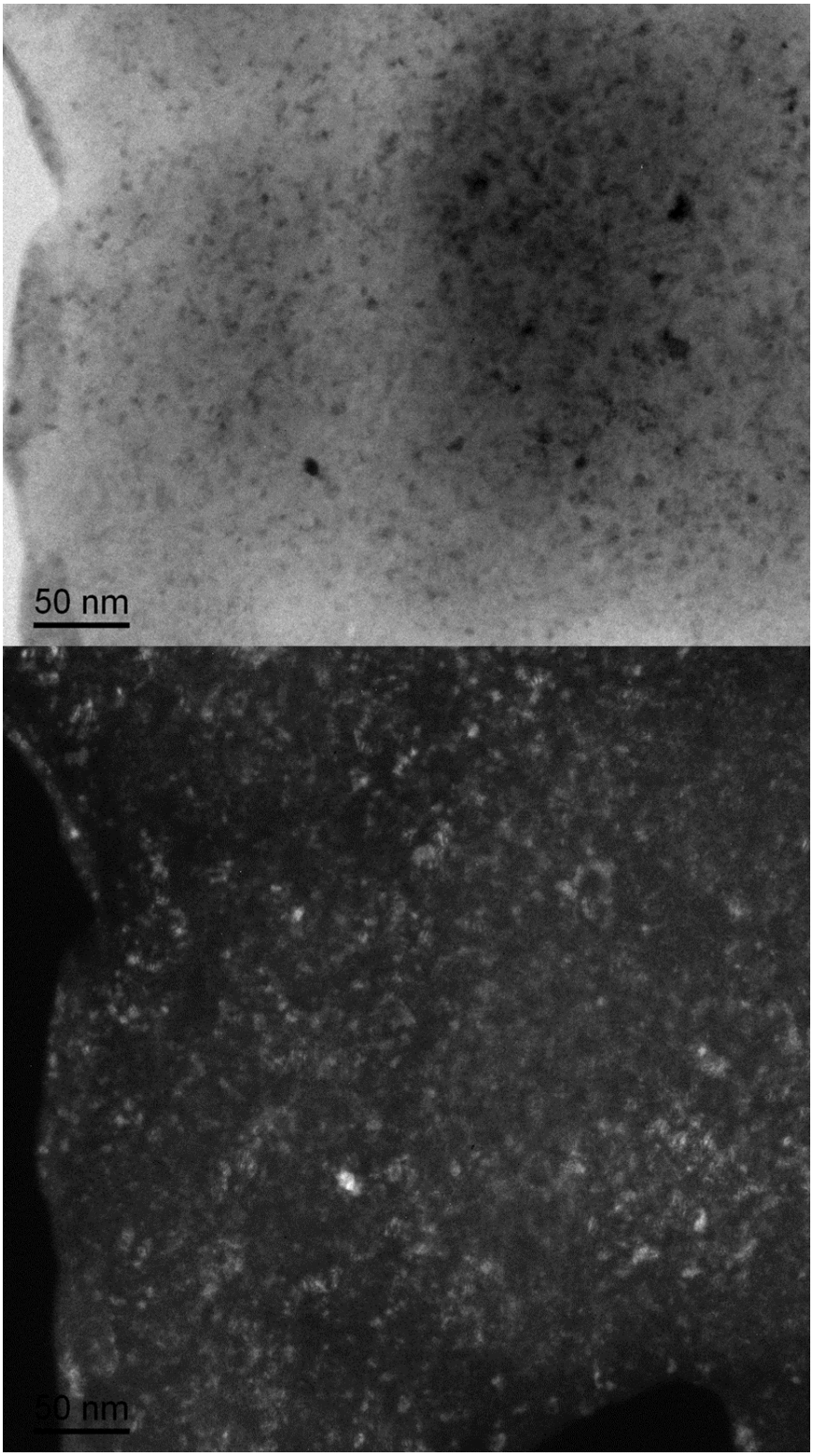

Figure 4.11: 375kX magnification bright field (top) image and associated dark field (bottom) image of thermally crystallized Ce_3Al ribbon. Light areas of the bright field image correspond to the low atom regions seen in Figure 4.10. Dark spots of the bright field image and bright spots of the dark field image correspond to crystallites that appear to generally be smaller than 10 nm.

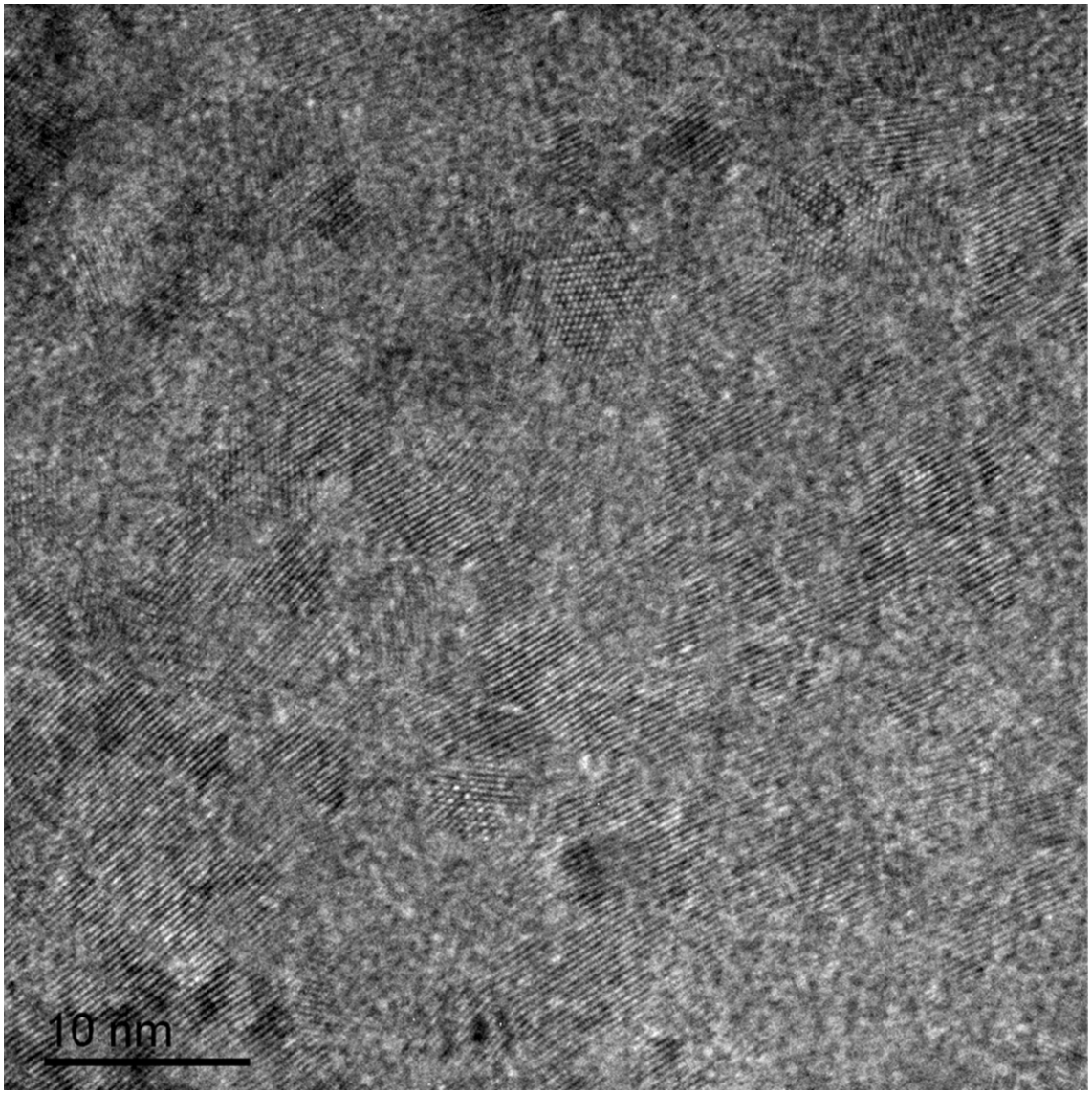

Figure 4.12: 3.6MX magnification bright field image of thermally crystallized Ce_3Al ribbon. Grains appear to have predominantly 2D morphology. Average grain size is 6.3 nm with a standard deviation of 2.4 nm. Measured d-spacings correspond well to the reference α-Ce_3Al phase and a smaller lattice parameter form of the α-Ce_3Al phase.

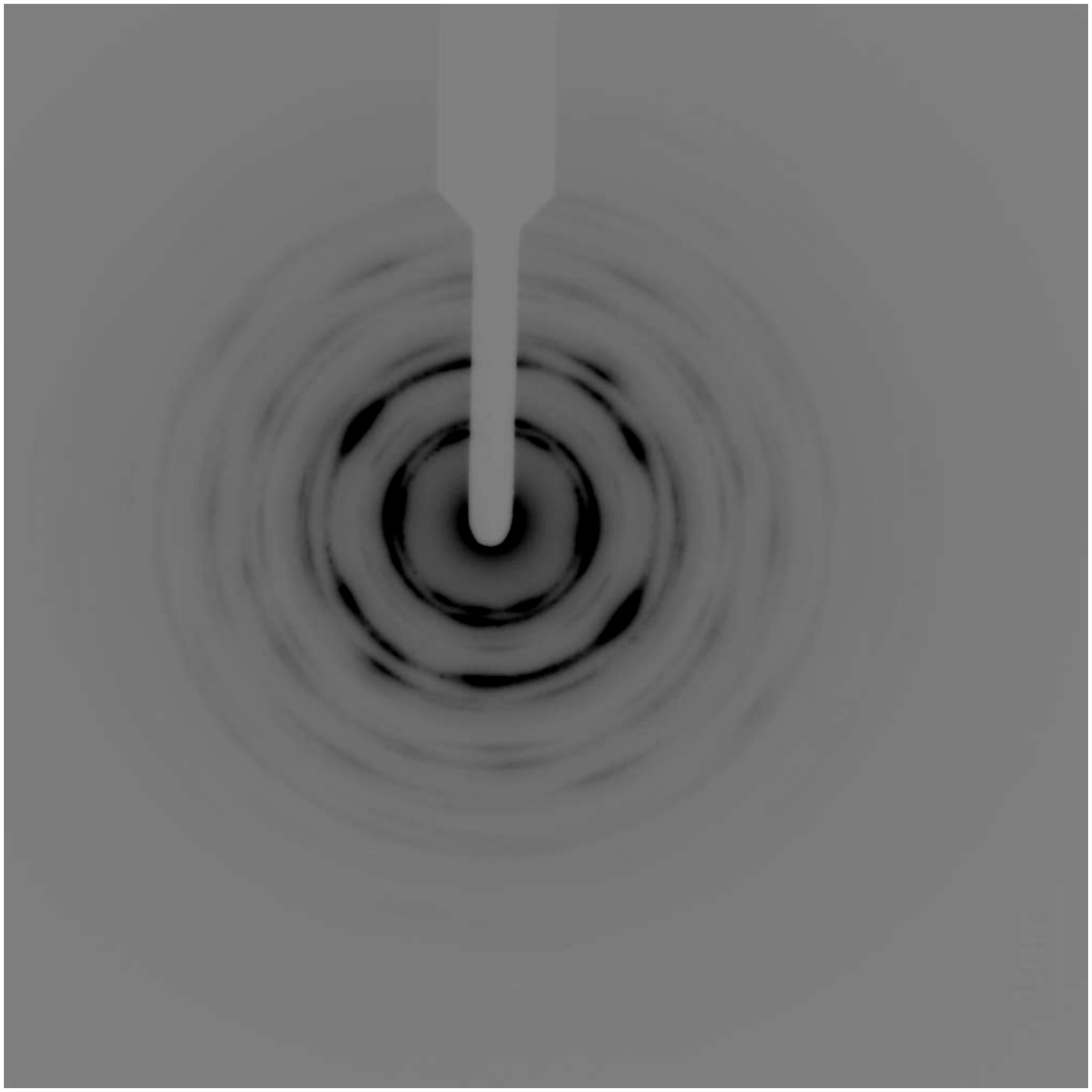

Figure 4.13: Inverted color select area electron diffraction (SAED) pattern for the region shown in Figure 4.11. Ring radii correspond to d-spacings shown in Table 4.3. Phase identification was not perfect, although values indicate the phase may be a distorted form of α-Ce_3Al.

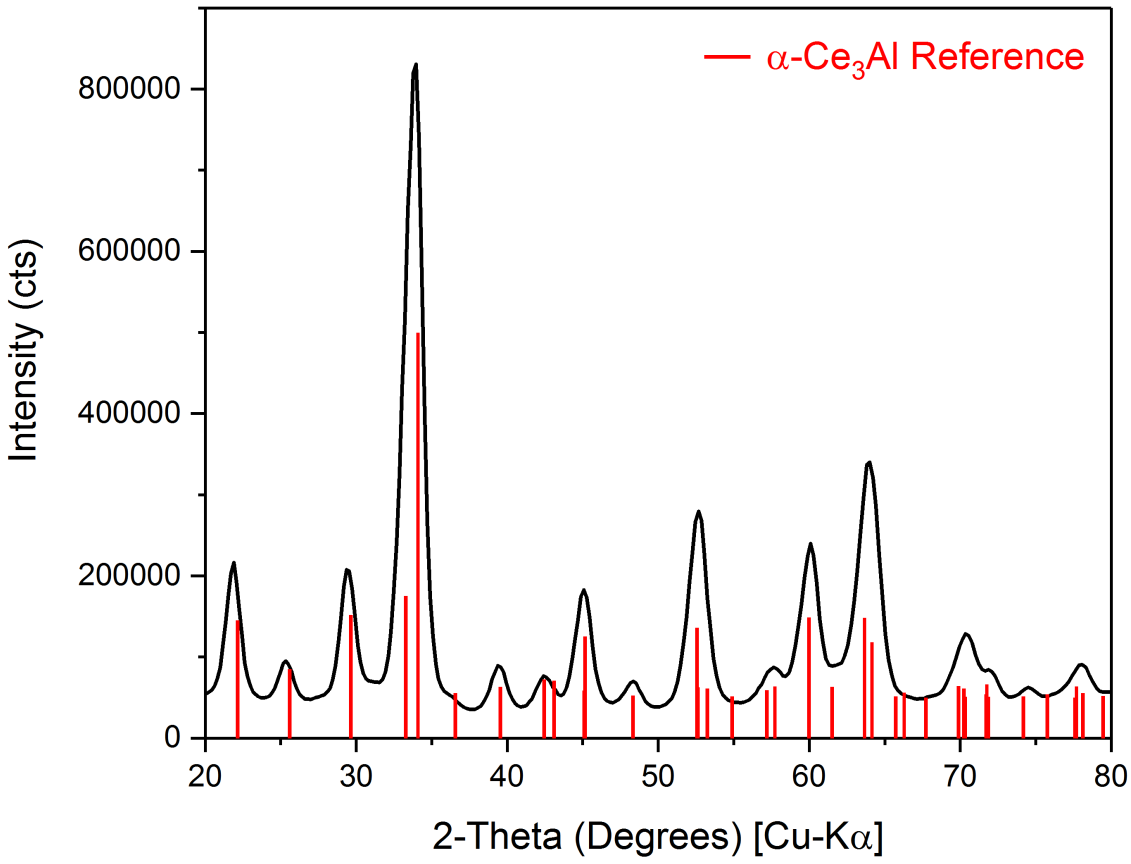

Figure 4.14: XRD trace of the thermally crystallized Ce_3Al MG. The vertical red lines correspond to the hexagonal α-Ce_3Al phase powder diffraction file reference. The sharp peaks which closely match with the reference indicate that thermally crystallizing the Ce_3Al MG results in the formation of the α-Ce_3Al phase.

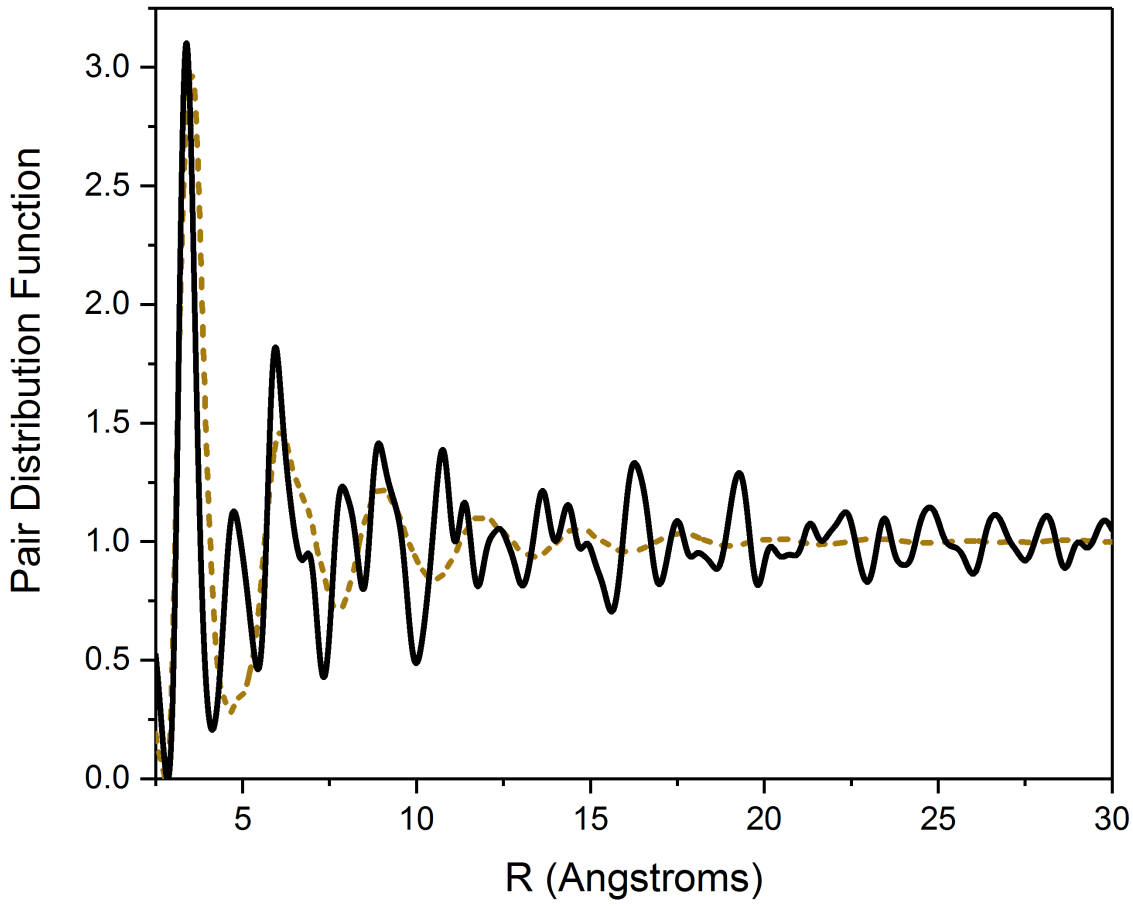

Figure 4.15: PDF trace of the thermally crystallized Ce_3Al ribbon (solid black line) as compared to the initial Ce_3Al MG PDF (dashed olive line). Crystallization is evident as additional peaks appear up to the maximum 30 Å, indicating increased MRO and LRO. Peak broadness is indicative of lattice distortions.

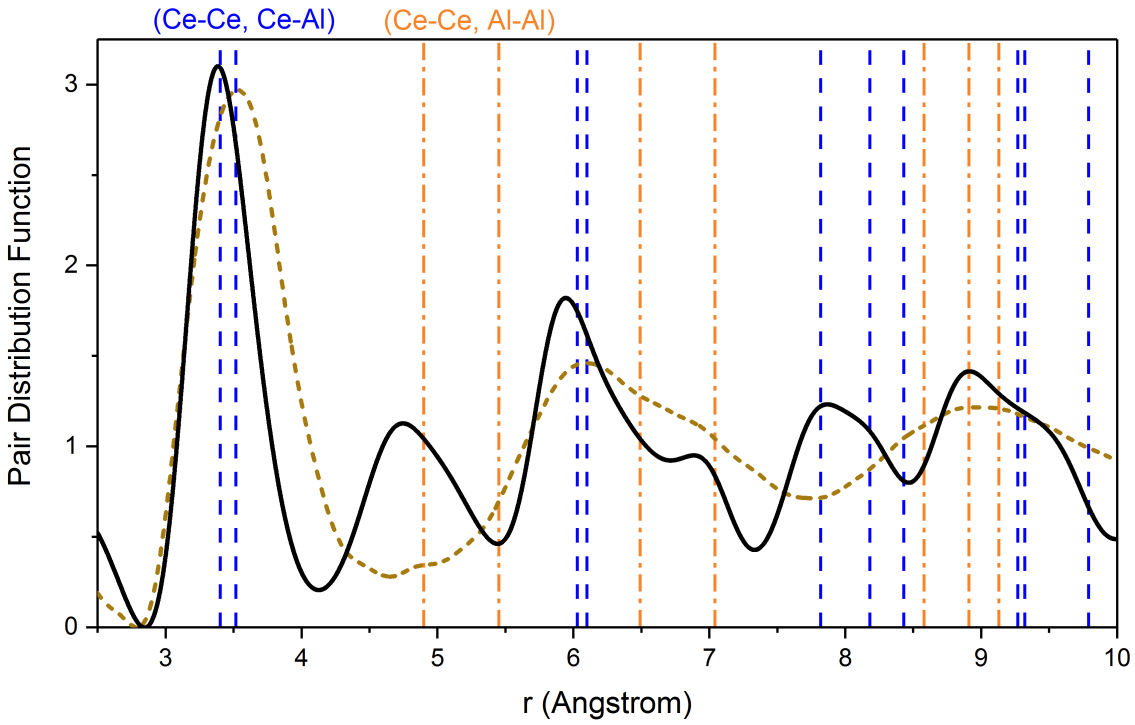

Figure 4.16: Magnified view of the PDF trace of the thermally crystallized Ce_3Al ribbon (solid black line) as compared to the initial Ce_3Al MG PDF (dashed olive line). Reference α-Ce_3Al bond-lengths are overlaid for comparison. The first peak is significantly narrower than the initial MG and shifted to lower radial distances, indicative of a smaller range of bond-lengths and shorter overall bonds for the nearest neighbor SRO. The peak at $4.9\,\text{Å}$ grew into a large peak, indicating an increased occupation of bonds at that length. Larger radial distance peaks from the MG separated into multiple peaks and grew, indicative of the bond order of lattice planes. The bond-lengths appear to be shorter than those of the reference α-Ce_3Al for many of the bonds, potentially indicating the source of observed lattice distortion.

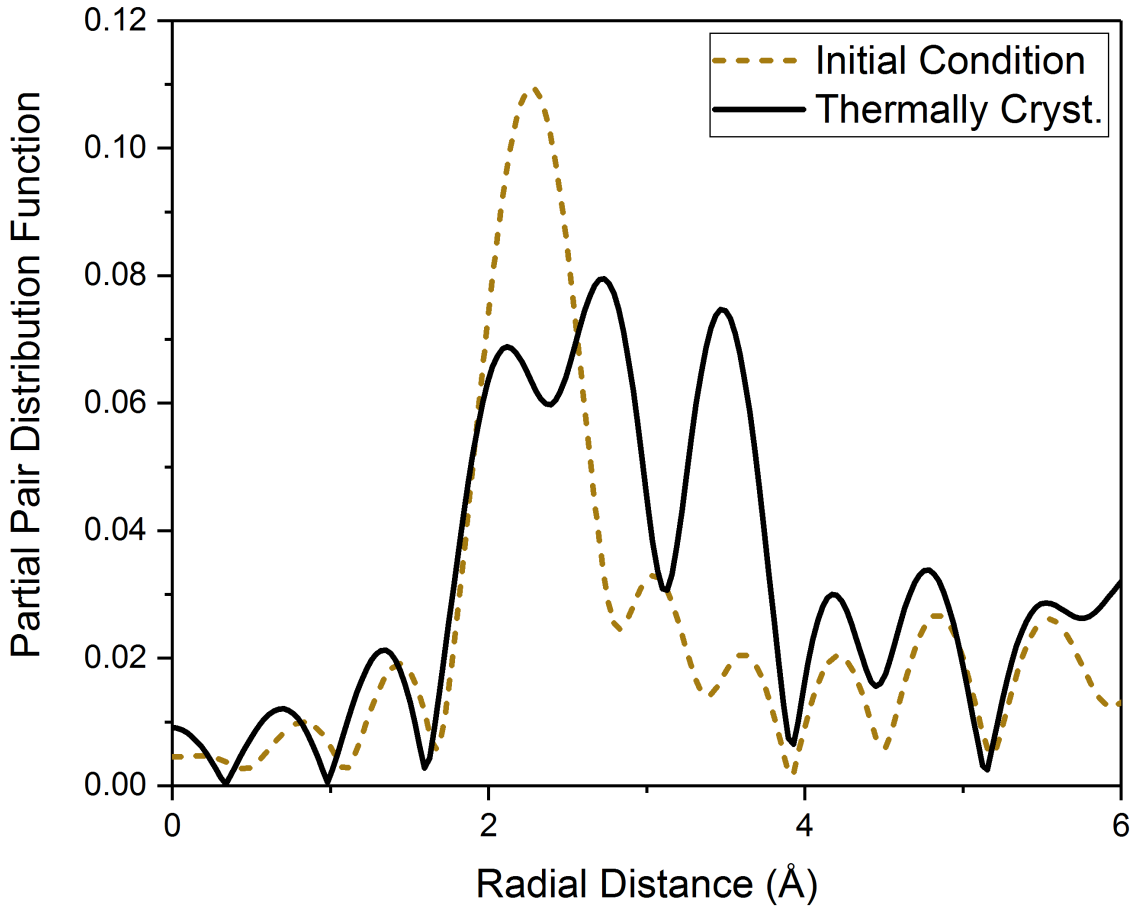

Figure 4.17: Partial PDF trace of the thermally crystallized Ce_3Al ribbon (solid black line) as compared to the initial Ce_3Al MG PDF (dashed olive line) for Ce-based bonds. The first three peaks of the initial PDF shift to lower values with thermal crystallization and amplitude shifts from the first peak into the next two. This is indicative of shorter Ce-Ce and Ce-Al bond lengths, but with a rearrangement of atoms that provides more bonds of a longer type.

4.5 Summary

Thermal characterization of Ce_3Al MG via TGA and DSC heating at rates of 1, 5, 10, 15, and 20 K/min shows crystallization occurring in two stages as is representative of primary crystallization. The analysis indicates that the samples have a low barrier for nucleation as: the reduced glass transition temperature T_{rg} is low at 0.43; there is a low activation energy for the onset of each stage of crystallization at $\sim$157.1 kJ/mol and 113.9 kJ/mol respectively; the frequency factor for crystallization k_0 is high at 4.3×10^{19}; and the activation energy for the onset of crystallization is lower than that for the peak for both stages of crystallization. There appears to be a strong resistance to crystallite growth, however, as the fragility is calculated to be $\sim$11.8. The calculated Avrami and dimensionality constants indicate crystallization occurs throughout the sample in 2D disk-like growth, although this analysis may not be conclusive. The overall results predict that the thermally crystallized structure has very small grain sizes with some anisotropy or texturing. There are no thermal events observed upon reheating the sample after crystallization and cooling, indicating that the crystalline structure is fairly thermally stable and resistant to growth, as predicted from the fragility.

Structural characterization of the thermally crystallized Ce_3Al ribbons was performed using TEM, XRD, PDF, and EXAFS evaluations. Phase characterization results indicate that there is only one phase, the thermodynamically preferred α-Ce_3Al hexagonal phase, after both stages of crystallization are completed. Therefore, the first stage of crystallization likely results in the formation of a metastable phase which converts to α-Ce_3Al during the second stage. The two-step process may be visible in the TEM wherein narrow regions were preferentially thinned during sample preparation as might be expected for limited phase separation during a two-stage crystallization process. Annealing of the samples at 423 K prior to TEM analysis does not appear to have affected the structure; the grain sizes from TEM match those of the XRD. This correlates well with the thermal stability observed

in DSC testing. High resolution bright field TEM analysis indicates that grain growth occurs via 2D crystallization when compared with the reference TEM pattern (shown in Section 2.2.3). Associated anisotropy is observed in the SAED pattern but is not matched in the XRD Rietveld analysis results, indicating differences in the bulk vs local preferred orientations. Bonds appear shorter in the PDF and partial PDF from EXAFS than those of the initial MG and the reference α-Ce_3Al, and these shorter bond lengths correlate with decreased lattice parameters in the Rietveld results. Relatively significant rearrangement is observed in the SRO of the thermally crystallized Ce_3Al phase as compared with the initial MG structure. The PDF shows significant growth of the second peak, and the EXAFS-derived partial PDF shows near equal distribution of atoms across three different bond lengths.

CHAPTER 5

ND:YAG LASER SHOCK COMPRESSION OF CE_3AL METALLIC GLASS

5.1 Overview

Laser shock compression studies on Ce_3Al metallic glass were performed using a $3\,\mathrm{J}$ Nd:YAG laser. Shock-induced crystallization was evidenced by presence of a two-wave particle velocity profile and structural changes revealed by XRD analysis of recovered material. A direct shock-compression setup was designed with $25\,\mu\mathrm{m}$ thick Ni driver foil, $40\,\mu\mathrm{m}$ thick Ce_3Al metallic glass ribbon, and $3\,\mathrm{mm}$ thick PMMA backer window for use with input laser energies varying from 100 to 2000 mJ and corresponding estimated (using a rule of mixtures equation of state for Ce_3Al) peak pressures of 1.4 to 4.1 GPa in Ce_3Al. Below 300 mJ laser input energy and $\sim$1.8 GPa in Ce_3Al, samples were recovered showing no visual or structural changes evidenced via XRD analysis. At input laser energies of 400 mJ and $\sim$1.8 GPa in Ce_3Al and above, samples are recovered showing visible deformation and crystallization evidenced by Rietveld analysis of diffraction patterns obtained from recovered samples. The corresponding velocity profiles also showed a distinct two wave structure, with the secondary wave increasing in magnitude with energy and the primary wave maintaining a constant velocity. The overall results reveal possible densification of the glass due to delocalization of 4f electrons in Ce at lower laser shock energies and pressures and increased crystallization with preferred orientation and distortion of the nanocrystals at higher energies and shock pressures.

5.2 Motivation and Approach

An Nd:YAG laser-driven shock-loading setup was developed, validated, and used to investigate the shock-compression response of Ce_3Al metallic glass. Strain rates achieved with

this loading condition are on the order of 10^6 - 10^7 s^{-1}. The setup allowed for samples to be safely recovered for *post-mortem* characterization via optical microscopy and XRD analysis. Velocity interferometry was also performed to elucidate the characteristics of shock-wave propagation in the amorphous alloy.

Shock-compression experiments on Ce_3Al metallic glass ribbons were performed using the 3 J tunable energy Nd:YAG laser at Georgia Tech described in Section 3.3.1. Laser energies were tuned within the range of 100 to 2000 mJ. For each experiment, the input energy was statistically determined by performing ten measurements of the laser energy at the sample position just prior to the experiment. The Us-Up equation of state (EOS) for Ce_3Al was calculated from the rule of mixtures and using the shock properties of Al and Ce. The calculated Ce_3Al linear Hugoniot EOS $U_s = C_0 + SU_p$ has constants sound speed C_0 = 1600 m/s and shock S = 1.8312. With the density of 6141 kg/m^3, this gives the shock impedance of 9.826×10^6 Pa·s/m.

Figure 5.1(a-d) schematically illustrates the laser setup used for the shock experiments and the various sample configurations that were developed in this work. As shown in Figure 5.1(a), the laser beam is shaped and then focused down to a $\sim$2mm diameter spot size on the back of a sample package. Experiments were first performed on a baseline sample package with a glass substrate, $25\,\mu m$ thick nickel ablator (also serving as the sample), and a PMMA backer window, as shown in Figure 5.1(b). Next, the experiments were repeated with the use of a $50\,\mu m$ thick Ni foil as a reference sample placed between the Ni ablator and PMMA backer, as shown in Figure 5.1(c). The final set of experiments was performed with the $50\,\mu m$ thick Ni foil replaced by $40\,\mu m$ thick Ce_3Al metallic glass ribbon sample as shown in Figure 5.1(d). Comparisons between the sets of experiments were performed by normalizing input laser energy to the spot size and driver material.

The laser-shock-compression experimental setup employed allowed for recovery of the samples with limited secondary shock effects. Recovered samples were characterized using low magnification optical microscopy imaging and synchrotron-based XRD analysis

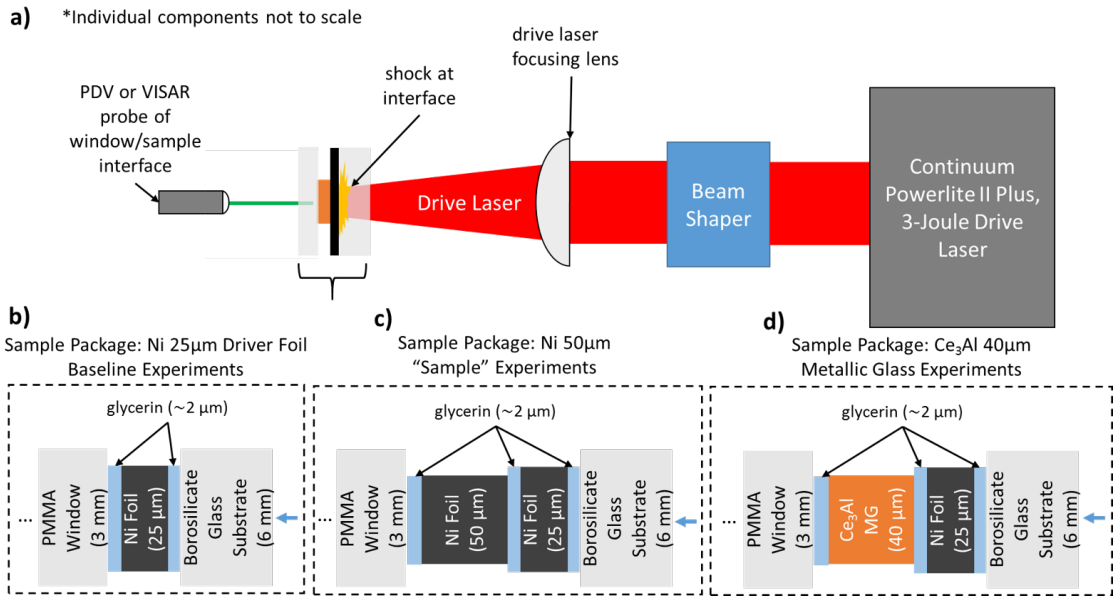

Figure 5.1: (Color Online) Schematics showing (a) Nd:YAG laser table used for direct shock experiments illustrating beam shaping and interferometry diagnostics, (b) sample package used for determining independent response of Ni ablator foil, (c) sample package used with $50\,\mu\mathrm{m}$ thick Ni foil, as reference material, to validate setup and determine thickness effects on wave dissipation, (d) sample package used for $40\,\mu\mathrm{m}$ thick Ce_3Al MG samples. All velocimetry measurements are performed at the PMMA backer interface with sample or driver foil. For each experiment, the Ni driver foil absorbs the laser energy and is ablated, rapidly expanding into a plasma and forming a shock wave which progresses into the sample and/or PMMA backer window.

performed at Brookhaven National Laboratory's NSLS-2 facility, beamline 28-ID-2. Optical microscopy provided macro-scale observations of laser shock-compression induced surface and bulk changes. X-ray diffraction provided atomic and micro-scale information of shock-compression-induced structural changes. X-ray diffraction measurements were performed as described in Section 3.4.1. Simultaneous velocimetry measurements were gathered during shock-compression using either Photon-Doppler Velocimetry (PDV) or Velocity Interferometer System for Any Reflector (VISAR) as described in Section 3.3.1.

5.3 Results

Direct-laser shock-compression experiments provide the ability to perform time-resolved measurements while also safely recovering the shocked samples for *post-mortem* microstruc-

tural characteristics. In this section, the physical and structural state of the recovered samples will be described first, followed by the data obtained from time-resolved interferometry measurements.

5.3.1 Characterization of Recovered State

A total of eight experiments were performed on Ce_3Al MG ribbons, with input laser energies varying from 100 - 2000 mJ. Figure 5.2 shows optical microscopy images illustrating the recovered states of the laser-shocked samples. Depending on the input laser energies, there appear to be three regimes of different visual changes: no visible surface or bulk deformation, visible deformation and surface darkening, and visible deformation with melting and resolidification. For input energies less than 300 mJ, the recovered sample looks identical to the initial state of the starting material, with no obvious surface or bulk deformation. For input energies of 300 - 500 mJ, the rough surface of the MG is visibly smoothed and some dark areas are observed, with the darkened area revealing indentation. For input energies of 1000 to 2000 mJ, the MG sample surface appears rippled and stretched, indicating features characteristic of melting and resolidification.

Figure 5.3 shows the X-ray diffraction traces of the initial metallic glass and the recovered samples after shock compression at laser energies up to 1500 mJ. The 2000 mJ shock-compression experiment resulted in bonding of the MG to the Ni driver foil, contaminating the XRD data, so it is not included. Laser energies below 200 mJ result in samples with amorphous structures seemingly equivalent to the initial unshocked state. At 300 mJ, the shock compression results in a sample with small amounts of very small crystallites, as revealed by the observation of a few broad peaks on an amorphous background. At 400mJ and above, multiple sharper peaks appear, revealing complete crystallization with no amorphous phase visible. The crystalline phase is identified as hexagonal α-Ce_3Al, the thermodynamically stable phase of Ce_3Al, and the first lattice planes are identified with vertical reference lines. As shown in the inset of Figure 5.3, increasing energies result in a

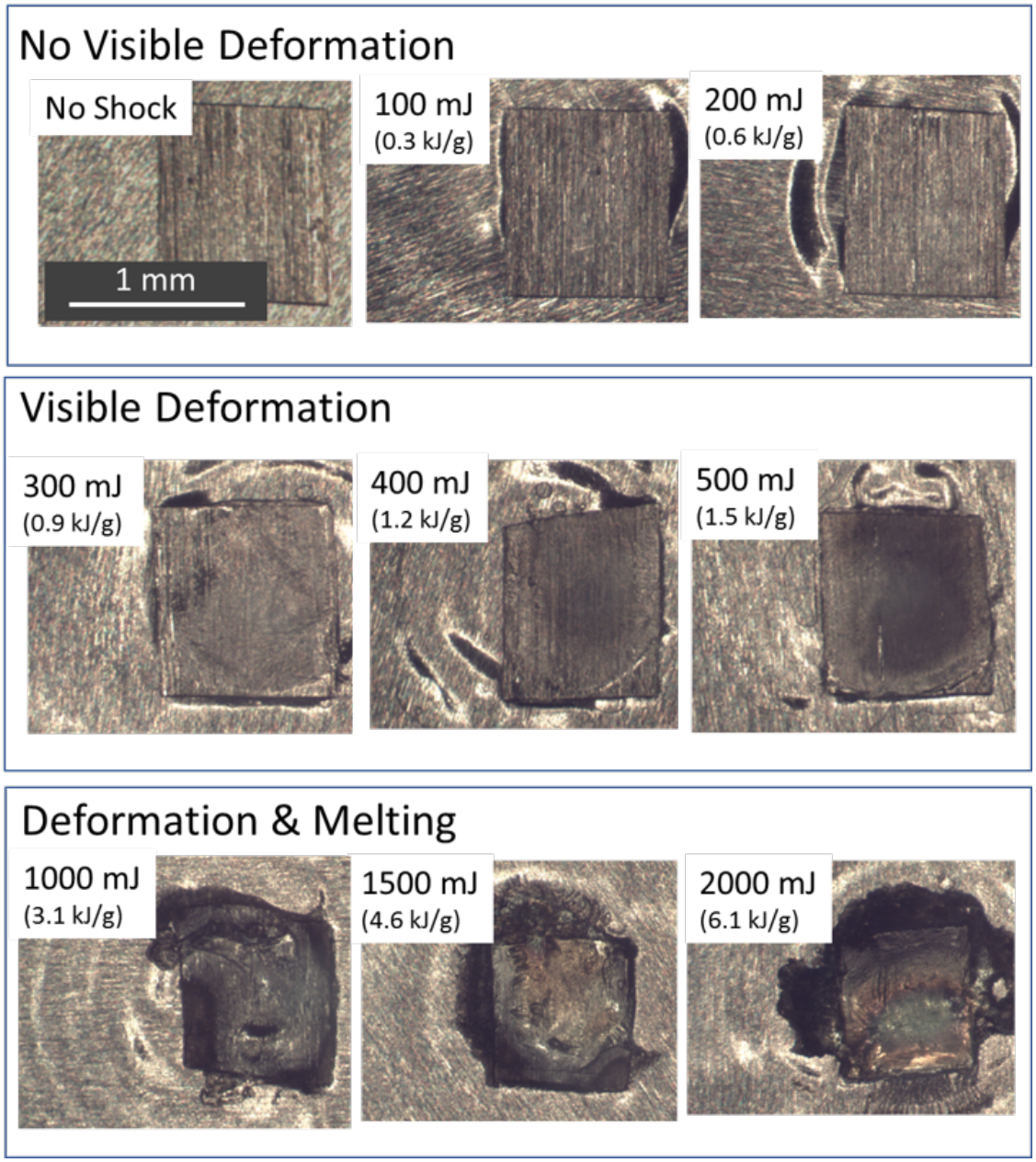

Figure 5.2: (Color Online) Optical microscope images of recovered Ce_3Al MG samples attached to Ni driver foils. Laser energies used for shock compression as well as their values after normalization by mass of irradiated material are indicated in the top left corner of the image. Images are separated based on visual features. No visible changes are observed with input energies up to 200 mJ. For 300 - 500 mJ, the rough surface is visibly smoothed and darkened. For 1000 - 2000 mJ, severe deformation and rippling is observed, with features characteristic of melting and resolidification.

higher angle position for the primary peak and variations in relative peak intensities.

The XRD data was analyzed using Rietveld analysis to obtain additional information

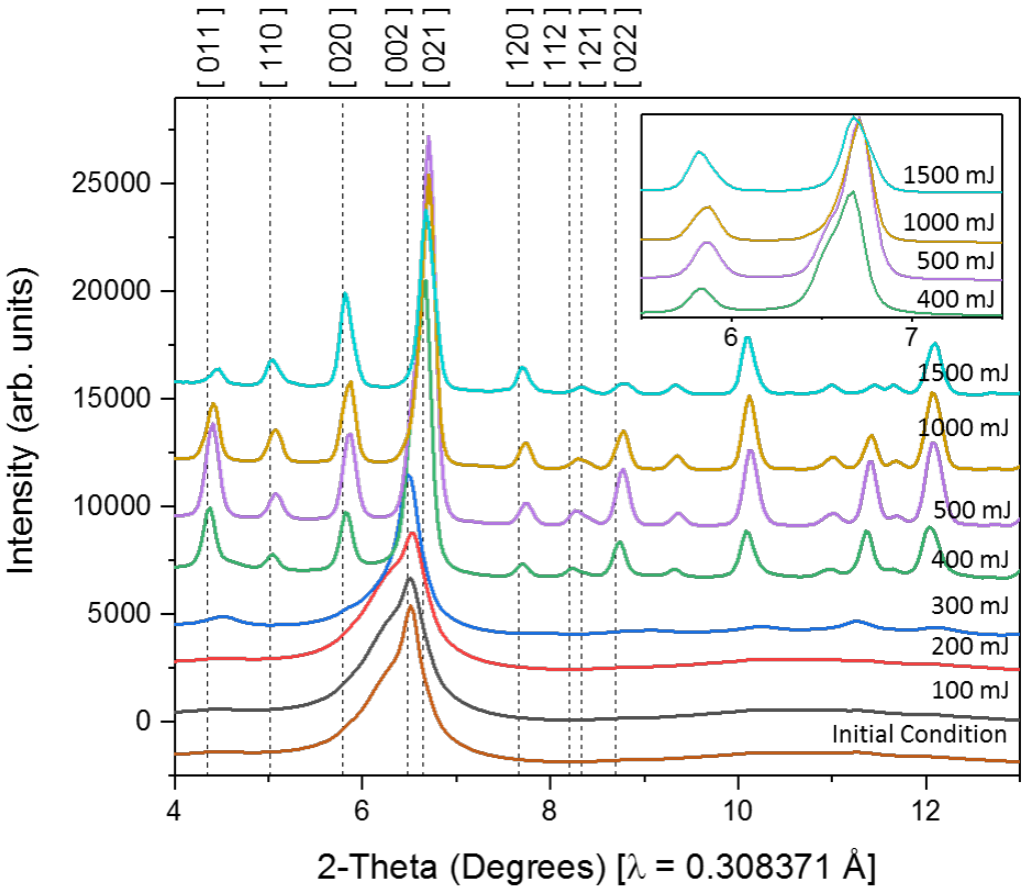

Figure 5.3: (Color Online) X-ray diffraction traces for initial Ce_3Al MG and recovered shock-compressed samples. Corresponding laser energies used for shock compression are listed to the right of each trace. Vertical dashed reference lines are drawn and labeled for the first α-Ce_3Al lattice planes. Inset is magnified view of first two major peaks. Samples remain amorphous with no obvious changes with input laser energies 200 mJ and below. Onset of crystallization is observed at 300 mJ with complete crystallization at 400 mJ and above. Increased input energies appear to first cause the primary peak position to increase in 2θ and then cause relative differences in intensity, indicating texturing.

about the changes in the crystalline phases formed. Table 5.1 illustrates the results from Rietveld analysis of the fully crystalline phases observed with X-ray diffraction. Shock-crystallized samples are found to reveal a 1-2% denser phase with smaller lattice parameters than the equilibrium α-Ce_3Al phase and the grain size on the order of 10 nm. Increasing the laser energy from 400 to 500 mJ increases the density, decreases the amount of preferred orientation, and further decreases the unit cell size. However, increasing the laser energy

from 500 to 1500 mJ increases the amount of preferred orientation and causes the *"a"* lattice parameter to grow while the *"c"* lattice parameter continues to shrink.

Table 5.1: Rietveld analysis results for recovered crystalline-shock-compressed Ce_3Al metallic glass ribbons. The shock-formed α-Ce_3Al phase is more dense, has smaller grain sizes, and has a smaller unit cell than the equilibrium phase. Increasing laser energy from 400 to 500 mJ results in increased density, decreased grain size, decreased preferred orientation, and reduced *"a"* lattice parameter. Increasing laser energy from 500 to 1500 mJ does not further affect density, but it slightly decreases grain size, increases the extent of preferred orientation, and increases the *"a"* lattice parameter. All increases in laser energy reduce the *"c"* lattice parameter.

Sample	Density (g/cm^3)	Grain Size (nm)	Pref. Orient. [hkl] | %	Lattice Param. c | a (Å)
Reference α-Ce_3Al	6.34	100+	0%	5.451 | 7.043
400 mJ Shocked	6.42 ± 0.01	13.2 ± 1.1	[020] | -31 $\pm$ 3%	5.426 ± 0.002 | 7.017 ± 0.002
500 mJ Shocked	6.48 ± 0.01	9.1 ± 0.1	[020] | -11 $\pm$ 2%	5.424 ± 0.002 | 6.986 ± 0.002
1000 mJ Shocked	6.47 ± 0.01	8.3 ± 0.1	[020] | +23 $\pm$ 2%	5.420 ± 0.003 | 6.995 ± 0.002
1500 mJ Shocked	6.48 ± 0.01	8.9 ± 0.4	[020] | +42 $\pm$ 1%	5.390 ± 0.006 | 7.010 ± 0.003

5.3.2 Time-Resolved Velocimetry Measurements

The direct laser shock experiments were performed using three different sample configurations as shown in Figure 5.1 (with Ni driver foil, Ni driver and Ni sample (as reference), and Ni driver with the metallic glass sample), and also employing velocity interferometry measurements of particle velocity. The measured velocimetry profiles for each setup under similar direct laser shock loading conditions were compared to elucidate potential deviations from expected responses in the Ce_3Al metallic glass samples. For each configuration, experiments were performed over $\sim$100 to $\sim$2000 mJ, the range of input laser energies achievable with the 3 J Nd:YAG laser (accounting for loss from optics).

$25\,\mu m$ *Ni Driver Foil Baseline Experiments*

The first configuration was used to determine the baseline response of the driver foil to different input laser energies. Figure 5.4 presents a representative particle velocity response time-synchronized with the intensity-time profile of the input laser pulse utilized with these experiments. It can be seen that the laser intensity profile and the particle velocity illustrate similar rise times. Time-resolved PDV measurements captured at the Ni driver and PMMA backer interface in the form of particle velocity profiles for all experiments are shown in Figure 5.5. As expected, the peak particle velocity at the interface between nickel and PMMA window increases as input laser energy increases. Other than reverberations due to ringing, no characteristic signatures are observed in the measured velocimetry profiles. Rise time to peak velocity was measured to be $\sim$5 ns for input energies above 500 mJ and $\sim$25ns for 100 mJ input energy. The PDV resolution might be too limited to detect meaningful details for the 100 and 250 mJ velocity traces. With input energies above 500 mJ, the particle velocity is observed to ring up to its maximum value over two oscillations, taking a total of $\sim$13 ns to reach peak velocity. The corresponding rise time for the input laser profile shown in Fig 5.4 is $\sim$11 ns to reach peak energy, and it remains at that energy for $\sim$11 ns indicating (after taking into account ringing up to peak particle velocity) that rise time data for the $25\,\mu m$ Ni driver foil matches relatively well with the laser pulse.

The inset in Figure 5.5 illustrates the conservative method used for determining the peak particle velocity from a representative trace. Maximum velocities were measured at the peak velocity and minimum at the trough of a secondary oscillation. Average values were taken between these two with the standard deviation defined based on the maximum and minimum values.

The peak particle velocities thus obtained for direct shock loading of $25\,\mu m$ Ni driver plotted as a function of the input energy (normalized by mass of irradiated Ni) are shown in Figure 5.6. A general power law trend showing an increase in measured particle velocity as a function of normalized input energy, following the direct transfer of laser energy to

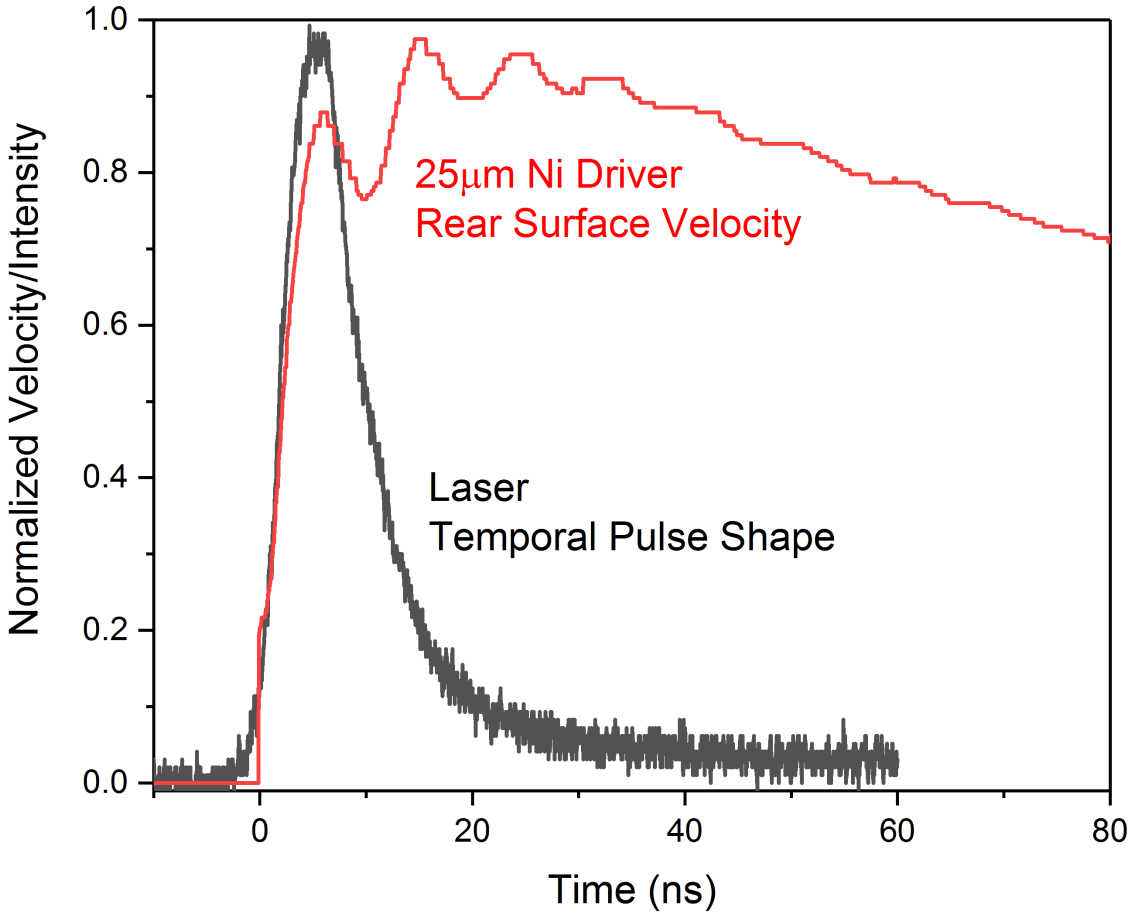

Figure 5.4: Representative profiles of the laser-driven shock-induced velocity profile at the $25\,\mu\mathrm{m}$ Ni driver foil rear interface with PMMA and temporal pulse shape of the drive laser. The velocity profile plotted was for 1000 mJ input laser energy. The PDV resolution precludes capture of the entire release.

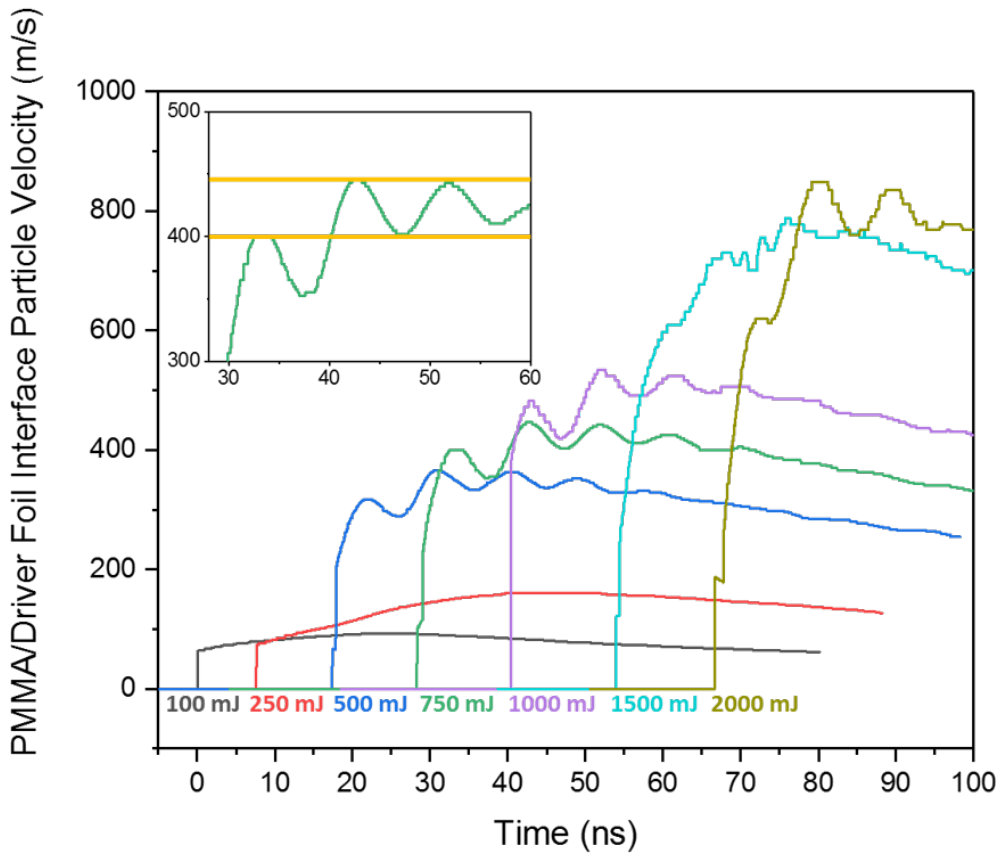

Figure 5.5: (Color Online) Particle velocity data measured at the interface between PMMA window and $25\,\mu m$ Ni driver foil at varying laser energies. At energies above 500 mJ, velocity profiles were observed to show ring up by the second oscillation. Inset shows how the peak velocity and its error was determined for the representative 750 mJ experiment. Bands at the peak velocity and subsequent trough define the maximum and minimum velocity values recorded.

kinetic energy [250], is observed and the representative equation is included in the plot. The corresponding maximum in pressure is found to be 20.9 GPa with input energy of 6.4 kJ/g.

$50\,\mu m$ *Ni Reference Sample Experiments*

The next experimental setup involved the use of a $50\,\mu m$ thick Ni sample (reference) placed between the $25\,\mu m$ Ni driver and PMMA window. Figure 5.7 presents a representative velocity response time synchronized with input laser pulse utilized with these experiments.

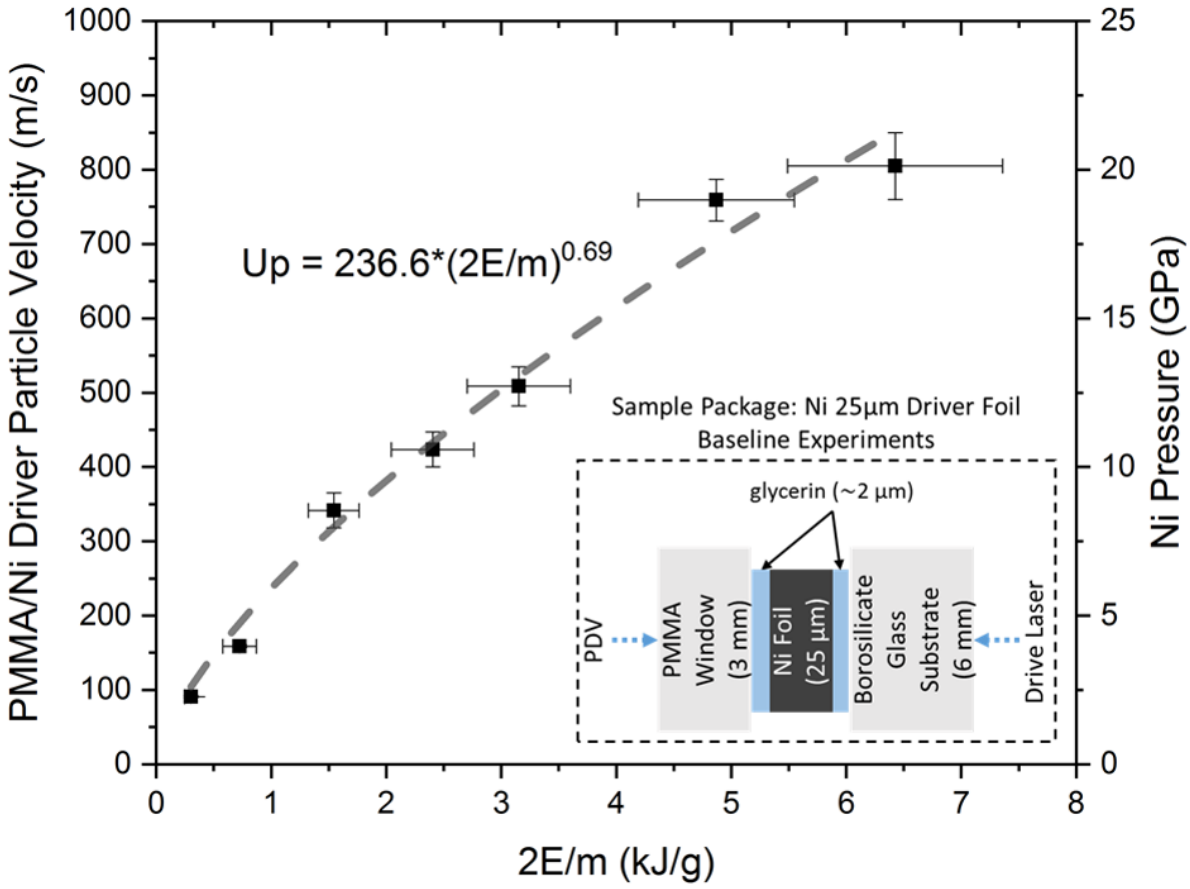

Figure 5.6: (Color Online) Peak particle velocity data for interface between PMMA window and $25\,\mu\mathrm{m}$ Ni driver foil as a function of input laser energy, normalized by mass of irradiated material. Overall relation follows a power law, traced with dashed line and defined by the indicated equation. Inset shows experimental sample package setup for these experiments.

PDV particle velocity profiles from experiments performed using this configuration with input energies from ~100 to ~2000 mJ are plotted in Figure 5.8. Unlike the $25\,\mu\mathrm{m}$ Ni driver and PMMA backer experiments, the experiments with the $50\,\mu\mathrm{m}$ Ni sample do not show the ringing up features, indicating that the peak pressures are reached without combination of reflected waves. There are also no observable characteristic signatures present in the wave front captured by the PDV. The peak velocities increase with increasing laser input energy; the rate of increase decreases above 1000 mJ. It is also observed that the peaks narrow in duration as increasing velocities decrease the wave transit time. The inset image in Fig. 5.8 illustrates the method used for peak velocity and error determination. Overall velocity

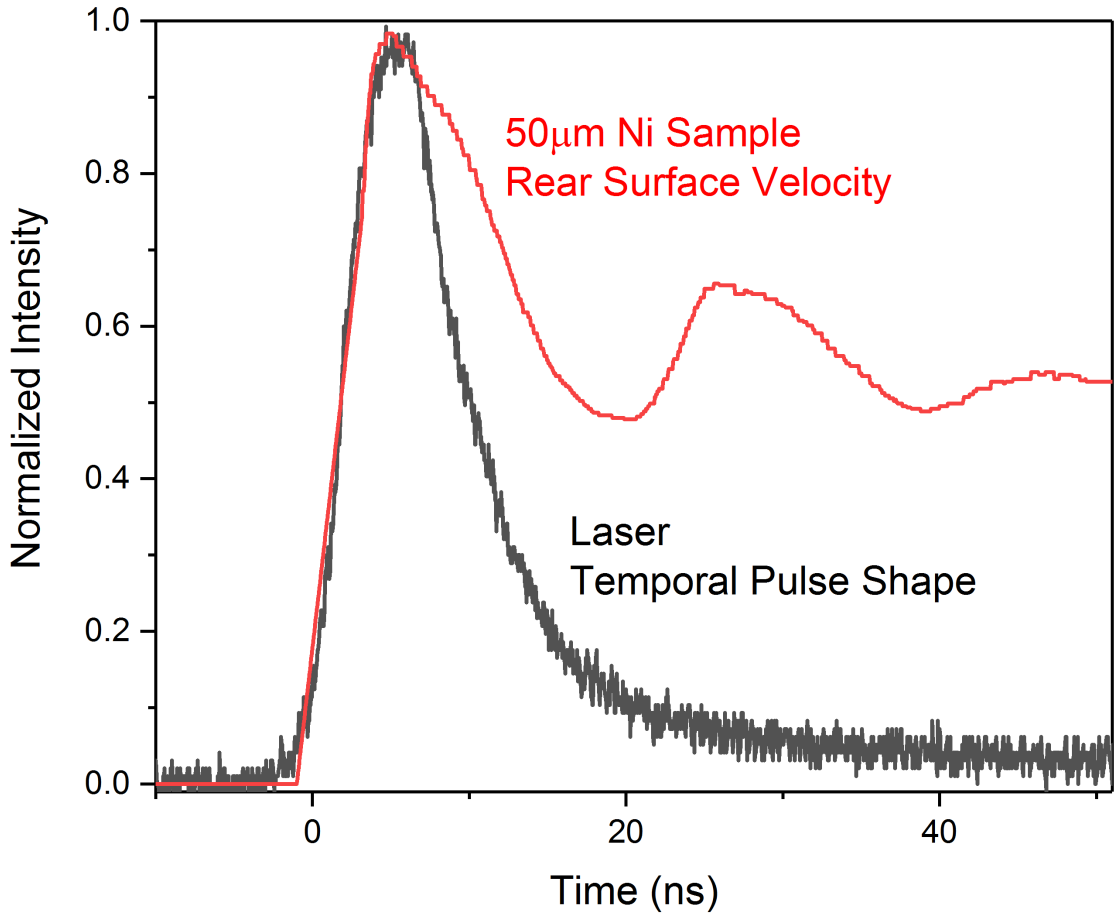

Figure 5.7: Representative profiles of the laser-driven shock-induced velocity profile at the $50\,\mu\mathrm{m}$ Ni reference sample rear interface with PMMA and temporal pulse shape of the drive laser. The velocity profile plotted was for 1000 mJ input laser energy. The PDV resolution precludes capture of the entire release.

trends determined using the wavelet and fast Fourier transform analyses were compared and averaged, with weighting given to the trends that had fewer erroneous deviations. Peak particle velocity values were determined from the average peak velocity and error was determined by averaging the error from each of the analysis techniques.

Figure 5.9 plots the peak particle velocities for the $50\,\mu\mathrm{m}$ Ni sample (reference) as a function of the corresponding input energies, normalized by mass of irradiated material. Compared to the experiments with only the $25\,\mu\mathrm{m}$ Ni driver, the maximum particle velocities in the Ni sample reference are reached at a lower input energy, and the peak velocities are lower, diverging downwards from the power law trend. The differences potentially cor-

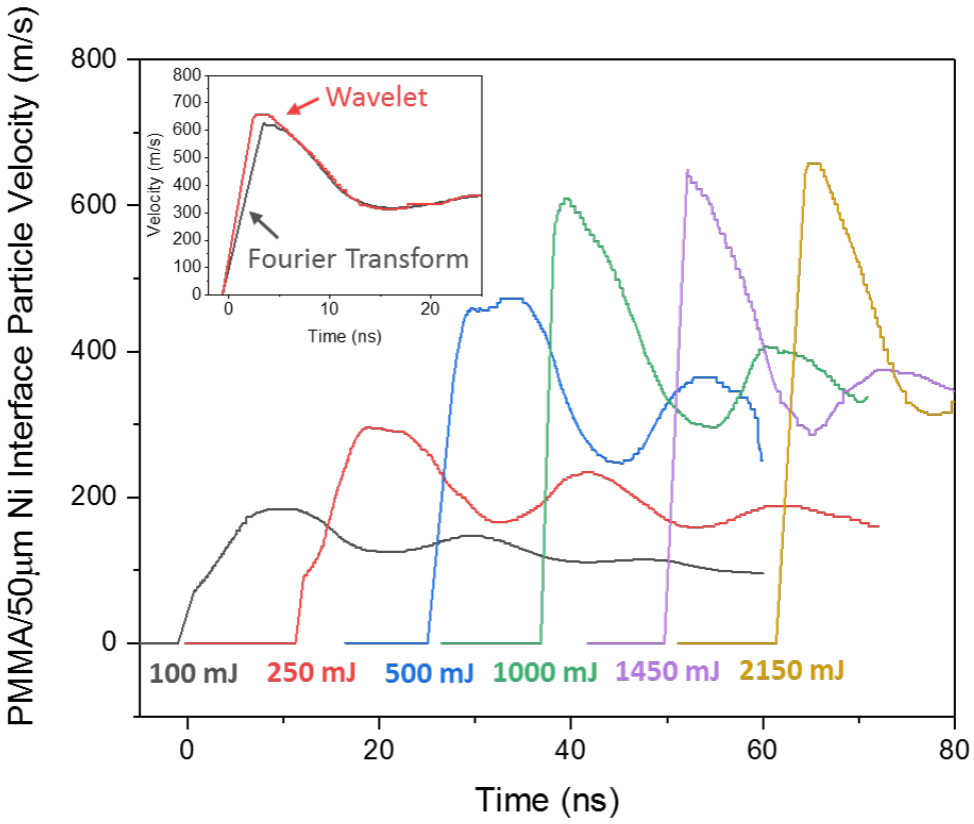

Figure 5.8: (Color Online) Selected velocimetry data for the interface between PMMA window and $50\,\mu m$ Ni sample (as reference) driven by the Nd:YAG laser at varying energies. No ringing up is visible. Velocities increase as input energy increases. At 1000 mJ and above, increasing the input energy has a marginal effect on increased peak particle velocity. Inset image illustrates effects of different statistical analysis techniques on peak shape and maximum velocity. Peak particle velocity values were averaged between the different techniques, and error was determined by averaging the error from the different techniques.

respond to the dissipation of the wave as it propagates from the driver to the Ni sample with glycerin in-between. The dissipation would be a result of the sample thickness, intrinsic material properties, and the input laser-induced pressure pulse shape. The high laser energy differences in the trend could also be due to breakdown of the glass substrate. The corresponding maximum in pressure with input laser energies in the range of 4.8 - 6.9 kJ/g is found to be 16.2 GPa.

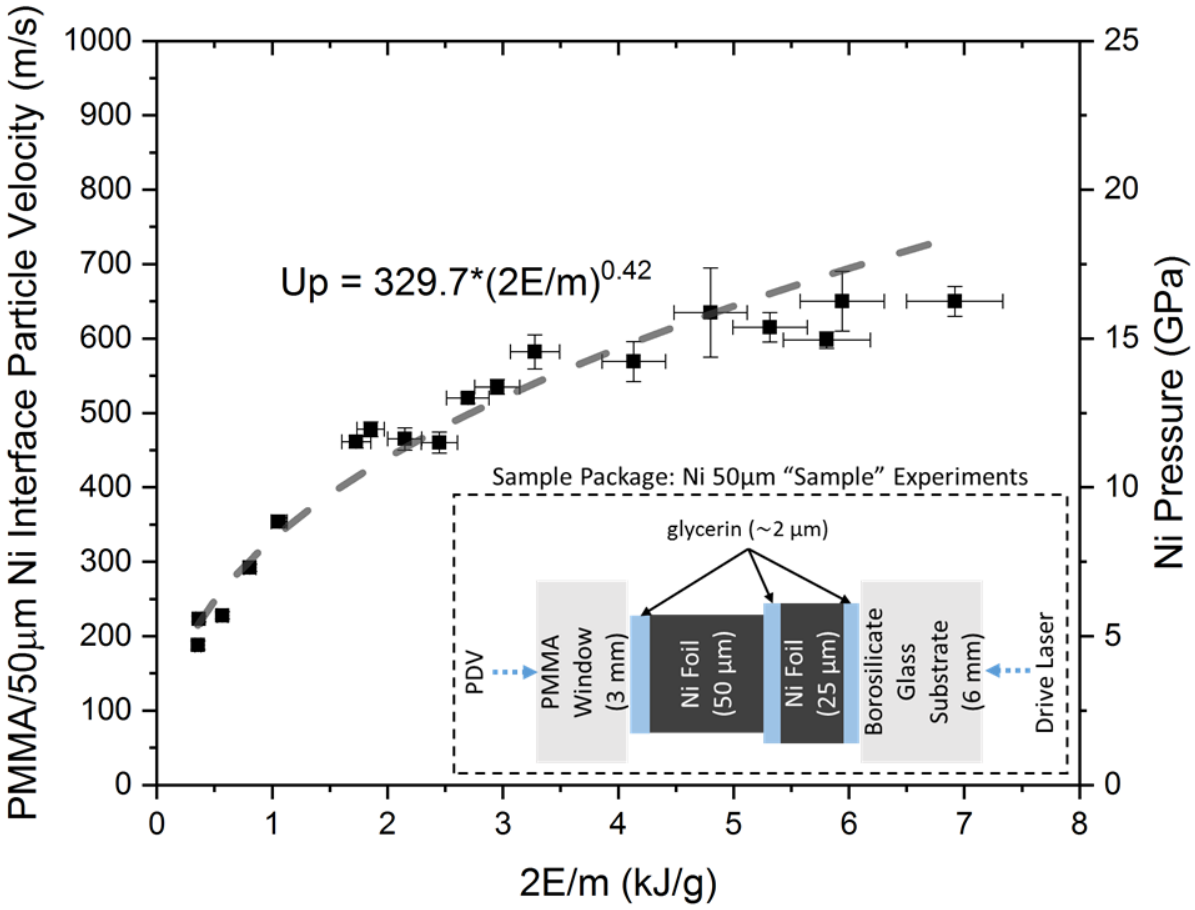

Figure 5.9: (Color Online) Peak particle velocity data for interface between PMMA window and $50\,\mu m$ Ni sample (as reference) as a function of input laser energy, normalized by mass of irradiated material. The velocities match well with those for only the $25\,\mu m$ Ni driver at input energies below 1 kJ/g but are noticeably lower than predicted by the power law trend (dashed line and equation) at higher energies. The deviations are indicative of energy saturation or wave dissipation effects within the $50\,\mu m$ Ni or glass substrate breakdown at high laser energies. Inset shows experimental sample package setup for these experiments.

$40\,\mu m$ *Ce_3Al MG Experiments*

The main set of experiments were performed with the $40\,\mu m$ thick Ce_3Al metallic glass samples sandwiched between the Ni-driver and PMMA window, as shown in Figure 5.1(d). The laser shock experiments were performed for input energies from ~100 to ~2000 mJ. Velocimetry measurements were done using VISAR, allowing for higher temporal resolution measurements of the particle velocity profiles. Figure 5.10 presents a representative

velocity response time synchronized with the input laser pulse utilized with these experiments. The inset shows a magnified view of the initial rise behavior for the laser and velocity profile. The VISAR velocity profiles plotted in Figure 5.11 show a two-wave structure, unlike that observed in the previous case of the Ni sample sandwiched between the Ni-driver and PMMA window. The two-wave structure in Figure 5.11 is seen to continue to evolve with increases in laser energy from 100 to 500 mJ and appears to be a direct consequence of material change. With further increases in laser energy, the magnitude of the first wave remains constant while the magnitude (peak) of the second wave continues to increase.

Figure 5.12 plots the variations of the peak values of the corresponding wave velocities as a function of input energy, normalized by mass of irradiated material. It can be seen that the magnitude of the first wave particle velocity and corresponding pressure is constant, approaching 2 GPa, while that of the second wave increases with increasing energy to about 4 GPa. The peak particle velocities and pressure are lower than that measured with the configuration employing the Ni sample (reference) sandwiched between the Ni driver and PMMA backer.

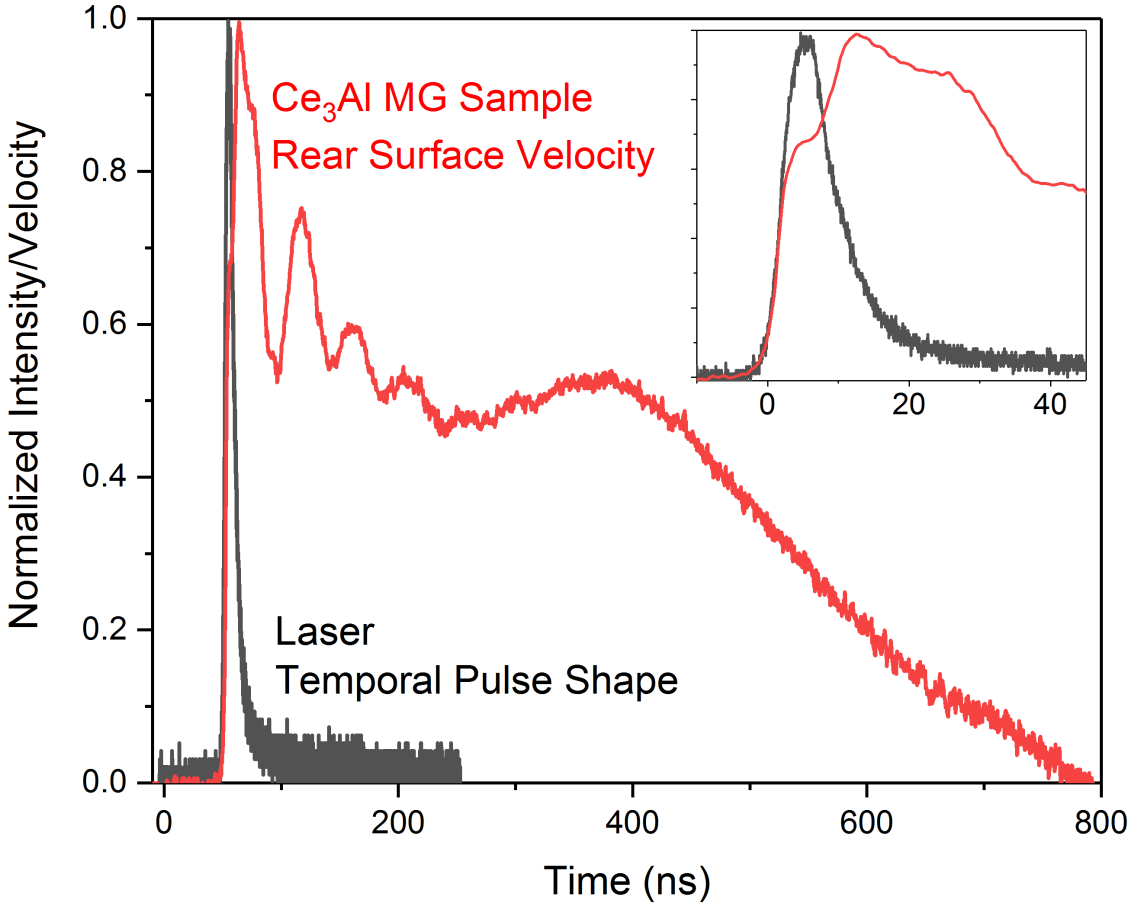

Figure 5.10: Representative profiles of the laser-driven shock-induced velocity profile at the $40\,\mu\mathrm{m}$ Ce_3Al MG sample rear interface with PMMA and temporal pulse shape of the drive laser. The velocity profile plotted was for 1000 mJ input laser energy. Inset shows a magnified view of the initial rise in the laser intensity and associated particle velocity profile.

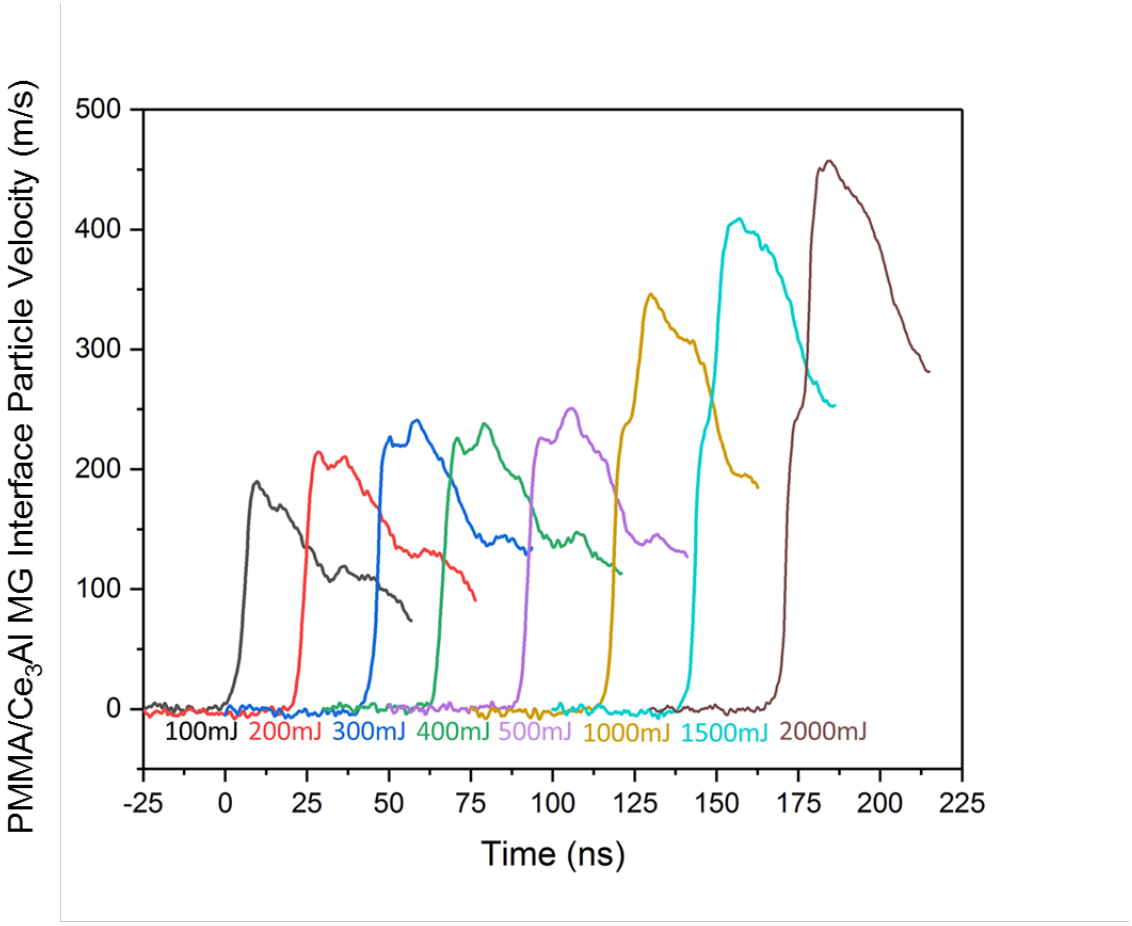

Figure 5.11: (Color Online) VISAR wave profiles for laser shock compression experiments performed on Ce_3Al MG samples sandwiched between Ni-driver and PMMA window with laser energies from $\sim$100 to $\sim$2000 mJ. The wave profiles illustrate a two-wave structure with the peak magnitude of the second wave increasing with increasing laser energy.

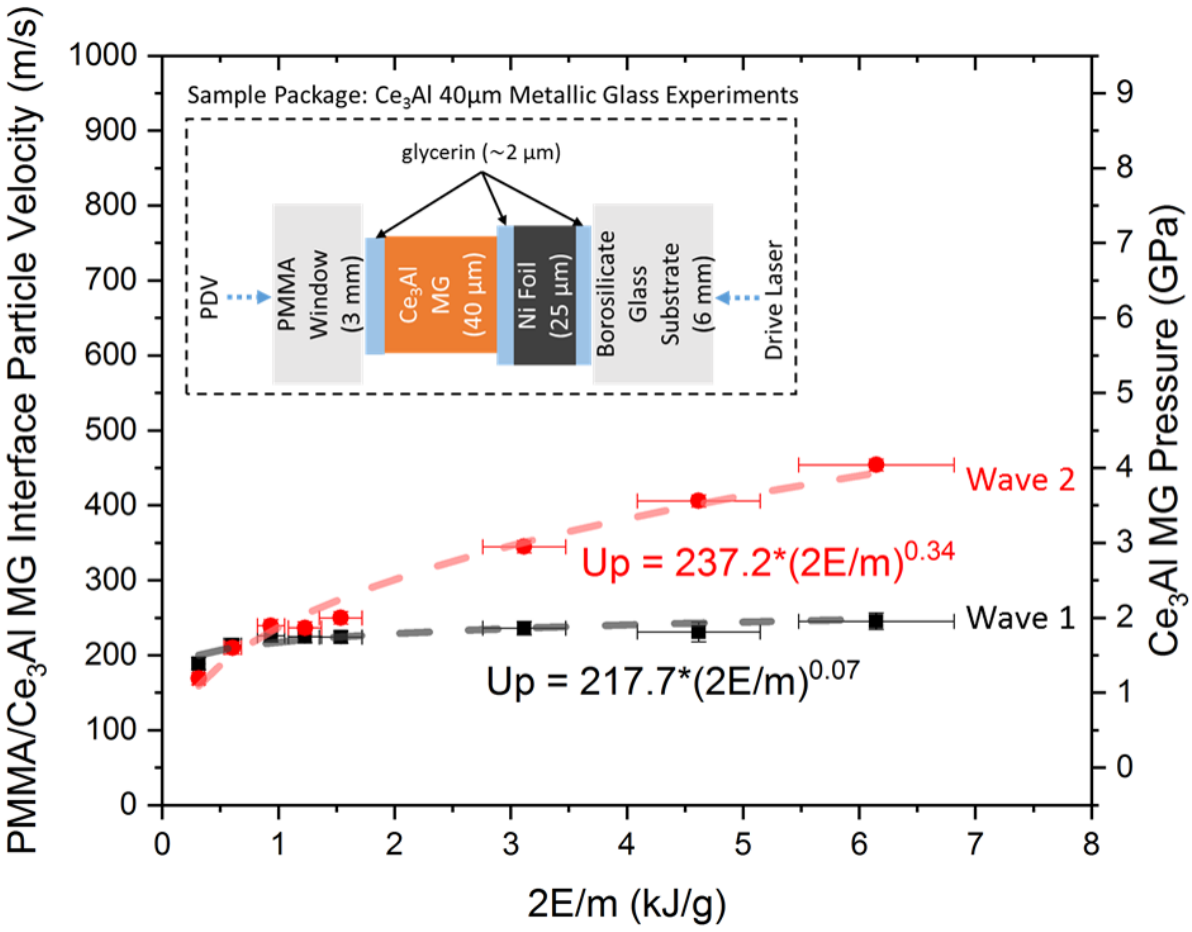

Figure 5.12: (Color Online) Peak particle velocity data for interface between PMMA window and $40\,\mu\mathrm{m}$ Ce_3Al MG sample as a function of input laser energy, normalized by mass of irradiated material. Particle velocity and corresponding pressure of each wave is plotted separately, with that of the first wave represented as squares and the peak of the second wave as circles. Each follows a different trend, as shown with dashed lines and equations. The first wave peak velocity rises quickly to a maximum and then stays constant at input energy above 400 mJ or ~1.2 kJ/g. The measured data for the second waves shows a continuous increase, although the peak values are lower than those for the Ni sample and Ni driver setup. Inset shows experimental sample package setup for these experiments.

5.4 Discussion of Results

Direct laser shock-compression of a Ni foil results in particle velocity and corresponding pressure increasing as a power law relationship as a function of laser energy. With the placement of a $50\,\mu\mathrm{m}$ Ni foil in contact with the Ni driver, the increase in velocity and corresponding pressure shows a similar continuous but subdued increase, relative to a power law trend. The deviation from the power law trend is seen more at higher energies above 1000 mJ, possibly due to laser energy saturation of the glass substrate or stress dissipation effects. Shock compression of the Ce_3Al MG sample placed in contact with the Ni driver also shows a continuous increase in peak particle velocity and corresponding pressure similar to the trend in the case of the Ni sample and driver. However, the particle velocity profile for the MG sample exhibits a two wave structure, with the magnitude of the first wave remaining constant at $\sim$2 GPa and that of the second wave increasing with laser energy. The magnitude of the peak velocity (and pressure) in the case of the MG sample is lower than it is for the Ni sample and Ni driver configuration. The peak pressure reached with the Ce_3Al MG is $\sim$4 GPa with the corresponding normalized input energy of 6 kJ/g, relative to the peak Ni pressure of $\sim$16.2 GPa (in the case of the Ni sample at the same normalized energy). The difference in the peak pressures is possibly an effect of the higher impedance of Ni relative to Ce_3Al. However, the occurrence of the two-wave structure in the Ce_3Al MG sample is indicative of a change of state from elastic to plastic and/or a phase change to a denser glassy or crystalline phase.

First Wave Effects and Meaning

Optical microscopy and XRD analysis of recovered samples at input laser energies of 100 and 200 mJ, respectively, reveal no visible deformation in the images (Fig 5.2) nor structural changes as evident from XRD peaks (Fig 5.3).

The two-wave structure captured in the wave velocity profiles (Fig 5.11) imply that

the first wave is akin to an elastic precursor event or represents densification of the metallic glass structure. Similar densification and polyamorphization yielding a higher density glassy state has also been observed in Zr-based BMG [35]. Chen et. al. [37] observed a $\sim$7% volume reduction of Ce_3Al MG upon shock compression at $\sim$2.3 GPa.

The role of Ce 4f delocalization in the observed effects is unclear. Densification may occur from both shear-driven reorganizations and 4f delocalization. Additionally, Ce 4f delocalization may also affect crystallization. As shown in the XRD Rietveld analysis results of recovered samples in Table 5.1, initially the overall density is greater than that of the reference sample of the same phase even though the grain size is much smaller - on the order of 10 nm. The increased density may be indicative of a Ce 4f delocalization effect. In this case, the Ce atoms effectively "shrink" during shock compression, and potentially rearrange into a denser form of the crystalline phase, and upon release are "trapped" in this denser arrangement. Indeed, as input laser energy increases from 400 to 500 mJ, the density increases further by $\sim$1%, which may indicate the Ce 4f delocalization is incomplete with the 400 mJ input energy, and, in all conditions, the unit cell is smaller than that of the reference.

Second Wave Effects and Meaning

For input laser energies above 300 mJ, there is visible deformation as seen in the images (Fig 5.2) and crystallization into α-Ce_3Al, as revealed by the multiple peaks seen in the XRD profiles in Fig 5.3. This is the first such observation of shock-compression-induced crystallization of the Ce_3Al MG into α-Ce_3Al.

Correspondingly, the VISAR profiles reveal a continuous increase in peak particle velocity (and corresponding pressure) while the first wave velocity remains constant which implies that the plastic deformation at pressures exceeding the elastic precursor in the Ce_3Al MG is occurring via concomitant crystallization.

Rietveld analysis of the density of samples at higher shock pressures (input laser en-

ergy of 1000 and 1500 mJ) illustrates that the density no longer increases, but instead the preferred orientation of the crystals increases in the [020] direction and the unit cell similarly stretches in the *"a"* direction. The extreme state of deformation and even possible melting of recovered samples (Fig 5.2) indicates competing effects of increased temperature and possibly shear bands and 4f delocalization being maximized, with no further "shrinkage" occurring with increased input energy. The increase in preferred orientation and unit cell distortion with larger input energies may represent a transition in the mechanism, wherein more crystallization of the type resulting in formation of nanocrystals with elongated shapes is occurring [18].

5.5 Summary

Laser-driven shock-compression experiments incorporating velocimetry and soft recovery were performed on Ce_3Al metallic glass ribbon samples. Velocity interferometry measurements indicate a two-wave particle velocity profile, with the first (precursor) wave most likely representing atomic densification of the glassy alloy. At shock conditions above the constant magnitude of this precursor wave, the velocity profiles show increasing peak velocity. The recovered samples show evidence of permanent deformation and X-ray diffraction patterns indicate formation of crystalline states. The results reveal possible densification of the glassy state during shock-compression at laser energies up to about 500 mJ (2 GPa pressure), and shock-induced crystallization followed by preferred orientation of nanocrystals at higher pressures.

CHAPTER 6

OMEGA LASER SHOCK COMPRESSION OF CE_3AL METALLIC GLASS

6.1 Overview

Shock-compression experiments were performed on Ce_3Al metallic glass melt-spun ribbons using the 50J laser shock loading system at the Omega laser facility. A multi-layered sample of $2\mathrm{mm}$ total thickness composed of stacks of $1\mathrm{mm}$ x $1.5\mathrm{mm}$ width and $40\mu\mathrm{m}$ thick ribbons bonded with $6\mu\mathrm{m}$ epoxy was used as the target in order to study the effects on the structural response of Ce_3Al metallic glass. Shock-induced changes were characterized *post-mortem* via high-intensity synchrotron x-ray diffraction (XRD) and extended x-ray absorption fine structure (EXAFS) analyses to obtain pair distribution functions (PDFs) in real space and structure factors in reciprocal space. The samples were observed to have visible deformation and increasing medium-range to long-range order evolution as deformation and input shock pressures increased. At farther distances from the initial shock, no visible deformation was observed and the samples were observed to remain generally amorphous, although they appeared to show short and medium-range ordering towards denser overall structures. The characteristics of the density and bond length changes in recovered shock-compressed samples were correlated to input conditions and discussed with respect to potential mechanistic processes associated with the evolving structural changes.

6.2 Motivation and Approach

This chapter will focus on the characterization of the structural effects of Omega laser-induced high-pressure shock compression of a stacked Ce_3Al metallic glass sample. The Omega laser at the Laboratory for Laser Energetics was utilized with a recovery setup wherein a thick sandwiched (stacked) sample is shocked, allowing for dispersion and de-

creasing pressures through the thickness, similar to the setup previously utilized to study the effects of shock compression in a single block of Ta [247]. Densification of the amorphous state via SRO and MRO changes and subsequent evolution of more medium-range and then long-range order was observed with increased pressure. The emphasis of sample characterization was placed on two regimes: areas near the initial loading and areas further away. The evolving short-, medium-, and long-range structural characteristics present in the recovered samples were then correlated with the general trend of the varying shock pressure.

Figure 6.1 schematically illustrates the setup used for performing the shock-compression recovery experiments at the Laboratory for Laser Energetics using the 50 J Omega laser. The overall setup, including the sample stack encased in the recovery tube and the connector to the Omega mount, is shown in Fig. 6.1(a). The circled region of Fig. 6.1(a) is expanded in Fig. 6.1(b) for further detail. It shows the stainless steel washers used to hold the stack in the recovery mount and the $2.5\,\mathrm{mm}$ opening in the front washer through which the laser beam was directed; the $300\,\mu\mathrm{m}$ thick polystyrene polymer reservoir used as a sacrificial laser ablator; and the $2\,\mathrm{mm}$ stack of $40\,\mu\mathrm{m}$ thick Ce_3Al MG samples, held together with $6\,\mu\mathrm{m}$ thick epoxy layers. Figure 6.1(c) shows a plot of the pressure calculated using one dimensional Hyades hydrodynamic code as a function of depth across the stacked sample layers.

Unlike the uniaxial-strain state achieved during shock-compression of individual Ce_3Al MG samples using the 3 J Nd:YAG lser, the shock loading with the Omega laser generates more complex and extreme states in the stacked layers of the MG samples. The pressure variation plotted as a function of the layer number in Figure 6.1(c) is only a qualitative representation illustrating the nature of pressure decrease in layers in the stack, calculated using an assumed equation of state of the MG sample and approximation of one-dimensional shock propagation as the laser interacts with the polymer buffer. It can be seen that initially the pressure decreases almost asymptotically through the first $\sim$10 layers and then more

gradually across the rest of the stacked layers. It should be noted that it will not be possible to make a direct comparison of the effects observed due to the loading conditions achieved with the Omega laser and those imposed with the Nd:YAG laser, although it is obvious that the sample layers in the front part of the stack in the Omega laser experiments are imposed to more extreme conditions than those generated with the 3 J Nd:YAG laser.

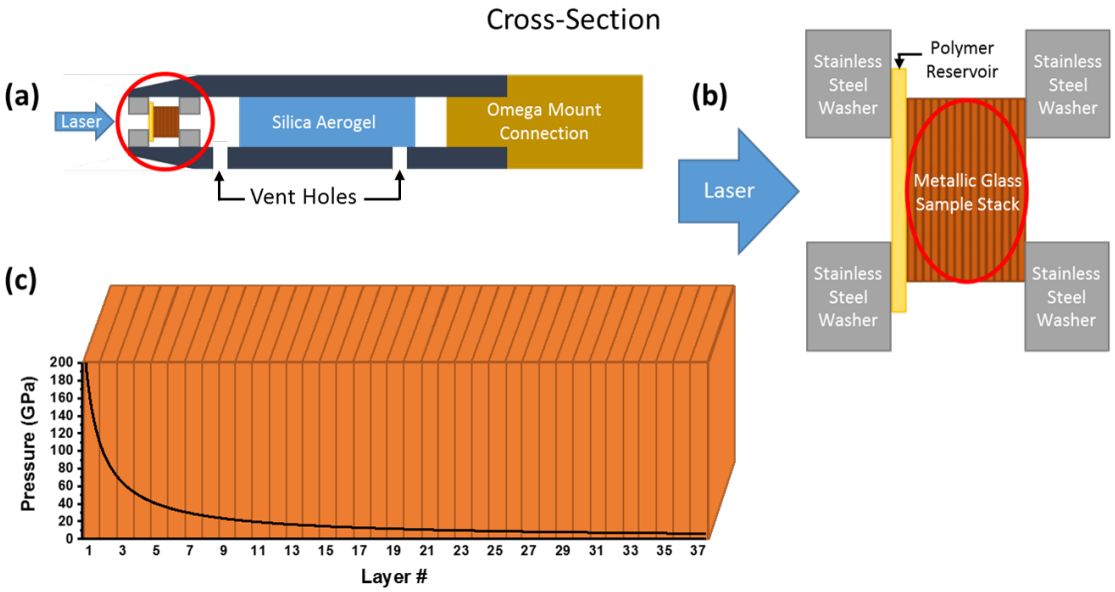

Figure 6.1: (Color Online) Schematic illustrations of (a) cross-section of the recovery tube used for Omega laser experiments showing sample stack, vent holes, and silica aerogel used to non-destructively catch the sample stack after shock, allowing for recovery without secondary effects; (b) magnified cross-sectional view of sample stack with $2.5\,\mathrm{mm}$ opening in the stainless steel washer for the laser beam, $300\,\mu\mathrm{m}$ thick polymer reservoir for shock generation, $2\,\mathrm{mm}$ thick stack of Ce_3Al metallic glass ribbons (each $40\,\mu\mathrm{m}$ thick), and backing stainless steel washer used to stabilize the sample stack within the recovery tube; (c) magnified view of metallic glass layers with an overlay of simulated pressures using HYADES code as a function of sample thickness. [257]

Following shock compression, the recovered sample stack was separated for XRD and EXAFS analyses performed using NSLS-2 and NSLS synchrotron sources. The methodologies for these measurements and analyses are presented in Section 3.4.

6.3 Experimental Results

Visual inspection of the recovered sample stack of layers following the Omega laser shock experiments reveal two distinct sets of effects, as shown in Figure 6.2. The stacked sample layers in the region (close to the polymer buffer) of higher and asymptotic pressure decrease (up to layer #9), exhibit extensive sample deformation, damage, and erosion, with only parts of the layers left behind. The rest of the sample stack (in particular layer #16 and beyond) subjected to lower and more gradual pressure variation exhibit no obvious deformation or sample damage.

For purpose of analysis, the samples were thus separated into two sets, namely highly deformed (layers 2-9) and undeformed (layers 16 to 37). Representative samples taken from these shocked and highly deformed and undeformed conditions were characterized with X-ray scattering and EXAFS. All of the 2D diffraction data was converted into structure factors and PDFs, and the EXAFS data was converted to partial PDFs using the methods detailed in Section 3.4.

6.3.1 Characteristics of Shock-Compressed and Recovered Deformed Samples

The results for the structure factors, total PDFs, and Ce-specific partial PDF of the first set of Ce_3Al MG recovered shock compressed samples, which show evidence of deformation, are presented in this section. Figure 6.3 shows the total structure factor traces for these shock-recovered samples along with the trace for the unshocked sample. For all samples, there is clear evidence of medium to long-range structural evolution in the form of increased numbers and amplitudes of peaks. At layer 8, there are extra, narrow peaks visibly separating from the broad amorphous peaks of the initial condition. The number and separation of these peaks increase as the layer number decreases, i.e., as the applied shock pressure increases. The layer 2 sample shock-compressed to $\sim 90\,\mathrm{GPa}$ appears to be fully crystalline with high Q peaks and no obvious amorphous background. Magnified views of

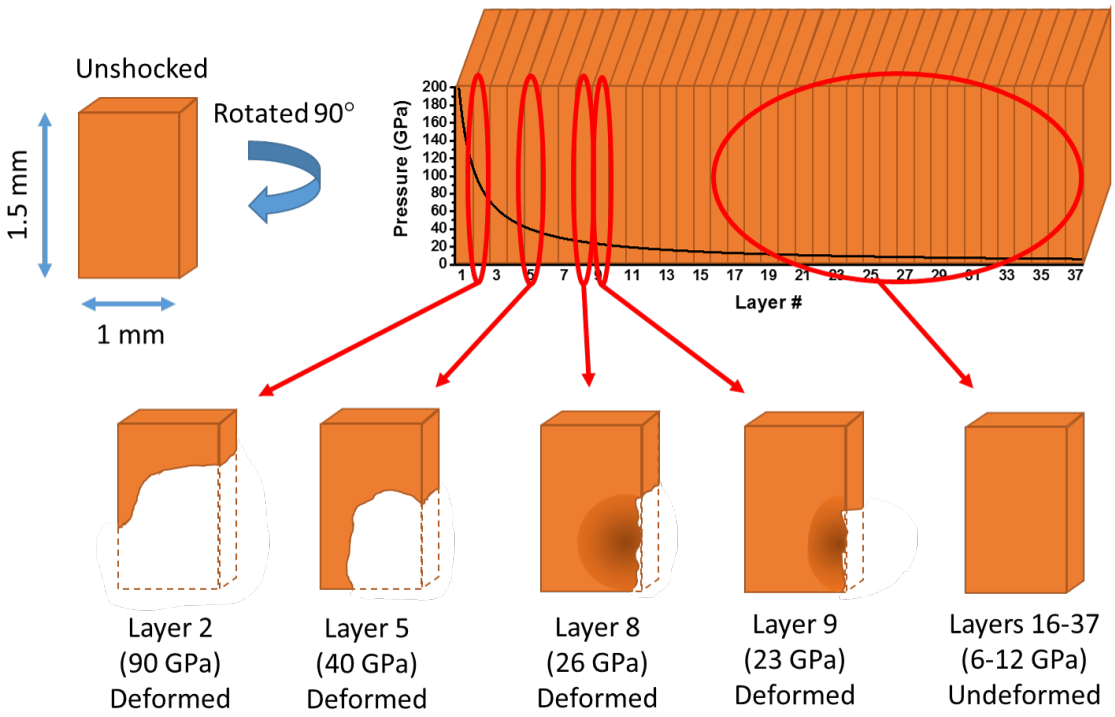

Figure 6.2: (Color Online) Schematic showing sample deformation states of shock-compressed and recovered samples. Initial state is shown in top left, rotated from the side view of the stack shown in the top right. Representative individual layers are shown to illustrate the relation of calculated shock pressures on visual state of recovered samples. White areas (enclosed in dashed lines) are indicative of sample erosion and darkened areas represent regions with visible indentation. The first set of approximately 10 layers, representing pressures from ∼20-100 GPa, show visible deformation and erosion/loss of material, while the second set of layers 16 and beyond, representing ∼10 GPa and below, reveal no sign of visible deformation or indentation.

the regimes from 1.5 to 3.0, 3.0 to 5.25, and 5.25 to 7.75 Å^{-1} for the four layers and initial sample are shown in Figures 6.4, 6.6, and 6.7, respectively.

Figure 6.4 shows a magnified view of the regime from 1.5 to 3.0 Å^{-1} of the structure factor for the shock-compressed Ce_3Al samples recovered with visible deformation (layers 2, 5, 8, 9) and unshocked Ce_3Al MG sample. The first sharp diffraction peak shows a trend of first increasing in Q at layer 9, further increasing but beginning to show separation into two peaks at layer 5, and further increasing but fully separating into two peaks at layer 2. These increases in the first sharp diffraction peak correspond to increases in density, as discussed in Section 3.4.2.

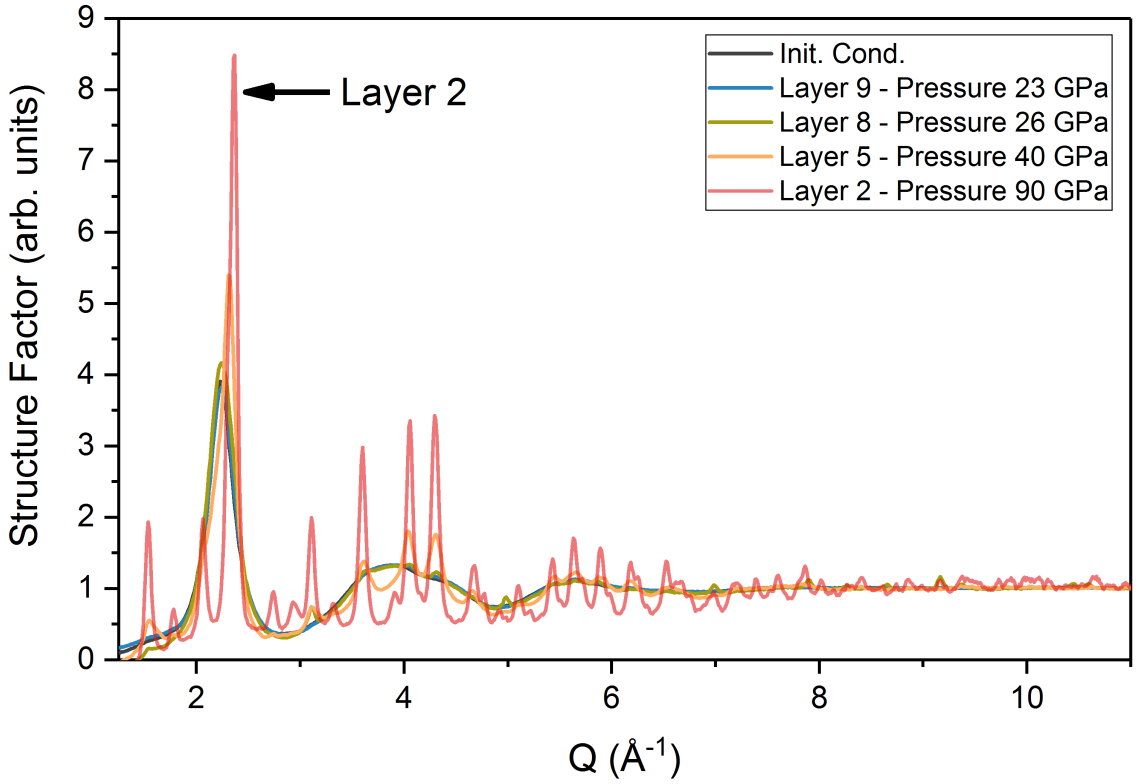

Figure 6.3: (Color Online) Structure factor traces for unshocked Ce_3Al MG and recovered shock-compressed samples (first set, layers 2-9) which had observable deformation. Layers 2 to 8 show clear development of long-range order, with additional peaks evolving at all angles up to and above $7\,\text{Å}^{-1}$. Increasing pressure results in further peak evolution, with layer 2 resulting in an apparently fully crystalline material. Additionally, the first sharp diffraction peak shifts to the right and separates into two peaks, one lower and one higher angle than the amorphous peak present in the unshocked sample, indicating decreasing atomic volume and increasing density with increasing pressure.

Figure 6.5 plots the position of the first sharp diffraction peak of the structure factor as a function of layer number, with the larger amplitude peak used for layer 2. Taking the position as a proxy for density wherein higher values are representative of higher densities, the "density" is observed to overall increase by 0.5% in layer 9, 0.5% in layer 8, 3.5% in layer 5, and 5.8% in layer 2. The reference crystalline phase is typically only $\sim$3% denser than the amorphous phase. The maximum 5.8% increase in density in the shock-compressed crystallized sample layer (closest to the shock), as compared to the unshocked Ce_3Al MG, needs to be verified on the basis of the method employed for the density determination.

Figure 6.6 shows a magnified view of the regime from 3.0 to $5.25\,\text{Å}^{-1}$ of the structure

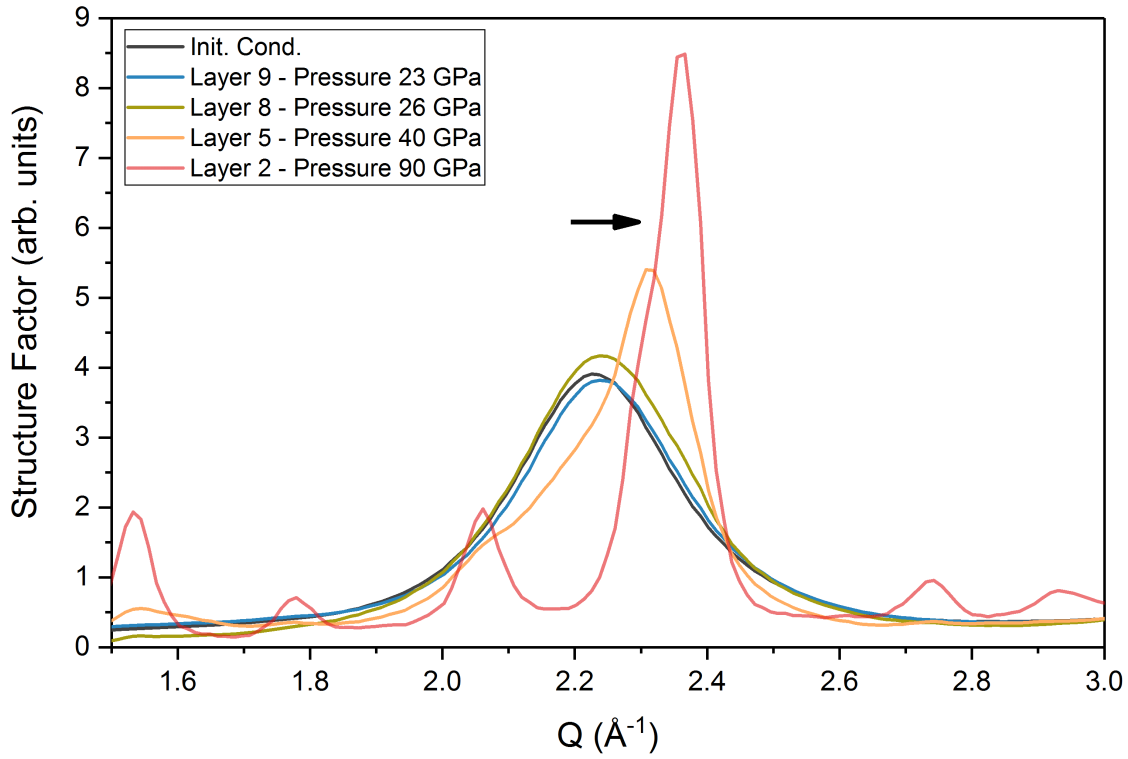

Figure 6.4: (Color Online) Magnified structure factor traces around the regime from 1.5 to 3.0 Å^{-1} for unshocked Ce_3Al MG and recovered shock-compressed samples layers 2-9. The first sharp diffraction peak of the unshocked and layers 9, 8, and 5 show a trend of increasing in Q as the layer number decreases and associated applied pressure increases. This shift in the first sharp diffraction peak to higher Q values is representative of an increase in density. At layer 2, the peak separates into two peaks, one below and one above the amorphous first sharp diffraction peak.

factor for the shock-compressed Ce_3Al samples recovered with visible deformation (layers 2, 5, 8, 9) and that for the unshocked Ce_3Al MG sample. The first evolved peaks of layer 8 are visible in this regime. As the shock-compression pressures increase, the peaks further grow and separate from the amorphous regime. The layer 5 sample shows more and more separated broad peaks over the background of the amorphous scattering structure. They are larger and greater in number than the peaks observed in the layer 8. The peaks in the fully crystalline layer 2 phase match strongly with those observed at lower shock-compression pressures, indicating the evolution of shock-compression-induced long-range order begins with nucleation of some small regions of similar structure. The structure factor peaks in the

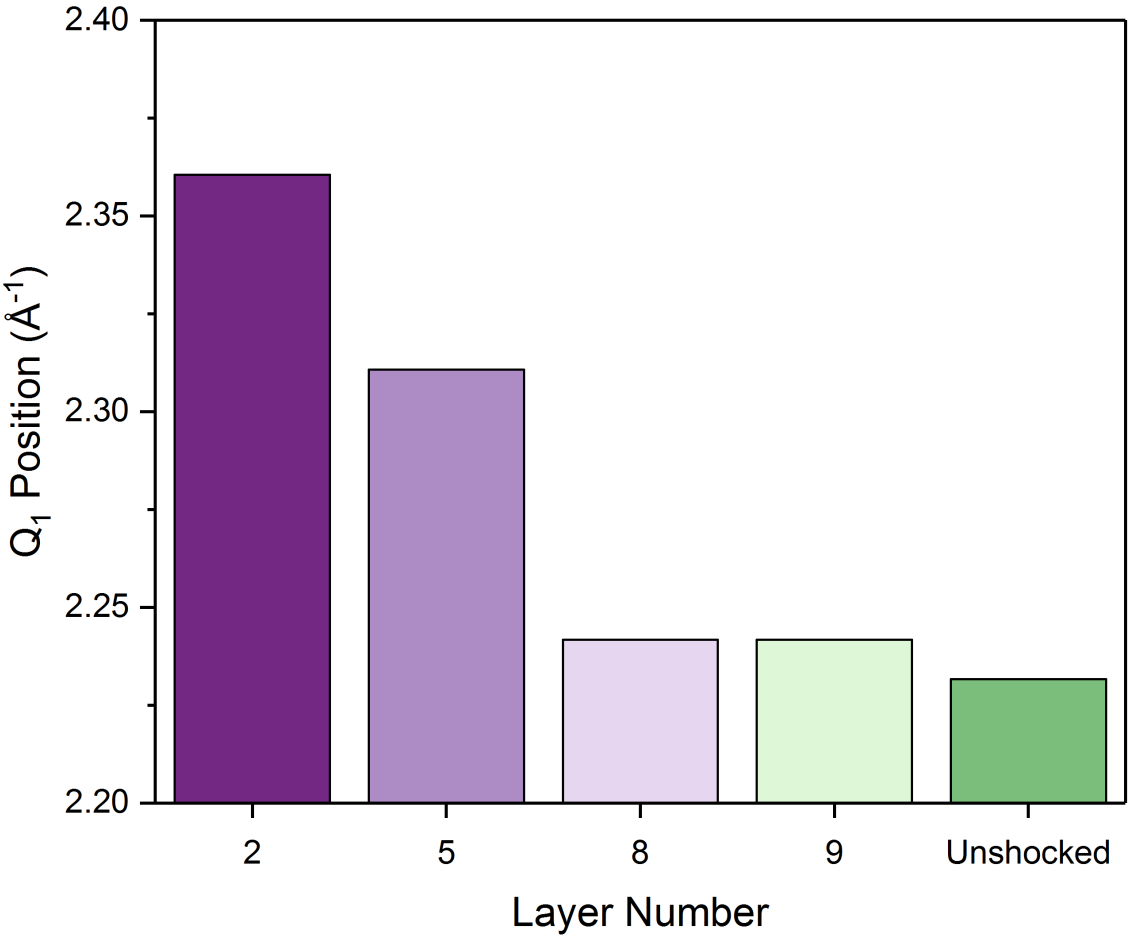

Figure 6.5: (Color Online) Bar chart of the position of the first sharp diffraction peak in the structure factor for the initial condition Ce_3Al MG and the shock-compressed, observably deformed, recovered Ce_3Al layers 2, 5, 8, and 9. Peak position is representative of density, with increasing Q positions indicating increased densities. Peak position increases 0.5% for layers 8 and 9, 3.5% for layer 5, and 5.8% for layer 2 as compared to the unshocked sample.

layer 2 remain broad, indicating that the fully crystalline phase retains significant disorder.

Figure 6.7 shows a magnified view of the regime from 5.25 to $7.25\,\text{Å}^{-1}$ of the structure factor for the shock-compressed Ce_3Al samples recovered with visible deformation (layers 2, 5, 8, 9) and unshocked Ce_3Al MG sample. The first evolved peaks of layer 8 are clearly visible in this regime as well, along with the beginnings of a peak evolving in layer 9 around $6.25\,\text{Å}^{-1}$ (indicated with an arrow). Peak evolution follows a similar trend with lower layer number and associated increasing pressure as the previous regimes.

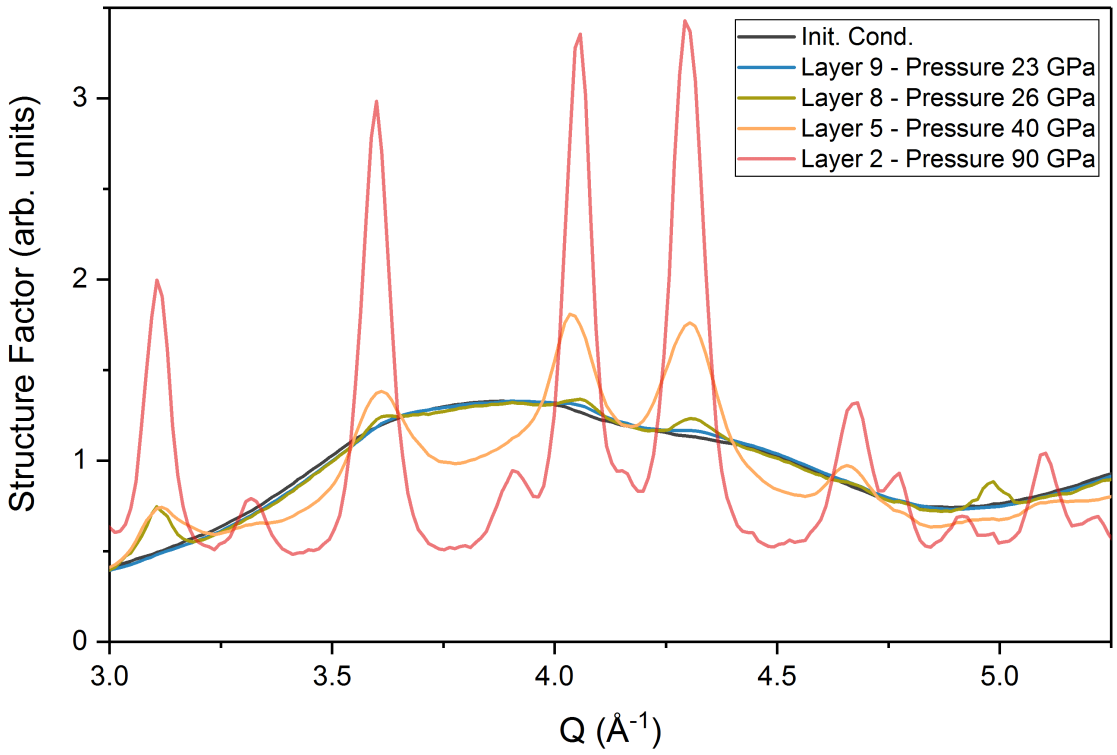

Figure 6.6: (Color Online) Magnified structure factor traces around the regime from 3.0 to $5.25\,\text{Å}^{-1}$ for unshocked Ce_3Al MG and recovered shock-compressed samples layers 2-9. The first evolution of medium-range order is visible in layer 8 as peaks evolve out of the amorphous signal visible in the unshocked sample. Layer 9 shows the beginnings of peak evolution at the same positions. Layer 5 shows significant growth of the peaks and new peaks, and the overall amorphous scattering decreases in amplitude. Layer 2 has significant growth of the peaks observed in the other layers with no obvious amorphous scattering remaining.

The structural changes observed in the structure factor were further analyzed via total PDF analysis. Figure 6.8 shows the PDF traces for the shock-compressed Ce_3Al MG samples (layers 2, 5, 8, 9) along with that of the initial unshocked sample. Overall, clear long-range order is evident in the shock-compressed layer 2 (highest pressure) as it shows discrete peaks with significant magnitudes up to the maximum plotted value of 30 Å. However, the peaks are broad, indicating the traditional *hkl* separations may have significant disorder as compared to a defect-free crystalline material. The shock-compressed layer 5 sample has small fluctuations visible at higher radial positions; however, the small and diminishing magnitude indicates that the sample does not have long-range order beyond 20

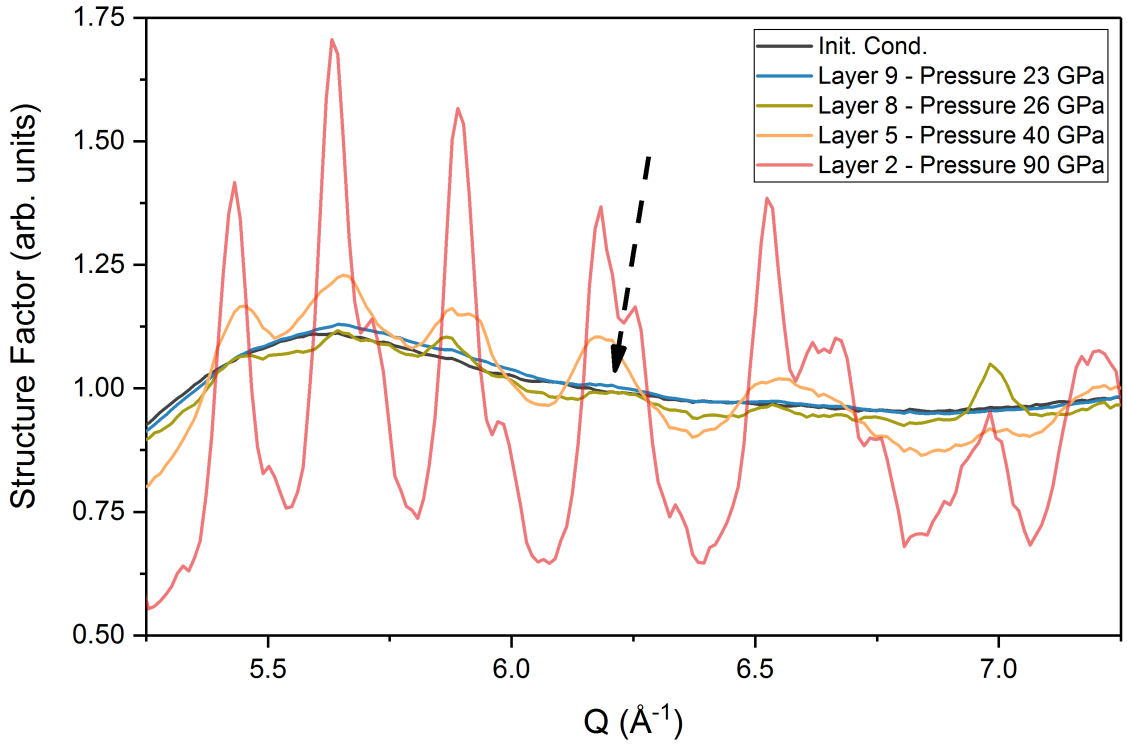

Figure 6.7: (Color Online) Magnified structure factor traces around the regime from 5.25 to 7.25 Å^{-1} for unshocked Ce_3Al MG and recovered shock-compressed samples layers 2-9. Clear evolution of medium-range order is visible in layer 8 as peaks evolve out of the amorphous signal visible in the unshocked sample. Layer 9 shows the beginnings of peak evolution at 6.25 Å^{-1} (indicated with an arrow). Layer 5 shows significant growth of the peaks and new peaks, and the overall amorphous scattering decreases in amplitude. Layer 2 has significant growth of the peaks observed in the other layers with no obvious amorphous scattering remaining.

to 30 Å. The shock-compressed layer 8 sample does not appear to have any larger position peaks similar to that for the initial condition, indicating that it remains amorphous.

Figure 6.9 shows a magnified image of the first peak of the total PDF for the unshocked Ce_3Al MG and shock-compressed sample layers 2-9. The first PDF peak displays a clear trend of decreasing first nearest-neighbor bond lengths, indicating that the short-range order (SRO) increases with applied pressure in this regime. The bond lengths decrease 0.4% in layer 9, 0.5% in layer 8, and 1.8% in layer 5. For layer 2, the peaks separate into three discrete peaks, making it difficult to compare.

Figure 6.10 shows a magnified view of the total PDF from Figure 6.8 for the regime

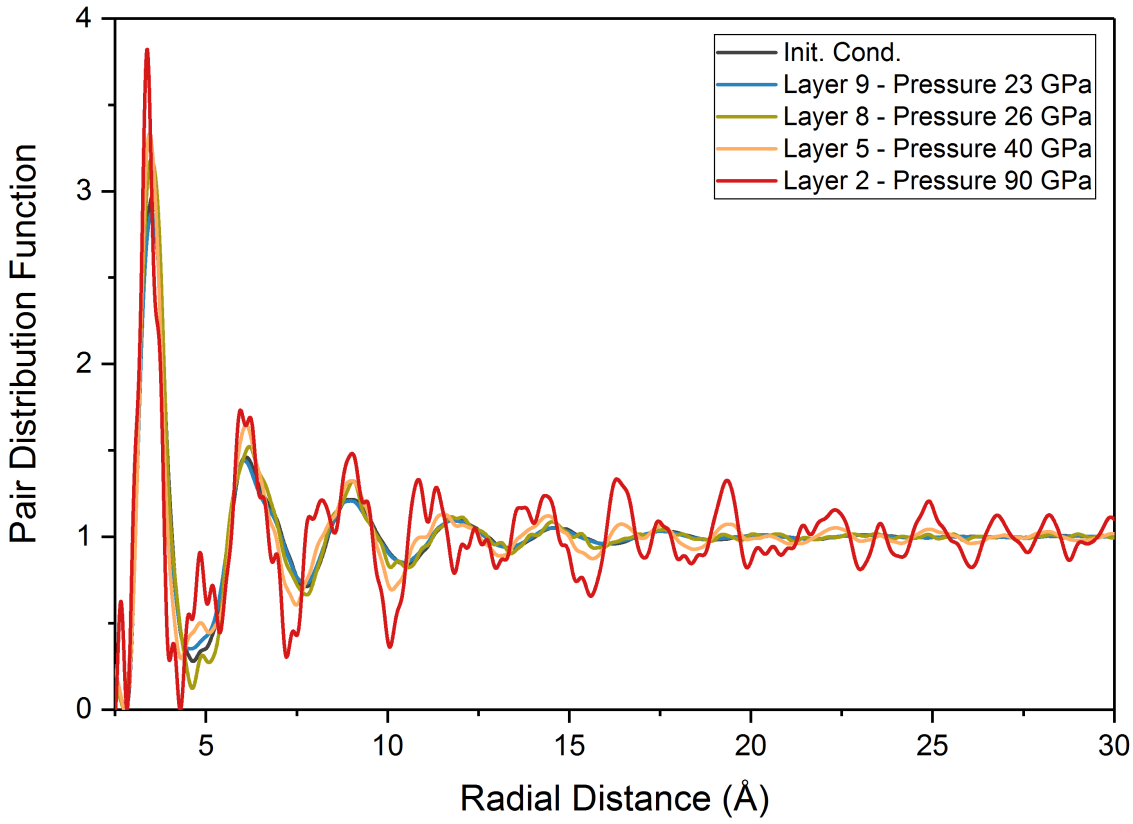

Figure 6.8: (Color Online) Pair distribution function plots for initial unshocked Ce_3Al MG and recovered shock-compressed samples which had observable deformation. In layers 2-8, there is clear evolution of increased order, as is evident from additional peaks appearing, representing separation into discrete packing groups. Layer 2 has long-range order up to at least 30 Å visible in the form of additional peaks, and the short and medium-range order has separated into more discrete hkl-like planes. The broadness of peaks in layer 2 indicate significant disorder remains even in the fully crystalline state. The limited peak separation in layers 5 and 8 conditions indicates these samples are mostly amorphous with medium-range order increasing along with pressure. Due to separation into multiple other peaks, there is no clear trend of peak shifts for the higher order peaks; however, the first peak appears to shift to lower bond lengths with pressure, indicating more efficient short range order packing.

from 5.25 to 7.75 Å wherein the second and third peaks of the total PDF for the unshocked Ce_3Al MG are centered. There is a clear separation of the peaks starting in layer 8, and the new peaks are indicative of localization of order or distinct MRO within that radial distance. For the crystalline layer 2 sample, the peaks are representative of *hkl* planes. Because the evolved peaks in layers 5 and 8 closely match those of layer 2, it appears that the MRO evolution in the MG, as it is subjected to increasing applied pressures, progresses

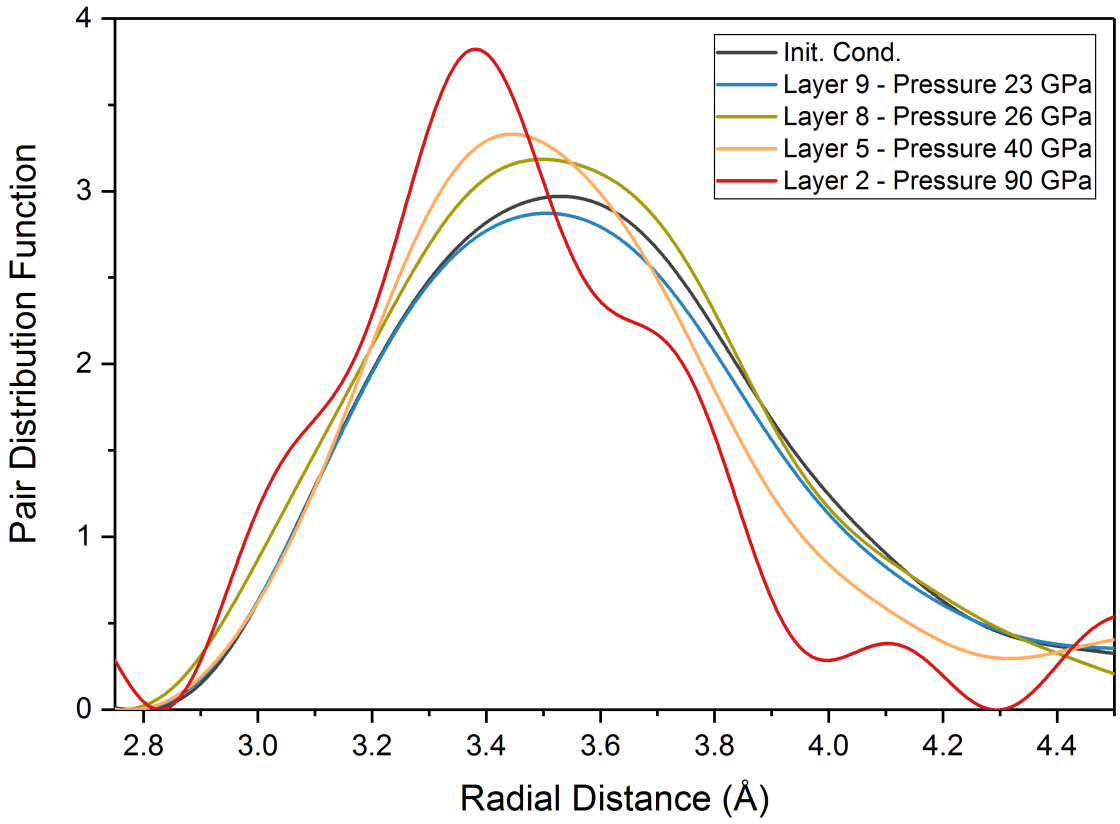

Figure 6.9: (Color Online) Magnified view of the first peak of the PDF traces for the unshocked Ce_3Al MG and recovered shock-compressed samples which had observable deformation (layers 2-9). The positions of the first peak for layers 2-9 increasingly decrease as the layer number decreases and associated applied pressure increases. At layer 2, the peak separates into three peaks, indicating distinct SRO order in the crystalline phase.

in a manner which emulates the MRO of the crystalline phase.

Figure 6.11 shows a magnified view of the total PDF from Figure 6.8 for the 7.75 to 10.5 Å region. The fourth peak of the amorphous PDF in the unshocked sample and layer 9 of the shock-compressed samples separates into multiple other peaks starting at layer 8. The peaks of layer 2 are indicative of the higher order *hkl* planes for the crystalline phase. The peaks of layers 8 and 5 appear to shift significantly with increasing applied pressure, indicating that the order at this length scale requires larger changes to become similar to the crystalline phase. Overall, the total PDF observations indicate that for the shock-compressed samples recovered with visible deformation, increasing applied pressure correlates with SRO densification followed by further SRO densification and evolution of

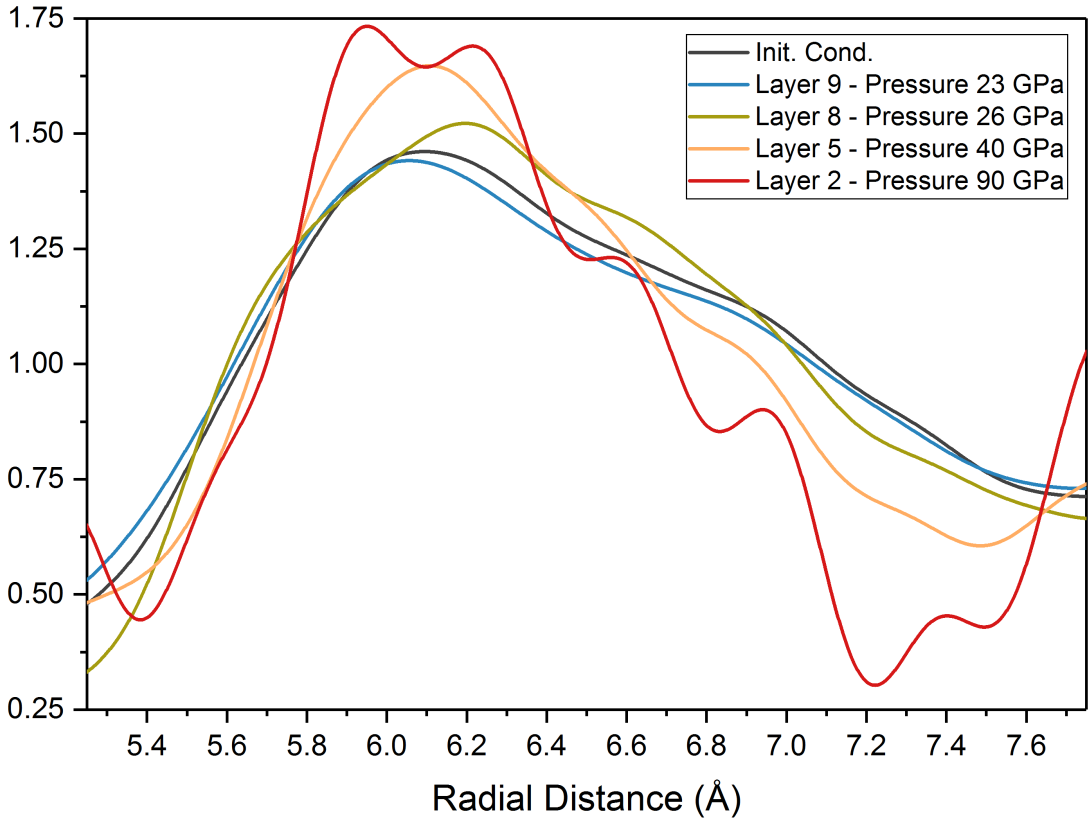

Figure 6.10: (Color Online) Magnified view of the regime from 5.25 to 7.75 Å for the PDF traces for the unshocked Ce_3Al MG and recovered shock-compressed samples which had observable deformation (layers 2-9). The initial amorphous second and third peaks separate into multiple independent peaks in layer 8, with more clear definition for the peaks evolving in layers 5 and 2. The evolution of these peaks are representative of increased segregation of the MRO packing of atoms into particular bond-lengths with applied pressure. The peaks for the crystalline layer 2 are representative of particular *hkl* values.

MRO similar to that of the crystalline phase and finally results in the LRO of the crystalline phase.

Figure 6.12 shows the partial PDF for Ce-Ce and Ce-Al bonds, based on EXAFS measurements, of the shock-compressed Ce_3Al MG sample layer 2, along with that for the initial unshocked condition. Although the total PDF shows separation of the first peak into three peaks, the partial PDF based only on Ce-Ce and Ce-Al bonds appears to only show one peak, possibly indicating the other two peaks of the total PDF come from Al-Al or more weakly detected Ce-Al bonds. After shock-compression, all peaks appear to have shorter bond lengths than the initial condition. The first main peak shifts to $\sim$3% lower

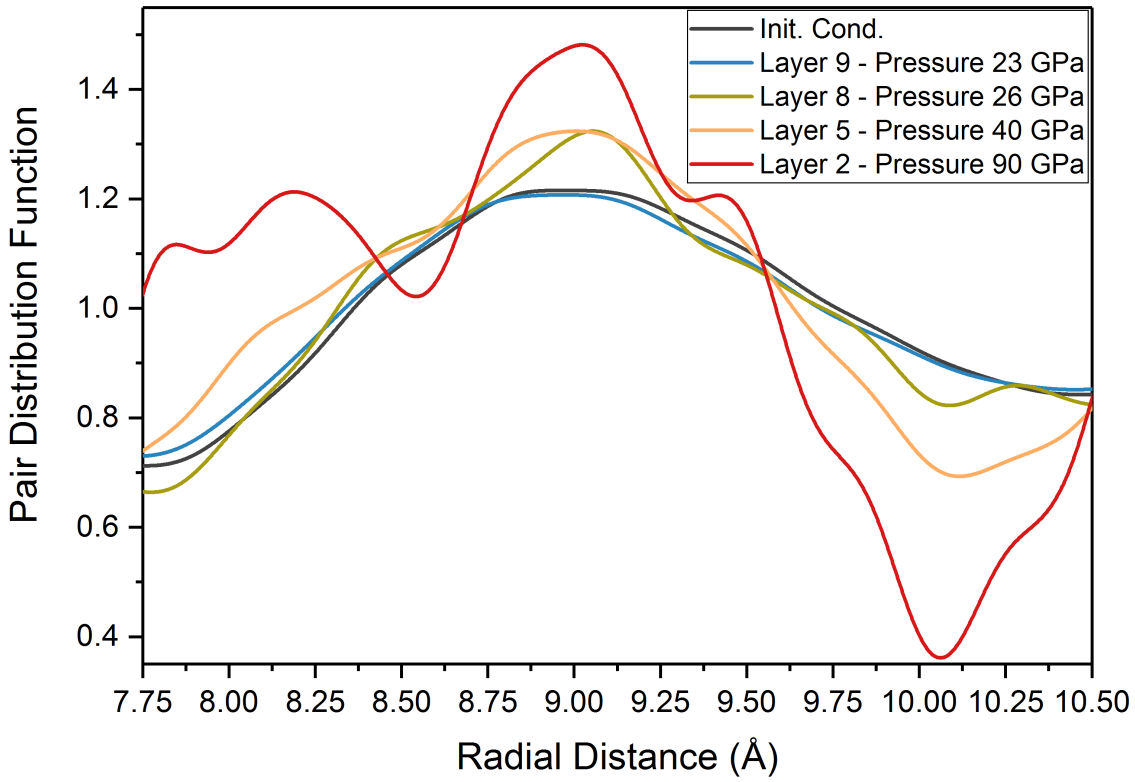

Figure 6.11: (Color Online) Magnified view of the regime from 7.75 to 10.5 Å for the PDF traces for the unshocked Ce_3Al MG and recovered shock-compressed samples which had observable deformation (layers 2-9). Layer 9 does not show any clear visible changes, but layers 8, 5, and 2 show separation of the peak in the unshocked sample into multiple other peaks. Significant shift is seen in peak position between layers, indicating significant rearrangement needed on this length scale for crystallization.

bond lengths.

6.3.2 Characteristics of Shock-Compressed and Recovered Undeformed Samples

The X-ray scattering and EXAFS data for the shock-compressed samples, which were recovered with no visible deformation, are presented in this section. The structure factor traces for the initial unshocked Ce_3Al MG and those of the shock-compressed, undeformed Ce_3Al samples (layers 18, 20, 24, 28, 37) are shown in Figure 6.13. The profiles corresponding to these shocked and unshocked samples do not show any obvious long- or medium-range order evolution at high Q. However, the peaks are noticeably shifted in the shock-compressed samples in comparison to those in the unshocked sample.

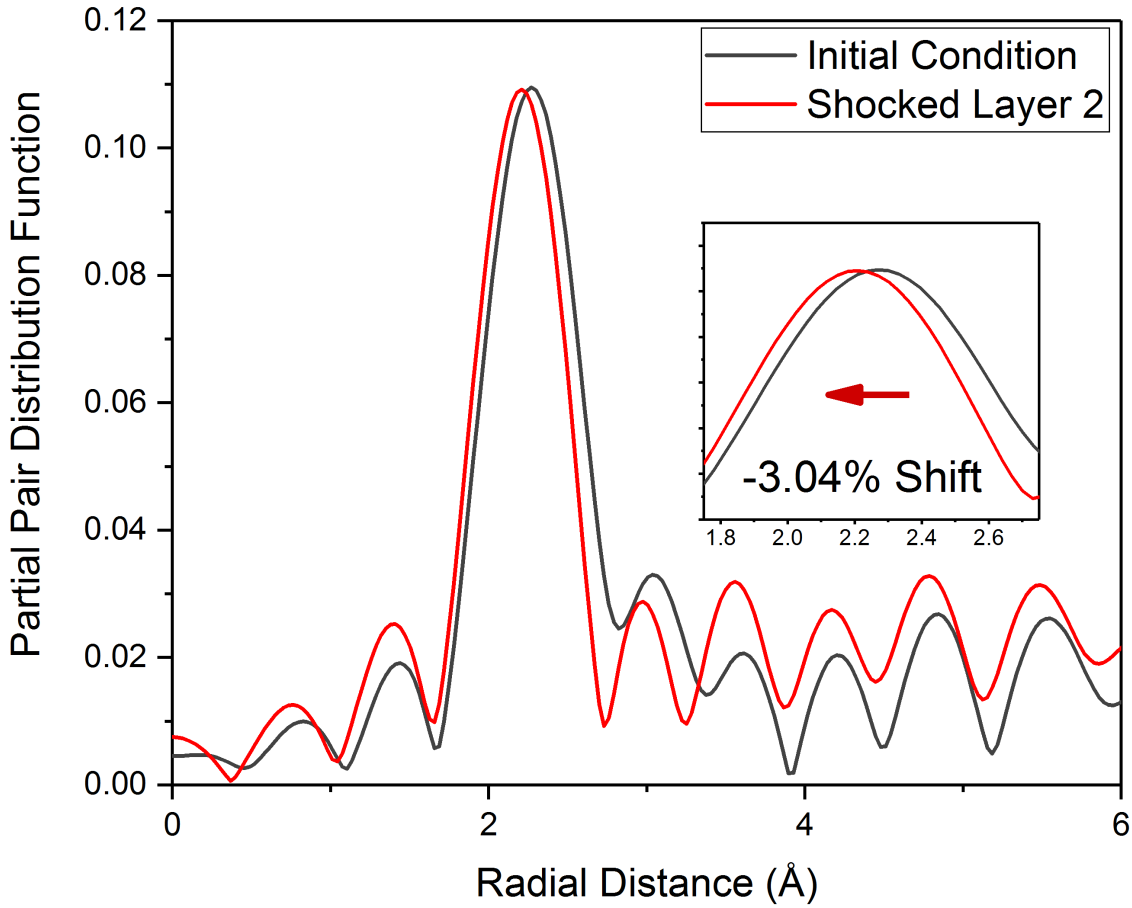

Figure 6.12: (Color Online) Ce-Al and Ce-Ce pair distribution function plots for unshocked Ce_3Al MG and the deformed, shock-recovered Ce_3Al MG sample layer 2. All peaks for the shock-compressed sample are of a lower bond length than those of the unshocked sample, indicating a permanent Ce-based (Ce-Ce and/or Ce-Al) bond length decrease after shock compression associated with crystallization. The inset shows a magnified view of the first peak wherein a $\sim$3% decrease is observed in the peak position.

Figure 6.14 magnifies and shows the first sharp diffraction peak where a clear shift to higher Q is visible. As discussed in Section 3.4.2, the position of the first sharp diffraction peak relates to the density of the sample according to Equation 3.9, and the shift to larger Q values indicates that the shock-compressed samples are more dense than the unshocked sample.

Figure 6.15 plots the calculated densities for each layer in comparison with the initial density. The densities increase from 2-6% after shock compression, which is significantly higher than the maximum of 1% density increase observed in typical relaxation [95, 96, 97,

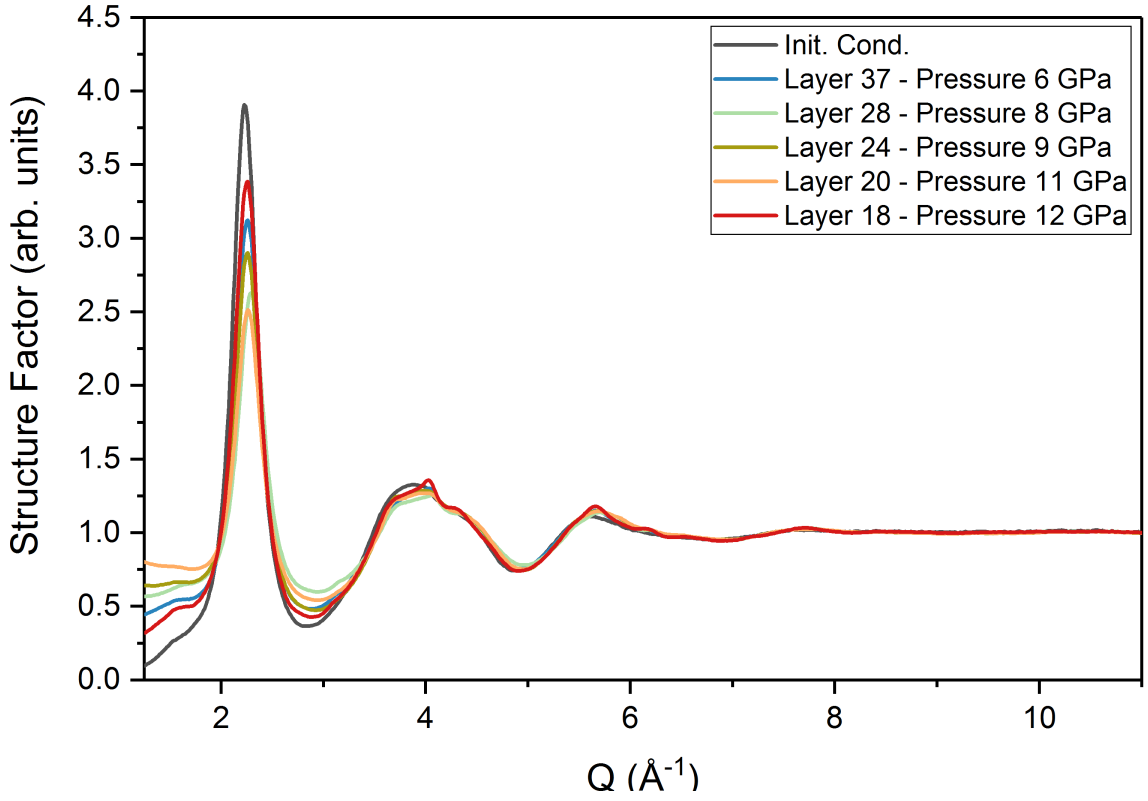

Figure 6.13: (Color Online) Structure factor traces comparing initial Ce_3Al MG and recovered shock-compressed samples (second set, layers 16-37), which were not observed to have any visually-identifiable deformation. Total structure factor ranges indicate no significant evolution of long-range order in the shocked samples, with only limited visible shifts in peak positions. Shocked samples remain amorphous.

98, 99, 100, 101].

Figure 6.16 magnifies and shows the second and third diffraction peaks where some small shifts and peaks evolve, indicating some degree of SRO and MRO changes. These atomic structure changes are more clearly defined in the real-space plots of the PDF.

The PDF traces for the shock-compressed samples recovered without any visible deformation (layers 18, 20, 24, 28, 37) and the unshocked reference sample are plotted in Figure 6.17. In both the unshocked and the shocked samples, there is no visible long-range order. However the PDF peaks for the shocked samples, like the structure factor peaks, appear to be shifted as compared to the unshocked sample. The first four major peaks are magnified in Figures 6.18, 6.19, and 6.20.

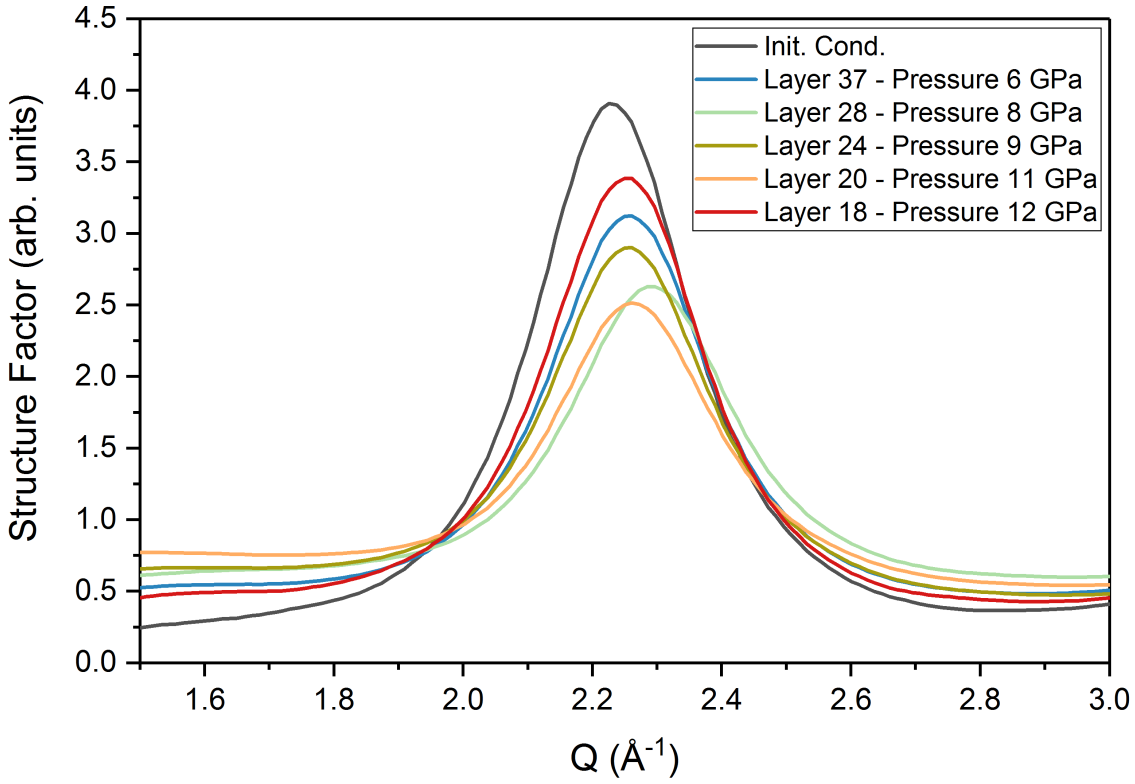

Figure 6.14: (Color Online) Magnified first peaks of the structure factor traces comparing initial Ce_3Al MG and recovered shock-compressed samples (second set, layers 16-37). Relative to that for the unshocked sample, there is an overall trend towards higher Q peak positions following shock compression. However, there is no clear relation between the extent of the shift and applied pressure.

Figure 6.18 shows a magnified view of the first peaks for the different samples. The first peak positions represent the range of bond lengths for the nearest neighbors. In all of the shocked samples, the nearest-neighbor bond lengths are decreased as compared to the unshocked condition. However, there is no clear trend relating applied pressure to the amount decreased.

Figure 6.19 illustrates a magnified view of the overlapping second and third peaks. In all of the shocked samples, the second peak, representing the distribution of bond lengths for the second nearest neighbors, shifts to shorter bond lengths as compared to the unshocked condition. The third peak, representing the range of bond lengths in the third nearest neighbors (which are indicative of medium-range packing of atomic clusters), was

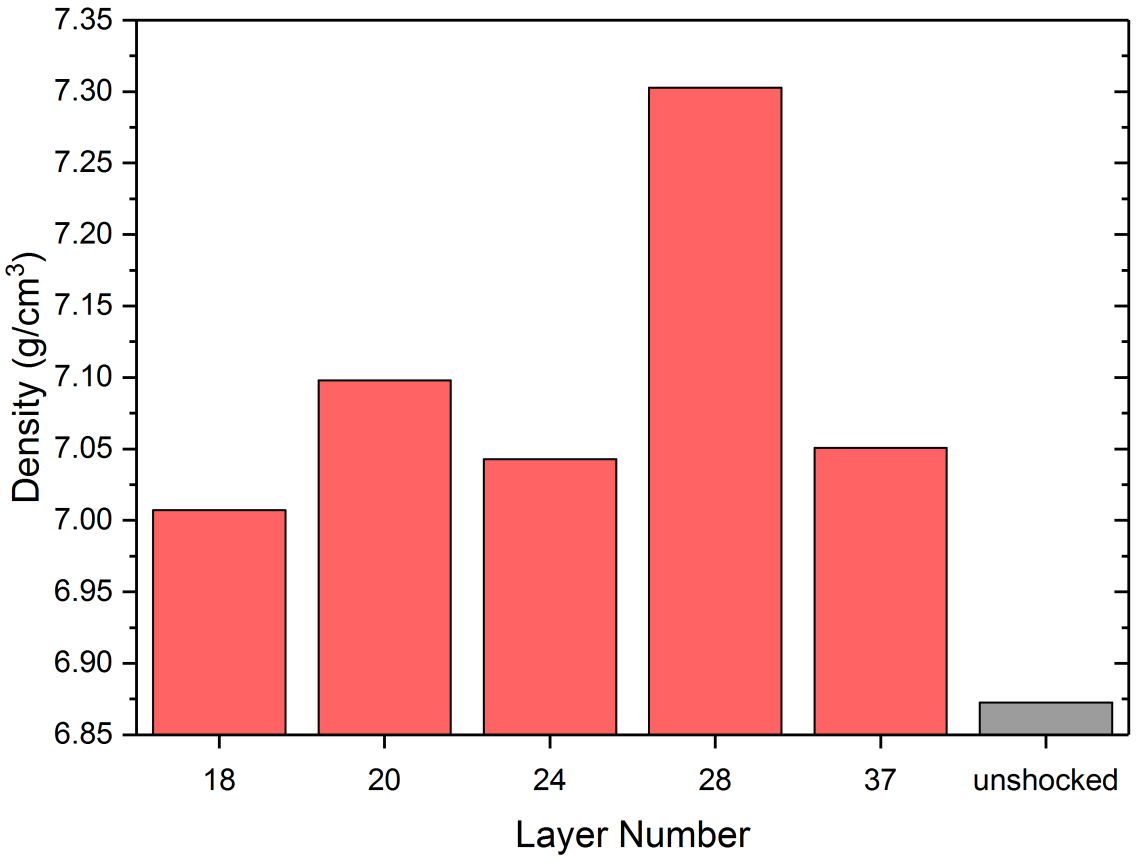

Figure 6.15: (Color Online) Calculated density of the initial Ce_3Al MG compared with the recovered shock-compressed samples (second set, layers 16-37). Values are based on the position of the first peak of the structure factor and do not account for the mesoscale structure including voids or large defects which might affect the density determined via other methods. Amorphous shocked samples have densities 2-6% larger than that of the initial unshocked sample.

deconvoluted from the second peak using a pseudo-Voigt peak fitting for each data set. Overall, the third peak appears to shift to longer bond lengths in the shock-compressed samples as compared to the unshocked sample, indicating the atomic changes are a rearrangement of atomic packing more significant than pure compression. There is no clear trend relating the magnitude of peak shifts to applied pressure.

Figure 6.20 shows a magnified view of the fourth major peak for the shocked (layers 18, 20, 24, 28, 37) and unshocked samples. The fourth peak is representative of the fourth nearest neighbors (similar to the third peak in being indicative of the medium-range order in the MG). In all shock-compressed samples, the fourth peak has a shorter position than

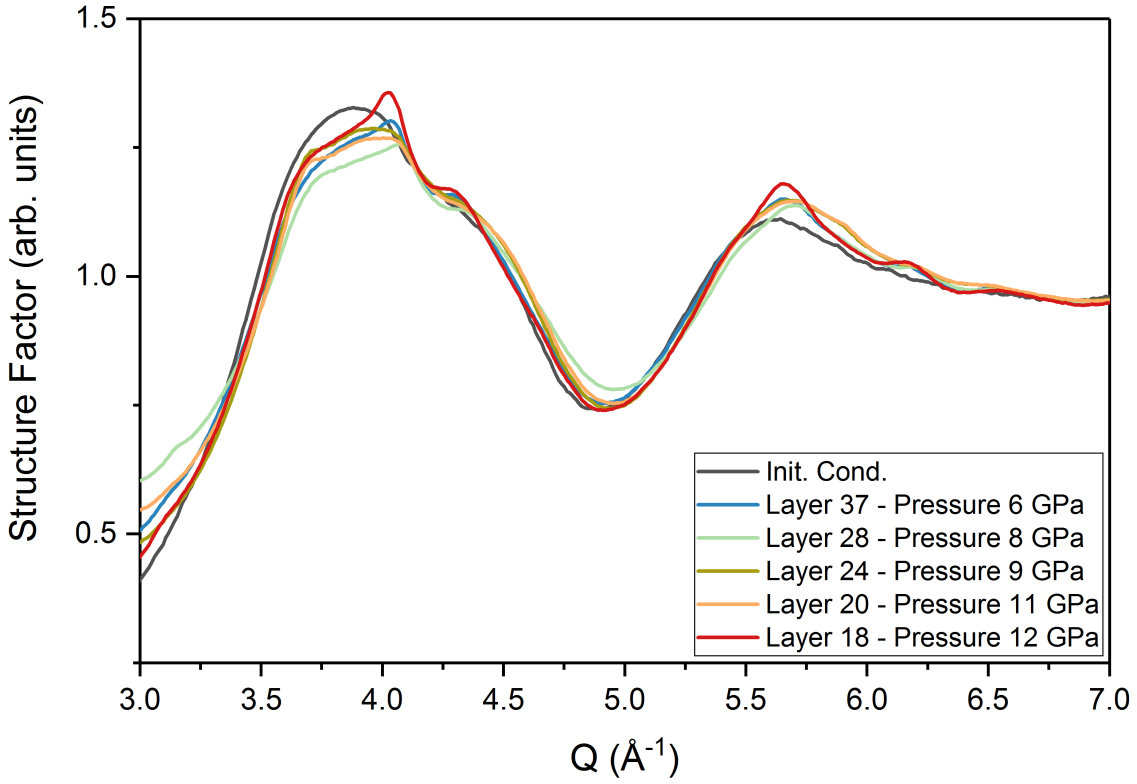

Figure 6.16: (Color Online) Comparison of magnified second and third peaks of the structure factor traces for the initial unshocked Ce_3Al MG and recovered shock-compressed samples (second set, layers 16-37). Relative to the unshocked sample, there is an overall trend towards higher Q peak positions and some medium-range ordering in the form of distinct peak evolution following shock compression. There is no clear relation between the extent of the shift or peak evolution and applied pressure.

the unshocked sample, indicating a more dense packing in the longer-range MRO after shock compression. There is no clear relation between the applied pressure and fourth peak position.

The first four peaks of the PDF profiles were fit with pseudo-Voigt curves to better determine the average bond-lengths that each peak represents. The center positions of each shock-compressed sample peak, in real space, are compared with those of the initial unshocked sample peak positions. The percent differences from the unshocked sample peak positions are plotted in Figure 6.21. Overall, there is a clear trend of decreasing bond lengths for the first, second, and fourth nearest neighbors (corresponding to the first, second, and fourth peaks of the PDF) as the layer number increases up to layer 28. Larger

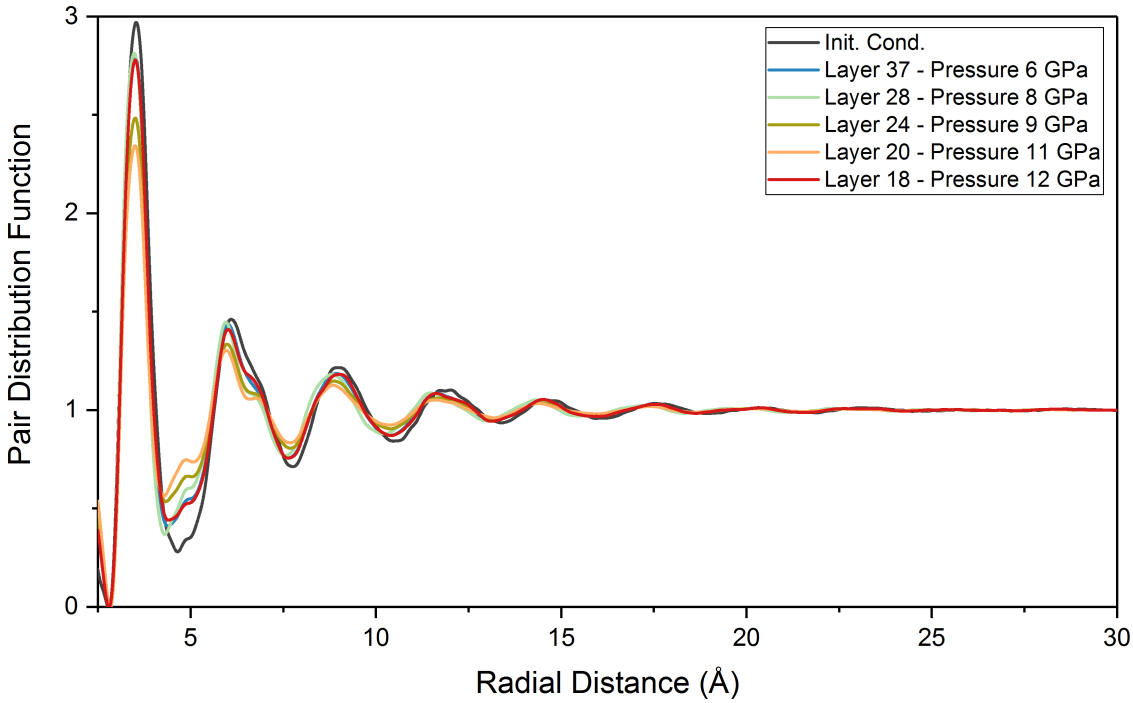

Figure 6.17: (Color Online) Pair Distribution Function (PDF) traces for the recovered shock-compressed Ce_3Al MG samples compared with the initial unshocked sample. Overall, no long range order is evident in any of the traces, as shown by all traces normalizing to the PDF value of one, indicative of random packing, by 30 Å.

layer numbers are representative of a decrease in pressure. This indicates that there may be some dilatory effect at higher pressures which counteracts densification, such as the formation of shear transformation zones (STZs) or heating. Layer 37 shows the trend reverts and the magnitude of peak shifts decrease as the layer number increases further than layer 28, indicating the densification effects decrease below a certain shock-compression pressure. At layer 28, the nearest neighbors are 1.4% closer, second nearest neighbors are 0.6% closer, and fourth nearest neighbors are 2.7% closer.

There is a slight shift in the trend for the third nearest neighbors (corresponding to the third PDF peak) wherein shock compression increases bond lengths. Similar to peaks 1, 2, and 4, as the layer number increases, the magnitude of deviation compared to the unshocked sample peak positions increases. This indicates that the same effects which counterbalance the magnitude of the first, second, and fourth peak densification with increased pressure

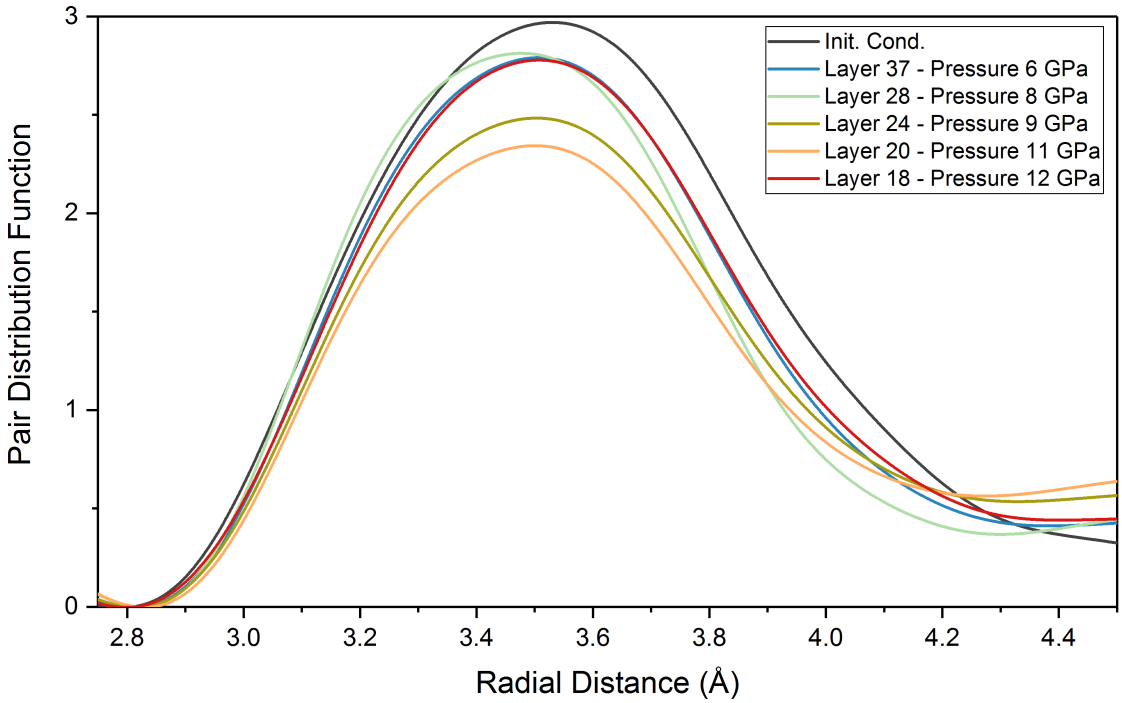

Figure 6.18: (Color Online) Magnified first peaks of the PDF traces for the recovered shock-compressed Ce_3Al MG samples (layers 16-37) compared with the unshocked sample. In all shocked samples, the peak appears to be at a shorter distance than the unshocked sample. There is no clear relation between applied pressure and magnitude of the peak shift.

(until layer 28 for peaks 1, 2, and 4) similarly counterbalance the dilatory effects on the third peak with increasing pressure. However, the maximum peak shift for the third peak is observed at layer 24 instead of layer 28. At this layer number, the third nearest neighbors are 1.4% further apart than those in the unshocked sample. As layer numbers increase and associated pressures decrease further, the trend reverses and the peak shift percentage decreases as the peaks begin to return to the positions of the unshocked sample. In addition to the peak shifts not all being to lower values with pressure, this difference in the trend relating applied pressure to shift percents for different peaks indicates that the mechanism for these structural rearrangements are not simple densification but more complex atomic-scale structure changes.

Figure 6.22 shows the partial PDF for Ce-Ce and Ce-Al bonds, determined via EXAFS, for the shock-compressed layer 24 and unshocked Ce_3Al MG samples. All peaks for the

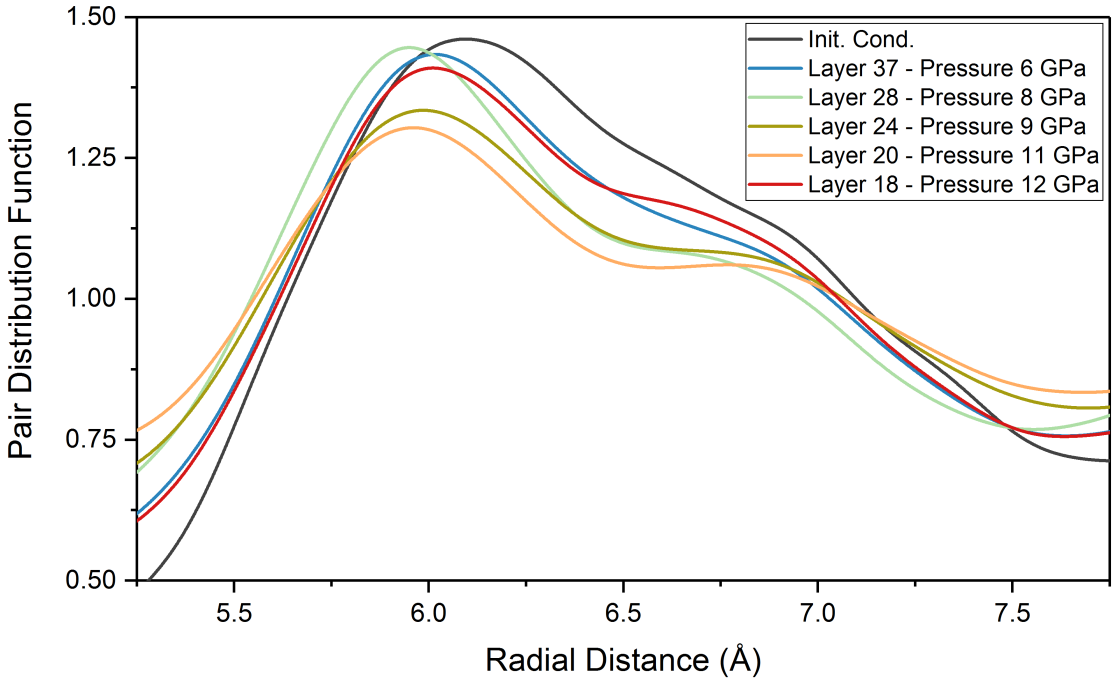

Figure 6.19: (Color Online) Magnified second and third peaks of the PDF traces for the recovered shock-compressed Ce_3Al MG samples (layers 16-37) compared with the unshocked sample. In all shocked samples, the second peak is decreased while the third peak is increased in radial distance as compared to the unshocked sample. There is no clear relation between applied pressure and amount of peak shift.

shock-compressed sample are of a shorter bond length than those of the unshocked sample, indicating the overall shorter bond lengths observed in the total PDFs have a large component that is due to shortening of the Ce-specific bonds. The inset image shows a magnified view of the first peak position, representing the nearest-neighbor bond lengths. The partial PDF shows a $\sim$1.3% decrease in the nearest-neighbor bond lengths whereas the total PDF shows a $\sim$0.7% reduction in the nearest-neighbor bond lengths. The difference may be accounted for Al-Al short-range order bonds increasing in length, indicating potentially significant rearrangements depending on the elemental bonding.

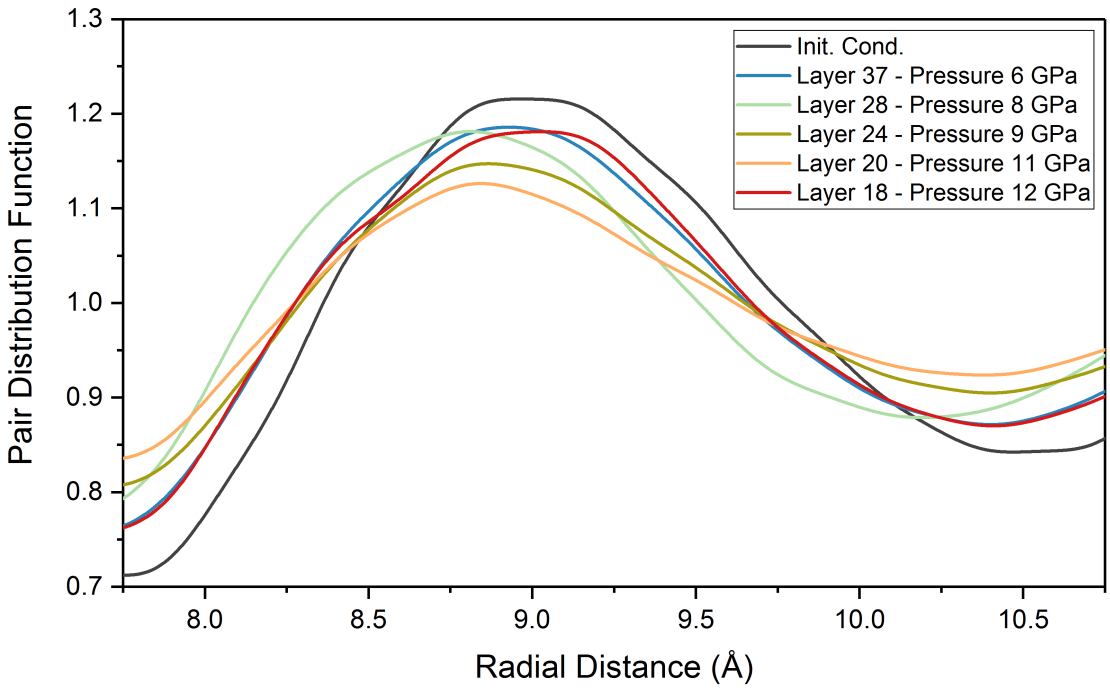

Figure 6.20: (Color Online) Magnified fourth peaks of the PDF traces for the recovered shock-compressed Ce_3Al MG samples (layers 16-37) compared with the unshocked sample. In all shocked samples, the fourth peak position is decreased as compared to the unshocked sample. There is no clear relation between the degree of peak shift and applied pressure.

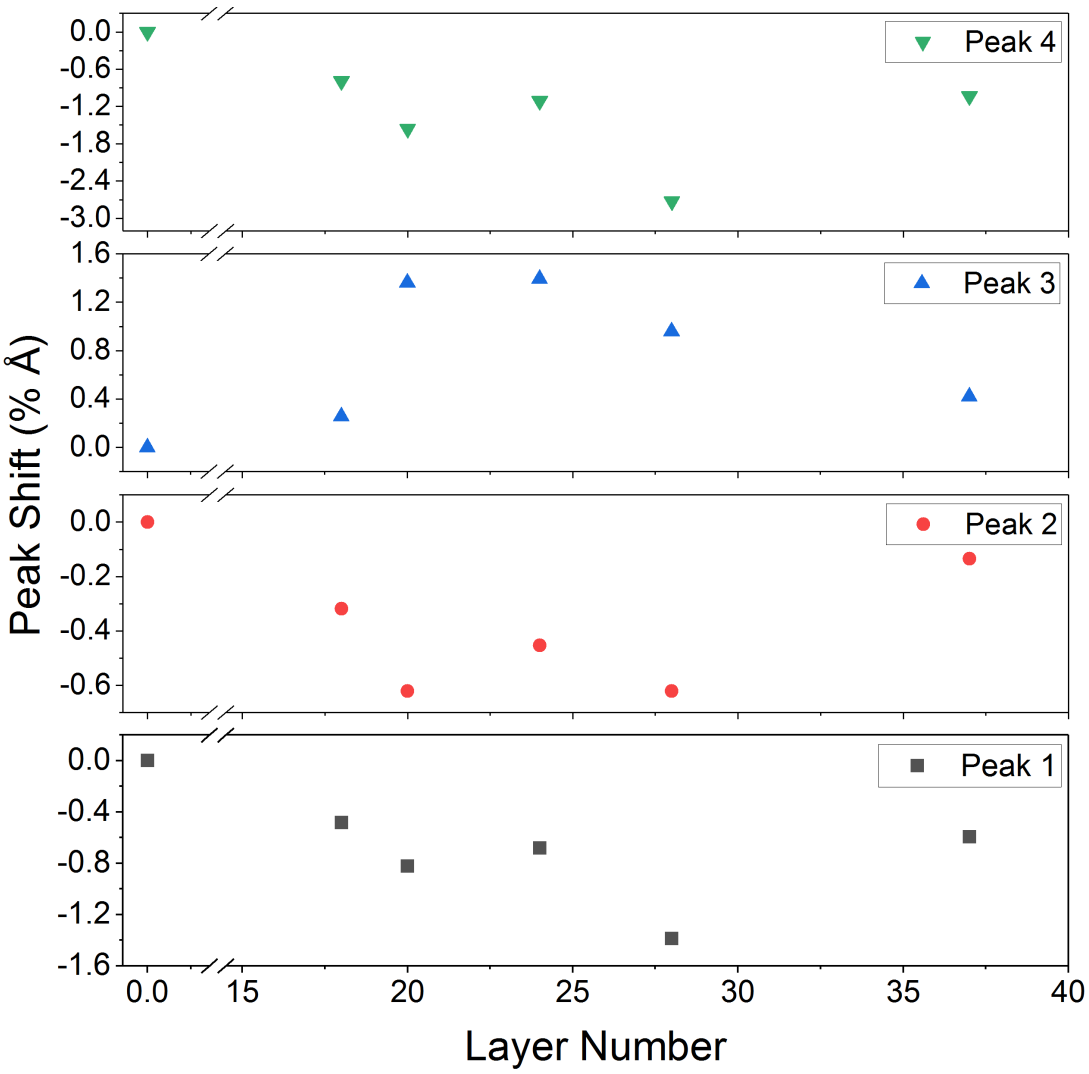

Figure 6.21: (Color Online) Plot of PDF peak position shift (%) relative to the unshocked Ce_3Al MG sample peak positions as a function of layer number of second set shock-compressed samples for peaks 1, 2, 3, and 4. Peaks 1, 2, and 4 show an overall decrease in peak position, and peak 3 shows an increase in peak position with shock compression. The overall trend shows an increase in percent change as layer numbers increase, indicating the applied pressure decreases. The maximum amount of change is observed at layer 28 for the peaks which decrease in position with shock compression and at layer 24 for the peak which increases with shock compression. At higher layers (and therefore lower applied pressures), the magnitude of the peak shifts decrease and they appear to return back to positions close to the unshocked condition. This trend of increasing magnitude of change with decreasing applied pressure indicates there may be a competing dilatory effects such as higher temperatures or formation of shear transformation zones (STZs) at higher pressures which limit the magnitude of densification possible in the samples. Shifts in different directions for the different peaks (1, 2, and 4 vs 3) indicate there may be atomic structural reorganization instead of a homogeneous densification due to compression.

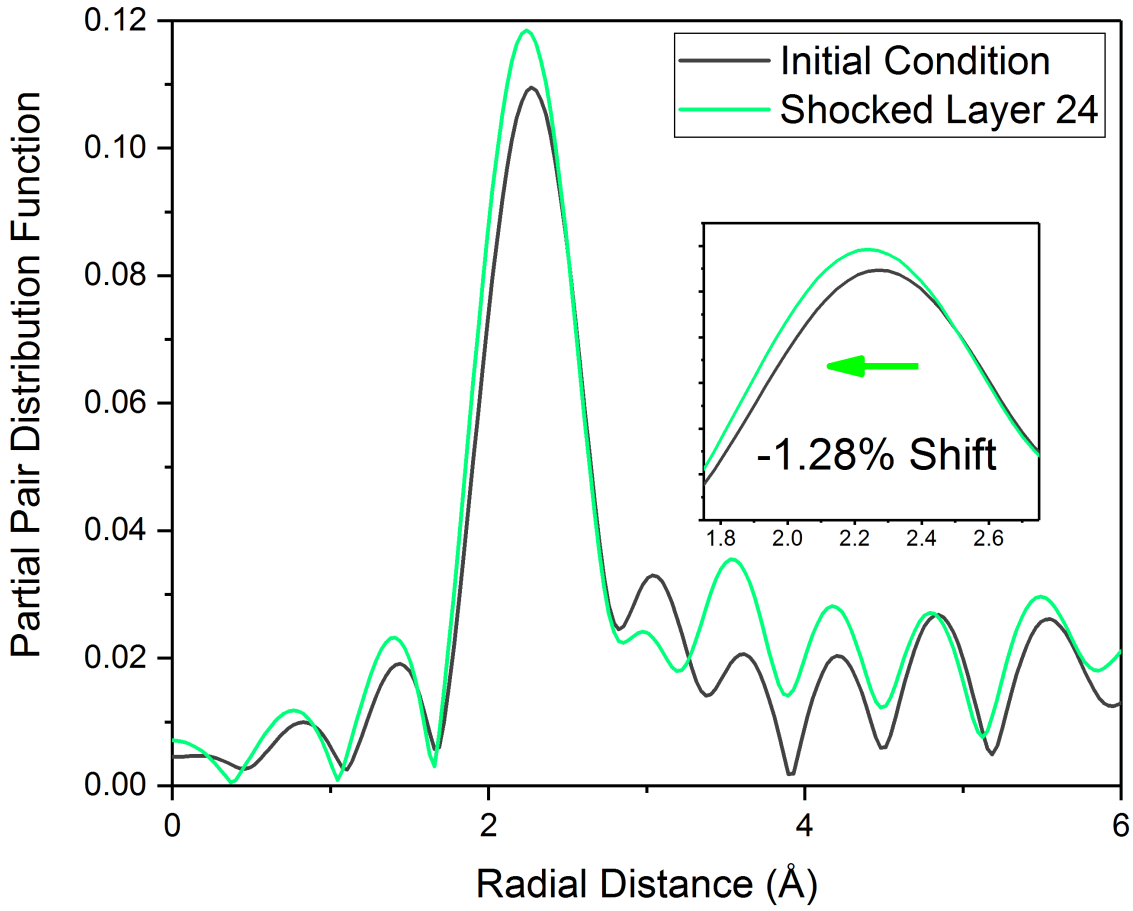

Figure 6.22: (Color Online) Ce-Al and Ce-Ce pair distribution function plots comparing unshocked Ce_3Al MG and shock-recovered undeformed, Ce_3Al layer 24 MG samples. All peaks for the shock-compressed sample are at a smaller radial distance, representative of a lower bond length, than those of the initial condition. The shift in the partial PDF indicates a permanent Ce-based (Ce-Ce and/or Ce-Al) bond length decrease after shock compression. The inset shows a magnified view of the first main peak, showing that the decrease in bond length after shock compression is $\sim$1.3%. This is 1.7% less of a decrease than was evident in the shock-compressed Ce_3Al MG sample layer 2.

6.4 Discussion of Results

Recovery experiments performed using the Omega 50 J laser yields shock-compressed Ce_3Al MG samples showing two different regimes of changes. These atomic-scale changes are correlated with the observation of visible deformation in the recovered samples.

In the deformed samples, there appears to be a clear trend of order evolution with increasing pressure. The sample (layer 9), farthest in this regime of deformed samples from the shock front, appears entirely amorphous with only the beginnings of a slight peak in the structure factor at high Q. In the sample (layer 8), the PDF and structure factor measurements indicate there are SRO shifts and evolution of distinctly ordered peaks, but the overall structure remains predominantly amorphous. As the pressure increases in the sample (layer 5), the structure factor shows clear deviation from the amorphous phase with distinct peak evolution, but there is still a strong amorphous background. The PDF further elucidates evolution of more distinct order on the medium-range, but it does not appear to have significant long-range order beyond 2-3 nm. The sample closest in the deformed regime to the shock front (layer 2) and shock compressed to the highest pressure, however, shows clear indications of complete crystallization with distinct peaks and no broad amorphous background in the structure factor and peaks with consistent and significant magnitude up to the maximum measured value of 3 nm in the PDF. Of note, the broadness of the peaks in the structure factor and PDF indicate that the crystalline phase formed by shock compression in this sample case results in a structure with very small grains and defects or disorder.

The mechanisms contributing to the observed short, medium, and long-range order evolution with increasing shock-compression pressures are expected to be arising from the complex loading of these deformed samples with portions removed partially due to the heat from the initial plasma and resulting shock compression along regions in the direct path of the shock wave. The remaining edges of the samples used for characterization, therefore, have complex residual effects which contribute to the observed behavior. Indeed, studies

of the thermal crystallization behavior of MGs indicates that order would likely evolve in a similar medium-range to long-range path [111]. In addition to the thermal effects dominating the transformation mechanisms, there may be contributing factors from initial local reorganization behind the shock front, as observed in the lower pressure undeformed sample regime, as well as from Ce 4f delocalization allowing for a wider range of structural reorganization options. The visibly deformed layer 9 remains entirely amorphous, indicating thermal effects may not be enough for crystallization. Deformation-based STZs may compete with densification due to compression in layer 9, similar to trends in the uncompressed samples.

Recovered samples which show no apparent deformation appear to remain entirely amorphous but have indications of short and medium-range structural rearrangements. The magnitudes of the rearrangements increase and then decrease as distance from the shock front increases. For these undeformed samples, shock compression leads to short and medium-range ordering into a more dense amorphous phase. The changing effective magnitudes with distance from the shock front indicate competing mechanisms affecting the atomic structure changes.

Simulations have shown [38, 40] that the coordination number should increase with pressure when the shock pressures begin to overtake the Hugoniot Elastic Limit (HEL). This may be the cause of the first peak changes to shorter bond lengths in the PDFs of the shock compressed, undeformed samples. Due to the dynamic nature of laser shock loading, the coordination number increases after shock compression may remain trapped within the sample. Simulations also show [38, 40] STZs increase in number and homogeneity with increased pressures and cause an increase in overall shock-induced temperatures within the sample. The dilatory effects of both the STZs and elevated temperatures should therefore increase as the applied pressures increase up to the point of elevated temperatures which cause melting. The increased duration and magnitude of diffusion from the increased temperatures, accelerated by the STZs, may also cause the increases in density at

lower temperatures to relax back over the time the sample is elevated in temperature prior to recovery.

EXAFS data indicates Ce-based bonds are permanently shortened by shock compression, possibly implying Ce 4f delocalization affects the mechanisms of the observed shock induced structural changes. Therefore, an additional competing mechanism for atomic structure changes is possibly the 4f delocalization within Ce at elevated pressures. It is likely that the short-range order is increased in density purely because of effective Ce "shrinking" with pressure as the 4f electrons delocalize. Similar to the coordination number increases, the high strain rate dynamic shock compression loading may limit the ability of the sample to relax before being "trapped" in its final form, causing the short-range structure to have permanently shorter Ce-based bonds. This then translates to the second nearest-neighbor changes observed in Figure 6.21. The related trends for the first, second, and fourth nearest-neighbor changes are again possibly due to simultaneously shared effects of Ce "shrinking" on all length scales. The increase in peak position for the third nearest neighbors may be indicative of the method by which the amorphous structure accommodates and rearranges with the new SRO and MRO clusters. Further analysis of the atomic structure changes via simulation are needed to better understand the meaning of the peak shifts.

The recovered polyamorphous states observed in the undeformed samples and indications of medium-range to long-range order evolution in the deformed samples are, to the author's knowledge, the first such experimental findings of their kind for shock compression of a metallic glass.

6.5 Summary

High energy, Omega laser-based shock-compression experiments were performed on a multilayer (stacked) arrangement of Ce_3Al MG samples. Dispersion of the shock wave allowed for decreasing effective pressures in the layers of samples as the distance of the

sample from the initial shock front increased. The recovered shock compressed samples show two regimes: visibly deformed (layers 2-9) and visibly undeformed (layers 16-37) corresponding to pressures from 90 to 26 GPa and 12 to 6 GPa, respectively. Synchrotron characterization of the samples allowed for the creation of structure factor, PDF, and partial PDF trends. Within the deformed sample regime, there appears to be evidence of ordering on the short- and medium-range and on the long-range as pressure is increased. Within the higher pressure undeformed sample regime, the samples remain amorphous; however, the short and medium-range order change, indicating that these are shock-induced polyamorphs of the Ce_3Al MG. The trend of structural changes shows the beginning of a hysteresis effect in relation to applied pressure, potentially indicating competing mechanisms which may contribute to the observed polyamorphism.

CHAPTER 7
DISCUSSION OF OVERALL RESULTS

7.1 Summary of Key Results

In this work, the thermal and shock-compression behavior of Ce_3Al MG was characterized. The goal was to characterize the atomic structure of the metallic glass, structural changes associated with the imposed temperature and pressure, and to determine the mechanisms for observed structural changes. A summary of the key results and findings are listed below.

Thermal Characteristics of Ce_3Al MG

1. Ce_3Al MG has a reduced glass transition temperature of 0.43, significantly below the value of 0.67 of a "good" glass former, and a fragility of $\sim$11.8, which is indicative of a very "strong" glass. These values indicate that Ce_3Al MG has poor resistance to nucleation of crystallites and strong resistance to growth of crystallites.

2. The frequency factor for crystallization was calculated to be 4.3×10^{19}, which is relatively high and indicative of a large number of nuclei (GUMs) in the glass resulting in easy and rapid nucleation.

3. Crystallization upon heating is observed to occur in two-stages wherein a metastable state forms first and fully converts to the observed α-Ce_3Al phase during the second stage.

4. Activation energies calculated for the onset of each stage of crystallization are relatively low, while the activation energies calculated for the peak of crystallization are higher, indicating an ease for nucleation but greater difficulty for crystallite growth. A low glass transition activation energy also signifies a low barrier for relaxation.

5. No exothermic event is observed on re-heating thermally crystallized samples, indicating significant thermal stability of the nanocrystalline structure.

6. Avrami number and dimensionality constants were calculated to be 3 and 2, respectively, representing, with some uncertainty, a 2D crystallization behavior. TEM SAED analysis showed preferred [020] orientation of crystallites, and XRD results indicate limited avoidance of [020] orientations, suggesting that the growth mechanism is highly heterogeneous or textured in the bulk.

Nd:YAG 3 J Laser-Driven Shock-Compression Studies

1. Particle velocity measurements during laser shock driven experiments reveal a particle velocity profile with a well-defined elastic precursor preceding the main wave for the Ce_3Al MG. The elastic wave has a magnitude of $\sim$1.8 GPa, while the second wave increases in magnitude with increasing laser energies.

2. Shock compressed samples recovered from experiments performed below the elastic limit show limited crystallization, while those at higher pressures (laser energy) show increased density, complete crystallization into the α-Ce_3Al phase with a grain size of 13 nm, and preferred orientation with a preference for [002] directionality changing to [020] directional preference at the highest shock pressures.

Omega 50 J Laser-Driven Shock-Compression Studies

1. Two regimes of shock-compression response are observed in the Ce_3Al MG in experiments performed using the Omega laser. Samples with visible deformation, damage, and crystallization (stack of sample layers closest to the shock front) and visibly undeformed samples (sample layers furthest from the shock front) with densification of the amorphous phase occurring via complex atomic rearrangements indicative of polyamorphism.

2. The recovered visibly deformed sample layers showed crystallization and order as a function of decreasing depth. Sample layers closest to the shock front showed LRO evolution with complete crystallization, significant MRO peak evolution while still remaining predominantly amorphous and high density SRO and limited MRO evolution in layers farther from the shock front.

3. The first, second, and fourth peaks of PDF for undeformed samples show decreased distances (representative of decreased bond lengths) and the third peaks showed an increase in position, representative of increased bond lengths. These atomic rearrangements are more complex than would be observed with simple compression or relaxation and result in density increases of 2-6%.

4. The magnitude of shift in PDF peaks for undeformed samples was shown to increase with further distance from shock front and therefore lower applied pressures, suggesting competing effects of dilation and densification on the atomic rearrangements.

The observed shock-compression-induced structural changes are the first of their kind and merit further discussion of potential mechanisms in the following section. A summary of the Rietveld-calculated properties observed for the crystalline sample XRD data are presented in Table 7.1. All samples crystallized from the MG phase result in formation of the hexagonal α-Ce_3Al phase with nanocrystalline grain sizes, smaller lattice parameters, and higher densities calculated from the lattice parameters. Preferred orientation is presented in relation to the [020] direction. Positive preferred orientation values represent a preference for this direction, and negative values imply avoidance of this direction.

Table 7.1: Comparison of reference α-Ce_3Al and Rietveld analysis results for recovered crystalline Nd:YAG and OMEGA shock-compressed and thermally crystallized Ce_3Al metallic glass ribbons. The shock-formed and thermally crystallized α-Ce_3Al phases are more dense, have smaller grain sizes, and have a smaller unit cell than the equilibrium phase. All preferred orientation is presented in terms of [020]. Positive values indicate preference for [020], and negative values suggest avoidance.

Sample	Density (g/cm^3)	Grain Size (nm)	Pref. Orient. [hkl] | %	Lattice Param. c | a (Å)
Reference α-Ce_3Al	6.34	100+	0%	5.451 | 7.043
Thermally Crystallized	6.59 ± 0.01	6.2 ± 0.3	[020] | $-10 \pm 5\%$	5.380 ± 0.005 | 6.958 ± 0.004
Nd:YAG 0.4 J Shock	6.42 ± 0.01	13.2 ± 1.1	[020] | $-31 \pm 3\%$	5.426 ± 0.002 | 7.017 ± 0.002
Nd:YAG 0.5 J Shock	6.48 ± 0.01	9.1 ± 0.1	[020] | $-11 \pm 2\%$	5.424 ± 0.002 | 6.986 ± 0.002
Nd:YAG 1 J Shock	6.47 ± 0.01	8.3 ± 0.1	[020] | $+23 \pm 2\%$	5.420 ± 0.003 | 6.995 ± 0.002
Nd:YAG 1.5 J Shock	6.48 ± 0.01	8.9 ± 0.4	[020] | $+42 \pm 1\%$	5.390 ± 0.006 | 7.010 ± 0.003
OMEGA 50 J Shock	6.53 ± 0.01	9.6 ± 0.4	[020] | $-40 \pm 5\%$	5.406 ± 0.003 | 6.972 ± 0.003

7.2 Structural Characteristics of Ce_3Al MG

Ce_3Al Metallic Glass

The Ce_3Al metallic glass is a binary MG which has "poor" stability with a small barrier to and many sites for nucleation of crystallites. The poor glass formability requires the glassy phase to be formed from the melt at very rapid cooling rates and limits sample geometries to melt-spun ribbons. Interestingly, the Ce_3Al MG also has a strong resistance to crystallite growth.

The amorphous structure of Ce_3Al MG showed evidence of broad XRD (Fig 3.4) peaks and loss of any measurable order at a radial distance from a representative center atom of 20 Å (Fig 3.5). The short-range order (nearest neighbors and second nearest neighbors) in the amorphous structure match well with that of the crystalline α-Ce_3Al phase although the higher order nearest neighbors are less clearly similar (Fig 3.6). There is no elemental segregation in the initial amorphous Ce_3Al detectable within a nanometer-resolution (Fig 3.9& 3.8).

Thermally Crystallized Ce_3Al MG Structure

Thermal crystallization of Ce_3Al MG occurs via two stages, starting with an initial metastable structure which on average entirely converts to α-Ce_3Al phase during the second stage (Fig 3.3& 4.1). However, TEM results indicate some of the initial phase remains after complete crystallization, segregated in rings around the main α-Ce_3Al and creating domain-like structures which get preferentially removed due to sample-preparation (Fig 4.10& 4.11). Both TEM and XRD results indicate the overall final grain size is on the order of 6 nm with much shorter lattice parameters than that observed in microcrystalline or larger grain α-Ce_3Al intermetallic. Both of these trends are expected for nanocrystalline metals formed from MGs. The crystallites formed have slight [002] preferred orientations.

The short-range order observed via PDF (first, second, and third nearest neighbors) ap-

pear to be similar to the initial amorphous phase with only slightly narrow peaks, indicative of significant distortion remaining in the atomic-scale structure after thermal crystallization. Short and medium-range order matches well with the structure expected for α-Ce_3Al (Fig 4.16). The Ce-specific partial PDF results indicate that significant rearrangement occurs in Ce-based bonds after thermal crystallization with the main peak intensity equally distributing into the first three peaks with an overall shift to lower bond lengths (Fig 4.17).

Structure of Hydrostatically Compressed Ce_3Al MG

Under hydrostatic compression, Ce_3Al MG has been observed to undergo a rapid decrease in the first peak position of the structure factor from 1.5 to 5 GPa, indicating a rapid increase in density [30, 29]. Further characterization and simulations show the cause for densification is formation of more, shorter Ce-based bonds as Ce effectively "shrinks" with increasing amounts of 4f delocalization from 1.5 to 5 GPa. As pressure is increased beyond 5 GPa, the P-V compressibility follows a standard trend representative of the higher density amorphous phase.

At 25 GPa, however, an instantaneous and complete crystallization into a single crystal of FCC phase occurs. This crystallization is attributed to long-range topological order of the FCC phase retained within the amorphous Ce_3Al MG due to the Ce and Al each forming FCC phases on their own. Hume Rothery rules for solid solutions are achieved as atomic sizes are more similar after 4f delocalization in Ce at high pressures [176, 45]. There is no α-Ce_3Al phase formed under hydrostatic pressure conditions.

Structure of Shock Compressed Ce_3Al MG

Two regimes of structural changes are observed for shock-compressed Ce_3Al MG: low pressure where no macroscopic deformation is observed and higher shock pressure regime where macroscopic deformation is observed. In the lower shock pressure regime, the samples remain fully amorphous. Polyamorphous reorganization is observed in some of these

samples, with the first peak of the structure factor moving to lower Q values indicative of overall density increases on the order of 2-6% (Fig 6.15), significantly greater than the maximum 1% increase observed from relaxation. Additionally, the PDF results indicate that the nearest neighbors, second nearest neighbors, and fourth nearest neighbors are all closer while the third nearest neighbors are farther apart after shock compression (Fig 6.21). The Ce-specific bonds maintain the same overall distribution with a slight increase in magnitude and a limited decrease in the main peak position, indicating a permanent decrease in Ce-based bond lengths and increase in number of bonds of this length (Fig 6.22). These two changes are indicative of shock pressure-induced 4f delocalization allowing for tighter nearest neighbor packing.

The higher shock pressure regime results in crystallization into the α-Ce_3Al phase and shows a trend of increasing crystallization with increasing pressures. Further, this crystallization evolves with increasing pressure, first with denser SRO and the evolution of structure factor peaks similar in position to those of the crystalline phase, then MRO evolution matching the crystalline phase, and finally formation of the LRO. With further increased shock pressures, the α-Ce_3Al *"c"* lattice parameter decreases and [020] preferred orientation increases. Initial increases in pressure also break apart grains into smaller sizes and increase the density within crystallites (Table 7.1). Interestingly, the Ce-specific partial PDF for the shock-crystallized Ce_3Al shows no significant changes in the amplitude or distribution of the bonds, although the bond length is significantly shorter than in the lower energy polyamorphous condition. This indicates the shock-induced crystalline phase maintains a somewhat similar Ce-based SRO to that of the initial amorphous MG.

7.3 Differences in Thermal and High Pressure Stability of Ce_3Al MG

Thermal crystallization of Ce_3Al progresses purely via a two-stage diffusion process. The thermally crystallized α-Ce_3Al structure has 6 nm grain sizes, small lattice parameters, and high densities. Previous work by Zeng et al.[29] has shown that Ce_3Al MG thermally

crystallizes into α-Ce_3Al even under additional hydrostatic pressure. When pressure is increased up to the onset of 4f delocalization, the temperature for crystallization is reduced, indicating pressure can mediate diffusion-based crystallization. However, at hydrostatic pressures above 1.5 GPa, the crystallization temperature increases, with the difference attributed to the higher density amorphous structure retarding diffusion. The FCC phase of Ce_3Al is, however, not observed to form with heating at the hydrostatic pressures characterized. The FCC Ce_3Al phase has only been observed under high hydrostatic compression (pressures $>$ 25 GPa).

Shock-compression induced crystallization results in formation of the α-Ce_3Al phase. Shock-induced crystallization occurs concomitantly with plastic deformation at shock pressures exceeding the Hugoniot Elastic Limit. The shock-crystallized α-Ce_3Al samples have significantly more [002] preferred orientation, as compared with the thermally crystallized α-Ce_3Al phase, which change to [020] preferred orientation at higher shock pressures. The shock-induced α-Ce_3Al and polyamorphous phases maintain similar Ce-based SRO distributions with only shorter bonds. In comparison, the thermally crystallized α-Ce_3Al phase has a significant redistribution of Ce-based SRO.

The overall results indicate that the Ce_3Al MG ribbons investigated in the present work thermally crystallizes via typical diffusion mechanisms, resulting in formation of nearly spherical (in bulk) α-Ce_3Al crystallites with an average grain size of 6 nm and densities of 6.59 g/cm^3. Shock-induced crystallization of Ce_3Al MG occurs via a non-diffusional process through a combination of Ce 4f delocalization, shear-driven reorganization, and localized increases in free volume in shear bands. Shock induced crystallization produces, at the first stages of complete crystallization, [002] preferred crystallites with average grain sizes of 10 - 13 nm and densities of 6.42 - 6.53 g/cm^3. Increasing shock pressures increases the density and reduces the grain size up to a point but increasingly results in [020] preferred orientation. The mechanism and characteristics of the shock induced crystallized Ce_3Al MG are different from the hydrostatic pressure-induced crystallization of Ce_3Al MG which

occurs via a coordinated and instantaneous rearrangement of all atoms into the FCC-Ce_3Al phase.

The dilatory effects and increased driving forces caused by shear bands and shock-induced heating are the likely causes of larger grain sizes in the shock-induced α-Ce_3Al phase as compared to the thermally crystallized phase. Similarly, the larger grain sizes reduce the effects (see Chapter 2) which cause decreased lattice parameters and increased densities (as in the thermally crystallized α-Ce_3Al). Needle-like preferred orientation is expected during the nucleation stage (up to $\sim$2 nm) of thermally induced crystallization, but with increased growth it is expected to convert into plate-like and then spherical crystallites. The crystallization during shock compression occurs in a nucleation-like collective rearrangement with limited kinetic allowance for growth, resulting in larger crystallites. The increased density, decreased grain size, and conversion to more [020] preferred orientations with higher shock pressures is possibly caused by a combination of larger driving forces allowing for the formation of the lower surface energy-to-volume plate-like structures and higher densities with simultaneous breaking apart of grains into smaller sizes.

CHAPTER 8
CONCLUSIONS AND SUGGESTIONS FOR FUTURE WORK

8.1 Conclusions

In this work, shock-compression induced structural changes were investigated in a binary Ce_3Al MG. The Ce_3Al MG has a low barrier to nucleation and a high barrier to growth of crystallites, with many nucleation sites available, indicating a large amount of geometrically unfavored motifs (GUMs) in the initial structure.

Thermal crystallization of Ce_3Al MG occurs in two-stages, with the first metastable stage almost entirely converting into α-Ce_3Al with the remaining amount distributed in domain-like rings around the α-Ce_3Al phase. The stable thermally crystallized α-Ce_3Al phase grain size is 6 nm, with significantly higher density than microcrystalline α-Ce_3Al due to shorter lattice parameters within the grains.

Shock-compression of Ce_3Al results in two regimes of changes as a function of shock pressure. Higher shock pressures result in visibly deformed and damaged samples which show evolution of crystallization into α-Ce_3Al via SRO, then MRO, and finally LRO development. At lower shock pressures, the recovered samples show shock-induced polyamorphism which increases in magnitude with decreased shock pressures before decreasing, indicating there are competing mechanisms for change between dilatory effects of heat and possibly shear transformation zones and densification effects of shear and Ce 4f delocalization.

Shock crystallized α-Ce_3Al phase has grain sizes of 9 - 13 nm with shorter lattice parameters and higher densities than the microcrystalline reference but larger lattice parameters and lower densities than the thermally crystallized α-Ce_3Al phase. Ce-specific SRO densification with few rearrangements is observed in the shock-induced α-Ce_3Al which dif-

fers from the significant Ce-specific SRO rearrangements observed in the thermally crystallized α-Ce_3Al phase. The differences in structure are due to the coordinated diffusion-less nucleation from a large cluster of atoms which occurs during shock crystallization as compared to the diffusional nucleation and growth incurred with thermal crystallization.

8.2 Suggestions for Future Work

There are several areas where further investigation could be performed to build off and grow the understanding of the shock-compression induced phase changes observed in this work.

1. Time-resolved studies of structure evolution during shock compression, such as may be available at the Linac Coherent Light Source (LCLS) or Dynamic Compression Sector (DCS), and MD simulations of the structural changes concomitant with shock compression in Ce_3Al MG would help elucidate the timing and stages of structural rearrangements induced with shock compression. Comparisons with the recovered structures would allow for better determination of the mechanisms for observed phase changes.

2. Development of an equation of state for the crystalline and amorphous forms of Ce_3Al MG would allow for more accurate simulations of the loading conditions imposed with shock-loading. Correlations of the loading conditions with the observed structural changes would improve mechanistic explanations.

3. Characterization of the recovered structures of Zr-based and Cu-based MG after shock compression would help determine if the observed phase changes are specific to MG compositions with solvent atoms which can undergo have pressure-induced electronic structure changes, or are more generally MG structure dependent.

Appendices

APPENDIX A
THERMAL ANALYSIS

This section of the appendix presents further detail and images for the methodology used during differential scanning calorimetry (DSC) characterization of the Ce_3Al MG. In particular, the DSC peak fitting methodology will be expanded upon and example images will be provided.

A.1 Differential Scanning Calorimetry

Peak fitting was performed within the Netzsch Proteus Thermal Analysis software included with the Netzsch DSC 404 F1 used for the thermal analysis studies. The peaks values are determined by finding the largest thermal value (μV/mg) in a range. The onset values are determined by fitting linear slopes to the rise or fall of the peak and previous region. Similarly, the glass transition is determined by a fit to the baseline trend prior to the glass transition event and a fit to the regime following.

Figure A.1 shows an example of the output set of peak, onset, and Tg values for the Ce_3Al MG heated at 15 K/min.

Figure A.2 shows a screenshot of the Proteus Thermal Analysis software wherein the Tg value was determined. The left bound was chosen to be in a region which was relatively flat in terms of μV/mg vs temperature and in the first differential μV/mg vs temperature. The right bound was chosen to be the peak of the first differential for the subsequent peak, so as to capture the trend of the rise and not the trend after the change in curvature.

Figure A.3 shows a screenshot of the Proteus Thermal Analysis software wherein the first crystallization event onset temperature was determined. The left bound was chosen to be in a region which was relatively flat in terms of μV/mg vs temperature and in the first differential of μV/mg vs temperature. The right bound was chosen to be the peak of the first

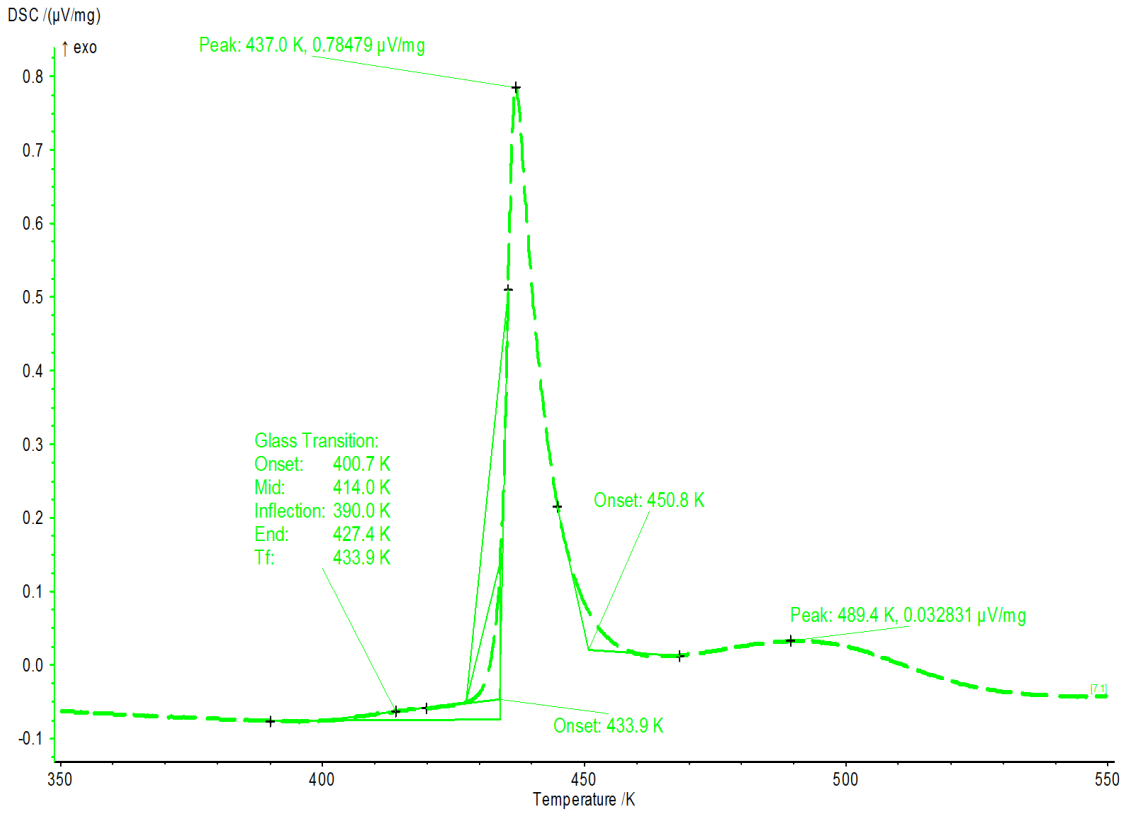

Figure A.1: DSC trace output from the Proteus Thermal Analysis software for the Ce_3Al MG heated at 15 K/min in 45 ml/min ultra-high purity argon flow. The fit glass transition, first crystallization onset, first crystallization, second crystallization onset, and second crystallization peak temperatures are labeled.

differential for the subsequent peak, so as to capture the trend of the entire rise (including change in curvature) and avoid the region of peak intensity descent.

.

Figure A.4 shows a screenshot of the Proteus Thermal Analysis software wherein the second crystallization event onset temperature was determined. The left bound was chosen iteratively to allow for the software to fit a proper trend to the slope of the descent of the first exothermic event peak. The right bound was chosen to be in a region after the onset which is relatively flat in terms of µV/mg vs temperature and in the first differential of µV/mg vs temperature.

.

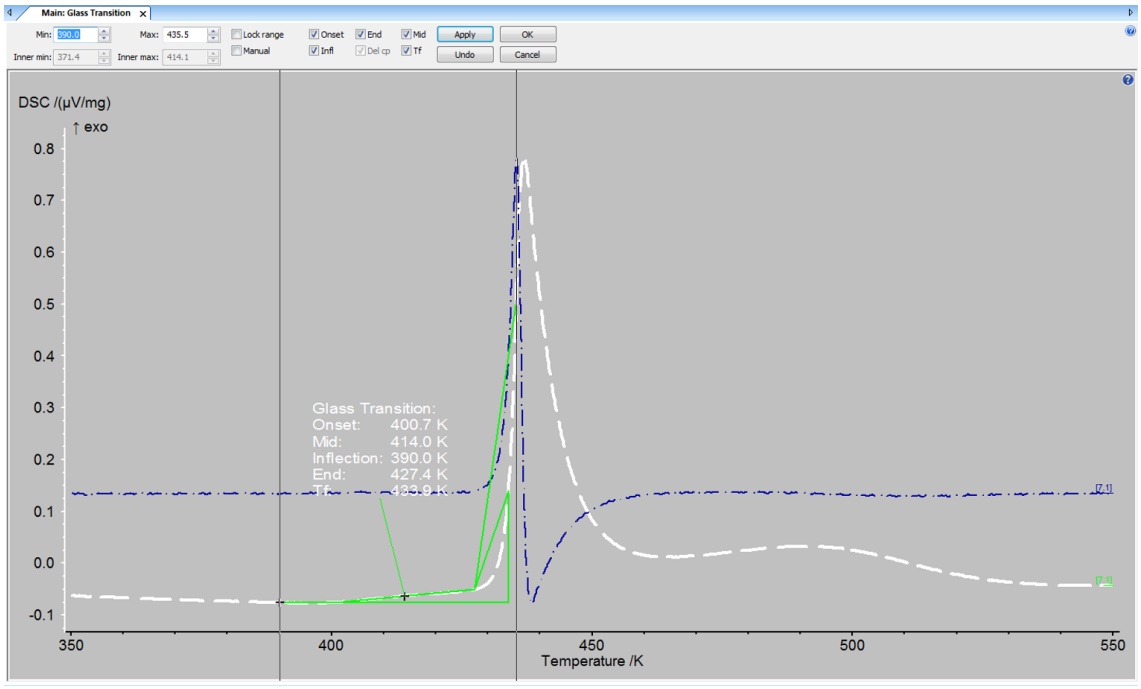

Figure A.2: Screenshot of Proteus Thermal Analysis software for the T_g fitting methodology. Bounds are chosen to ensure proper meaning is derived. DSC trace shown is the Ce_3Al MG sample heated at 15 K/min.

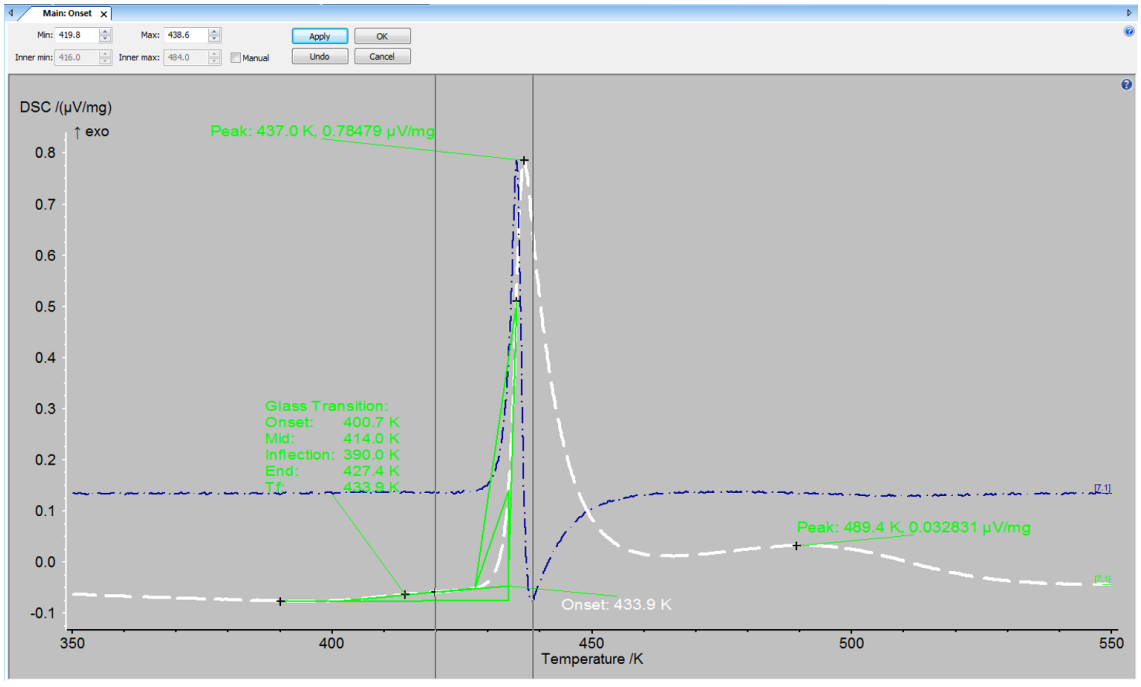

Figure A.3: Screenshot of Proteus Thermal Analysis software for the T_{x1} fitting methodology. Bounds are chosen to ensure proper meaning is derived. DSC trace shown is the Ce_3Al MG sample heated at 15 K/min.

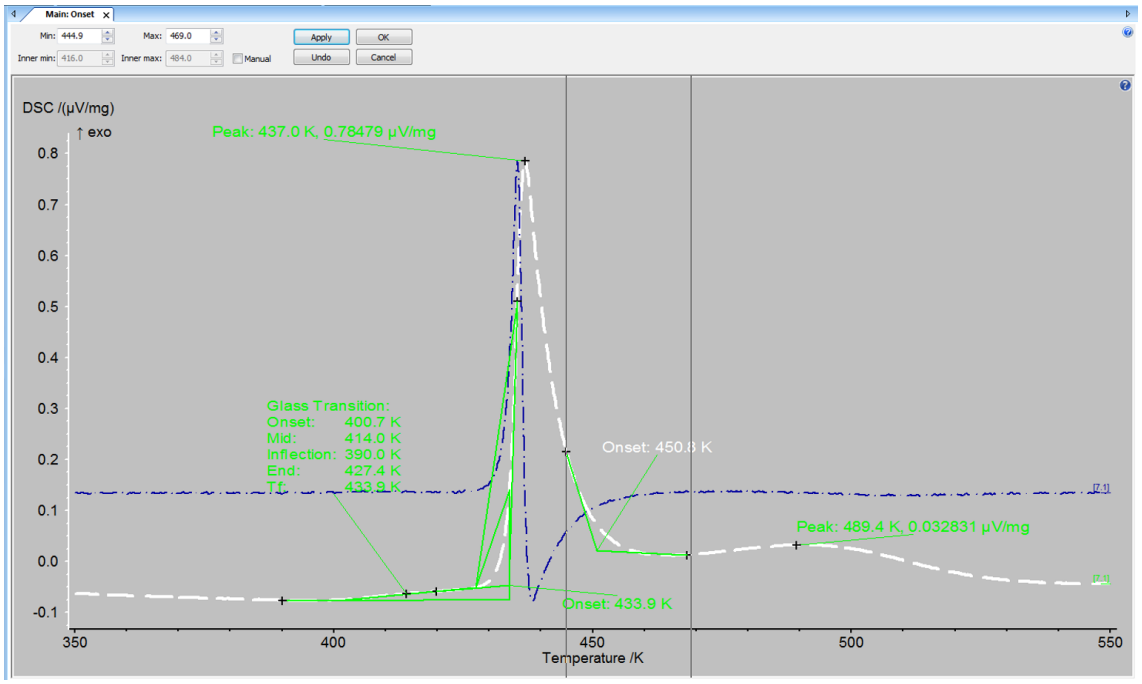

Figure A.4: Screenshot of Proteus Thermal Analysis software for the T_{x2} fitting methodology. Bounds are chosen to ensure proper meaning is derived. DSC trace shown is the Ce_3Al MG sample heated at 15 K/min.

APPENDIX B

X-RAY DIFFRACTION DATA ANALYSIS AND CONVERSION

This Appendix section will present information about the methodology for analyzing synchrotron 2D X-ray diffraction (XRD) data. This includes the development and use of a mask and conversion to 1D using Fit2D software.

B.1 Creating a mask for Fit2D

The creation of a mask is done to ensure the erroneous portions of the raw 2D data are not integrated into the 1D data, causing the peaks to be misshapen or unreal as well as significantly affecting the slope of the curve at high angles. The latter is important for pair distribution function calculations as erroneous high angle values cause the PDF values to be inaccurate. Figure B.1 shows an example of the raw 2D diffraction pattern of a reference Ni powder. Figure B.2 shows an example of the same diffraction pattern with a mask included.

To create the mask, select the "mask" option of the Fit2D graphical user interface. There will be options for drawing shapes as well as automatically masking based on thresholds. The goal is to automatically threshold any obviously erroneous data points which represent dead pixels on the 2D detector as well as to draw a mask to cover the beam blocker and whichever sections of the scan represent areas where the X-rays will have scattered off things other than the sample (e.g., the beam blocker or sample stage) and therefore would produce XRD patterns that are not representative of the actual sample. In Figure B.2, the top area is representative of the bottom area of Fig 3.16, where there is a chance X-rays scattered off the sample subsequently scattered off the sample holder or beam blocker.

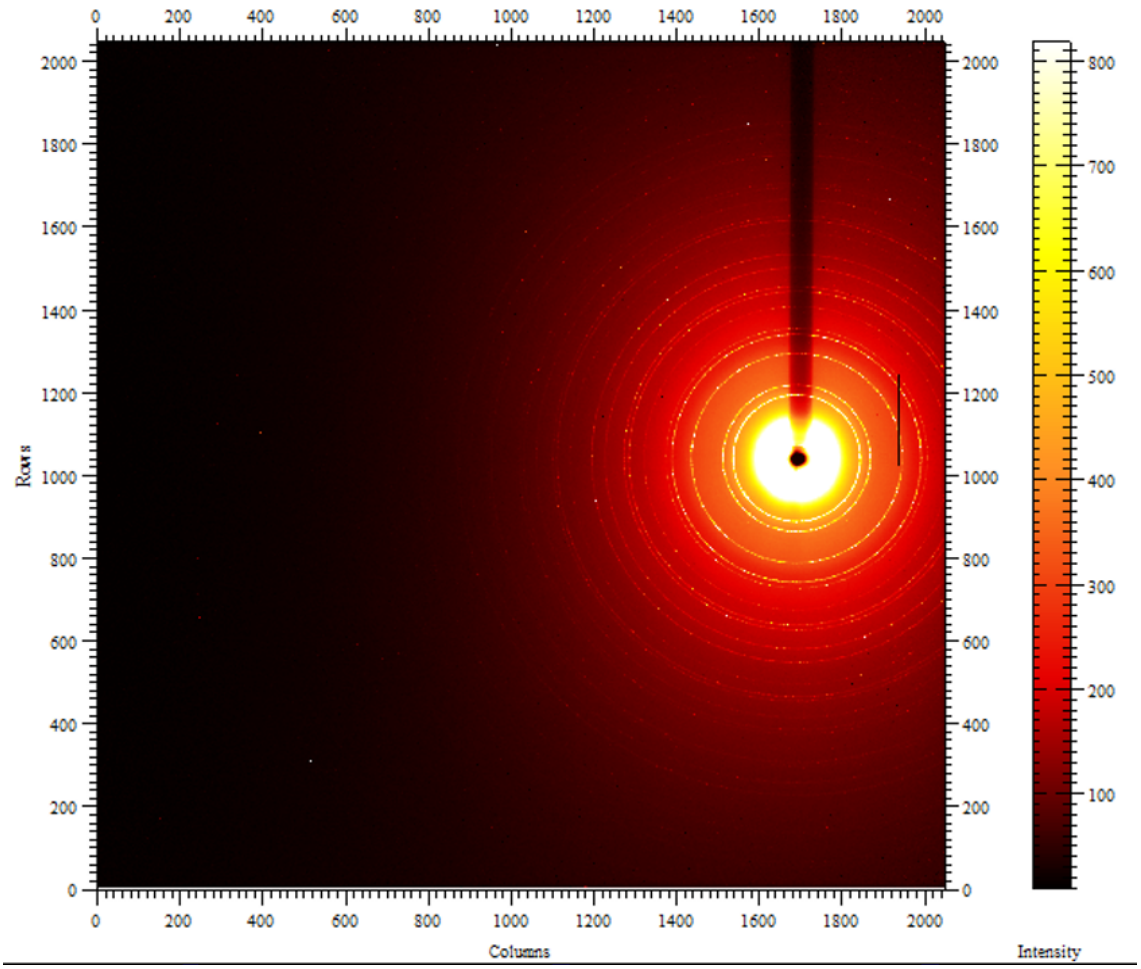

Figure B.1: Example 2D diffraction pattern for a Ni reference powder. The beam blocker is visible as a rod blocking coming from the top of the image to block the center of the rings where the incident X-rays were measured. Very clear detector artifacts are visible like the vertical black line to the right of the beam center and a white pixel in the bottom left corner.

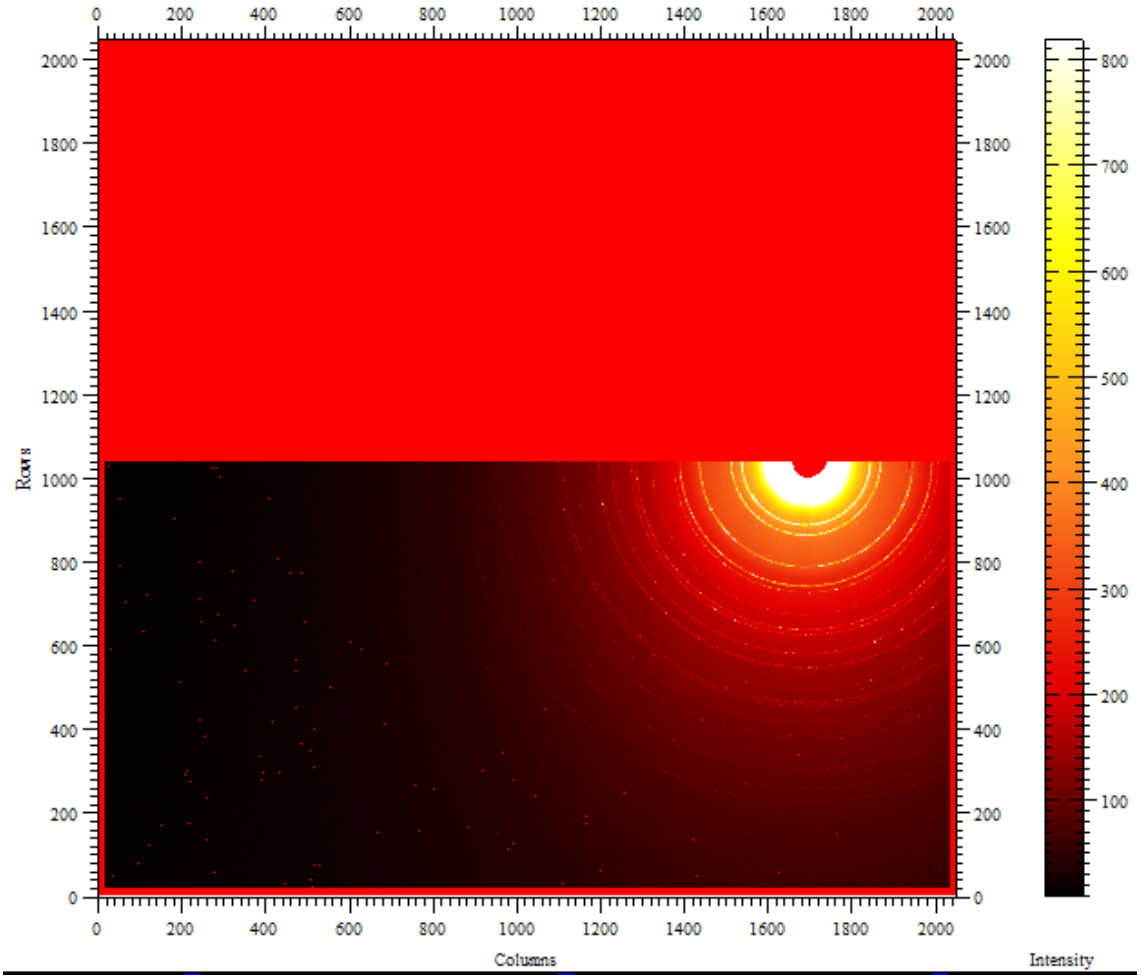

Figure B.2: Example 2D diffraction pattern for a Ni reference powder with a mask applied over top. The mask is visible as bright red spaces and means the data covered will not be integrated when converting to 1D. It is difficult to see the red on the previously vertical black line due to the similarity of color with the data behind it, but there is a red line now covering that black line. Similarly, red dots in the bottom left corner represent dead pixels which were covered after thresholding.

B.2 Converting from 2D to 1D XRD

In order to convert the 2D pattern to a 1D pattern in Fit2D, simply select “Integrate” in the drop down box below the data set, as shown in Figure B.3. Save the output as a “chi” file for further data processing.

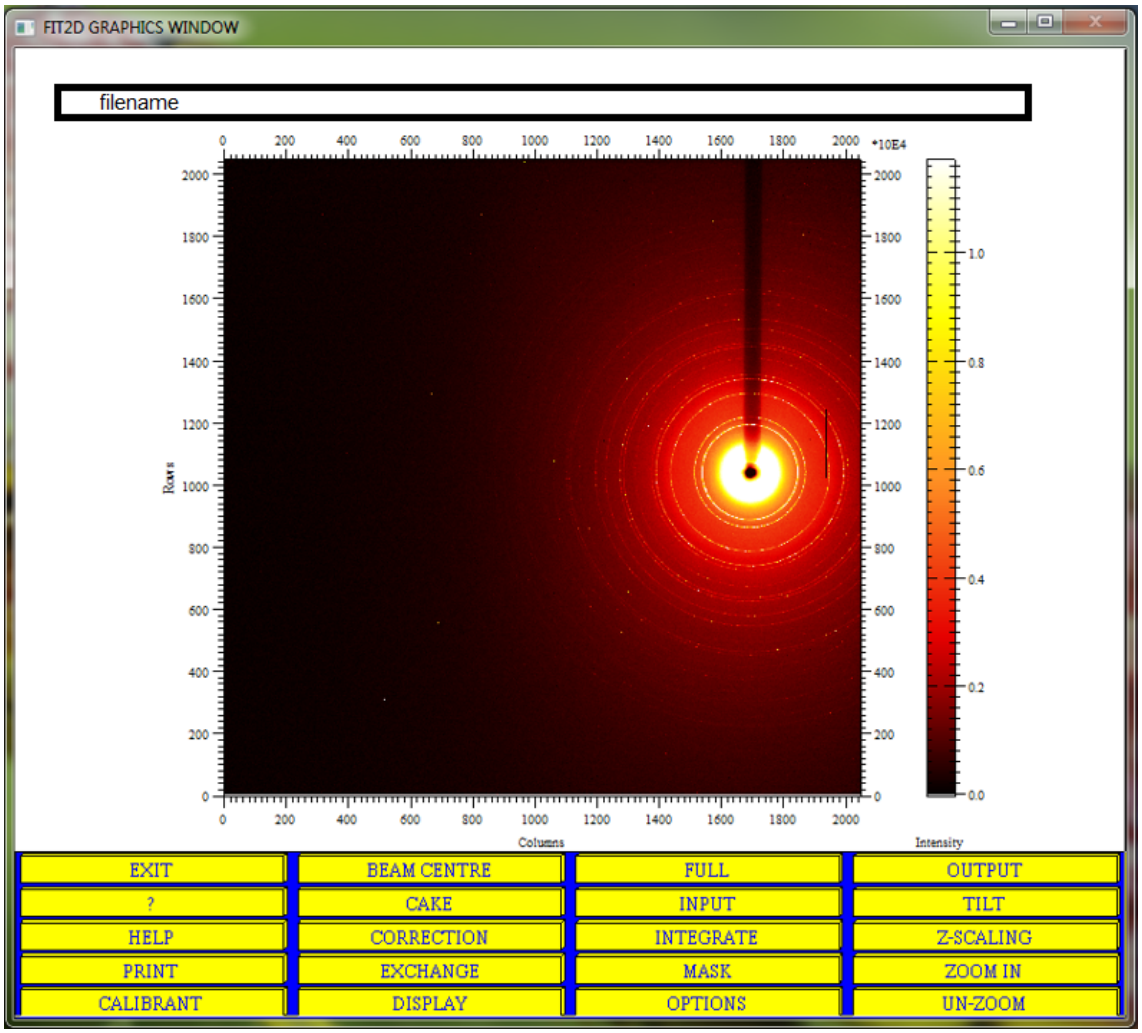

Figure B.3: Example Fit2D software interface showing options for data analysis. When the 2D data is corrected as you might wish (e.g., masked), select “Integrate” to convert 1D.

APPENDIX C

PAIR DISTRIBUTION FUNCTION ANALYSIS

This section of the appendix will cover details for the determination of the values used in the conversion from 1D diffraction data to the pair distribution function for the measured Ce_3Al MG data. The method of conversion to total PDF is discussed in Section 3.4.3.

C.1 Conversion from 1D XRD to reduced PDF

The process of using PDFgetX3 to convert from a 1D diffraction data set to the reduced PDF and structure factor is covered in detail in the documentation for the software. In order to best optimize, we used manually determined scale factors for each data set. Since the synchrotron intensity fluctuates with time, there was no one relation between the reference background scan and measured data. The value of the scale factor was determined by manually adjusting a multiplicative scale factor for the XRD background reference data as compared to the sample data such that the low angle values overlapped, erring on the side of a lower background than sample if it appeared to follow a different pattern.

REFERENCES

[1] C Suryanarayana and A. Inoue, *Bulk metallic glasses*. CRC Press, 2010.

[2] T. M. Hayes, J. W. Allen, J. Tauc, B. C. Giessen, and J. J. Hauser, "Short-Range Order in Metallic Glasses," *Physical Review Letters*, vol. 40, no. 19, pp. 1282–1285, May 1978.

[3] L. Zhang, Y. Wu, X. Bian, H. Li, W. Wang, and S. Wu, "Short-range and medium-range order in liquid and amorphous $Al_{90}Fe_5Ce_5$ alloys," *Journal of Non-Crystalline Solids*, vol. 262, no. 13, pp. 169–176, Feb. 2000.

[4] H. W. Sheng, W. K. Luo, F. M. Alamgir, J. M. Bai, and E. Ma, "Atomic packing and short-to-medium-range order in metallic glasses," *Nature*, vol. 439, no. 7075, pp. 419–425, Jan. 2006.

[5] D. B. Miracle, "A structural model for metallic glasses," *Nature Materials*, vol. 3, no. 10, pp. 697–702, Oct. 2004.

[6] D. B. Miracle, "The efficient cluster packing model An atomic structural model for metallic glasses," *Acta Materialia*, vol. 54, no. 16, pp. 4317–4336, Sep. 2006.

[7] P. K. Gupta and D. B. Miracle, "A topological basis for bulk glass formation," *Acta Materialia*, vol. 55, no. 13, pp. 4507–4515, Aug. 2007.

[8] D. B. Miracle, A. L. Greer, and K. F. Kelton, "Icosahedral and dense random cluster packing in metallic glass structures," *Journal of Non-Crystalline Solids*, vol. 354, no. 34, pp. 4049–4055, Sep. 2008.

[9] D. B. Miracle, "A Physical Model for Metallic Glass Structures: An Introduction and Update," *JOM*, vol. 64, no. 7, pp. 846–855, Jul. 2012.

[10] D. B. Miracle, "The density and packing fraction of binary metallic glasses," *Acta Materialia*, vol. 61, no. 9, pp. 3157–3171, May 2013.

[11] T. C. Hufnagel, "Metallic glasses: Cryogenic rejuvenation," *Nature Materials*, vol. 14, no. 9, pp. 867–868, Sep. 2015.

[12] S. V. Ketov, Y. H. Sun, S. Nachum, Z. Lu, A. Checchi, A. R. Beraldin, H. Y. Bai, W. H. Wang, D. V. Louzguine-Luzgin, M. A. Carpenter, and A. L. Greer, "Rejuvenation of metallic glasses by non-affine thermal strain," *Nature*, vol. 524, no. 7564, pp. 200–203, Aug. 2015.

[13] W. Dmowski, Y. Yokoyama, A. Chuang, Y. Ren, M. Umemoto, K. Tsuchiya, A. Inoue, and T. Egami, "Structural rejuvenation in a bulk metallic glass induced by severe plastic deformation," *Acta Materialia*, vol. 58, no. 2, pp. 429–438, Jan. 2010.

[14] D. Pan, Y. Yokoyama, T. Fujita, Y. H. Liu, S. Kohara, A. Inoue, and M. W. Chen, "Correlation between structural relaxation and shear transformation zone volume of a bulk metallic glass," *Applied Physics Letters*, vol. 95, no. 14, p. 141 909, Oct. 2009.

[15] T. Yano, Y. Yorikado, Y. Akeno, F. Hori, Y. Yokoyama, A. Iwase, A. Inoue, and T. J. Konno, "Relaxation and Crystallization Behavior of the $Zr_{50}Cu_{40}Al_{10}$ Metallic Glass," *Materials Transactions*, vol. 46, no. 12, pp. 2886–2892, 2005.

[16] H. C. Chen, "The influence of structural relaxation on the density and Youngs modulus of metallic glasses," *Journal of Applied Physics*, vol. 49, no. 6, pp. 3289–3291, Jun. 1978.

[17] K. F. Kelton and F. Spaepen, "Kinetics of structural relaxation in several metallic glasses observed by changes in electrical resistivity," *Physical Review B*, vol. 30, no. 10, pp. 5516–5524, Nov. 1984.

[18] A. L. Greer, Y. Q. Cheng, and E. Ma, "Shear bands in metallic glasses," *Materials Science and Engineering: R: Reports*, vol. 74, no. 4, pp. 71–132, Apr. 2013.

[19] H. Chen, Y. He, G. J. Shiflet, and S. J. Poon, "Deformation-induced nanocrystal formation in shear bands of amorphous alloys," *Nature*, vol. 367, no. 6463, p. 541, Feb. 1994.

[20] N. Boucharat, R. Hebert, H. Rsner, R. Z. Valiev, and G. Wilde, "Synthesis routes for controlling the microstructure in nanostructured $Al_{88}Y_7Fe_5$ alloys," *Journal of Alloys and Compounds*, Proceedings of the 12th International Symposium on Metastable and Nano-Materials (ISMANAM-2005), vol. 434-435, no. Supplement C, pp. 252–254, May 2007.

[21] K. Wang, T. Fujita, Y. Q. Zeng, N. Nishiyama, A. Inoue, and M. W. Chen, "Micromechanisms of serrated flow in a $Ni_{50}Pd_{30}P_{20}$ bulk metallic glass with a large compression plasticity," *Acta Materialia*, vol. 56, no. 12, pp. 2834–2842, Jul. 2008.

[22] A. Shibata, M. Sone, and Y. Higo, "Characterization of deformation-induced structural change of $Pd_{78}Cu_6Si_{16}$ metallic glass using a micro-sized cantilever-beam specimen," *Scripta Materialia*, vol. 62, no. 5, pp. 309–312, Mar. 2010.

[23] D. T. A. Matthews, V. Ocelk, P. M. Bronsveld, and J. T. M. De Hosson, "An electron microscopy appraisal of tensile fracture in metallic glasses," *Acta Materialia*, vol. 56, no. 8, pp. 1762–1773, May 2008.

[24] G. Wilde and H. Rsner, "Nanocrystallization in a shear band: An in situ investigation," *Applied Physics Letters*, vol. 98, no. 25, p. 251 904, Jun. 2011.

[25] F. O. Mar, B. Doisneau, A. R. Yavari, and A. L. Greer, "Structural effects of shot-peening in bulk metallic glasses," *Journal of Alloys and Compounds*, 14th International Symposium on Metastable and Nano-Materials (ISMANAM-2007), vol. 483, no. 1, pp. 256–259, Aug. 2009.

[26] F. Ye and K. Lu, "Crystallization kinetics of amorphous solids under pressure," *Physical Review B*, vol. 60, no. 10, pp. 7018–7024, Sep. 1999.

[27] J. Z. Jiang, J. S. Olsen, L. Gerward, S. Abdali, J. Eckert, N. Schlorke-de Boer, L. Schultz, J. Truckenbrodt, and P. X. Shi, "Pressure effect on crystallization of metallic glass $Fe_{72}P_{11}C_6Al_5B_4Ga_2$ alloy with wide supercooled liquid region," *Journal of Applied Physics*, vol. 87, no. 5, pp. 2664–2666, Feb. 2000.

[28] A. R. Yavari, K. Georgarakis, J. Antonowicz, M. Stoica, N. Nishiyama, G. Vaughan, M. Chen, and M. Pons, "Crystallization during Bending of a Pd-Based Metallic Glass Detected by X-Ray Microscopy," *Physical Review Letters*, vol. 109, no. 8, p. 085 501, Aug. 2012.

[29] Q. Zeng, V. V. Struzhkin, Y. Fang, C. Gao, H. Luo, X. Wang, C Lathe, W. L. Mao, F. Wu, H.-K. Mao, *et al.*, "Properties of polyamorphous $Ce_{75}Al_{25}$ metallic glasses," *Physical Review B*, vol. 82, no. 5, p. 054 111, 2010.

[30] Q.-s. Zeng, Y. Ding, W. L. Mao, W. Yang, S. V. Sinogeikin, J. Shu, H.-k. Mao, and J. Jiang, "Origin of pressure-induced polyamorphism in $Ce_{75}Al_{25}$ metallic glass," *Physical review letters*, vol. 104, no. 10, p. 105 702, 2010.

[31] Q. Zeng, H. Sheng, Y. Ding, L. Wang, W. Yang, J.-Z. Jiang, W. L. Mao, and H.-K. Mao, "Long-range topological order in metallic glass," *Science*, vol. 332, no. 6036, pp. 1404–1406, 2011.

[32] L. F. Liu, L. H. Dai, Y. L. Bai, and B. C. Wei, "Initiation and propagation of shear bands in Zr-based bulk metallic glass under quasi-static and dynamic shear loadings," *Journal of Non-Crystalline Solids*, vol. 351, no. 40, pp. 3259–3270, Oct. 2005.

[33] M. D. Demetriou and W. L. Johnson, "Shear flow characteristics and crystallization kinetics during steady non-isothermal flow of Vitreloy-1," *Acta Materialia*, vol. 52, no. 12, pp. 3403–3412, Jul. 2004.

[34] M. M. Trexler and N. N. Thadhani, "Mechanical properties of bulk metallic glasses," *Progress in Materials Science*, vol. 55, no. 8, pp. 759–839, 2010.

[35] M. Martin, T. Sekine, T. Kobayashi, L. Kecskes, and N. N. Thadhani, "High-Pressure Equation of the State of a Zirconium-Based Bulk Metallic Glass," *Metallurgical and Materials Transactions A*, vol. 38, no. 11, pp. 2689–2696, Aug. 2007.

[36] T. Mashimo, H. Togo, Y. Zhang, Y. Uemura, T. Kinoshita, M. Kodama, and Y. Kawamura, "Hugoniot-compression curve of Zr-based bulk metallic glass," *Applied Physics Letters*, vol. 89, no. 24, p. 241 904, Dec. 2006.

[37] L. Chen, D. Eakins, D. Chapman, N Thadhani, D. Swift, and M Kumar, "Dynamic behavior of a Ce-Al bulk metallic glass," in *Journal of Physics: Conference Series*, vol. 500, IOP Publishing, 2014, p. 112 016.

[38] W. R. Jian, X. H. Yao, L. Wang, X. C. Tang, and S. N. Luo, "Short- and medium-range orders in $Cu_{46}Zr_{54}$ metallic glasses under shock compression," *Journal of Applied Physics*, vol. 118, no. 1, p. 015 901, Jul. 2015.

[39] P. Wen, B. Demaske, D. E. Spearot, and S. R. Phillpot, "Shock compression of Cu_xZr_{100-x} metallic glasses from molecular dynamics simulations," *Journal of Materials Science*, vol. 53, no. 8, pp. 5719–5732, Apr. 2018.

[40] B. Arman, S.-N. Luo, T. C. Germann, and T. Cagin, "Dynamic response of $Cu_{46}Zr_{54}$ metallic glass to high-strain-rate shock loading: Plasticity, spall, and atomic-level structures," *Physical Review B*, vol. 81, no. 14, p. 144 201, Apr. 2010.

[41] W. L. Johnson, "Bulk Glass-Forming Metallic Alloys: Science and Technology," *MRS Bulletin*, vol. 24, no. 10, pp. 42–56, Oct. 1999.

[42] E. Ma, "Tuning order in disorder," *Nature Materials*, vol. 14, no. 6, pp. 547–552, Jun. 2015.

[43] U. Kster and U. Herold, "Crystallization of metallic glasses," in *Glassy Metals I*, H.-J. Gntherodt and H. Beck, Eds., vol. 46, Berlin, Heidelberg: Springer Berlin Heidelberg, 1981, pp. 225–259, ISBN: 978-3-540-10440-7 978-3-540-38477-9.

[44] H. W. Sheng, H. Z. Liu, Y. Q. Cheng, J. Wen, P. L. Lee, W. K. Luo, S. D. Shastri, and E. Ma, "Polyamorphism in a metallic glass," *Nature Materials*, vol. 6, no. 3, pp. 192–197, 2007.

[45] Q. Zeng, H. Sheng, Y. Ding, L. Wang, W. Yang, J.-Z. Jiang, W. L. Mao, and H.-K. Mao, "Long-range topological order in metallic glass," *Science*, vol. 332, no. 6036, pp. 1404–1406, 2011.

[46] Y. Q. Cheng and E. Ma, "Atomic-level structure and structureproperty relationship in metallic glasses," *Progress in Materials Science*, vol. 56, no. 4, pp. 379–473, 2011.

[47] B. R. Rao, "Bulk metallic glasses: Materials of future," *DRDO Science Spectrum*, pp. 212–218, 2009.

[48] D. Ma, A. D. Stoica, and X.-L. Wang, "Power-law scaling and fractal nature of medium-range order in metallic glasses," *Nature Materials*, vol. 8, no. 1, pp. 30–34, Jan. 2009.

[49] Q. Zeng, Y. Kono, Y. Lin, Z. Zeng, J. Wang, S. V. Sinogeikin, C. Park, Y. Meng, W. Yang, H.-K. Mao, and W. L. Mao, "Universal Fractional Noncubic Power Law for Density of Metallic Glasses," *Physical Review Letters*, vol. 112, no. 18, p. 185 502, May 2014.

[50] Q. Zeng, Y. Lin, Y. Liu, Z. Zeng, C. Y. Shi, B. Zhang, H. Lou, S. V. Sinogeikin, Y. Kono, C. Kenney-Benson, C. Park, W. Yang, W. Wang, H. Sheng, H.-k. Mao, and W. L. Mao, "General 2.5 power law of metallic glasses," *Proceedings of the National Academy of Sciences*, p. 201 525 390, Feb. 2016.

[51] T. Egami and S. J. Billinge, *Underneath the Bragg peaks: structural analysis of complex materials*. Elsevier, 2003, vol. 16.

[52] M. C. Wilding, M. Wilson, and P. F. McMillan, "Structural studies and polymorphism in amorphous solids and liquids at high pressure," *Chemical Society Reviews*, vol. 35, no. 10, pp. 964–986, Sep. 2006.

[53] J. Bednarcik, S. Michalik, V. Kolesar, U. Rtt, and H. Franz, "In situ XRD studies of nanocrystallization of Fe-based metallic glass: A comparative study by reciprocal and direct space methods," *Physical Chemistry Chemical Physics*, vol. 15, no. 22, pp. 8470–8479, May 16, 2013.

[54] H. J. Chang, E. S. Park, Y. C. Kim, and D. H. Kim, "Observation of artifact-free amorphous structure in CuZr-based alloy using transmission electron microscopy," *Materials Science and Engineering: A*, vol. 406, no. 1, pp. 119–124, Oct. 2005.

[55] L.-Y. Chen, Y. Zeng, Q.-P. Cao, B.-J. Park, Y. Chen, K. Hono, U. Vainio, Z.-L. Zhang, U. Kaiser, X.-D. Wang, and J.-Z. Jiang, "Homogeneity of the superplastic $Zr_{64.13}Cu_{15.75}Ni_{10.12}Al_{10}$ bulk metallic glass," *Journal of Materials Research*, vol. 24, no. 10, pp. 3116–3120, Oct. 2009.

[56] L.-Y. Chen, Q.-P. Cao, J. Z. Jiang, and J.-W. Deng, "Reply to the comments of Y.H. Liu: Ion sputter erosion in metallic glassA response to Comment on: Homogeneity of $Zr_{64.13}Cu_{15.75}Ni_{10.12}Al_{10}$ bulk metallic glassi by L-Y. Chen, Y-W. Zeng, Q-P. Cao, B-J. Park, Y-M. Chen, K. Hono, U. Vainio, Z-L. Zhang, U. Kaiser, X-D. Wang,and J-Z Jiang [J. Mater. Res. 24, 3116 (2009)]," *Journal of Materials Research*, vol. 25, no. 3, pp. 602–604, Mar. 2010.

[57] B. B. Sun, Y. B. Wang, J. Wen, H. Yang, M. L. Sui, J. Q. Wang, and E. Ma, "Artifacts induced in metallic glasses during TEM sample preparation," *Scripta Materialia*, vol. 53, no. 7, pp. 805–809, Oct. 2005.

[58] J. Li, Z. L. Wang, and T. C. Hufnagel, "Characterization of nanometer-scale defects in metallic glasses by quantitative high-resolution transmission electron microscopy," *Physical Review B*, vol. 65, no. 14, p. 144 201, Mar. 2002.

[59] A. Hirata, Y. Hirotsu, S. Kuboya, and T. G. Nieh, "Local structural fluctuation in PdNiP bulk metallic glasses examined using nanobeam electron diffraction," *Journal of Alloys and Compounds*, 14th International Symposium on Metastable and Nano-Materials (ISMANAM-2007), vol. 483, no. 1, pp. 64–69, Aug. 2009.

[60] M. Chen, A. Inoue, W. Zhang, and T. Sakurai, "Extraordinary Plasticity of Ductile Bulk Metallic Glasses," *Physical Review Letters*, vol. 96, no. 24, p. 245 502, Jun. 2006.

[61] G. Li, K. B. Borisenko, Y. Chen, D. Nguyen-Manh, E. Ma, and D. J. H. Cockayne, "Local structure variations in $Al_{89}La_6Ni_5$ metallic glass," *Acta Materialia*, vol. 57, no. 3, pp. 804–811, Feb. 2009.

[62] A. Hirata, P. Guan, T. Fujita, Y. Hirotsu, A. Inoue, A. R. Yavari, T. Sakurai, and M. Chen, "Direct observation of local atomic order in a metallic glass," *Nature Materials*, vol. 10, no. 1, pp. 28–33, Jan. 2011.

[63] E. Ma and Z. Zhang, "Amorphous alloys: Reflections from the glass maze," *Nature Materials*, vol. 10, no. 1, pp. 10–11, Jan. 2011.

[64] G. Cargill III, "Dense random packing of hard spheres as a structural model for non-crystalline metallic solids.," DTIC Document, Tech. Rep., 1969.

[65] D Weaire, M. Ashby, J Logan, and M. Weins, "On the use of pair potentials to calculate the properties of amorphous metals," *Acta Metallurgica*, vol. 19, no. 8, pp. 779–788, 1971.

[66] D. Polk, "The structure of glassy metallic alloys," *Acta metallurgica*, vol. 20, no. 4, pp. 485–491, 1972.

[67] N Valenkov and E Poray-Koshitz, "X-ray investigation of the glassy state," *Zeitschrift für Kristallographie-Crystalline Materials*, vol. 95, no. 1, pp. 195–229, 1936.

[68] B. Warren, "X-ray diffraction in random layer lattices," *Physical Review*, vol. 59, no. 9, p. 693, 1941.

[69] A. Bienenstock and B. G. Bagley, "Calculation of upper bounds to the small-angle scattering from crystallite models of amorphous materials," *Journal of Applied Physics*, vol. 37, no. 13, pp. 4840–4847, 1966.

[70] P. Maitrepierre, "Structure of Amorphous Ni-Pd-P and Fe-Pd-P Alloys," *Journal of Applied Physics*, vol. 40, no. 12, pp. 4826–4834, 1969.

[71] K. J. Laws, D. B. Miracle, and M. Ferry, "A predictive structural model for bulk metallic glasses," *Nature Communications*, vol. 6, p. 8123, Sep. 2015.

[72] W. K. Jun, R. H. Willens, and P. Duwez, "Non-crystalline Structure in Solidified GoldSilicon Alloys," *Nature*, vol. 187, no. 4740, pp. 869–870, Sep. 1960.

[73] J. H. Na, M. D. Demetriou, M. Floyd, A. Hoff, G. R. Garrett, and W. L. Johnson, "Compositional landscape for glass formation in metal alloys," *Proceedings of the National Academy of Sciences*, vol. 111, no. 25, pp. 9031–9036, Jun. 2014.

[74] J. Orava and A. L. Greer, "Fast and slow crystal growth kinetics in glass-forming melts," *The Journal of Chemical Physics*, vol. 140, no. 21, p. 214 504, Jun. 2014.

[75] A. L. Greer, *New horizons for glass formation and stability*, Comments and Opinion, May 2015.

[76] D. Turnbull, "Under what conditions can a glass be formed?" *Contemporary Physics*, vol. 10, no. 5, pp. 473–488, 1969.

[77] C. A Angell, "Relaxation in liquids, polymers and plastic crystals strong/fragile patterns and problems," *Journal of Non-Crystalline Solids*, Proceedings of the International Discussion Meeting on Relaxations in Complex Systems, vol. 131-133, pp. 13–31, Jun. 1991.

[78] B. Zhang, R. J. Wang, D. Q. Zhao, M. X. Pan, and W. H. Wang, "Properties of ce-based bulk metallic glass-forming alloys," *Physical Review B*, vol. 70, no. 22, p. 224 208, Dec. 2004.

[79] V. N. Novikov and A. P. Sokolov, "Poisson's ratio and the fragility of glass-forming liquids," *Nature*, vol. 431, no. 7011, pp. 961–963, Oct. 2004.

[80] M. Jiang and L. Dai, "Intrinsic correlation between fragility and bulk modulus in metallic glasses," *Physical Review B*, vol. 76, no. 5, p. 054 204, Aug. 2007.

[81] A. Inoue, "Stabilization of metallic supercooled liquid and bulk amorphous alloys," *Acta Materialia*, vol. 48, no. 1, pp. 279–306, Jan. 2000.

[82] M. Telford, "The case for bulk metallic glass," *Materials Today*, vol. 7, no. 3, pp. 36–43, Mar. 2004.

[83] Y. Q. Cheng, E. Ma, and H. W. Sheng, "Atomic Level Structure in Multicomponent Bulk Metallic Glass," *Physical Review Letters*, vol. 102, no. 24, p. 245 501, Jun. 2009.

[84] Y. Cheng, A. Cao, H. Sheng, and E. Ma, "Local order influences initiation of plastic flow in metallic glass: Effects of alloy composition and sample cooling history," *Acta Materialia*, vol. 56, no. 18, pp. 5263–5275, Oct. 2008.

[85] J. Ding, S. Patinet, M. L. Falk, Y. Cheng, and E. Ma, "Soft spots and their structural signature in a metallic glass," *Proceedings of the National Academy of Sciences*, vol. 111, no. 39, pp. 14 052–14 056, Sep. 2014.

[86] J. Xu and E. Ma, "Damage-tolerant ZrCuAl-based bulk metallic glasses with record-breaking fracture toughness," *Journal of Materials Research*, vol. 29, no. 14, pp. 1489–1499, Jul. 2014.

[87] J. Yi, W. H. Wang, and J. J. Lewandowski, "Sample size and preparation effects on the tensile ductility of Pd-based metallic glass nanowires," *Acta Materialia*, vol. 87, pp. 1–7, Apr. 2015.

[88] J. Ding, Y.-Q. Cheng, and E. Ma, "Full icosahedra dominate local order in $Cu_{64}Zr_{34}$ metallic glass and supercooled liquid," *Acta Materialia*, vol. 69, pp. 343–354, May 2014.

[89] Y. T. Shen, T. H. Kim, A. K. Gangopadhyay, and K. F. Kelton, "Icosahedral Order, Frustration, and the Glass Transition: Evidence from Time-Dependent Nucleation and Supercooled Liquid Structure Studies," *Physical Review Letters*, vol. 102, no. 5, p. 057 801, Feb. 2009.

[90] J. Ding, Y.-Q. Cheng, H. Sheng, and E. Ma, "Short-range structural signature of excess specific heat and fragility of metallic-glass-forming supercooled liquids," *Physical Review B*, vol. 85, no. 6, Feb. 2012.

[91] J. Ding, Y. Cheng, and E. Ma, "Charge-transfer-enhanced prism-type local order in amorphous $Mg_{65}Cu_{25}Y_{10}$: Short-to-medium-range structural evolution underlying liquid fragility and heat capacity," *Acta Materialia*, vol. 61, no. 8, pp. 3130–3140, May 2013.

[92] W. Zhao, T. Xu, S. Feng, Y. Wang, L. Qi, G. Li, and R. Liu, "Effect of hydrostatic pressure on reinforcing bulk metallic glasses investigated by synchrotron radiation and molecular dynamics simulations," *Materials Science and Engineering: A*, vol. 596, pp. 59–63, Feb. 2014.

[93] G. Ruitenberg, P. De Hey, F. Sommer, and J. Sietsma, "Pressure-Induced Structural Relaxation in Amorphous $Pd_{40}Ni_{40}P_{20}$: The Formation Volume for Diffusion Defects," *Physical Review Letters*, vol. 79, no. 24, pp. 4830–4833, Dec. 1997.

[94] M. YOUSUF and K. G. RAJAN, "Pressure induced structural relaxation in amorphous solids-example of $Fe_{40}Ni_{40}P_{14}B_6$," *Journal of Materials Science Letters*, vol. 3, pp. 149–152, 1984.

[95] X. Hu, S. C. Ng, Y. P. Feng, and Y. Li, "Cooling-rate dependence of the density of $Pd_{40}Ni_{10}Cu_{30}P_{20}$ bulk metallic glass," *Physical Review B*, vol. 64, no. 17, p. 172 201, Oct. 2001.

[96] A. Inoue, T. Negishi, H. M. Kimura, T. Zhang, and A. R. Yavari, "High Packing Density of Zr- and Pd-Based Bulk Amorphous Alloys," *Materials Transactions, JIM*, vol. 39, no. 2, pp. 318–321, 1998.

[97] H. S. Chen, "Glassy metals," *Reports on Progress in Physics*, vol. 43, no. 4, p. 353, 1980.

[98] T. Masumoto, H. Kimura, A. Inoue, and Y. Waseda, "Structural stability of amorphous metals," *Materials Science and Engineering*, vol. 23, no. 2-3, pp. 141–144, May 1976.

[99] T. Zhang and A. Inoue, "Density, Thermal Stability and Mechanical Properties of ZrTiAlCuNi Bulk Amorphous Alloys with High Al Plus Ti Concentrations," *Materials Transactions, JIM*, vol. 39, no. 8, pp. 857–862, 1998.

[100] C. Nagel, K. Rtzke, E. Schmidtke, J. Wolff, U. Geyer, and F. Faupel, "Free-volume changes in the bulk metallic glass $Zr_{46.7}Ti_{8.3}Cu_{7.5}Ni_{10}Be_{27.5}$ and the undercooled liquid," *Physical Review B*, vol. 57, no. 17, pp. 10 224–10 227, May 1998.

[101] X. Tong, G. Wang, Z. H. Stachurski, J. Bednark, N. Mattern, Q. J. Zhai, and J. Eckert, "Structural evolution and strength change of a metallic glass at different temperatures," *Scientific Reports*, vol. 6, p. 30 876, Aug. 2016.

[102] S.-C. Lee, C.-M. Lee, J.-W. Yang, and J.-C. Lee, "Microstructural evolution of an elastostatically compressed amorphous alloy and its influence on the mechanical properties," *Scripta Materialia*, vol. 58, no. 7, pp. 591–594, Apr. 2008.

[103] O. Haruyama, K. Kisara, A. Yamashita, K. Kogure, Y. Yokoyama, and K. Sugiyama, "Characterization of free volume in cold-rolled $Zr_{55}Cu_{30}Ni_5Al_{10}$ bulk metallic glasses," *Acta Materialia*, vol. 61, no. 9, pp. 3224–3232, May 2013.

[104] K.-W. Park, C.-M. Lee, M. Wakeda, Y. Shibutani, M. L. Falk, and J.-C. Lee, "Elastostatically induced structural disordering in amorphous alloys," *Acta Materialia*, vol. 56, no. 19, pp. 5440–5450, Nov. 2008.

[105] K.-W. Park, C.-M. Lee, M. Wakeda, Y. Shibutani, E. Fleury, and J.-C. Lee, "Homogeneous deformation of bulk amorphous alloys during elastostatic compression and its packing density dependence," *Scripta Materialia*, vol. 59, no. 7, pp. 710–713, Oct. 2008.

[106] S.-C. Lee, C.-M. Lee, J.-C. Lee, H.-J. Kim, Y. Shibutani, E. Fleury, and M. L. Falk, "Structural disordering process of an amorphous alloy driven by the elastostatic compression at room temperature," *Applied Physics Letters*, vol. 92, no. 15, p. 151 906, Apr. 2008.

[107] C.-M. Lee, K.-W. Park, B.-J. Lee, Y. Shibutani, and J.-C. Lee, "Structural disordering of amorphous alloys: A molecular dynamics analysis," *Scripta Materialia*, vol. 61, no. 9, pp. 911–914, Nov. 2009.

[108] C.-C. Wang, Y.-W. Mao, Z.-W. Shan, M. Dao, J. Li, J. Sun, E. Ma, and S. Suresh, "Real-time, high-resolution study of nanocrystallization and fatigue cracking in a cyclically strained metallic glass," *Proceedings of the National Academy of Sciences*, vol. 110, no. 49, pp. 19 725–19 730, Dec. 2013.

[109] D. A. Porter, K. E. Easterling, and M. Sherif, *Phase Transformations in Metals and Alloys, Third Edition*, 3 edition. Boca Raton, FL: CRC Press, Feb. 2009, ISBN: 978-1-4200-6210-6.

[110] X. J. Liu, G. L. Chen, X. D. Hui, H. Y. Hou, K. F. Yao, and C. T. Liu, "Growth mechanism from nano-ordered clusters to nanocrystals in a deeply undercooled melt of Zr-Ni-Ti metallic glass," *Journal of Applied Physics*, vol. 102, no. 6, p. 063 515, Sep. 2007.

[111] X. J. Liu, G. L. Chen, H. Y. Hou, X. Hui, K. F. Yao, Z. P. Lu, and C. T. Liu, "Atomistic mechanism for nanocrystallization of metallic glasses," *Acta Materialia*, vol. 56, no. 12, pp. 2760–2769, Jul. 2008.

[112] D. V Louzguine and A Inoue, "Crystallization behaviour of Al-based metallic glasses below and above the glass-transition temperature," *Journal of Non-Crystalline Solids*, vol. 311, no. 3, pp. 281–293, Dec. 2002.

[113] H. Iwasaki and T. Masumoto, "Effect of high pressure on the crystallization of an amorphous $Pd_{80}Si_{20}$ alloy," *Journal of Materials Science*, vol. 13, no. 10, pp. 2171–2176, Oct. 1978.

[114] M. elikbilek, A. E. Ersundu, and S. Ayd, "Crystallization Kinetics of Amorphous Materials," in *Advances in Crystallization Processes*, 2012, p. 37, ISBN: 978-953-51-0581-7.

[115] T. Kulik, "Nanocrystallization of metallic glasses," *Journal of Non-Crystalline Solids*, vol. 287, no. 1-3, pp. 145–161, Jul. 2001.

[116] T. LaGrange, D. S. Grummon, B. W. Reed, N. D. Browning, W. E. King, and G. H. Campbell, "Strongly driven crystallization processes in a metallic glass," *Applied Physics Letters*, vol. 94, no. 18, p. 184 101, May 2009.

[117] D. Q. Zhao, M. X. Pan, W. H. Wang, B. C. Wei, T. Okada, and W. Utsumi, "Melting and crystallization of $Nd_{60}Al_{10}Fe_{20}Co_{10}$ bulk metallic glass under high pressure," *Journal of Physics: Condensed Matter*, vol. 15, no. 50, p. L749, 2003.

[118] J. Z. Jiang, K. Saksl, J. Saida, A. Inoue, H. Franz, K. Messel, and C. Lathe, "Evidence of polymorphous amorphous-to-quasicrystalline phase transformation in $Zr_{66.7}Pd_{33.3}$ metallic glass," *Applied Physics Letters*, vol. 80, no. 5, pp. 781–783, Jan. 2002.

[119] D. J. Lacks and M. J. Osborne, "Energy Landscape Picture of Overaging and Rejuvenation in a Sheared Glass," *Physical Review Letters*, vol. 93, no. 25, Dec. 2004.

[120] B. Gun, K. J. Laws, and M. Ferry, "Static and dynamic crystallization in Mg-Cu-Y bulk metallic glass," *Journal of Non-Crystalline Solids*, vol. 352, no. 36, pp. 3887–3895, Oct. 2006.

[121] X. Liu, X. Hui, G. Chen, and M. Sun, "In situ synchrotron SAXS study of nanocrystallization in $Zr_{65}Ni_{25}Ti_{10}$ metallic glass," *Intermetallics*, vol. 16, no. 1, pp. 10–15, Jan. 2008.

[122] K. Lu, "Nanocrystalline metals crystallized from amorphous solids: Nanocrystallization, structure, and properties," *Materials Science and Engineering: R: Reports*, vol. 16, no. 4, pp. 161–221, Apr. 1996.

[123] H. Y. Zhang, Z. Q. Hu, and K. Lu, "Transformation from the amorphous to the nanocrystalline state in pure selenium," *Nanostructured Materials*, vol. 5, no. 1, pp. 41–52, Jan. 1995.

[124] M. M Nicolaus, H. R Sinning, and F Haessner, "Crystallization behaviour and generation of a nanocrystalline state from amorphous $Co_{33}Zr_{67}$," *Materials Science and Engineering: A*, vol. 150, no. 1, pp. 101–112, Feb. 1992.

[125] K. Lu, X.D. Liu, and F.H. Yuan, "Synthesis of the $NiZr_2$ intermetallic compound nanophase materials," *Physica B: Condensed Matter*, vol. 217, no. 1, pp. 153–159, Jan. 1996.

[126] T. Spassov and U. Köster, "Grain-growth in nanocrystalline zirconium-based alloys," *Journal of Materials Science*, vol. 28, no. 10, pp. 2789–2794, Jan. 1993.

[127] K. Lu, W. Wei, and J. Wang, "Microhardness and fracture properties of nanocrystalline nip alloy," *Scripta metallurgica et materialia*, vol. 24, no. 12, pp. 2319–2323, 1990.

[128] A. L. Greer, "Crystallisation kinetics of $Fe_{80}B_{20}$ glass," *Acta Metallurgica*, vol. 30, no. 1, pp. 171–192, Jan. 1982.

[129] D. G. Morris, "Crystallisation of the metglas 2826 amorphous alloy," *Acta Metallurgica*, vol. 29, no. 7, pp. 1213–1220, Jul. 1981.

[130] H. Y. Tong, B. Z. Ding, H. G. Jiang, K. Lu, J. T. Wang, and Z. Q. Hu, "Formation kinetics of nanocrystalline FeBSi alloy by crystallization of the metallic glass," *Journal of Applied Physics*, vol. 75, no. 1, pp. 654–656, Jan. 1994.

[131] Guo H.Q., Reininger T., Kronmüller H., Rapp M., and Skumrev V. Kh., "Magnetism and microstructure in nanocrystalline FeCoZr ferromagnets," *physica status solidi (a)*, vol. 127, no. 2, pp. 519–527, Feb. 2006.

[132] X. Liu, J. Wang, and B. Ding, "Preparation and properties of nanocrystalline $(Fe_{0.99}Mo_{0.01})_{78}Si_9B_{13}$ alloys," *Scripta metallurgica et materialia*, vol. 28, no. 1, pp. 59–64, 1993.

[133] P. G. Boswell and G. A. Chadwick, "The formation and crystallization of an amorphous phase in an iron-carbon alloy," *Journal of Materials Science*, vol. 11, no. 12, pp. 2287–2296, Dec. 1976.

[134] T. Kulik, T. Horubał, and H. Matyja, "Flash annealing nanocrystallization of Fe-Si-B-based glasses," *Materials Science and Engineering: A*, vol. 157, no. 1, pp. 107–112, Sep. 1992.

[135] P. Gorria, I. Orue, F. Plazaola, M. L. Fernandez-Gubieda, and J. M. Barandiaran, "Magnetic and Mossbauer study of amorphous and nanocrystalline $Fe_{86}Zr_7Cu_1B_6$ alloys," *IEEE Transactions on Magnetics*, vol. 29, no. 6, pp. 2682–2684, Nov. 1993.

[136] M. L. Trudeau, J. Y. Huot, R. Schulz, D. Dussault, A. Van Neste, and G. L'Espérance, "Nanocrystalline Fe-(Co,Ni)-Si-B: The mechanical crystallization of amorphous alloys and the effects on electrocatalytic reactions," *Physical Review B*, vol. 45, no. 9, pp. 4626–4636, Mar. 1992.

[137] F. Q. Guo and K. Lu, "Formation of a single α-Fe nanophase during mechanically driven crystallization of an FeMoSiB metallic glass," *Nanostructured Materials*, vol. 7, no. 5, pp. 509–517, Jul. 1996.

[138] R. Birringer, "Nanocrystalline materials," *Materials Science and Engineering: A*, vol. 117, pp. 33–43, Sep. 1989.

[139] C. Suryanarayana and F. Froes, "Production of nanostructure titanium-based alloys by mechanical alloying," *Nanostructured Materials*, vol. 1, no. 2, pp. 191–196, Mar. 1992.

[140] H. Tong, B. Ding, H. Jiang, Z. Hu, L. Dong, and Q. Zhou, "An in situ TEM observation on the thermal stability of a nanocrystalline FeBSi alloy," *Materials Letters*, vol. 16, no. 5, pp. 260–264, May 1993.

[141] K. Lu, W. D. Wei, and J. T. Wang, "Grain growth kinetics and interfacial energies in nanocrystalline NiP alloys," *Journal of Applied Physics*, vol. 69, no. 10, pp. 7345–7347, May 1991.

[142] K. Lu, Z. F. Dong, I. Bakonyi, and . Cziraki, "Thermal stability and grain growth of a melt-spun $HfNi_5$ nanophase alloy," *Acta Metallurgica et Materialia*, vol. 43, no. 7, pp. 2641–2647, Jul. 1995.

[143] K. Isonishi and K. Okazaki, "Grain growth in nanocrystalline $NbAl_3$ prepared by mechanical alloying," *Journal of Materials Science*, vol. 28, no. 14, pp. 3829–3834, Jan. 1993.

[144] K. Lu, "The thermal instability of nanocrystalline Ni-P materials with different grain sizes," *Nanostructured Materials*, vol. 2, no. 6, pp. 643–652, Nov. 1993.

[145] Gamarnik M. Ya., "Change of Lattice Parameters in Highly Disperse Nickel Powders," *physica status solidi (b)*, vol. 168, no. 2, pp. 389–395, Dec. 1991.

[146] Ya Gamarnik M., "The Physical Nature of Changes of Lattice Parameters in Small Particles," *physica status solidi (b)*, vol. 178, no. 1, pp. 59–69, Jul. 1993.

[147] X. D. Liu, H. Y. Zhang, K. Lu, and Z. Q. Hu, "The lattice expansion in nanometre-sized Ni polycrystals," *Journal of Physics: Condensed Matter*, vol. 6, no. 34, p. L497, 1994.

[148] Gamarnik M. Ya. and Sidorin Yu. Yu., "Change of the Unit Cell Parameters in Highly Dispersed Gold, Silver, and Copper Powders," *physica status solidi (b)*, vol. 156, no. 1, K1–K4, Nov. 1989.

[149] W. Qin, T. Nagase, Y. Umakoshi, and J. A. Szpunar, "Relationship between microstrain and lattice parameter change in nanocrystalline materials," *Philosophical Magazine Letters*, vol. 88, no. 3, pp. 169–179, Mar. 2008.

[150] A. Stukowski, J. Markmann, J. Weissmüller, and K. Albe, "Atomistic origin of microstrain broadening in diffraction data of nanocrystalline solids," *Acta Materialia*, vol. 57, no. 5, pp. 1648–1654, Mar. 2009.

[151] S. M. Sharma and S. K. Sikka, "Pressure induced amorphization of materials," *Progress in Materials Science*, vol. 40, no. 1, pp. 1–77, Jan. 1996.

[152] R. J. Hemley, A. P. Jephcoat, H. K. Mao, L. C. Ming, and M. H. Manghnani, "Pressure-induced amorphization of crystalline silica," *Nature*, vol. 334, no. 6177, pp. 52–54, Jul. 1988.

[153] Y. Tsuchida and T. Yagi, "New pressure-induced transformations of silica at room temperature," *Nature*, vol. 347, no. 6290, pp. 267–269, Sep. 1990.

[154] T. D.Bennett, P. Simoncic, S. A.Moggach, F. Gozzo, P. Macchi, D. A.Keen, J.-C. Tan, and A. K.Cheetham, "Reversible pressure-induced amorphization of a zeolitic imidazolate framework (ZIF-4)," *Chemical Communications*, vol. 47, no. 28, pp. 7983–7985, 2011.

[155] C. A. Perottoni and J. A. H. d. Jornada, "Pressure-Induced Amorphization and Negative Thermal Expansion in ZrW_2O_8," *Science*, vol. 280, no. 5365, pp. 886–889, May 1998.

[156] A. Jayaraman, "Diamond anvil cell and high-pressure physical investigations," *Reviews of Modern Physics*, vol. 55, no. 1, pp. 65–108, Jan. 1983.

[157] T. J. Duignan and J. Autschbach, "Impact of the KohnSham Delocalization Error on the 4f Shell Localization and Population in Lanthanide Complexes," *Journal of Chemical Theory and Computation*, vol. 12, no. 7, pp. 3109–3121, Jul. 2016.

[158] C. W. Greeff, "Phase changes and the equation of state of Zr," *Modelling and Simulation in Materials Science and Engineering*, vol. 13, no. 7, p. 1015, 2005.

[159] K. Kotmool, B. Li, S. Chakraborty, T. Bovornratanaraks, W. Luo, H.-k. Mao, and R. Ahuja, "High pressure-induced distortion in face-centered cubic phase of thallium," *Proceedings of the National Academy of Sciences*, vol. 113, no. 40, pp. 11 143–11 147, Oct. 2016.

[160] R. Li, J. Liu, L. Bai, J. S. Tse, and G. Shen, "Pressure-induced changes in the electron density distribution in α-Ge near the α - β transition," *Applied Physics Letters*, vol. 107, no. 7, p. 072 109, Aug. 2015.

[161] J. S. Tse, M. Hanfland, R. Flacau, S. Desgreniers, Z. Li, K. Mende, K. Gilmore, A. Nyrow, M. Moretti Sala, and C. Sternemann, "Pressure-Induced Changes on The Electronic Structure and Electron Topology in the Direct FCC $\rightarrow$ SH Transforma-

tion of Silicon," *The Journal of Physical Chemistry C*, vol. 118, no. 2, pp. 1161–1166, Jan. 2014.

[162] A. Svane, P. Strange, W. M. Temmerman, Z. Szotek, H. Winter, and L. Petit, "Pressure-Induced Valence Transitions in Rare Earth Chalcogenides and Pnictides," *physica status solidi (b)*, vol. 223, no. 1, pp. 105–116, Jan. 2001.

[163] S. Heathman, R. G. Haire, T. Le Bihan, A. Lindbaum, K. Litfin, Y. Mresse, and H. Libotte, "Pressure Induces Major Changes in the Nature of Americium's 5f Electrons," *Physical Review Letters*, vol. 85, no. 14, pp. 2961–2964, Oct. 2000.

[164] A. Jayaraman, R. C. Newton, and J. M. McDonough, "Phase Relations, Resistivity, and Electronic Structure of Cesium at High Pressures," *Physical Review*, vol. 159, no. 3, pp. 527–533, Jul. 1967.

[165] A. Dewaele, C. Denoual, S. Anzellini, F. Occelli, M. Mezouar, P. Cordier, S. Merkel, M. Vron, and E. Rausch, "Mechanism of the α - ϵ phase transformation in iron," *Physical Review B*, vol. 91, no. 17, May 2015.

[166] A. P. Jephcoat, H.-k. Mao, and P. M. Bell, "Static compression of iron to 78 GPa with rare gas solids as pressure-transmitting media," *Journal of Geophysical Research: Solid Earth*, vol. 91, no. B5, pp. 4677–4684, Apr. 1986.

[167] H. Mao, W. A. Bassett, and T. Takahashi, "Effect of Pressure on Crystal Structure and Lattice Parameters of Iron up to 300 kbar," *Journal of Applied Physics*, vol. 38, no. 1, pp. 272–276, Jan. 1967.

[168] Wei Qingguo, McCammon Catherine, and Gilder Stuart Alan, "High-Pressure Phase Transition of Iron: A Combined Magnetic Remanence and Mössbauer Study," *Geochemistry, Geophysics, Geosystems*, vol. 18, no. 12, pp. 4646–4654, Dec. 2017.

[169] L. Sun, W. K. Wang, D. W. He, W. H. Wang, Q. Wu, X. Y. Zhang, Z. X. Bao, and Q. Zhao, "Reversible phase transition between amorphous and crystalline in $Zr_{41.2}Ti_{13.8}Cu_{12.5}Ni_{10}Be_{22.5}$ under high pressure at room temperature," *Applied Physics Letters*, vol. 76, no. 20, pp. 2874–2876, May 2000.

[170] Q. S. Zeng, Y. C. Li, C. M. Feng, P. Liermann, M. Somayazulu, G. Y. Shen, H.-k Mao, R. Yang, J. Liu, T. D. Hu, and J. Z. Jiang, "Anomalous compression behavior in lanthanum/cerium-based metallic glass under high pressure," *Proceedings of the National Academy of Sciences*, vol. 104, no. 34, pp. 13 565–13 568, Aug. 2007.

[171] Q. Luo, G. Garbarino, B. Sun, D. Fan, Y. Zhang, Z. Wang, Y. Sun, J. Jiao, X. Li, P. Li, N. Mattern, J. Eckert, and J. Shen, "Hierarchical densification and negative thermal expansion in Ce-based metallic glass under high pressure," *Nature Communications*, vol. 6, p. 5703, Feb. 2015.

[172] L. Belhadi, F. Decremps, S. Pascarelli, L. Cormier, Y. Le Godec, S. Gorsse, F. Baudelet, C. Marini, and G. Garbarino, "Polyamorphism in cerium based bulk metallic glasses: Electronic and structural properties under pressure and temperature by x-ray absorption techniques," *Applied Physics Letters*, vol. 103, no. 11, p. 111 905, Sep. 2013.

[173] G. Li, Y. Y. Wang, P. K. Liaw, Y. C. Li, and R. P. Liu, "Electronic Structure Inheritance and Pressure-Induced Polyamorphism in Lanthanide-Based Metallic Glasses," *Physical Review Letters*, vol. 109, no. 12, p. 125 501, Sep. 2012.

[174] X. R. Liu and S. M. Hong, "Evidence for a pressure-induced phase transition of amorphous to amorphous in two lanthanide-based bulk metallic glasses," *Applied Physics Letters*, vol. 90, no. 25, p. 251 903, Jun. 2007.

[175] S. V. Buldyrev, G. Malescio, C. A. Angell, N. Giovambattista, S. Prestipino, F. Saija, H. E. Stanley, and L. Xu, "Unusual phase behavior of one-component systems with two-scale isotropic interactions," *Journal of Physics: Condensed Matter*, vol. 21, no. 50, p. 504 106, 2009.

[176] Q.-S. Zeng, Y. Ding, W. L. Mao, W. Luo, A. Blomqvist, R. Ahuja, W. Yang, J. Shu, S. V. Sinogeikin, Y. Meng, D. L. Brewe, J.-Z. Jiang, and H.-k. Mao, "Substitutional alloy of Ce and Al," *Proceedings of the National Academy of Sciences*, vol. 106, no. 8, pp. 2515–2518, 2009.

[177] H. B. Lou, Y. K. Fang, Q. S. Zeng, Y. H. Lu, X. D. Wang, Q. P. Cao, K. Yang, X. H. Yu, L. Zheng, Y. D. Zhao, W. S. Chu, T. D. Hu, Z. Y. Wu, R. Ahuja, and J. Z. Jiang, "Pressure-induced amorphous-to-amorphous configuration change in Ca-Al metallic glasses," *Scientific Reports*, vol. 2, p. 376, Apr. 2012.

[178] A. Argon, "Plastic deformation in metallic glasses," *Acta metallurgica*, vol. 27, no. 1, pp. 47–58, 1979.

[179] M. L. Falk and J. S. Langer, "Dynamics of viscoplastic deformation in amorphous solids," *Physical Review E*, vol. 57, no. 6, pp. 7192–7205, Jun. 1998.

[180] F. Delogu, "Identification and Characterization of Potential Shear Transformation Zones in Metallic Glasses," *Physical Review Letters*, vol. 100, no. 25, Jun. 2008.

[181] D. Srolovitz, V. Vitek, and T. Egami, "An atomistic study of deformation of amorphous metals," *Acta Metallurgica*, vol. 31, no. 2, pp. 335–352, Feb. 1983.

[182] W. L. Johnson and K. Samwer, "A Universal Criterion for Plastic Yielding of Metallic Glasses with a $(T/T_g)^{(2/3)}$ Temperature Dependence," *Physical Review Letters*, vol. 95, no. 19, p. 195 501, Nov. 2005.

[183] B. Yang, C. T. Liu, and T. G. Nieh, "Unified equation for the strength of bulk metallic glasses," *Applied Physics Letters*, vol. 88, no. 22, p. 221 911, May 2006.

[184] Y. Q. Cheng, H. W. Sheng, and E. Ma, "Relationship between structure, dynamics, and mechanical properties in metallic glass-forming alloys," *Physical Review B*, vol. 78, no. 1, p. 014 207, Jul. 2008.

[185] Y. H. Liu, C. T. Liu, W. H. Wang, A. Inoue, T. Sakurai, and M. W. Chen, "Thermodynamic Origins of Shear Band Formation and the Universal Scaling Law of Metallic Glass Strength," *Physical Review Letters*, vol. 103, no. 6, Aug. 2009.

[186] D. Rodney and C. Schuh, "Distribution of Thermally Activated Plastic Events in a Flowing Glass," *Physical Review Letters*, vol. 102, no. 23, Jun. 2009.

[187] D. J. Safarik and R. B. Schwarz, "Elastic constants of amorphous and single-crystal $Pd_{40}Cu_{40}P_{20}$," *Acta Materialia*, vol. 55, no. 17, pp. 5736–5746, Oct. 2007.

[188] W. H. Wang, "Correlation between relaxations and plastic deformation, and elastic model of flow in metallic glasses and glass-forming liquids," *Journal of Applied Physics*, vol. 110, no. 5, p. 053 521, Sep. 2011.

[189] H. B. Yu, X. Shen, Z. Wang, L. Gu, W. H. Wang, and H. Y. Bai, "Tensile Plasticity in Metallic Glasses with Pronounced β Relaxations," *Physical Review Letters*, vol. 108, no. 1, Jan. 2012.

[190] H.-B. Yu, W.-H. Wang, and K. Samwer, "The β relaxation in metallic glasses: An overview," *Materials Today*, vol. 16, no. 5, pp. 183–191, May 2013.

[191] S. G. Mayr, "Activation Energy of Shear Transformation Zones: A Key for Understanding Rheology of Glasses and Liquids," *Physical Review Letters*, vol. 97, no. 19, Nov. 2006.

[192] S. Ogata, F. Shimizu, J. Li, M. Wakeda, and Y. Shibutani, "Atomistic simulation of shear localization in CuZr bulk metallic glass," *Intermetallics*, Fourth International Conference on Bulk Metallic Glasses, vol. 14, no. 8, pp. 1033–1037, Aug. 2006.

[193] Y. Q. Cheng and E. Ma, "Intrinsic shear strength of metallic glass," *Acta Materialia*, vol. 59, no. 4, pp. 1800–1807, Feb. 2011.

[194] F. Shimizu, S. Ogata, and J. Li, "Yield point of metallic glass," *Acta Materialia*, vol. 54, no. 16, pp. 4293–4298, Sep. 2006.

[195] B. Yang, M. L. Morrison, P. K. Liaw, R. A. Buchanan, G. Wang, C. T. Liu, and M. Denda, "Dynamic evolution of nanoscale shear bands in a bulk-metallic glass," *Applied Physics Letters*, vol. 86, no. 14, p. 141 904, Mar. 2005.

[196] B. Yang, C. T. Liu, T. G. Nieh, M. L. Morrison, P. K. Liaw, and R. A. Buchanan, "Localized heating and fracture criterion for bulk metallic glasses," *Journal of Materials Research*, vol. 21, no. 4, pp. 915–922, Apr. 2006.

[197] Y. Q. Cheng, Z. Han, Y. Li, and E. Ma, "Cold versus hot shear banding in bulk metallic glass," *Physical Review B*, vol. 80, no. 13, Oct. 2009.

[198] A. J. Cao, Y. Q. Cheng, and E. Ma, "Structural processes that initiate shear localization in metallic glass," *Acta Materialia*, vol. 57, no. 17, pp. 5146–5155, Oct. 2009.

[199] C. E. Packard and C. A. Schuh, "Initiation of shear bands near a stress concentration in metallic glass," *Acta Materialia*, vol. 55, no. 16, pp. 5348–5358, Sep. 2007.

[200] S. X. Song, X. L. Wang, and T. G. Nieh, "Capturing shear band propagation in a Zr-based metallic glass using a high-speed camera," *Scripta Materialia*, vol. 62, no. 11, pp. 847–850, Jun. 2010.

[201] Z. Han and Y. Li, "Cooperative shear and catastrophic fracture of bulk metallic glasses from a shear-band instability perspective," *Journal of Materials Research*, vol. 24, no. 12, pp. 3620–3627, Dec. 2009.

[202] D. B. Miracle, A. Concustell, Y. Zhang, A. R. Yavari, and A. L. Greer, "Shear bands in metallic glasses: Size effects on thermal profiles," *Acta Materialia*, vol. 59, no. 7, pp. 2831–2840, Apr. 2011.

[203] C Schuh, T Hufnagel, and U Ramamurty, "Mechanical behavior of amorphous alloys," *Acta Materialia*, vol. 55, no. 12, pp. 4067–4109, Jul. 2007.

[204] L. Tian, Y.-Q. Cheng, Z.-W. Shan, J. Li, C.-C. Wang, X.-D. Han, J. Sun, and E. Ma, "Approaching the ideal elastic limit of metallic glasses," *Nature Communications*, vol. 3, p. 609, Jan. 2012.

[205] A. R. Yavari, A. L. Moulec, A. Inoue, N. Nishiyama, N. Lupu, E. Matsubara, W. J. Botta, G. Vaughan, M. D. Michiel, and k. Kvick, "Excess free volume in metallic glasses measured by X-ray diffraction," *Acta Materialia*, vol. 53, no. 6, pp. 1611–1619, Apr. 2005.

[206] J. Li, F. Spaepen, and T. C. Hufnagel, "Nanometre-scale defects in shear bands in a metallic glass," *Philosophical Magazine A*, vol. 82, no. 13, pp. 2623–2630, Sep. 2002.

[207] Y. M. Chen, T. Ohkubo, T. Mukai, and K. Hono, "Structure of shear bands in $Pd_{40}Ni_{40}P_{20}$ bulk metallic glass," *Journal of Materials Research*, vol. 24, no. 1, pp. 1–9, Jan. 2009.

[208] A. C. Y. Liu, D. M. Paganin, L. Bourgeois, P. N. H. Nakashima, R. T. Ott, and M. J. Kramer, "Quantitative microscopic measurement of void distribution in shear bands in $Zr_{66.7}Cu_{33.3}$ metallic glass," *Physical Review B*, vol. 84, no. 9, Sep. 2011.

[209] W. Dmowski and T. Egami, "Observation of structural anisotropy in metallic glasses induced by mechanical deformation," *Journal of Materials Research*, vol. 22, no. 2, pp. 412–418, Feb. 2007.

[210] S. Karmakar, E. Lerner, and I. Procaccia, "Plasticity-induced anisotropy in amorphous solids: The Bauschinger effect," *Physical Review E*, vol. 82, no. 2, Aug. 2010.

[211] B. Yang, P. K. Liaw, G. Wang, M. Morrison, C. T. Liu, R. A. Buchanan, and Y. Yokoyama, "In-situ thermographic observation of mechanical damage in bulk-metallic glasses during fatigue and tensile experiments," *Intermetallics*, Bulk Metallic Glasses III, vol. 12, no. 10, pp. 1265–1274, Oct. 2004.

[212] W. H. Jiang, H. H. Liao, F. X. Liu, H. Choo, and P. K. Liaw, "Rate-Dependent Temperature Increases in Shear Bands of a Bulk-Metallic Glass," *Metallurgical and Materials Transactions A*, vol. 39, no. 8, pp. 1822–1830, Aug. 2008.

[213] J. J. Lewandowski and A. L. Greer, "Temperature rise at shear bands in metallic glasses," *Nature Materials*, vol. 5, no. 1, pp. 15–18, Jan. 2006.

[214] Y. Zhang and A. L. Greer, "Thickness of shear bands in metallic glasses," *Applied Physics Letters*, vol. 89, no. 7, p. 071 907, Aug. 2006.

[215] A. V. Sergueeva, N. A. Mara, J. D. Kuntz, E. J. Lavernia, and A. K. Mukherjee *, "Shear band formation and ductility in bulk metallic glass," *Philosophical Magazine*, vol. 85, no. 23, pp. 2671–2687, Aug. 2005.

[216] A. L. Greer, K. L. Rutherford, and I. M. Hutchings, "Wear resistance of amorphous alloys and related materials," *International Materials Reviews*, vol. 47, no. 2, pp. 87–112, Apr. 2002.

[217] M. L. Trudeau, R. Schulz, D. Dussault, and A. Van Neste, "Structural changes during high-energy ball milling of iron-based amorphous alloys: Is high-energy ball milling equivalent to a thermal process?" *Physical Review Letters*, vol. 64, no. 1, pp. 99–102, Jan. 1990.

[218] Y. He, G. J. Shiflet, and S. J. Poon, "Ball milling-induced nanocrystal formation in aluminum-based metallic glasses," *Acta Metallurgica et Materialia*, vol. 43, no. 1, pp. 83–91, Jan. 1995.

[219] J.-J. Kim, Y. Choi, S. Suresh, and A. S. Argon, "Nanocrystallization During Nanoindentation of a Bulk Amorphous Metal Alloy at Room Temperature," *Science*, vol. 295, no. 5555, pp. 654–657, Jan. 2002.

[220] H. J. Chang, D. H. Kim, Y. M. Kim, Y. J. Kim, and K. Chattopadhyay, "On the origin of nanocrystals in the shear band in a quasicrystal forming bulk metallic glass $Ti_{40}Zr_{29}Cu_9Ni_8Be_{14}$," *Scripta Materialia*, vol. 55, no. 6, pp. 509–512, Sep. 2006.

[221] R. J. Hebert and J. H. Perepezko, "Effect of Intense Rolling and Folding on the Phase Stability of Amorphous Al-Y-Fe Alloys," *Metallurgical and Materials Transactions A*, vol. 39, no. 8, pp. 1804–1811, Aug. 2008.

[222] W. H Jiang and M Atzmon, "The effect of compression and tension on shear-band structure and nanocrystallization in amorphous $Al_{90}Fe_5Gd_5$: A high-resolution transmission electron microscopy study," *Acta Materialia*, vol. 51, no. 14, pp. 4095–4105, Aug. 2003.

[223] J. Vierke, G. Schumacher, V. P. Pilyugin, I. A. Denks, I. Zizak, C. Wolf, N. Wanderka, M. Wollgarten, and J. Banhart, "Deformation-induced crystallization in amorphous $Al_{85}Ni_{10}La_5$ alloy," *Journal of Alloys and Compounds*, vol. 493, no. 1, pp. 683–691, Mar. 2010.

[224] G. Mazzone, A. Montone, and M. V. Antisari, "Effect of plastic flow on the kinetics of amorphous phase growth by solid state reaction in the Ni-Zr system," *Physical Review Letters*, vol. 65, no. 16, pp. 2019–2022, Oct. 1990.

[225] G. J. Fan, M. X. Quan, Z. Q. Hu, W. Lser, and J. Eckert, "Deformation-induced microstructural changes in $Fe_{40}Ni_{40}P_{14}B_6$ metallic glass," *Journal of Materials Research*, vol. 14, no. 9, pp. 3765–3774, Sep. 1999.

[226] R. J. Hebert, N. Boucharat, J. H. Perepezko, H. Rsner, and G. Wilde, "Calorimetric and microstructural analysis of deformation induced crystallization reactions in amorphous $Al_{88}Y_7Fe_5$ alloy," *Journal of Alloys and Compounds*, Proceedings of the 12th International Symposium on Metastable and Nano-Materials (ISMANAM-2005), vol. 434-435, no. Supplement C, pp. 18–21, May 2007.

[227] G. N. Greaves, A. L. Greer, R. S. Lakes, and T. Rouxel, "Poisson's ratio and modern materials," *Nature Materials*, vol. 10, no. 11, pp. 823–837, Nov. 2011.

[228] M. A. Meyers, *Dynamic behavior of materials*. John Wiley & Sons, 1994.

[229] H. Togo, Y. Zhang, Y. Kawamura, and T. Mashimo, "Properties of Zr-based bulk metallic glass under shock compression," *Materials Science and Engineering: A*,

Proceedings of the 12th International Conference on Rapidly Quenched & Metastable Materials, vol. 449-451, pp. 264–268, Mar. 2007.

[230] F. Birch, "Finite Elastic Strain of Cubic Crystals," *Physical Review*, vol. 71, no. 11, pp. 809–824, Jun. 1947.

[231] F. Murnaghan, "The compressibility of media under extreme pressures," *Proceedings of the National Academy of Sciences*, vol. 30, no. 9, pp. 244–247, 1944.

[232] R. Ravelo, B. L. Holian, T. C. Germann, and P. S. Lomdahl, "Constant-stress Hugoniostat method for following the dynamical evolution of shocked matter," *Physical Review B*, vol. 70, no. 1, p. 014 103, Jul. 2004.

[233] Z. D. Sha, Y. P. Feng, and Y. Li, "Statistical composition-structure-property correlation and glass-forming ability based on the full icosahedra in CuZr metallic glasses," *Applied Physics Letters*, vol. 96, no. 6, p. 061 903, Feb. 2010.

[234] L. Jin, Y.-B. Kang, P. Chartrand, and C. D. Fuerst, "Thermodynamic evaluation and optimization of Al-La, Al-Ce, Al-Pr, Al-Nd and Al-Sm systems using the Modified Quasichemical Model for liquids," *Calphad*, vol. 35, no. 1, pp. 30–41, Mar. 2011.

[235] T. C. Ozawa and S. J. Kang, "Balls&Sticks: Easy-to-use structure visualization and animation program," *Journal of Applied Crystallography*, vol. 37, no. 4, pp. 679–679, Aug. 2004.

[236] J Van Vucht, "Contribution to the knowledge of the system cerium-aluminum," *Z. Metallkd*, vol. 48, p. 253, 1957.

[237] C. S. Ray, W. Huang, and D. E. Day, "Crystallization Kinetics of a LithiaSilica Glass: Effect of Sample Characteristics and Thermal Analysis Measurement Techniques," *Journal of the American Ceramic Society*, vol. 74, no. 1, pp. 60–66, Jan. 1991.

[238] T. Ozawa, "Kinetics of non-isothermal crystallization," *Polymer*, vol. 12, no. 3, pp. 150–158, Mar. 1971.

[239] J. A. Augis and J. E. Bennett, "Calculation of the Avrami parameters for heterogeneous solid state reactions using a modification of the Kissinger method," *Journal of Thermal Analysis*, vol. 13, no. 2, pp. 283–292, Apr. 1978.

[240] K Matusita and S. Sakka, "Kinetic study on non-isothermal crystallization of glass by thermal analysis," *Bull. Inst. Chem. Res. Kyoto Univ*, vol. 59, no. 3, pp. 159–171, 1981.

[241] K. Matusita, T. Komatsu, and R. Yokota, "Kinetics of non-isothermal crystallization process and activation energy for crystal growth in amorphous materials," *Journal of Materials Science*, vol. 19, no. 1, pp. 291–296, Jan. 1984.

[242] F. X. Qin, H. F. Zhang, B. Z. Ding, and Z. Q. Hu, "Nanocrystallization kinetics of Ni-based bulk amorphous alloy," *Intermetallics*, Bulk Metallic Glasses III, vol. 12, no. 10, pp. 1197–1203, Oct. 2004.

[243] R. Brning and K. Samwer, "Glass transition on long time scales," *Physical Review B*, vol. 46, no. 18, pp. 11 318–11 322, Nov. 1992.

[244] K. J. Crowley and G. Zografi, "The use of thermal methods for predicting glass-former fragility," *Thermochimica Acta*, New Advances in Pharmaceutical Thermal Analysis, vol. 380, no. 2, pp. 79–93, Dec. 2001.

[245] Vyazovkin Sergey, Sbirrazzuoli Nicolas, and Dranca Ion, "Variation in Activation Energy of the Glass Transition for Polymers of Different Dynamic Fragility," *Macromolecular Chemistry and Physics*, vol. 207, no. 13, pp. 1126–1130, Jun. 2006.

[246] J. W. Forbes, *Shock wave compression of condensed matter: a primer*. Springer Science & Business Media, 2013.

[247] B. R. Maddox, H. S. Park, C. H. Lu, B. A. Remington, S. Prisbrey, B. Kad, R. Luo, and M. A. Meyers, "Isentropic/shock compression and recovery methodology for materials using high-amplitude laser pulses," *Materials Science and Engineering: A*, vol. 578, pp. 354–361, Aug. 2013.

[248] A. A. Banishev, W. L. Shaw, W. P. Bassett, and D. D. Dlott, "High-Speed Laser-Launched Flyer Impacts Studied with Ultrafast Photography and Velocimetry," *Journal of Dynamic Behavior of Materials*, vol. 2, no. 2, pp. 194–206, Jun. 2016.

[249] R. Fabbro, J. Fournier, P. Ballard, D. Devaux, and J. Virmont, "Physical study of laserproduced plasma in confined geometry," *Journal of Applied Physics*, vol. 68, no. 2, pp. 775–784, Jul. 1990.

[250] D. L. Paisley, S.-N. Luo, S. R. Greenfield, and A. C. Koskelo, "Laser-launched flyer plate and confined laser ablation for shock wave loading: Validation and applications," *Review of Scientific Instruments*, vol. 79, no. 2, p. 023 902, Feb. 2008.

[251] S. C. Kelly, "Shock-compression of ni-al nanolayered foils using controlled laser-accelerated thin foil impact," PhD Dissertation, Georgia Institute of Technology, Department of Materials Science and Engineering, 2013.

[252] S. N. Luo, S. R. Greenfield, D. L. Paisley, R. P. Johnson, T. Shimada, D. D. Byler, E. N. Loomis, S. N. DiGiacomo, B. M. Patterson, K. J. McClellan, R. M. Dickerson, P. D. Peralta, A. C. Koskelo, and D. L. Tonks, "Long pulse laser driven shock wave loading for dynamic materials experiments," in *High-Power Laser Ablation VII*, vol. 7005, International Society for Optics and Photonics, May 2008, p. 700 514.

[253] S. Liu, D. Wang, T. Li, G. Chen, Z. Li, and Q. Peng, "Analysis of photonic Doppler velocimetry data based on the continuous wavelet transform," *Review of Scientific Instruments*, vol. 82, no. 2, p. 023 103, Feb. 2011.

[254] D. Scripka, "Statistical analysis of interferometer profiles," PhD thesis, Georgia Institute of Technology, 2017.

[255] D. Wackerbarth, *Plotdata v. 4.47*, Jun. 2016.

[256] J. T. Larsen and S. M. Lane, "Special Issue Radiative Properties of Hot Dense Matter HYADES-A plasma hydrodynamics code for dense plasma studies," *Journal of Quantitative Spectroscopy and Radiative Transfer*, vol. 51, no. 1, pp. 179–186, Jan. 1994.

[257] C. Wehrenberg, "Unpublished results: Hyades simulation."

[258] A. P. Hammersley, "FIT2d: A multi-purpose data reduction, analysis and visualization program," *Journal of Applied Crystallography*, vol. 49, no. 2, pp. 646–652, Apr. 2016.

[259] A. P. Hammersley, S. O. Svensson, A. Thompson, H. Graafsma, . Kvick, and J. P. Moy, "Calibration and correction of distortions in twodimensional detector systems," *Review of Scientific Instruments*, vol. 66, no. 3, pp. 2729–2733, Mar. 1995.

[260] A. P. Hammersley, S. O. Svensson, M. Hanfland, A. N. Fitch, and D. Hausermann, "Two-dimensional detector software: From real detector to idealised image or two-theta scan," *High Pressure Research*, vol. 14, no. 4-6, pp. 235–248, Jan. 1996.

[261] T. Degen, M. Sadki, E. Bron, U. Knig, and G. Nnert, "The HighScore suite," *Powder Diffraction*, vol. 29, no. S2, S13–S18, Dec. 2014.

[262] W. A. Dollase, "Correction of intensities for preferred orientation in powder diffractometry: Application of the March model," *Journal of Applied Crystallography*, vol. 19, no. 4, pp. 267–272, Aug. 1986.

[263] P. Juhs, T. Davis, C. L. Farrow, and S. J. L. Billinge, "PDFgetX3: A rapid and highly automatable program for processing powder diffraction data into total scattering pair distribution functions," *Journal of Applied Crystallography*, vol. 46, no. 2, pp. 560–566, Apr. 2013.

[264] T. Egami and S. J. L. Billinge, *Underneath the Bragg Peaks: Structural Analysis of Complex Materials*. Elsevier, 2003, ISBN: 978-0-08-042698-3.

[265] I. Bakonyi, "Atomic volumes and local structure of metallic glasses," *Acta Materialia*, vol. 53, no. 8, pp. 2509–2520, May 2005.

[266] B. Ravel and M. Newville, "ATHENA, ARTEMIS, HEPHAESTUS: Data analysis for X-ray absorption spectroscopy using IFEFFIT," *Journal of Synchrotron Radiation*, vol. 12, no. 4, pp. 537–541, Jul. 2005.

[267] Deepika, P. K. Jain, K. S. Rathore, and N. S. Saxena, "Structural characterization and phase transformation kinetics of $Se_{58}Ge_{42x}Pb_x$ (x=9, 12) chalcogenide glasses," *Journal of Non-Crystalline Solids*, vol. 355, no. 22, pp. 1274–1280, Jul. 2009.

[268] M. D. Migahed and T. Fahmy, "Structural relaxation around the glass transition temperature in amorphous polymer blends: Temperature and composition dependence," *Polymer*, vol. 35, no. 8, pp. 1688–1693, Apr. 1994.